The Star Formation and Dynamics of Nearby Galaxies

Keoikantse Moses Mogotsi

June 2016

Thesis presented for the degree of Doctor of Philosophy
in the Department of Astronomy.
UNIVERSITY OF CAPE TOWN

Supervisors: Prof. C. Carignan (UCT); Prof. G.R. Meurer (ICRAR UWA) & Prof. W.J.G. de Blok (ASTRON, UCT)

Abstract

A scaling relation between the surface density of star formation and gas in the disks of galaxies has become the basis of our understanding of extragalactic star formation on scales of hundreds of parsecs and larger. This is an empirical law but star formation is a complex process - the presence of gas at sufficiently high densities to collapse and form stars depends on a wide variety of physical processes. These processes can be thought of in terms of the stability of galaxy disks, which is a balance between the gravitational force and competing forces such as the outward force due to pressure. In this study I explore how star formation is related to galaxy dynamics in the central regions of galaxies. This is done by determining the dominant contributor to the inner dynamics of galaxies and developing star formation models based on self-regulating disks that maintain a constant sub-critical stability parameter. Stability parameters for a gas-only disk and a two-fluid disk containing both gas and stars are considered. These models are tested in the central regions of a sample of galaxies with a wide range of H I masses, sizes, morphologies and stellar masses. The analysis is performed using Hα integral field spectroscopy, R-band, narrowband Hα, and near-infrared photometry to determine the star formation rates and kinematics of the galaxies. In agreement with previous studies I find that the central stellar surface density is tightly correlated with the central velocity gradient, which traces the steepness of the inner gravitational well. The baryonic fractions found in the analysis suggest that baryons dominate the central density of most galaxies in the sample, but better constraints on these are needed to make more firm conclusions. There are correlations between the star formation surface density and velocity gradient, however the observed relations do not match predictions from the models. Tests suggest that the failure of the models is due to the implied stability parameters in the galaxy centers not being constant across the galaxy sample, and that the star formation laws used in the analysis may not hold over the full parameter space of the sample.

Acknowledgements

I would like to thank my supervisors for their support and help through my studies. I would also like to thank Pat Knezek and other observers for the great WIYN SparsePAK observing work. I would like to thank Tom Jarrett for to the surface brightness profiles of the WISE data and for help and advice on using the data. I am also grateful to the members of the HIPASS, SINGG, SUNGG, and WISE for their contributions to these projects which were crucial to this work. Thank you to the National Astronomy and Space Science Programme, Square Kilometre Array Africa, NRF, G.R. Meurer, C. Carignan and E. de Blok for the generous funding and grants which have allowed me to study astronomy at a postgraduate level and to do this research.

Ke leboga Mme, Ntate, Naome, Thabang... ke fitlhile kwano ka thuso, lerato, le tumelo ya lona.

Thank you to my family and friends! In no particular order:

The former members of the old MSc office, Fishbowl, and the current cool office: thanks for the great memories, camaraderie and help through all the years. Thuso, Iniyan, Riona, Kosma, Sally, Deanne, Ianja, Toky, Tom, Khaled, Zolile... your help with a huge variety of astro stuff is much appreciated! Rhodes Physics & Electronics class and Biochem group, NASSP 2009 Honours - thanks for all the good memories. For the first people I got to kind-of mentor: the NASSP Honours 2010 group, especially Mpati, Toky, Rajin, Michelle, Eli - I am proud of you, your success has helped push me along this long journey. Thank you to the UCT Astronomy Department for providing an environment where I could do my work; special thanks to Roz, Kurt, Sarah, Garry, Brad for your kindness and encouragement at various points while I've been in the department. Thanks to the NASSP organizers for providing the opportunity for me to go on this great adventure, special thanks to Nicky and Peter for their support and kindness. Thank you Claude for helping me, the encouragement, and help with getting

me funding through the last stretch. To Lesego, Kamo and Nozi: thanks guys, still appreciate all those good times with you to this day! We made it!

Thank you to Ellen for providing for being a kind and great host to me whenever I came to WA; Masterchef after a long day's work was a blast. I'd like to also thank Gerhardt, Anne & Lyra for being so welcoming and for the great cake, flower, guinea-pig, and plant excursions! Thanks to ICRAR-UWA for hosting me whenever I was in Perth, for the space, computer time and kindness by people there. Special shout-out to Jacinta, Gio, Rebecca, Sean, Scott, Stefan, Laura, Sarah and Toby for the good memories (minus all the Tim Tams I had to see) and letting me be a part of the group while I was there.

Christina, Iniyan, Thuso (+Millie), Riona thanks for the being around and helping me through this (I'd thank Zolile but he'd probably doubt that I mean it), you guys made being part of the department great and helped me navigate through some rough patches. Sally, thanks for all the helpful dassies. Andrea, Vere, Jackie, Eve, Cathy, Gopolang, Sue, Nikhi, Rajin, Anne-Marie, Shona, Olivia, Sal, Alan, Bronwyn, Nathaneal, Sipho, Lebohang, Joy, Francois, Tess, Anne, Nicola, Silvia F., Silvia V., Deanne, Rocco, Kosma, Wendy, and others thank you for filling the past few years with such good experiences and memories. Meg, thanks a lot for helping me get through the last stretch (the breaks were awesome) and for help with some of the editing - it means a lot and is much appreciated! Shells, thanks for helping out and listening to all my complaints, frustrations and shouts of joy through the ups and downs of this thesis. Thanks to everyone that has contributed to the soundscapes and fictional worlds that have accompanied me and helped me on this journey. Sometimes the College Dropouts inspire us more than most to get our degrees. And it turns out that K-Dot was right: "We gon' be Alright".

And thank you to the many other people who have helped contribute to my life and this journey. If I've forgotten anyone important it was not on purpose.

Plagiarism Declaration

I, Keoikantse Moses Mogotsi, know the meaning of plagiarism and declare that all of the work in the document, save for that which is properly acknowledged, is my own.

,

Contents

Outline

In the Introduction (Chapter 1) I introduce galaxies and star formation. I describe developments in our understanding of star formation in nearby galaxies focusing on how star formation is observed, the star formation law, the stability of galaxy disks and conclude with the aims of the thesis.

In Chapter 2 (Theory) I derive the models that are used and in this analysis and I determine the relationships that the data will be used to test. I use the following chapter (Chapter 3 : Data) to discuss the how the data that is used in the study was acquired and reduced.

Chapter 4 (Measurements) deals with the kinematic analysis of the data such as the methods used to determine the kinematic parameters that are required for the study. I discuss different methods and functions used to determine the kinematic parameters and their effectiveness and I analyze the outputs from these methods. I also discuss the conversion of the photometric data to quantities that are used in the analysis.

Chapter 5 and 6 deal with using all the data and fitted parameters to study the how the stellar component of galaxies relates to inner dynamics of galaxies (Chapter 5) and how the star formation surface density is related to galaxy dynamics (Chapter 6). In these chapters I test the models derived in Chapter 2 and determine if those models hold and what the results tell us about the star formation and dynamics of the inner parts of galaxies.

The Appendix contains multi-panel plots of the results of the kinematic analysis for the galaxy sample I use for this analysis.

Chapter 1

Introduction

1.1 Galaxies

Galaxies are large gravitationally bound collections of stars, gas and dark matter. Our solar system, the other visible stars and billions of other stars too faint to see with the naked eye and their associated planetary systems all belong to a galaxy called the Milky Way. There are three other galaxies visible to the naked eye; they are the neighbouring large and small magellanic clouds (LMC and SMC) and our large and similarly shaped neighbour: Andromeda (M31). Ever since Galileo Galilei first used a telescope to observe astronomical objects, telescopes have been used to explore objects increasingly further away from our planet at increasing levels of detail beyond what our naked eyes can do. The objects that we call galaxies were first identified as nebulae within our own Galaxy (which was originally believed to be the extent of the Universe). Their location within the Milky Way and distance from us was debated during "The Great Debate" between Curtis and Shapley in 1921. These nebuale were different from the points of light identified as stars and planets since they were larger and their light was more diffuse. Eventually observations by Hubble (1922) provided evidence that some of the objects that were identified as nebulae were too far from the earth to be within our Galaxy. These extragalactic nebulae, which were later termed galaxies came in a wide array of shapes and sizes. Early observations were of the combined starlight from these fuzzy and diffuse galaxies. As technology improved larger and better telescopes with more sensitive detectors were built and resolved stars within these nearby galaxies. These improvements in the photometric observations led to studies of the different shapes of galaxies and the structures within them. Further improvements in technology led to the use of different observing filters which resulted in observations of the objects in small frequency bands and for the colours of these objects to be determined. Colour is defined as the ratio in flux (written as the difference between the logarithms of the flux) between two observing bands (filters). Blue objects are objects which emit more

of their light at short wavelengths (within the observing bands used in the analysis). Therefore colours are useful for determining the rough wavelength dependence of light emitted from an object. The development of spectrographs allowed observations of the amount of light received from these galaxies as a function of wavelength (spectra). Stars of different types have different surface temperatures. They behave like black body radiators which means that their fluxes peak at different wavelengths. Their spectra have different features due to the composition of their photospheres. Therefore photometry and spectroscopy can be used to determine the composition of stellar populations in galaxies. Due to the Doppler effect the spectra also provide information about the relative velocities of galaxies. These observing methods were used to study the nature, structure, evolution and internal processes of galaxies.

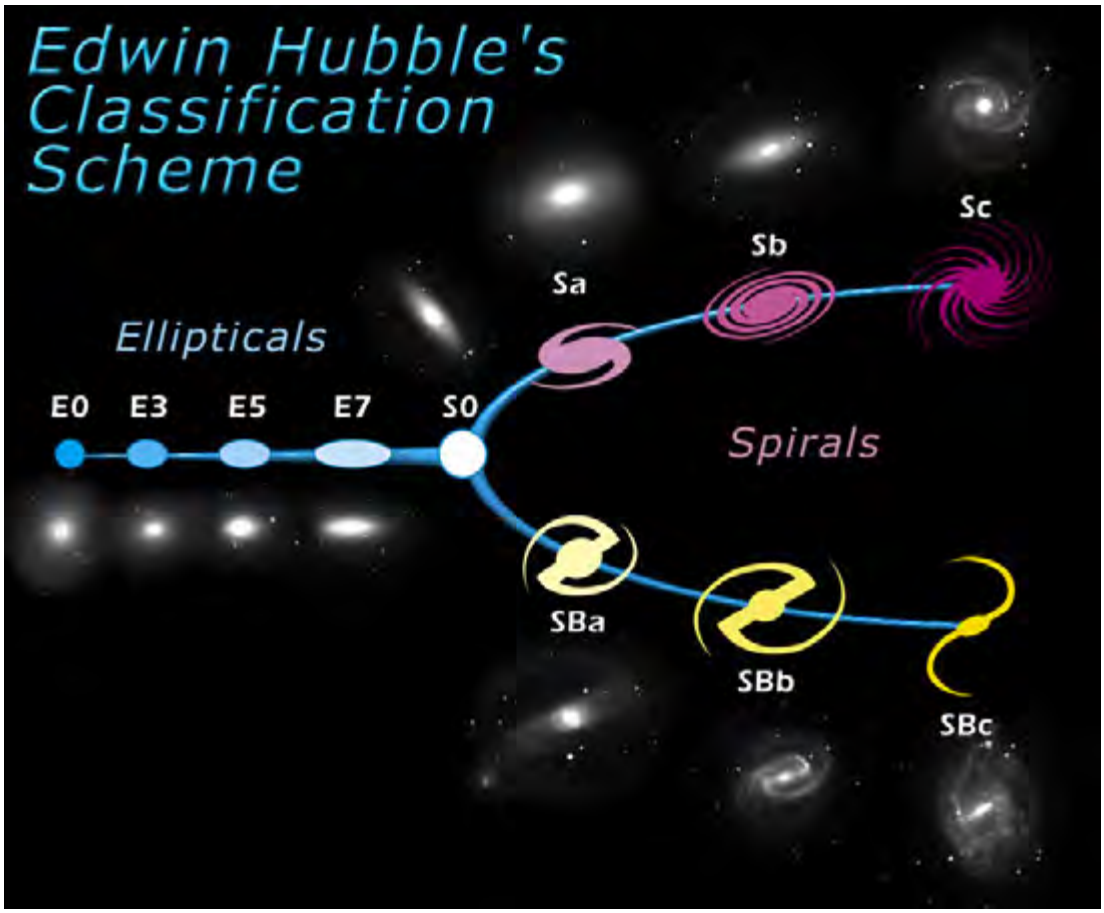

Figure 1.1: A modern representation of the Hubble's classification scheme called the Hubble Tuning Fork, showing the classification of elliptical and spiral galaxies. *Image credit: NASA and ESA. http://www.spacetelescope.org/images/heic9902o*

Hubble (1922b) proposed a method of galaxy classification based on photographic

images. It was extended by Hubble (1926) and they divided galaxies into different classes: ellipticals (E), normal and barred spirals (S and SB respectively) and irregular galaxies (Irr). A visual representation of the Hubble classification scheme is shown in Figure 1.1 . The ellipticals are described as having rotational symmetry and being relatively featureless objects. They were classified according to their ellipticity, where the sequence from E0 to E7 is defined by their ellipticity and E7 is where the juncture between spirals and ellipticals occurs. Spirals have substructure: spiral arms emanate from a bright central region. The Hubble classification system for spirals is based on the size of the nuclear bulge relative to the disk, how unwound the spiral arms are, and how well resolved the arms and disk are (Hubble 1926, Sandage 1975). Spiral galaxies closest to E7 galaxies have very big nuclear regions with tightly wound spiral arms that are unresolved. Spiral galaxies are divided into two groups: those with what is described as a bar of nebulosity that extends diametrically across the nucleus (Hubble 1926) which were called barred spirals (SB), and those without such a structure (S). Both types of spirals follow the same sequence. The sequence moves from the suffixes "a", "b", to "c" according to how unwound and more pronounced the spiral arms are compared to the nuclear region. The sequence follows an increase in observed structural complexity. Hubble (1926) used the terms "early" and "late" types to describe this increase in complexity. The terms are still used to this day. Irregular galaxies are not symmetric and lack a bright nuclear region. Hubble believed that galaxies evolved from early to late types, however, modern observations have been more supportive of the opposite scenario (evolution from late to early types). More observations revealed types of galaxies that the original classification did not cover: S0 galaxies (lenticular galaxies, they fill the gap between E7 and Sa galaxies; Spitzer & Baade 1951,Sandage 1961), dwarf galaxies (Shapley 1938a, 1938b) and interacting and peculiar galaxies (e.g., Vorontsov-Velyaminov 1959, Zwicky 1959) are some examples of these galaxies. The original spiral sequence was extended to Sd galaxies and then further to so-called magellanic spirals based on the weak spiral structures seen in the LMC (de Vaucouleurs 1954, 1955). The Hubble classification (and its variants) is still the most commonly used classification scheme and is very useful for describing the general structure and shapes of galaxies. Further studies revealed why the structures of spirals, ellipticals and irregulars differ from each other. More differences between them were discovered and their evolution is a popular topic of study to this day.

1.2 Star Formation

Studying the colours of galaxies can provide information about their stellar content. Early studies by Pettit (1954), Stebbins & Whitford (1952), Baum (1959), Tifft (1958), de Vaucouleurs (1960a, 1960b), Holmberg (1975), Sandage (1975), Hodge (1973) and many others provided studies of the broad-band colours of galaxies (Sandage 1975). These measurements showed that the central regions of Irr and Sc galaxies are blue and have many hot stars; and the spiral arms of Sc, Sb and Sa galaxies also contain many of these hot stars (Sandage 1975). Spectroscopic studies provide a more precise window into the stellar content of galaxies because the spectra of the galaxies can be treated as composites of all their stars. The presence and relative strength of spectral features can then be used to determine the fraction of different types of stars. Humason (1936) and Humason et al. (1956) performed spectroscopic observations of nearby galaxies and determined which stellar spectral types best described the galaxy spectra. They found that the spectra of early type galaxies (E, Sa/SBa, Sb) are dominated by stars that are cooler than those found in later type galaxies (Sc). Therefore their spectra showed that light from late type galaxies (spirals) is composed of a higher fraction of hot blue stars than early type galaxies (i.e., the fraction of blue giants decreases as galaxies move from Sc to Sa to E) (Roberts 1963). Mayall (1960), Munch (1960) and Morgan (1958) showed that blue extragalactic spectra also showed signs of very high mass stars (B− to O types). Morgan & Mayall (1957) analyzed the spectra of nearby galaxies and found that the spectra of early type galaxies are characterized by older and less massive stars compared to those of later types. This trend was confirmed in spectra that extended into longer wavelengths than other studies (Spinrad 1962). Hot massive stars cannot maintain their energy production for billions of years (Whipple 1946) and therefore have shorter lifetimes than the less massive and cooler stars. Whipple (1946) suggested that their short lifespans and presence in galaxies mean that there must be current star formation in galaxies. The presence of these young stars put constraints on the history of star formation in galaxies and proved to be an indicator of recent (within a few hundred million years) star formation.

Whipple (1946) outlined a possible process of how star formation occurs. The initial stages of the process involves particles in the interstellar medium (ISM) getting attracted to each other by forces described by Spitzer (1941b). Spitzer (1941b) proposed that while being irradiated, when two dust particles absorb the radiation, the radiation density between them decreases and the radiation pressure causes them to be attracted to each other. If large enough concentrations of particles form and are dense and far from bright stars, they can attract other particles. They can then grow

fast enough to accumulate enough material that they can eventually become dense enough for nuclear fusion to begin (Whipple 1946). The accumulation of material by a dense concentration of gas and dust followed by collapse to form a star is now the accepted process by which stars form. Stars therefore form from the interstellar medium. Clouds need to be large, dense and have high opacities in order to withstand the effects of galactic shear and eventually form stars (Whipple 1946). These "dark", high opacity clouds were already being observed at the time (e.g., McCuskey 1941). These clouds are now called molecular clouds, and giant molecular clouds (GMCs) which contain many molecular clouds are the sites of star formation. Whipple (1946) noted that studies (especially Spitzer's) suggested that the lack of hot supergiant stars in ellipticals is linked to the lack of aggregation of interstellar material in these systems and that the presence of these stars in spiral galaxies is connected to how their rotation can maintain their large angular momentum and "dark" clouds.

The simplest and most common form of baryonic matter in the Universe is neutral atomic hydrogen gas: H I. It is detected by its forbidden hyperfine spin-flip transition that occurs at a wavelength of 21 cm which was predicted by van de Hulst (1945). Ewen & Purcell (1951) were the first to detect it and the detection was confirmed by Muller & Oort (1951). Thackeray (1948), Biermann (1955), van den Bergh (1957) studied how star formation depletes the interstellar medium of galaxies. The gas is either turned into stars or expelled by the stars (van den Bergh 1957). The fraction of H I in galaxies was observed to increase as galaxies became more late types (e.g., it increases as you move from Sb to Sc to Irr galaxies) (Epstein 1962, Roberts 1962, Roberts 1963). Therefore galaxies with a younger stellar population had higher fractions of H I than those with older, cooler and less massive stars. In the dense parts of galaxies (the so called "dark clouds") the temperatures and densities allow the formation of molecular gas. The most abundant molecule in the Universe is H_2. The H_2 molecule has no permanent electric dipole moment and therefore has no dipolar rotational transitions. The lowest energy transitions of the molecule are in the infrared, are very weak and excited by gas temperatures that are very high (compared to the typical environment where the molecules are found) (Bolatto et al. 2013, Dabrowski 1984). The most abundant elements in the ISM besides hydrogen and helium are oxygen and carbon, in the same dense regions where H_2 is expected to form they combine to form CO (Bolatto et al. 2013). This molecule has a weak permanent dipole, its ground rotational transition has an excitation energy of 5.53 K, and its first rotational transition is observable from the ground. These properties have made it an ideal tracer of the hard to detect H_2 gas (Bolatto et al. 2013). Carbon monoxide was used as a tracer of molecular hydrogen H_2 by studies such as Sanders et al. (1984), Bloemen et al. (1986) and Dickman et

al. (1986). Stars form in regions of high density gas therefore one would expect the molecular gas to be correlated with star formation. The CO was indeed found to correlate with indicators of star formation (blue luminosity) by Young & Scoville (1982). Further studies of star formation related the presence of gas (the fuel) and its density to star formation. The accurate quantification of both atomic and molecular gas in galaxies has become increasingly important in order to understand star formation and to make better constraints on models that describe star formation.

1.2.1 Star Formation Measurements and Tracers

In early star formation studies the fraction of hot young stars was used as an indicator of the amount of star formation in galaxies. Tinsley (1968, 1972) developed galaxy evolution models which predicted galaxy colours, and from these they predicted the first quantitative star formation rates. Their models and those by Searle et al. (1973) agreed with studies by Roberts (1963) that star formation rates (SFR) are higher in late type galaxies than in early types. The determination of star formation rates from observations were not easy and required tracers. Identifying and counting individual young stars is difficult because some of them may be too faint or unresolved and detailed observations would be required in order to determine their ages and stellar types. This would be too impractical to do for an entire galaxy, whereas ideally these studies should be performed for a large number of galaxies, some too far away to even resolve individual clusters of stars.

Emission line studies proved to be very useful for this because the young hot supergiant stars could heat the surrounding gas causing it to emit radiation. The [O II] emission was initially the most promising to use as a star formation tracer. Curtis (1933) and Mayall (1939) were the first to perform emission line studies of galaxies. Mayall (1939) showed that the strength and intensity of forbidden λ 3727 [O II] emission is related to the strength of other emission lines such as Hβ and Hδ and that it is related to the strength of near-ultraviolet emission (near UV). The central regions of late type spirals had higher concentrations of [O II] emission centers than early types (Mayall 1939). Late types were found to have intense [O II] emission in prominent spiral structures such as spiral arms and rings (Mayall 1939). As an extension to the analysis by Hubble (1922), Mayall (1939) suggested that the emission comes from gaseous nebulae that are heated by young stars. The [O II] emission was found to behave in a similar manner to hot young stars (Roberts 1963), as data from Humason (1956) and Mayall (1958) showed that the occurrence of the [O II] line increases for later type galaxies

(Roberts 1963). However, oxygen is not as abundant and prevalent in the Universe as hydrogen is and the wavelength of the emission line is relatively short compared to other optical lines and is therefore quite susceptible to absorption by intervening material. The luminosity of forbidden lines such as [O II] is sensitive to the ionization state. These drawbacks along with the relative difficulty of mapping [O II] emission allowed Hα emission to become a more successful and widely used tracer.

Recombination lines such as Hα are due to the short wavelength emission from massive stars (stars with masses greater than 10 $M_\odot$ which have lifetimes less than 20 Myr) being re-emitted by the hydrogen in the nebulae surrounding these massive stars. The amount of hydrogen gas and its ionization equilibrium determine the amount of Hα emission. Observations by Israel & van der Kruit (1974) and Oort (1974) showed that the amount of Hα emission in spiral galaxies is limited by ionization and is therefore dependent on the number of O and high-mass B stars (Cohen 1976). Cohen (1976) observed that there is a relationship between colour and Hα emission: bluer galaxies have more Hα emission. This confirmed that bluer galaxies have a higher fraction of young high-mass stars than red ones, and the young stars can be traced by Hα emission. Work by Bagnuolo (1976) and Huchra (1977) extended this analysis. Kennicutt & Kent (1983) extended their analysis and determined SFRs for 200 galaxies using their integrated Hα emission. This began a new era of using Hα to determine and study the star formation rates of galaxies. Hα is an indirect tracer, measurements of direct radiation from stars were also used as star formation tracers. Ultraviolet (UV) radiation became widely used for this purpose.

The Far-UV flux ($\lambda < 2500$ Å) from spiral galaxies and irregulars are dominated by O and B stars (Lequeux 1980), which are massive and short-lived, therefore this flux is an indicator of current massive star formation (Lequeux 1980, Vangioni-Flam et al. 1980). Early observations by Israel & Koornneef (1979), Vangioni-Flam et al. (1980), Lequeux et al. (1981) studied the star formation in H II regions of a few nearby galaxies. Donas & Deharveng (1984) used UV observations to determine the star formation rates of 40 nearby spiral and irregular galaxies. Many studies since then such as Donas et al. (1987), Buat (1992), Deharveng et al. (1994) and Meurer et al. (1995), Wong (2006), Salim et al. (2007), and Gil de Paz et al. (2007) increased the database for galaxies observed in the UV and studied star formation in nearby galaxies using this tracer. UV emission is directly linked to direct emission from hot young stars (typcially with masses above 5 $M_\odot$ and lifetimes less than a few million years in the commonly used UV observation range: 1500 to 2500 Å) and this makes it an ideal star formation

tracer (Kennicutt 1998). However this method is very sensitive to dust extinction and the form of the initial mass function. The spatial distribution of the extinction is very patchy and can have a large effect on the observed UV emission (Buat 1992, Buat & Xu 1996, Calzetti et al. 1994, Kennicutt 1998).

Interstellar dust absorbs radiation from stars and re-emits it at infrared wavelengths (typically at 10 to 300 μm). Due to its nature it preferentially absorbs short wavelength radiation which is produced by massive stars. Therefore infrared emission from dust can be used to trace the presence of massive young stars and hence determine star formation rate (Lequeux 1980). Serra et al. (1980) performed a study of the efficiency of dust heating and confirmed that massive stars are more efficient at heating the dust than low-mass stars. Studies by Mezger (1978) and Smith et al. (1978) studied the rate at which Lyman continuum photons (photons with wavelengths shorter than 912 Å) are emitted by O stars in the Galaxy and what fraction of that is absorbed by dust. They used these studies to estimate the rate of star formation in the Galaxy. Near-infrared observations of more than a hundred galaxies were made from 2 μm to 300 μm by Kleinman & Low (1970), Rieke & Low (1972), Rieke & Low (1975), Rieke & Lebofsky (1978) and Telesco & Harper (1980). Telesco & Harper (1980) showed that infrared emission is common in spiral galaxies. The far-infrared emission was found to be associated with ongoing and recent star formation (Gatley & Becklin 1981, Rieke & Lebofsky 1982), can thus be used as a measure of the current rate of star formation (Stein & Soifer 1983). Stein & Soifer (1983) referred to the dust as a "frequency converter" that absorbs short-wavelength photons by the young stars and reemits it in the far-infrared.

Further studies by Rickard & Harvey (1982) showed that far-infrared flux is strongly correlated with the flux of high density molecular gas (in the form of CO). Scoville et al. (1983) performed a 10 μm study of 53 nearby spiral galaxies in the Virgo cluster, they associated the near-infrared flux to massive star formation in the galaxies through the absorption and reprocessing of Lyman α photons by dust. They concluded that the mid-infrared emission indicates that all spiral galaxies have star formation in their centers and determined the average star formation rate of the sample from this emission. The Infrared Astronomical Satellite (IRAS) mission (Neugebauer et al. 1984) revolutionized infrared studies of nearby galaxies and set the stage for more studies of the ISM and star formation through infrared observations (e.g., de Jong et al. 1984, Soifer et al. 1984, Helou 1986, Moshir et al. 1992). Questions were raised about the origin of the observed far-infrared flux. Some of the flux was attributed to star formation and

heating from hot young stars and the infrared luminoisty was correlated with UV and Hα luminosities (Lonsdale & Helou 1987, Sauvage & Thuan 1992, Buat & Xu 1996), but some was attributed to older stars heating dust (Lonsdale & Helou 1987, Buat & Deharveng 1988, Sauvage & Thuan 1992, Walterbos & Greenawalt 1996). Monochromatic mid-infrared tracers such as the 8 μm emission, which is dominated by emission from polycyclic aromatic hydrocarbons (PAHs, Leger & Puget 1984, Sellgren 1984, 1990, Li & Draine 2002, Boselli et al. 2004, Tielens 2008) and 24 μm emission were found to trace star formation (e.g., Calzetti et al. 2005, Perez-Gonzalez et al. 2006, Kennicutt et al. 2007). They became the preferred infrared tracers of star formation in nearby galaxy studies (e.g., Calzetti et al. 2007, Kennicutt et al. 2007, Smith et al. 2007, Prescott et al. 2007, Leroy et al. 2008), especially with the arrival of the *Spitzer* Space Telescope (Werner et al. 2004). The *Herschel Space Observatory* (Pilbratt et al. 2010), *AKARI* mission (Murakami et al. 2007) and *Wide-field Infrared Survey Explorer* (Wright et al. 2010). have recently contributed to the wealth of infrared star formation studies over different parts of the infrared spectrum. Work by Calzetti et al. (2007) led to the use of hybrid star formation tracers that combined UV or Hα emission with mid-infrared tracers such as 8 μm and 24 μm to determine the total star formation rate. This combines the strength of tracers whose emission comes directly from the stars (UV) or surrounding gas (Hα) (but are sensitive to dust extinction) and tracers which are dependent on dust (which causes extinction of) or molecules reprocessing the light emitted by hot young stars .

The Hα, infrared, UV and other star formation indicators were used to determine and study star formation rates for large samples of galaxies. Understanding how star formation works and how it relates to other galaxy properties is done through star formation models and laws.

1.2.2 Star Formation Models

Schmidt (1959) developed a simple empirical power law relation where the star formation rate only depends on the local gas density ρ_g:

$$SFR = a\rho_g^n, \tag{1.1}$$

where a and n are constants. This relation was widely adopted and used to describe the star formation in nearby galaxies. Dieter (1960) found a positive correlation between OB stars and dense HI regions. Muhleman & Walker (1964) found a negative correlation between O-type stars and HI regions. In their analysis Sanduleak (1969) found that there is a correlation between the density of young stars ρ_s and gas density

in the SMC : $\rho_s \sim \rho_g^{1.8}$. Sanduleak (1969) proposed that for thin disks the surface density can be used to represent the volume density. Other studies such as Hamajima & Tosa (1975), Emerson (1977) and Berkhuijsen (1977) confirmed that there is a correlation between the surface density of H II regions, young OB associations and HI surface density; they found that the distribution of HII regions and dense HI gas are correlated. The H I emission was also seen to coincide with dust lanes (Emerson 1977). They found that the power law index of the Schmidt (1959) relation was $n \sim 2$. However there were other studies like Hartwick (1971), Madore et al. (1974), Mezger & Smith (1976), Madore (1977) and Freedman (1984) which found that n ranged from 1 to 4. Schmidt (1963) suggested that n is not constant - it is larger for more massive stars than it is for low-mass stars. The use of H II regions as opposed to bright stars, beam smearing, missing atomic or molecular gas and the different correlation methods used were suggested as reasons for discrepancies in n determined in different studies (e.g., Talbot 1971, Einasto 1972, Madore 1977, Talbot 1980).

Further studies raised more questions about the value of n and whether the Schmidt law with a constant n is universal (e.g., Miller & Scalo 1979, Twarog 1980, Kennicutt 1983, Schommer & Bothun 1983, Donas & Deharveng 1984, Bushouse 1987, Kennicutt et al. 1987, Lord 1987, van Driel 1987, Skillman 1987, Guiderdoni 1987). Talbot & Arnett (1975), Dopita (1985), Wyse (1986), Silk (1987) and other authors proposed new star formation laws or variations of the Schmidt law. Talbot & Arnett (1975) modeled the radial structure, components and star formation of disk galaxies. Dopita (1985) proposed a star formation law based on the star formation and stellar disk pressurizing the interstellar medium and therefore maintaining the pressure support of the gas. This law related the star formation rate per unit gas mass to the ratio of gas to total surface densities. Tacconi & Young (1986) and Wyse (1986) proposed Schmidt law that incorporates H I and molecular gas. Studies such as Hunter & Gallagher (1986) even suggested that there might not be a global law which describes star formation.

The seminal study of Kennicutt (1989) studied the Schmidt star formation law and tested it using different galaxies all put on the same absolute scale. This analysis was done by using Hα surface brightness to determine the absolute star formation rate; H I and CO emission were used to trace atomic and molecular gas and to therefore determine the total gas density. This study involved 15 galaxies and allowed for studies of star formation over a larger range of gas densities and star formation environments than in previous studies. The result of the study was that the surface density version of the Schmidt law describes the behaviour of regions with high star formation density

and gas density; and the power-law index of the relation was 1.3 ± 0.3 :

$$\Sigma_{\rm SFR} = A\Sigma_g^N, \tag{1.2}$$

where A is the constant of proportionality and describes the efficiency of star formation, and N is the power law index of the relationship ($N = 1.3$ in the Kennicutt 1989 case). Further studies of the Schmidt law using UV and far-infrared data to derive star formation rates (SFRs) confirmed the correlation and found power-law index values ranging from 0.9 to 1.7 (Buat et al. 1989, Buat 1992, Deharveng et al. 1994). Kennicutt (1998) tested the relation with up to date (at the time) Hα, H I, CO and far-infrared data and found a power law index of 1.4 ± 0.15. Variations in the initial mass function used for the star formation law and the conversion from CO luminosity to H_2 mass (also called the $X(CO)$) are sources of uncertainty that can change the derived value of the power-law index by 0.2 to 0.3 (Kennicutt & Evans 2012, Narayanan et al. 2012). Subsequent work by Martin & Kennicutt (2001), Wong & Blitz (2002), Boissier et al. (2003) and others confirmed the correlation (with varying values of N) between gas and star formation. Studies that focused on the relationship between star formation surface density and the molecular gas surface density such as Heyer et al. (2004), Komugi et al. (2005) and Schuster et al. (2007) found that the relationship holds when only molecular gas is considered. Deviations in the integrated law were found for low metallicity galaxies and low surface brightness galaxies (Wyder et al. 2009, Kennicutt & Evans 2012). The law was tested for highly star-forming galaxies (e.g., starbursts) extending to high redshifts ($z \geq 2$) (Bouché et al. 2007, Daddi et al. 2010, Genzel 2010) and it was found that these tend to follow the same relation as the low redshift normal star forming galaxies but with higher values of A. Higher A values mean higher efficiencies, therefore these galaxies form stars at higher efficiencies than normal star forming galaxies. The results are highly dependent on $X(CO)$ and complex behaviour could result in a single power law for these galaxies.

Improvements in H I, mid-infrared, and CO observations led to The H I Nearby Galaxy Survey (THINGS, Walter et al. 2008), the *Spitzer* Infrared Nearby Galaxy Survey (SINGS, Kennicutt et al. 2003) and HERA Extragalactic CO Line Survey (HERACLES, Leroy et al. 2009). These surveys were used to perform systematic and sub-kiloparsec scale studies of the star formation in galaxies (using multiple star formation tracers) and how it is related to the gas density and dynamical properties of nearby galaxies at unprecedented sensitivity and resolution (Bigiel et al. 2008, Leroy et al. 2008, Tamburro et al. 2008). Bigiel et al. (2008) confirmed the presence of the $\Sigma_{\rm SFR} = A\Sigma_g^N$ correlation at sub-kpc scales, but their results showed when the total gas surface density is considered there are three different regimes (low density, intermediate

and high density regimes) where N varied. The most significant result from their study is that there is a tight correlation between molecular gas surface density and $\Sigma_{\rm SFR}$ with $N \sim 1.0 \pm 0.2$. Further studies such as Schruba et al. (2011) showed that the relation extends to regions where molecular gas is not the dominant gas component. It should be noted that other studies which use CO to trace the molecular gas density have found higher values of N (e.g., Verley et al. 2010, Suzuki et al. 2010, Liu et al. 2011, Rahman et al. 2011, Momose et al. 2012, 2013) and others found similar values of N (e.g., Eales et al. 2010, Rahman et al. 2012). Some authors have used extragalactic observations of higher gas density tracers like HCN (Gao & Solomon 2004) to suggest that the relation is tighter for higher density tracers because the underlying relationship is between star formation surface density and the amount of high density gas (Lada et al. 2012).

The so-called Kennicutt - Schmidt relation is an empirical scaling law, and other authors have attempted to use it and other methods to derive a more physically based star formation law. Simple assumptions such as assuming the disk collapses on timescales similar to free-fall timescales lead to similar scaling relations as the Kennicutt-Schmidt law (e.g., Leroy et al. 2008). These can be extended for cases of varying disk densities (Krumholz & McKee 2005) and pressures (Elmegreen 1989) to produce more complex star formation laws (e.g., Leroy et al. 2008). Assuming that the star formation rate scales with the growth rate of perturbations in the disk the Kennicutt-Schmidt relation is retrieved with $N = 1.5$ (Kennicutt 1998). Star formation laws based on how the fraction of molecular to atomic gas and the likelihood of the formation of overdensities in the interstellar medium are dependent on the pressure in the disk (Elmegreen 1989, Elmegreen 1993, Elmegreen & Parravano 1994) have developed based on work by Elmegreen (1989), Wong & Blitz (2002) and Blitz & Rosolowsky (2006). An extension of this (because the pressure is affected by the stellar density) is the scaling relation between the star formation surface density and a combination of the gas and stellar surface densities which were also considered by Dopita & Ryder (1994) and Shi et al. (2011). Correlations between the stellar and star formation surface densities have been observed in nearby galaxies (Hunter et al. 1998). Krumholz et al. (2012) extended star formation models based on the free-fall timescale by developing a volumetric star formation law where the volume density was estimated by using the local free fall time scale and gas surface density. Tan (2000) developed a star formation law based on star formation being triggered by gas cloud collisions and these collisions therefore setting the star formation timescale. Elmegreen (2000) suggested that the rate of star formation is proportional to the density of high density cores within molecular clouds and the fraction of gas within these cores. A commonly used dynamical star formation law is based on work by Silk (1997) and Elmegreen (1997), they proposed a star formation

law based on the dynamical timescale, whereby the star formation surface density is set by the surface density of the gas and its orbital timescale (which is related to the dynamical timescale). Similar models had been studied before by Wyse (1986) and Wyse & Silk (1989). Kennicutt (1998) tested the model and found that it holds for galaxy-averaged integrated gas densities and star formation surface densities and orbital timescales measured at the edge of the disk.

Leroy et al. (2008) performed a comprehensive study of different star formation rate relations and the efficiency of star formation on sub-kiloparsec scales. They confirmed the tight relationship between star formation surface density and molecular gas density and that the efficiency of star formation is constant for molecular gas. This trend extends to regions where the molecular gas is not the dominant gas component (Schruba et al. 2011). It should be noted that these studies are based on the disks of bright, gas-rich, nearby galaxies with intermediate gas densities (between $\sim 10\,M_{\odot}/pc^2$ and $200\,M_{\odot}/pc^2$) and near solar metallicities. In the following study we will test some of these star formation laws on the central regions at sub-kiloparsec scales of a larger range of galaxies than explored by the Bigiel et al. (2008) and Leroy et al. (2008) studies.

1.2.3 Disk Stability

Stars form from the collapse of gas clouds, therefore the question of what it takes for the gas in galaxy disks to collapse is an important one. Related to this is the question of which regions of galaxies form stars, or rather what does it take for gas to form stars. A method to address this question is to determine "thresholds" above which stars can form. A simple form of this is determining the gas densities above which stars can form. Studies such as Skillman (1987), Schaye (2004) and de Blok & Walter (2006) found that H I density thresholds can be used to predict where stars form in galaxies. An interpretation of this threshold is that these are the densities that gas becomes gravitationally unstable and forms the GMCs where stars form (Schaye 2004). Schaye (2004) determined this threshold H I density to be $\Sigma_{HI} = 10 M_{\odot}/pc^2$. This is the density above which H I becomes saturated (i.e., higher densities of gas only exist in the molecular phase, H I densities themselves do not exceed this threshold) in bright, nearby and high metallicity galaxies (Martin & Kennicutt 2001, Wong & Blitz 2002, Bigiel et al. 2008). Neutral hydrogen is the major component of the neutral medium. This neutral medium can be divided into a warm neutral medium that has temperatures of a few thousand Kelvin and densities of $n \sim 0.1$ - $1\,\mathrm{atoms/cm^3}$ (Cox 2005) and the cold neutral medium which has temperatures less than 100 K and densities greater than $10\,\mathrm{atoms/cm^3}$ (Field et al. 1969, Cox 2005). The cold neutral medium is the

phase between warm H I and molecular gas (which has temperatures that can be as low as 10 K and densities exceeding 20 atoms/cm^3, Kennicutt & Evans 2002). Therefore the ability to form stars can be related via the aforementioned thresholds and others to the ability to form the cold neutral medium, which can regulate the formation of giant molecular clouds and hence star formation (McKee & Ostriker 1977, Wolfire 2003, Schaye 2004). Models where the formation of molecular clouds is regulated by galactic shear (clouds would have to form before the shear tears them apart) have also been put forward (Hunter et al. 1998).

An important factor in physically motivated star formation laws and in understanding large-scale star formation is the stability of galaxy disks against gravitational collapse. Galaxy disks can be described by the early models developed by Freeman (1970). There are many early studies of the stability of self-gravitating disks (e.g., Toomre 1964, Goldreich & Lynden-Bell 1965, Elmegreen 1979, Cowie 1981, Jog & Solomon 1984, Larson 1983, 1988), and it was applied to star formation in galaxies by authors such as Spitzer (1968) and Quirk (1972). The simplest and most widely used stability parameter is the Toomre Q parameter which is based on work of Toomre (1964). It describes the stability of a thin isothermal purely gaseous disk as a function of the gas surface density Σ_g, sound speed c_s (usually parameterized in the form of the typical width of the gas velocity profiles: the velocity dispersion σ_g) and the epicyclic frequency κ (which parameterizes the rate of change of the rotation velocity in a galaxy as a function of radius) in the following form:

$$Q = \frac{c_s \kappa}{\pi G \Sigma_g}. \tag{1.3}$$

Quirk (1972) hypothesized that gas in rotating galaxy disks self-regulates and has stability parameters just above the critical density at which collapse occurs. Kennicutt (1989) found that the threshold densities and radii predicted by the simple gas-only Toomre parameter match observations and the gas in the galaxies is subcritical with Q_g roughly constant at $Q_g \sim 1.6$. Despite its simplicity the gas-only Toomre criterion has been found to match observations (e.g., Caldwell 1992, van der Hulst 1993, Ferguson et al. 1998, Martin & Kennicutt 2001). A roughly constant $Q_g \sim 1.5$ was found by Martin & Kennicutt (2001). Hunter et al. (1998) disscuss how various processes such as stellar feedback all contribute to maintaining a roughly constant Q. There were also studies such as Hunter et al. (1998) and Wong & Blitz (2002) which did not find a correlation between Q_g and star formation. The limitations of the model have been studied by many authors (e.g., Jog & Solomon 1984, Romeo 1992, Elmegreen 1992, Wang & Silk 1994, Ferguson et al. 1998, Hunter et al. 1998, Kim & Ostriker 2001, 2007, de Blok & Walter 2006, Romeo & Wiegert 2011, Elmegreen 2011, Romeo & Falstad 2013, Zheng

2013). They range from the non-inclusion of the stellar component of disks (e.g., Jog & Solomon 1984, Wang & Silk 1994, Hunter et al. 1998, Rafikov 2001), incorrect and changing velocity dispersions (Ferguson et al. 1998, de Blok & Walter 2006), increased disk thickness (e.g., Romeo 1992, Romeo & Wiegert 2011), non-linear non-axisymmetric instabilities (Kim & Ostriker 2001, 2007), magnetic fields (Elmegreen 1992) and others. Shu (1968), Jog & Solomon (1984), Bertin & Romeo (1988), Bertin et al. (1989a,b), Wang & Silk (1994), Rafikov (2001) and others extended the stability analysis and parameterization by accounting for the effect of the stellar disk. The relatively simple parameterization by Wang & Silk (1994) has become the most widely used stability criterion that incorporates both the stellar and gas disk (two-fluid Q), despite concerns about its validity (e.g., Jog 1996, Romeo & Wiegert 2011). Studies by Leroy et al. (2008) and Meurer et al. (2013) indicate that there are regions within galaxies where both the gas-only Q and the two-fluid Q are constant and subcrititcal.

1.2.4 Disk Dynamics

The dynamics of galaxies are crucial in order to understand star formation. Stability criteria rely on quantities such as the stellar and gas mass, pressure, epicyclic frequency, shear and velocity dispersion. These are all quantities that provide information about the dynamics of galaxies. Quantities such as the shear and epicyclic frequency are tied to the rotation of the components of disk galaxies. The rotation velocity is set by the potential well of the galaxy which is determined by the mass density. This rotation velocity can be quantified by a rotation curve - which is the rotation velocity as a function of radius. Slipher (1914) and Wolf (1914) discovered that galaxies rotate through absorption line studies of a few nearby galaxies: M31, the Sombrero galaxy (both by Slipher 1914) and M81 (Wolf 1914). Observations by Pease (1916, 1918) resulted in the first plot of the radial velocity as a function of radius. The mass density of the galaxy sets the rotation curve. Therefore observations of the rotation curve and comparisons to the observed stars can give information about the mass density and distribution of galaxies. The rotation velocity was expected to follow a solid body relation (i.e., $V \propto r$) in the inner parts and a "Keplerian decline" ($V \propto 1/r$) in the outer parts of the observed disk.

Babcock (1939)'s absorption line observations and study of rotation velocities of M31 showed constant angular velocities in the outer parts of the galaxy. The light from the stars declines with radius, this implies that the mass-to-light ratio of galaxies increases at large radii. This was one of the earliest indications that dark matter dominates the outer part of galaxies. Oort (1940) stated that the distribution of matter in NGC 3115 bears no relation to the light and that the stars could only account for

$\sim 0.5\%$ of the mass in the outer parts of that galaxy. Page (1952) and Burbidge & Burbidge (1960) performed spectroscopic observations of Hα and [N II] emission lines from the H II regions of spiral galaxies. They led the way for new high sensitivity optical spectroscopic studies of rotation curves that extended from an inner rising part (dominated by stellar matter) to a turnover where the rotation curve flattens off. Early kinematic studies of the neutral hydrogen in spiral galaxies were made through the radio observations by van de Hulst et al. (1957), Volders (1959) and Argyle (1965); some of these studies are discussed by van der Kruit & Allen (1978). Rotation curves derived from H I observations extend out to much further than the rotation curves derived from optical observations. Radio spectral line observations provide frequency information at each spatial pixel. They are used to map the frequency at which the peak amplitude of the spectral line occurs. These frequencies can be converted to velocities thus creating a map of the spatial distribution of velocities. The mean velocity of the galaxy can be subtracted from these to create a spatial map of the rotational velocity. The first published map of the velocity (velocity field) was by Argyle (1965). The largest disadvantage of H I observations is that in general they have lower resolution than optical observations. Therefore in the case of rotation curve studies of galaxies the two observing methods can be used together to obtain a complete picture of rotation curves from the inner parts of the galaxy where high spatial resolution is important (due to high velocity gradients in the rising parts of rotation curves) to the outer parts where there were questions about whether the rotation curve was flat (van de Hulst 1957, Volders 1959) and if it was what was the reason for this flatness (e.g., Roberts & Rots 1973).

Developments in Fabry-Perot interferometric observations resulted in observations of Hα velocity fields (Courtès 1960, 1964, Tully 1974). Fabry-Perot observations have better spatial coverage and higher spectral resolution than slit spectroscopy (Marcelin et al. 1983) are still being used today to study Hα kinematics of galaxies (e.g., Blais-Ouellette et al. 1999, Epinat et al. 2008). Advances in technology have allowed for multi-fiber and integral field instruments which are an improvement on long-slit spectrsocopy because multiple spectra of different regions of the observed field can be take simultaneously in one exposure. Integral field instruments now have very good spatial resolution that is oftentimes limited by the seeing. All of these advances have led to multi-fiber and integral field surveys of large samples of galaxies. Surveys such as ATLAS-3D (Cappellari et al. 2011), CALIFA (Sanchez et al. 2012 and García-Lorenzo et al. 2015) and SAMI (Allen et al. 2015) have provided optical (Hα and other optical emission lines) kinematics for large samples of galaxies.

The early velocity fields determined from H I and Hα observations were converted to rotation curves by methods such as those outlined in Warner et al. (1973) van der Kruit (1976), and these methods involved the fitting of other kinematic parameters relating to the orientation, centering and zero-point of the velocity field. Further observations of rotation curves in the outer parts of galaxies confirmed that they are flat or slowly declining rotation curves (e.g., Hutchmeier 1975, Roberts & Whitehurst 1975, Combes et al. 1977, Bosma 1978, 1981, Rubin et al. 1978, 1980, Carignan & Freeman 1985). These indications of large "invisible" halos in the outer parts of galaxies were supported by studies such as those of Ostriker et al. (1974) and Turner & Ostriker (1977). The observations established the presence of a dark matter component in galaxies which exists as a spheroidal halo (e.g., Binney 1978, Tubbs & Sanders 1979, Monet et al. 1981). The nature of this dark matter is still under debate but a class of particles called Cold Dark Matter (CDM) is now a part of the most commonly accepted and used cosmological paradigm : ΛCDM, along with the cosmological constant Λ. The ΛCDM model provides a good description of the large scale structure in the Universe (e.g., York et al. 2000, Jones et al. 2004) and of the cosmic microwave background (CMB) power spectrum (Primack 2003, Spergel et al. 2003, Planck Collaboration et al. 2014). The presence of dark matter affects the dynamics of galaxies, this can become important for star formation if the effect is large at radii where large scale star formation occurs. A key factor in controlling this is the fraction of mass due to dark matter in the star forming parts of galaxy disks. A standard method of analyzing the radial mass distributions of galaxies from their rotation curves and observations of stellar light called the multi-component method was developed by Carignan (1983) and it has been used in rotation curve mass composition studies since then. Mass decomposition studies have in general showed that the stellar component dominates the mass density at the small radii (e.g., van Albada et al. 1985, Carignan & Freeman 1985, Puche & Carignan 1991, Blais-Ouellette et al. 1999, de Blok et al. 2008) where star formation is most intense. However, dwarf galaxies are dark matter dominated throughout large parts of their disks and can have large H I fractions (e.g., Carignan & Freeman 1988, de Blok et al. 2008, Oh et al. 2011, 2015). The mass models of these dwarf galaxies indicates that the difference between contributions of the stars, gas and dark matter decreases at low radii, and the fraction of dark matter decreases at low radii (Oh et al. 2011), however the resolutions of the analyses do not extend far into the central regions. Most studies of star formation and disk stability do not directly consider the effects of dark matter, although by using parameters such as the epicyclic frequency (κ) derived directly from the rotation curves of galaxies they are incorporating the effects of the total mass density and therefore indirectly incorporating its effect on disk stability.

The models that are developed and tested in this analysis are based on galaxy disks that self-regulate and have constant stability parameters. They relate the dynamics of galaxies to their star formation surface densities and will provide more physically-motivated star formation laws that the Kennicutt-Schmidt law.

1.3 Thesis Aims

The star formation and gas surface density relations (Kennicutt-Schmidt Law and Molecular star formation law) are still the most popular and effective methods for describing and modeling star formation in galaxies. However, these relations do not describe the physical processes that control star formation or its distribution within galaxies. A model which connects the distribution of star formation and the dynamics of galaxy disks is essential in order to understand how star formation works and is connected to the physical processes of the disks. Studies have been made to test star formation laws that incorporate galaxy dynamics. However, these have usually been done over small samples of galaxies, or on big, bright and gas-rich star forming galaxies or the studies have been performed for properties averaged over entire galaxies. The density relations tell us that high star formation rate densities occur in regions where there are high gas densities. They do not explain and cannot predict where the high gas density regions will occur, and what controls these densities. The aim of this thesis is to develop and test dynamically based star formation models that describe how the star formation surface density is related to galaxy dynamics in the inner regions of a sample of galaxies that covers a wide range of properties.

The initial step will be to determine which mass components dominate and drive galaxy dynamics in the inner parts of galaxies. This will be followed by the development and testing of star formation models that relate galaxy dynamics to the star formation surface density. The models are based on the Quirk (1972) hypothesis that disks self-regulate and maintain a constant Q close to the stability threshold. The single-fluid (gas-only) Q and the two-fluid (gas + stars) Q parameters will be used to describe the disk stability in these models. The molecular star formation law and orbital timescale star formation laws will be used to connect the gas surface density and star formation surface densities in these models. These models

will predict the star formation surface density from the observed kinematics of galaxies. They will be tested in the central regions of a sample of galaxies that cover a wide range of H I masses, galaxy types and star formation rates.

Chapter 2

Theory

I aim to determine how the star formation surface density is related to the dynamics of the inner parts of galaxies. The initial step will be to determine which mass components dominate and drive galaxy dynamics in the inner parts of galaxies. This will be followed by the development and testing of star formation models that relate galaxy dynamics to the star formation surface density. The gravitational potential in these inner regions affects the gas dynamics and is crucial to understanding the relationship. The stellar disk dominates the baryonic mass in the inner parts of disk galaxies, therefore the stellar component has a large effect on the inner potential well and dynamics of gas in these regions. Understanding how much the stars affect the potential well is important in order to understand how the star formation is related to the inner galaxy dynamics. The relationship between the stellar surface density and the potential well will be derived. This will be followed by derivations of the relationship between the star formation surface density and the gradient using various disk compositions (gas only disks and gas + stellar disks) and star formation laws.

2.1 Velocity Gradient and Stellar Surface Brightness

Following derivations by Lelli et al. (2013) and Lelli (2014) in this section I determine the relationship between the stellar surface density and the gravitational potential well by deriving the relationship between the orbital velocity gradient and the stellar surface brightness in the central regions of galaxies. This will be done by assuming a galaxy with a central region with finite mass density and a linearly rising rotation curve.

The circular velocity of a test particle orbiting in a 3D distribution of mass at radius r can be described as :

$$\frac{V^2}{r} = m_s \frac{GM}{r^2} \tag{2.1}$$

where M is the mass within r and m_s is a parameter that is dependent on the distribution of mass. $m_s = 1$ for a spherically symmetric mass distribution and it varies between 0.5 and 1 for exponential disks throughout most of the galaxy (Freeman 1970, Binney & Tremaine 1994, Lelli et al. 2014). The above relation can be described in terms of the mean interior mass density : $\rho = M/\frac{4}{3}\pi r^3$ as follows:

$$\frac{V^2}{r} = \frac{4}{3}\pi m_s G \rho r. \tag{2.2}$$

The masses and densities described above are all dynamical. This can be rewritten as :

$$\frac{V}{r} = \sqrt{\frac{4}{3}\pi m_s G \rho}. \tag{2.3}$$

Therefore if I assume a linear rise to the rotation curve or in the central region (where r approaches 0, assuming that the central region has a finite mass density) I can relate this to the velocity gradient α via the following:

$$\frac{dV}{dr} = \alpha = \frac{V}{r} = \sqrt{\frac{4}{3}\pi m_s G \rho}. \tag{2.4}$$

The variable V/r is also defined as the orbital frequency or angular velocity Ω. The variables Ω and α are functionally the same variable ($\Omega \equiv \alpha$) but Ω is generally in time units and is measured at the outer parts of disks. The rotation gradient α is defined as the measured slope of the rotation curve and is generally used for the inner regions of the galaxy, it is in units of velocity per galactic physical scale. For this analysis I will be using α. The dynamical mass density can be described in terms of the baryonic mass fraction (f_b) and the baryonic mass density ρ_b, such that $f_b = \rho_b/\rho$. This leads to :

$$\alpha = \sqrt{\frac{4}{3}\pi m_s G \frac{\rho_b}{f_b}}. \tag{2.5}$$

The central stellar surface density Σ_s can be determined by multiplying the observed stellar surface brightness S_s with the mass-to-light ratio. The central stellar surface brightness (in solar luminosity per area units) is related to ρ_b by:

$$S_s = \frac{2\rho_b \Delta z}{(M_b/L)} \tag{2.6}$$

where Δz is half of the thickness of the disk and M_b/L is the baryonic mass-to-light ratio. Therefore (as in Lelli 2014)

$$\alpha = \sqrt{\frac{2\pi m_s G(M_b/L)}{3\Delta z f_b}}\sqrt{S_s} \tag{2.7}$$

Therefore $\alpha \propto \sqrt{S_s} \propto \sqrt{\Sigma_s}$, in other words the steepness of the potential well (α) is proportional to the stellar surface density if we assume that $\sqrt{\frac{2\pi m_s G(M_b/L)}{3\Delta z f_b}}$ is constant. The stellar surface density is not measured directly and is calculated from the observed surface densities of light from the stellar emission. The relation can be determined for the observed surface brightness in magnitude units. The observed surface brightness (μ) (in mag/arcsec^2 units) is related to ρ_b via:

$$\mu = -2.5\log\left(\frac{\rho_b \Delta z}{(M_b/L)}\right) + C_\mu. \tag{2.8}$$

C_μ is the magnitude zero point. This is a more general form (in terms of magnitude scale) than what Lelli et al. (2013) derived. It should be noted that the observed μ is affected by dust extinction, this can be mitigated by performing dust corrections on μ. For this derivation I assume that μ is the dust-corrected surface brightness because μ will be corrected for dust absorption in the analysis. The AB magnitude system (Oke & Gunn 1983) will be used in this analysis and $C_\mu = -48.6$ for the AB magnitude system. When the above equation is combined with the relation for α I find:

$$\alpha = \left(10^{\mu + C_\mu}\right)^{-0.2}\sqrt{\frac{2G\pi m_s (M_b/L)}{3\Delta z f_b}}. \tag{2.9}$$

That in log form is:

$$\log\alpha = -0.2\mu - 0.2C_\mu + 0.5\log\left(\frac{2G\pi m_s (M_b/L)}{3\Delta z f_b}\right). \tag{2.10}$$

Therefore $\log\alpha$ is linearly correlated with μ if $\sqrt{\frac{2\pi m_s G(M_b/L)}{3\Delta z f_b}}$ is constant, and if μ is measured in magnitude units the slope of the relation is -0.2 . The power law index of the α - Σ_s relation is 0.5. Lelli et al. (2013) and Lelli (2014) found a correlation between α and μ, which suggests that $\sqrt{\frac{2\pi m_s G(M_b/L)}{3\Delta z f_b}}$ is constant. This relationship relates the inner potential well to the stellar surface density. R-band emission and near-infrared (NIR) WISE observations can be used to determine the observed surface density due to stellar light; the relation will be compared to the -0.2 slope that is expected. The observed surface densities will be converted to stellar surface densities (in $M_\odot/pc^2$ units) by using the M_b/L values calculated at each observing band, the power law index will be compared to the theoretical value 0.5. Studies of the kinematics and mass composition of disk galaxies have shown that the stellar component dominates the baryonic matter in the inner few kiloparsecs of most normal spiral galaxies (e.g., Carignan & Freeman 1985, de Blok et al. 2008). The gas also contributes to the baryonic matter in the central regions of galaxies, but will be ignored until the following

section. I will also use the relationship to determine what the baryonic fraction of the inner parts of galaxies is.

2.2 Velocity Gradient Star Formation Correlation

In this section I derive the relationship between star formation and the dynamics of galaxies. Relationships will be derived using different star formation laws and for the commonly used case of a gas disk and the case of a disk whose stability is affected by the gas and stars.

2.2.1 Single Fluid Q

Following the Meurer et al. (1998) hypothesis of a correlation between $\Sigma_{\rm SFR}$ and α^2 I derive the relationship between $\Sigma_{\rm SFR}$ and α for a constant Q disk. The Toomre (1964) stability criterion (Q) can be used to quantify the stability of a gas disk. The gas stability parameter can be described by:

$$Q_g = \frac{\sigma_g \kappa}{\pi G \Sigma_g}, \tag{2.11}$$

(Toomre 1964, Wang & Silk 1994, Rafikov 2001) and is dependent on the velocity dispersion of the gas σ_g, the epicyclic frequency κ and the gas surface density Σ_g. The gas surface density is dominated by atomic and molecular gas. In a gas disk with $Q_g < 1$ the gravitational force of the disk is larger than those supporting the disk and the disk collapses, when $Q_g > 1$ the pressure support (parameterized by σ_g) and centrifugal acceleration (parameterized by κ) are large enough to support the disk and to keep it stable against gravitational collapse. Studies show that disk galaxies have marginally stable disks (e.g., Quirk 1972, Kennicutt 1989, Leroy et al. 2008), the disks do not collapse but gravitational collapse occurs locally in molecular clouds, which results in the observed widespread star formation in these disks. Studies such as Leroy et al. (2009) and Meurer et al. (2013) showed that Q_g is relatively constant and subcritical for large regions within disk galaxies. From their observations of marginally stable disks Quirk (1972) developed a model of gas disks with constant self-regulating Q, and Zheng et al. (2013) further developed this constant-Q star formation model. For this analysis I assume a constant Q model where the disk regulates itself to maintain a constant Q via processes such as star formation feedback. Following the Meurer et al. (1998) star formation model I assume a linearly rising inner rotation curve for this derivation, therefore $\alpha = V/r$ is constant. The dynamical timescale is generally defined as $t_{dyn} = \frac{1}{\sqrt{G\rho}}$ and is related to the orbital timescale (or orbital frequency) t_{orb} as

follows: $t_{orb} = \sqrt{\frac{3}{\pi}} t_{dyn}$. Therefore $t_{dyn} \approx t_{orb}$. For ease of use in their star formation analysis Kennicutt et al. (1998) redefined t_{dyn} such that:

$$t_{orb} = t_{dyn} = \frac{2\pi}{\alpha}. \tag{2.12}$$

This redefinition was used in subsequent analysis of the Kennicutt (1998) work and it will be used in this analysis. The epicyclic frequency κ is defined as:

$$\kappa = \sqrt{r\frac{d\alpha^2}{dr^2} + 4\alpha^2}. \tag{2.13}$$

Since the rotation curve is linear in this region and α is constant the derivative of α is zero and the equation for κ reduces to:

$$\kappa = 2\alpha. \tag{2.14}$$

Q_g can be rewritten in terms of Σ_g and α :

$$\Sigma_g = \frac{2\sigma_g \alpha}{\pi G Q_g}. \tag{2.15}$$

Work by authors like Kamphuis & Sancisi (1993) and Tamburro et al. (2009) showed that the H I velocity dispersions decrease with increasing radius. The changes can be up to a factor of 2 or greater (from the center to outside the optical disk). The different phases of the atomic gas were shown to have different velocity dispersions (Ianjamasimana et al. 2012) which also vary with radius, Ianjamasimana et al. (2012) found that the narrow component (attributed to the cold phase) has $\sigma = 6.5\,\mathrm{km/s}$ and broad component: $16.8\,\mathrm{km/s}$. Studies of molecular gas found that the velocity dispersions of it vary with radius (Mogotsi et al. 2016), the molecular gas and atomic gas dispersions are not the same but are within a factor of 1.4 within each other (Caldu-Primo et al. 2013, Mogotsi et al. 2016) and the ratio varies depending on the phase of the emission. The dispersion attributed to bright and dense molecular gas (which, like the narrow H I is very tightly associated with star forming regions) was found to be $7.3\,\mathrm{km/s}$. When considering disk stability most studies (e.g., Kennicutt 1989, Kennicutt 1998, Martin & Kennicutt 2001, Wong & Blitz 2002, Leroy et al. 2008) assume a constant σ_g. There are models and studies such as Zheng et al. (2013) that consider the effects of varying σ_g on disk structure and they find that the effects are small. Therefore for this analysis I assume a constant σ_g.

The gas surface density is proportional to α for the assumed constant σ_g and Q_g. Now that the gas density is defined as a function of α , the following derivation will relate the star formation surface density Σ_{SFR} to Σ_g and therefore α. Astronomers typically

parameterize $\Sigma_{\rm SFR}$ as a function of Σ_g by the Kennicutt-Schmidt Star Formation Law :

$$\Sigma_{\rm SFR} = A_0 \Sigma_g^N \tag{2.16}$$

(e.g., Schmidt 1959, Schmidt 1963, Kennicutt 1989, Kennicutt 1998), where A_0 and N are constants. Kennicutt (1989, 1998) found that:

$$\Sigma_{\rm SFR} \propto \Sigma_g^{1.4}. \tag{2.17}$$

Silk (1997), Elmegreen (1997) and Kennicutt (1998) suggested a different dynamically-based form of the star formation law:

$$\Sigma_{\rm SFR} \propto \left(\frac{\Sigma_g}{t_{dyn}}\right)^N. \tag{2.18}$$

This type of law is expected to hold for cases where the triggering of star formation by bars and galaxy arms is dominant, and is therefore dependent on the dynamical timescale of the disk. I will refer to it as the t_{orb}-SFR Law. Kennicutt (1998) found that the galaxies they observed fit this relationship and they find that the equation can be rewritten as:

$$\Sigma_{\rm SFR} = 0.017 \Sigma_g \alpha. \tag{2.19}$$

This assumes that $N = 1$. Making the constant-Q assumption and defining the constant of proportionality as the orbital efficiency ϵ_{orb} such that $\epsilon_{orb} = 0.017(2\pi)$, the above equation can be rewritten as:

$$\Sigma_{\rm SFR} = \frac{\epsilon_{orb}\sigma}{\pi^2 Q_g G}\alpha^2. \tag{2.20}$$

In terms of α:

$$\alpha = \sqrt{\frac{\pi^2 Q_g G \Sigma_{\rm SFR}}{\epsilon_{orb}\sigma_g}}. \tag{2.21}$$

It should be noted that Lelli et al. (2014) also determined a relationship between α and the gas surface density for a single fluid gas only disk, and they arrived at a similar relation to our Equation 2.20, but their equation does not relate the α to the star formation surface density. Therefore for gas dominated disks with constant Q_g and σ_g I expect that $\alpha \propto {\Sigma_{\rm SFR}}^{1/2}$. This relationship will be tested in this analysis.

2.2.2 Two Fluid Disk Q Formulation

Galaxy disks contain gas and stars and therefore the gas-only Q_g does not fully describe the stability of a gas disk. Jog & Solomon (1984) derived the stability parameter for a infinitesimally thin two-fluid disk where both components are dissipative. Rafikov (2001) confirmed their findings for a two-fluid disk, then extended it to consider a collisionless stellar disk in addition to a dissipative gas component and used this to re-derive their formulation of the two-fluid disk stability parameter Q_{2f}. The Rafikov (2001) expression for the total Q is :

$$\frac{1}{Q_R} = \frac{2}{Q_s}\frac{q}{1+q^2} + \frac{2\sigma_g}{Q_g\sigma_{s,r}}\frac{q}{1+q^2\left(\frac{\sigma_g}{\sigma_{s,r}}\right)^2}, \tag{2.22}$$

where Q_s and Q_g are the stability parameters for the stellar and gas disk respectively, and $q = k\sigma_{s,r}/\kappa$, with k being the wavenumber of the instability and $\sigma_{s,r}$ is the radial component of the stellar velocity dispersion. Wang and Silk (1994) derived a simple approximation of Q_{2f}:

$$\frac{1}{Q_{WS}} = \frac{1}{Q_g} + \frac{1}{Q_s}. \tag{2.23}$$

In these formulations the stellar stability parameter is defined as:

$$Q_s = \frac{\sigma_{s,r}\kappa}{\pi G\Sigma_s}, \tag{2.24}$$

(Jog & Solomon 1984, Rafikov 2001, Wang & Silk 1994) where Σ_s is the stellar surface density. The $\sigma_{s,r}$ is difficult to observe directly therefore some assumptions need to be made in order to estimate it. Following Leroy et al. (2008) I assume that the stellar exponential scale height h_s does not vary with radius and that it is related to the stellar scale length l_s by $l_s/h_s = 7.3 \pm 2.2$ (Kregel et al. 2002). Assuming a disk that is in hydrostatic equilibrium and isothermal in the z-direction (i.e., vertical), van der Kruit (1988) found that:

$$\sigma_{s,z} = \sqrt{2\pi G(\Sigma_s/2)h_s} = \sqrt{\pi G\Sigma_s h_s}, \tag{2.25}$$

where $\sigma_{s,z}$ is the stellar velocity dispersion in the z-direction. The stellar surface density in this equation is for half of the disk (i.e., $\Sigma_s/2$). Using the Leroy et al. (2008) assumption of a fixed ratio $\sigma_{s,z} = 0.6\sigma_{s,r}$, based on the typical velocity ellipsoids for late-type galaxies (e.g., Shapiro et al. 2003). I arrive at the relation:

$$\sigma_{s,r} \sim \sqrt{G\Sigma_s l_s}. \tag{2.26}$$

Therefore I estimate $\sigma_{s,r}$ from observations of l_s and Σ_s.

The derivation of the Wang & Silk (1994) approximation has been criticized by Jog (1996). Jog (1996) points out that the minimum wavenumber (wavenumber at which the fluid is least stable) should be for the combined two-component fluid and not for each component treated separately (as Wang & Silk 1994 did) and that the definition of Q is not correct. This is a valid criticism, however, this formulation has been extensively used and found to offer results similar to other formulations (e.g., Zheng et al. 2013, who found it to be within a factor of 1.6 of other stability formulations). Romeo & Wiegert (2011) found that the formulation underestimates the total Q and they improved it. Their total Q formulations for an infinitesimally thin disk $Q_{RW,thin}$ for cases where $Q_s \geq Q_g$ is:

$$\frac{1}{Q_{RW,thin}} = \frac{W}{Q_s} + \frac{1}{Q_g}, \tag{2.27}$$

when $Q_g \geq Q_s$:

$$\frac{1}{Q_{RW,thin}} = \frac{1}{Q_s} + \frac{W}{Q_g}, \tag{2.28}$$

where the parameter W is defined as follows:

$$W = \frac{2\sigma_s\sigma_g}{\sigma_s^2 + \sigma_g^2}. \tag{2.29}$$

Romeo & Wiegert (2011) found that increasing disk thickness increases the stability of the gas and stars by a factor T, which is dependent on the ratio of vertical σ_z to radial velocity dispersion σ_r :

$$T \sim 0.8 + 0.7\frac{\sigma_z}{\sigma_r}. \tag{2.30}$$

This holds for disks where the range of velocity anisotropy is $0.5 \leq \sigma_z/\sigma_r \leq 1$, which is the usual range (Romeo & Wiegert 2011). They used this to adapt their total Q formulation for a thick disk ($Q_{RW,thick}$):

$$\frac{1}{Q_{RW,thick}} = \frac{W}{T_sQ_s} + \frac{1}{T_gQ_g}, \tag{2.31}$$

where $T_sQ_s \geq T_gQ_g$; and

$$\frac{1}{Q_{RW,thick}} = \frac{1}{T_sQ_s} + \frac{W}{T_gQ_g}, \tag{2.32}$$

where $T_gQ_g \geq T_sQ_s$. T_s and T_g are the T factors for the stellar and gas disk respectively. Assuming that $(\sigma_z/\sigma_r)_g = 1$ and $(\sigma_z/\sigma_r)_s = 0.6$ as Leroy et al. (2008) did

$T_s \sim 1.22$ and $T_g \sim 1.5$.

I chose the Wang & Silk (1994) approximation due to its simplicity, that it provides similar results to other stability formulations (e.g., Zheng et al. 2013) and in order to be able to compare our results with other studies such as Leroy et al. (2008), who used it. In future studies I will perform this derivation and analysis using the Romeo & Wiegert (2011), Romeo & Falstad (2013) and other more complex formulations. The Wang & Silk approximation Q_{WS} has been used in many studies (e.g., Martin & Kennicutt 2001, Boissier et al. 2003, Corbelli 2003, Bournaud & Elmegreen 2009, Wong 2016). Taking Equation 2.23 and expanding it leads to:

$$\frac{1}{Q_{WS}} = \frac{\pi G \Sigma_g}{\sigma_g \kappa} + \frac{\pi G \Sigma_s}{\sigma_s \kappa}. \tag{2.33}$$

For the case of a linearly rising rotation curve α can be substituted into the equation, which results in:

$$\frac{1}{Q_{WS}} = \frac{\pi G}{2\alpha} \left(\frac{\Sigma_g}{\sigma_g} + \frac{\Sigma_s}{\sigma_s} \right). \tag{2.34}$$

Including Equation 2.26 and simplifying leads to the following expression for Q_{WS}:

$$\frac{1}{Q_{WS}} = \frac{\pi G}{2\alpha} \left(\frac{\Sigma_g}{\sigma_g} + \sqrt{\frac{\Sigma_s}{G l_s}} \right). \tag{2.35}$$

This can be rearranged in terms of Σ_s as follows:

$$\Sigma_s = l_s \left(\frac{2\alpha}{\pi \sqrt{G} Q_{WS}} - \frac{\sqrt{G}\Sigma_g}{\sigma_g} \right)^2. \tag{2.36}$$

The equation indicates how Σ_s is related to Σ_g for a constant Q_{WS} disk. The t_{orb} and surface density star formation laws will be used to relate Σ_g to $\Sigma_{\rm SFR}$. This will result in dynamical star formation laws that relate Σ_s to $\Sigma_{\rm SFR}$.

The t_{orb} Star Formation Law

If I assume the Kennicutt (1998) t_{orb} star formation law the above equation can be written in terms of $\Sigma_{\rm SFR}$:

$$\sqrt{\Sigma_s} = \frac{2\alpha\sqrt{l_s}}{\pi\sqrt{G}Q_{WS}} - \frac{\sqrt{G l_s}}{\sigma_g} \frac{2\pi\Sigma_{\rm SFR}}{\epsilon_{orb}\alpha}. \tag{2.37}$$

That can be rewritten as:

$$\Sigma_{\rm SFR} = \frac{\sigma_g \epsilon_{orb} \alpha}{\pi\sqrt{G}} \left(\frac{\alpha}{\pi Q_{WS}\sqrt{G}} - \frac{\sqrt{\Sigma_s}}{2\sqrt{l_s}} \right) \tag{2.38}$$

This shows that if the stellar component is used to calculate the disk stability, the $\Sigma_{\rm SFR}$ is dependent on Σ_g and Σ_s. l_s can be estimated using scaling relations or assuming an exponential disk such that it is related to the effective radius r_e by $l_s = 1.678 r_e$ (Erroz-Ferrer 2016). From Equation 2.38 we see that if I assume constant Q_{WS} and ϵ_{orb} and estimate l_s, Σ_s and α can be used to calculate $\Sigma_{\rm SFR}$.

Molecular Star Formation Law

The Kennicutt-Schmidt star formation law (K-S Law) relates the total gas surface density and the star formation rate and early studies were made using both H I and CO (as a proxy for molecular gas) (e.g., Kennicutt 1989, Kennicutt 1998). These were globally averaged studies and determined the slope of the K-S Law. Improved molecular gas and H I studies allowed resolved high sensitivity studies such as Bigiel et al. (2008), Leroy et al. (2008) and Schruba et al. (2011) to be made to study star formation within nearby galaxies. Studies show that the total gas K-S Law changes slope in different density regimes (e.g., Bigiel et al. 2008), and for densities below the H I saturation density and where the gas is dominated by H I the correlation is weaker than for the higher density regions (Bigiel et al. 2008). Studies by Bigiel et al. (2008), Leroy et al. (2008) and Schruba et al. (2011) showed that there is a tighter correlation between $\Sigma_{\rm SFR}$ and the molecular gas surface density Σ_{H2} than for the H I (Σ_{HI}) and Σ_g for azimuthally average values within galaxies. Therefore the K-S Law for molecular gas has less scatter than when the other two gas surface densities are used. The CO-derived molecular gas Kennicutt-Schmidt law (molecular star formation law) fitted by Bigiel et al. (2008) underpredicts the $\Sigma_{\rm SFR}$ for starburst and highly star forming redshift galaxies (e.g., Genzel et al. 2010). N for the molecular K-S Law is closer to unity than the value fitted for total gas studies. Bigiel et al. (2008) found $N = 1.0 \pm 0.2$ for their molecular K-S Law power index, which is lower than the Kennicutt (1998) $N = 1.40 \pm 0.15$ K-S index for the total gas.

Due to the tighter correlation between Σ_{H2} and $\Sigma_{\rm SFR}$ I will use the molecular K-S Law in the analysis of star formation model for Q_{WS} and the K-S Law. If I use the tighter molecular K-S Law, I need to determine the fraction of gas that is in molecular form. I assume that $\Sigma_g = \Sigma_{HI} + \Sigma_{H2}$, and define the molecular fraction to be $R_{mol} = \Sigma_{H2}/\Sigma_{HI}$. This means that $\Sigma_g = (1 + 1/R_{mol})\Sigma_{H2}$. The molecular fraction R_{mol} can be calculated by an empirical relation that is dependent on the hydrostatic pressure P_h :

$$R_{mol} = \left(\frac{P_h}{1.7 \times 10^4 \, cm^{-3} \, K k_B} \right)^{0.8} \tag{2.39}$$

(Leroy et al. 2008), where k_B is Boltzmann's constant and P_h is:

$$P_h = \frac{\pi}{2} G \Sigma_g \left(\Sigma_g + \frac{\sigma_g}{\sigma_{s,z}} \Sigma_s \right) \tag{2.40}$$

(Elmegreen 1989). R_{mol} can be calculated by the empirical Σ_s scaling relation fitted by Leroy et al. (2008) :

$$R_{mol} = \frac{\Sigma_s}{81 M_\odot \, pc^{-2}}. \tag{2.41}$$

Leroy et al. (2008) also found an empirical relationship between R_{mol} and t_{orb}:

$$R_{mol} = \left(\frac{t_{orb}}{1.8 \times 10^8 \, yr} \right)^{-2}. \tag{2.42}$$

Leroy et al. (2008) tested various versions of R_{mol} and found that the P_h, Σ_s and t_{orb} relations can be used to determine R_{mol}. They found that the best performing were the Σ_s and P_h relations, however the Σ_s scaling worked marginally better than the P_h relation in their SFE analysis. Wong et al. (2016) found that the P_h based R_{mol} worked best when modeling the H I based integrated star formation efficiencies of galaxies. The Leroy et al. (2008) analysis was based on the central parts of galaxies which will be the focus of this study, while the Wong et al. (2016) studies were more sensitive to outer disk regions. Since I am concerned with the inner disks of galaxies I will use the Leroy et al. (2008) Σ_s scaling relation to calculate R_{mol}.

To take into account the change between non-starburst galaxies and starburst galaxies in the molecular star formation law (MSFL) in the Bigiel et al. (2008) and Kennicutt (1998) analysis, Wong et al. (2016) developed a MSFL with a functional form for N (power law index):

$$\Sigma_{\rm SFR} = 8.66 \times 10^{-4} \Sigma_{H2} 10^{0.84(arctan(5(\log(\Sigma_{H2})-2.5))/\pi+0.5)}, \tag{2.43}$$

$\Sigma_{\rm SFR}$ is in units of $M_\odot/{\rm kpc}^2/{\rm yr}$ and Σ_{H2} is in units of $M_\odot/{\rm pc}^2$ and includes contributions from helium and heavy elements.

This is based on the changing A_0 between starbursts and non-starbursts while assuming a constant N, the function:

$$\Sigma_{H2} = \frac{1}{A_1} \Sigma_{\rm SFR} \tag{2.44}$$

can be used, where A_1 is the Bigiel et al. (2008) value: $10^{-3.06}\,{\rm Myr}^{-1}$ for $\Sigma_{\rm SFR}$ less than $2.5\,M_\odot/{\rm kpc}^2/{\rm yr}$ and a value more appropriate to starbursts at higher $\Sigma_{\rm SFR}$ values. Therefore the total gas surface density is:

$$\Sigma_g = \left(1 + \frac{1}{R_{mol}}\right)\Sigma_{H2} = \left(1 + \frac{1}{R_{mol}}\right)\frac{1}{A_1}\Sigma_{\rm SFR}. \quad (2.45)$$

Equation 2.36 can be written in terms of R_{mol} as follows:

$$\Sigma_s = l_s\left(\frac{2\alpha}{\pi\sqrt{G}Q_{WS}} - \frac{\sqrt{G}\Sigma_{\rm SFR}}{2\sigma_g A_1}\left(1 + \frac{1}{R_{mol}}\right)\right)^2 \quad (2.46)$$

This can be rewritten in terms of $\Sigma_{\rm SFR}$ as:

$$\Sigma_{\rm SFR} = \frac{A_1\sigma_g\Sigma_s}{81M_\odot/pc^2 + \Sigma_s}\left(\frac{2\alpha}{\pi G Q_{WS}} - \sqrt{\frac{\Sigma_s}{Gl_s}}\right). \quad (2.47)$$

Therefore for a disk with a constant 2-fluid Q, $\Sigma_{\rm SFR}$ is related to α and Σ_s. The relationships between them have been derived for the MSFL and the t_{orb}-SFR Law, and they were derived using the Wang & Silk (1994) 2-fluid Q model and empirical scaling relations for R_{mol} and σ_s.

2.3 Summary

The derivation showed that $\alpha \propto \Sigma^2_{\rm SFR}$ is the expected relationship between the gradient of the potential well and star formation for a gas disk with constant Q_g where there is a linearly rising rotation curve and the t_{orb}-SFR Law holds. In the case where the stars contribute to the stability of the disk, the Q_{WS} formulation was used to determine that the $\Sigma_{\rm SFR}$ is related to α and Σ_s. The relationships were derived for a constant Q_{WS} gas+stellar disk where the t_{orb}-SFR Law and the MSFL hold. The aim of this study is to test these relationships in the central parts of a wide range of galaxies. In order to do this I will use Hα, 22 μm and 12 μm observations to determine the $\Sigma_{\rm SFR}$ of the central regions of galaxies. R-band, 3.4 μm and 4.6 μm will be used to determine the central Σ_s. Hα spectroscopic observations will be used to study the kinematics of galaxies in order to determine the central α values. The constant Q_g and Q_{WS} and constant ϵ_{orb} and A_1 assumptions will also be examined in the analysis.

The observations used to determine Σ_s and α will be used to test the relationship that was derived between the gravitational potential and Σ_s: $\alpha \propto \Sigma_s^{0.5}$. This will be tested for the central regions of galaxies and the results will be used to study the central baryonic fraction of galaxies and the star formation models for gas and stellar disks.

Chapter 3

Data

3.1 Sample

In order to study star formation we require a comprehensive sample that is unbiased towards optical properties. H I is the fuel for star formation therefore any galaxies that form stars contain H I. Using an H I-based selection will allow for the selection of star forming galaxies without being strongly biased toward optical properties. Due to the H I selection the sample is biased towards late type galaxies, but these dominate the overall star formation. The Survey for Ionization in Neutral Gas Galaxies (SINGG: Hanish et al. 2006, Meurer et al. 2006) is a Hα and R-band imaging survey of 468 galaxies. The SINGG sample was selected using H I flux from the H I Parkes All Sky Survey (HIPASS: Meyer et al. 2004). The selection criteria is described in Meurer et al. (2006). Criteria were applied in order to ensure a uniform sample of galaxies between 8 and 10.4 $\log$ MH I that is not biased towards any optical parameters. More specifically a H I flux density cut-off was used; the preliminary sample was then divided into H I mass bins and the closest galaxies in each bin were selected. These were in addition to other selection criteria described in Meurer et al. (2006), such as sufficient projected distances from the Galactic plane, LMC, SMC and Milky Way. The Survey for Ultraviolet Emission in Neutral Gas Galaxies (SUNGG: Wong 2006) is the UV follow-up to the SINGG survey. The data from the SINGG and SUNGG surveys were analyzed and Hα, R-band and UV properties of the galaxies were determined. Due to observing time constraints not all galaxies that are in the sample were observed as a part of SINGG and SUNGG. A further description of the SINGG observations is given in Section 3.3.

I aim to test dynamically based star formation models over a wide range of galaxies. The predicted relationship between central velocity gradients and star formation surface densities in the inner regions of galaxies will be tested for a wide range of galaxy

morphologies, H I masses, stellar masses and star formation rates. In order to do this I reduce and analyze data from an optical kinematic survey of a subsample of galaxies taken from the SINGG survey that cover a wide range of H I masses. They were selected to ensure a uniform sample across the SINGG H I mass range. Initially only galaxies with UV data with more than 5 H II regions and accessible by the WIYN 3.5m telescope were selected. In order to increase the number of galaxies studied the restrictions on the number of H II regions was not used for later runs. The final sample is shown in Table 3.1. The table lists the H I masses and HIPASS derived distances for the galaxies in the sample. The distances were derived from the heliocentric velocities measured from the H I profiles corrected for the multi-pole attractor model (Mould et al. 2000) using $H_0 = 70\,\mathrm{km/s/Mpc}$. The H I masses were calculated using the standard Roberts (1962) formula:

$$M_{HI} = 2.36 \times 10^5 M_{\odot} D^2 F_{HI}, \tag{3.1}$$

where D is the distance in Mpc and F_{HI} is the H I flux in Jy km/s. Table 3.1 shows that the galaxies in the sample cover a wide range of total masses (indicated by W_{50}), H I masses, stellar masses (indicated by M_R), sizes and star formation rates (indicated by $S_{H\alpha}$). This coverage is important in order to test whether there are correlations between the inner velocity gradients and central star formation surface densities of galaxies and their physical and kinematic properties, and how these properties affect their agreement with the models I developed.

3.2 WIYN Kinematic Survey

The kinematic observations were performed using the formatted fiber unit SparsePAK feeding the spectrograph on the 3.5m Wisconsin Indiana Yale NOAO (WIYN) Telescope (Bershady et al. 2004, 2005). The layout of the 82 fibers of SparsePAK consists of a densely filled diamond ($39'' \times 24''$) centered in a sparsely filled square $72'' \times 71''$ within seven "sky" fibers in an L-shaped pattern $62''$ to $86''$ from the central fiber. Each fiber has a diameter of 4.5". This translates into physical distances of 0.17 kpc for a distance of 7.8 Mpc (distance to nearest galaxy in the sample), 0.43 kpc for 20 Mpc (the median galaxy distance of the sample is 19.8 Mpc) and 2.9 kpc for a distance of 135 Mpc (distance to the furthest galaxy in the sample). SparsePAK is described in detail by Bershady et al. (2004). Figure 3.1 and Figure 3.2 show the SparsePAK instrument and its sky-footprint.

Observations were carried out over 12 runs from 2004 to 2013. The Bench Spectrograph (Bershady et al. 2008) was used for the initial observation Runs 1 to 5 and the STA1 spectrograph (Bershady et al. 2008) was used from Run 6 onwards. The spectral

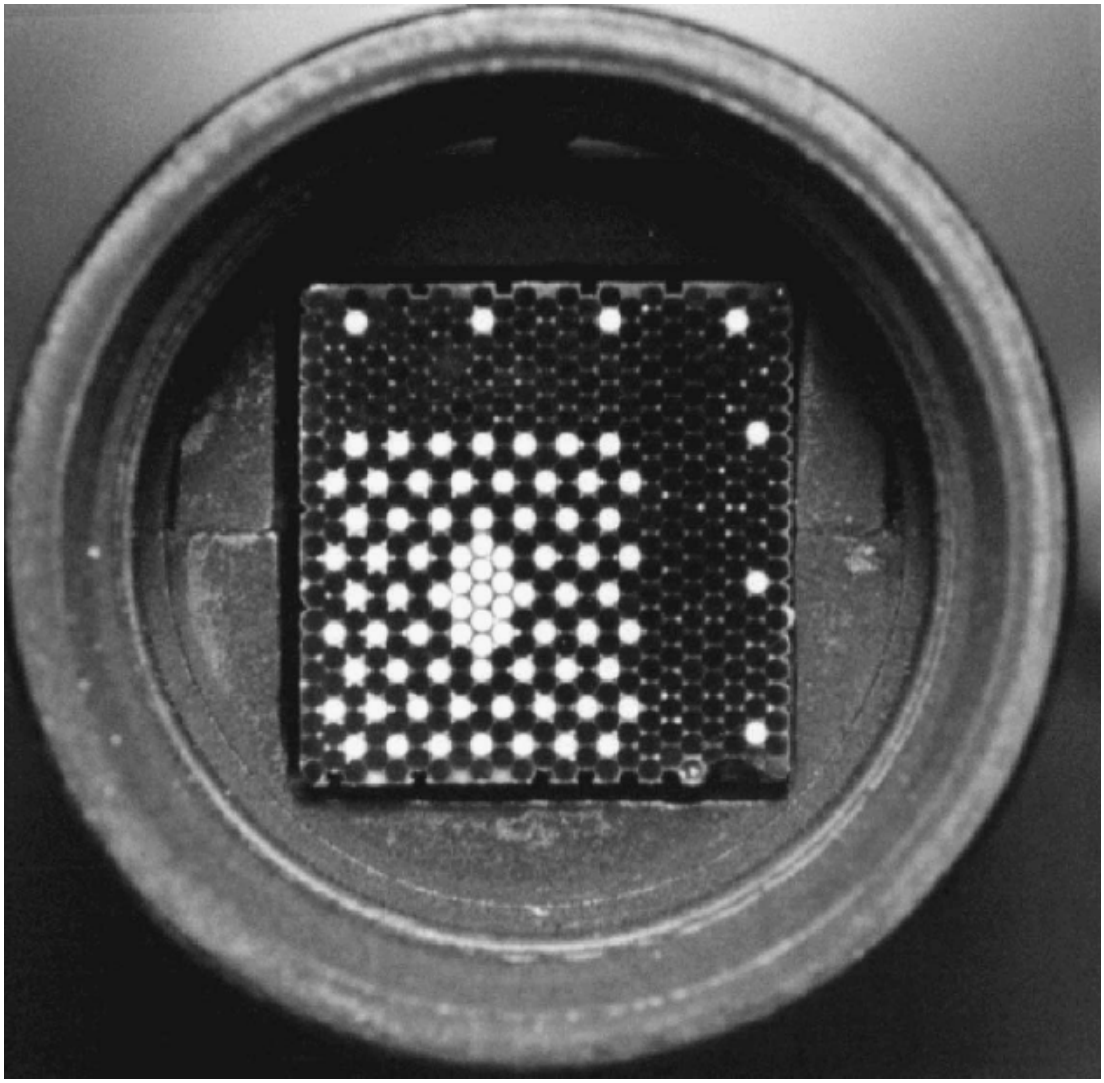

Figure 3.1: The head of the SparskePAK instrument in its mount. The back-illuminated fibers are the active fibers. Image taken from Bershady et al. (2004)

range was centered on the Hα line and chosen to cover redshifted Hα and other nearby bright lines, which are typically $[N\,II]\lambda\lambda$6548.05, 6583.75, $[S\,II]\lambda\lambda$6716.44, 6730.82. The 316@63.4 grating was used for all observations. It was used at a grating angle of 76^{o} and order 9 for the first run. For the rest of the runs a grating angle of 64^{o} and order 8 was used. The setup on the first run provided a dispersion of 0.12 Å /pixel the dispersion for the other runs was 0.2 Å /pixel . The final dispersion of each spectrum after final reduction was therefore set to $\sim$ 0.2 Å /pixel ($\sim$ 9 km/s /pixel). More detailed information on the observing runs (including the names of the observers) is provided in Table 3.2 .

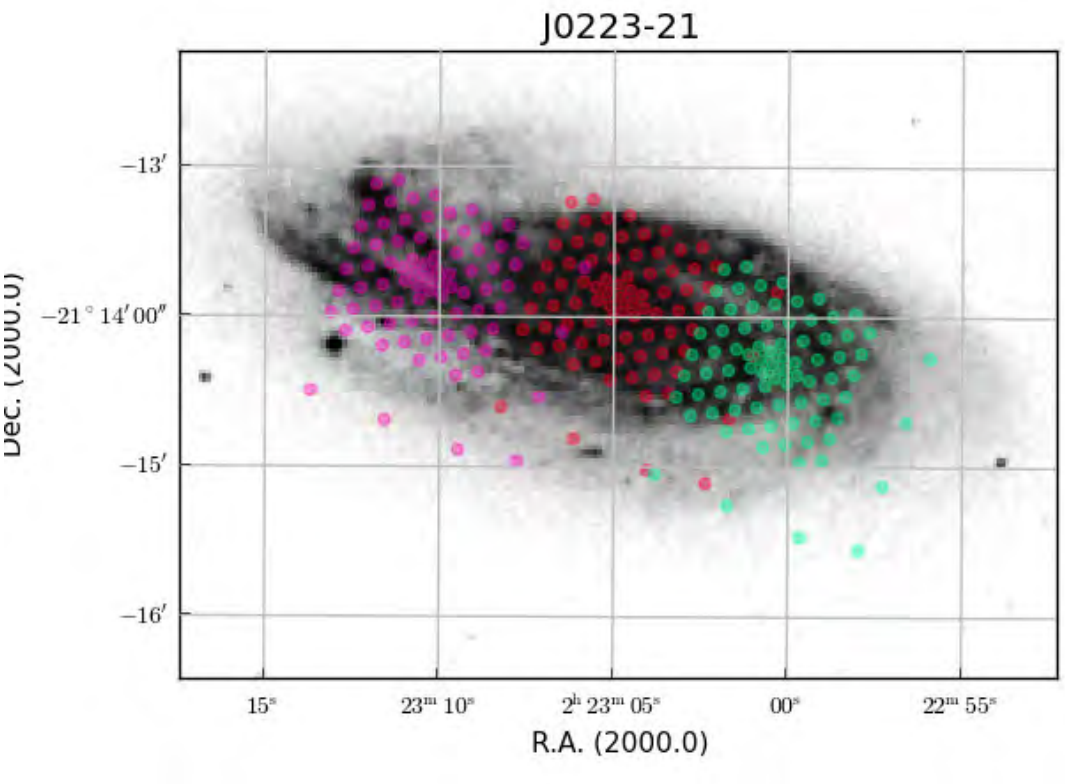

Figure 3.2: Overlay of the sky footprint of 3 different pointings of the WIYN SparsePAK instrument on the galaxy J0223-21.

Each telescope pointing was made using offsets from a bright star near the target galaxy. This star was used to home the telescope coordinate system and therefore the World Coordinate System of the resulting dataset. Where available the offset star was selected from SINGG Images, which were used to determine its coordinates. DSS images were used when SINGG images were not available. During the data reduction the pixel coordinates of the fibers were converted to sky coordinates using the PYWCS package. Multiple exposures were made for each pointing in order to mitigate contamination from cosmic rays. Each exposure ranged from 600 s (high surface brightness galaxies) to 1800 s (low surface brightness galaxies) in duration when the Bench Spectrograph was used, after the upgrade to STA1 the exposures ranged from 400 s to 1200 s. Details about the exposure times and number of pointings used for each galaxy are shown in Table 3.3 .

Table 3.1: Properties of the WIYN Sample.

Galaxy	Opt	D [Mpc]	M_{HI} [$M_\odot$]	W_{50} [km/s]	S	M_R [ABmag]	r_e [″]	$S_{H\alpha}$ [erg/s/cm^2]
1	2	3	4	5	6	7	8	9
J0019-22	M04-02-003	9.8	8.6	121.0	Y	-15.5	13.9	-15.5
J0031-22	E473-G024	7.9	8.0	47.9	Y	-13.9	24.1	-16.2
J0034-08	-	23.4	9.9	220.8	N	-	-	-
J0039-14a	NGC0178	20.6	9.4	75.2	Y	-19.3	18.6	-15.3
J0040-13	-	23.1	9.9	281.4	N	-	-	-
J0045-15	NGC0244	13.5	8.3	55.9	Y	-17.9	11.0	-14.8
J0112+00	-	16.5	9.7	160.0	N	-	-	-
J0130-22	-	22.7	9.9	266.8	N	-	-	-
J0140-05:S1	M01-05-014	18.1	8.1	59.1	Y	-15.2	13.0	-16.4
J0140-05:S2	-	18.1	8.1	59.1	Y	-17.3	25.0	-16.9
J0223-21	-	20.9	9.6	375.1	N	-	-	-
J0230-02:S1	NGC0958	80.0	10.6	547.6	Y	-23.7	30.5	-15.3
J0230-02:S2	-	80.0	10.6	547.6	Y	-19.6	13.7	-16.0
J0239-08	-	17.4	9.0	242.6	N	-	-	-
J0241-06	-	18.1	9.2	185.8	N	-	-	-
J0246-07	-	19.7	9.8	295.5	N	-	-	-
J0249-02	UGCA044	15.5	8.9	88.9	Y	-16.1	27.6	-16.9
J0302-18	-	24.8	9.8	188.5	N	-	-	-
J0335-24	NGC1371	20.4	9.8	391.4	Y	-21.9	49.5	-17.0
J0404-02	NGC1507	12.4	9.2	178.8	Y	-19.1	39.6	-15.6
J0441-02	NGC1637	10.4	9.3	188.3	Y	-20.1	57.9	-15.6
J0504-16:S1	M03-13-063	47.7	10.1	86.5	Y	-20.1	16.9	-15.4
J0935-05	-	23.1	8.8	49.6	Y	-16.3	19.6	-16.2
J0942+00	NGC2967	30.3	10.1	131.2	Y	-21.4	25.3	-15.0
J0943-05b	UGCA175	31.8	9.4	89.9	Y	-20.1	24.2	-15.8
J1002-06	UGCA193	9.7	8.6	128.6	Y	-15.9	40.7	-16.6
J1005-16:S1	NGC3128	70.7	10.3	348.0	Y	-21.7	22.0	-15.7
J1005-16:S2	M03-26-021	70.7	10.3	348.0	Y	-21.0	21.3	-15.9
J1005-16:S3	NGC3127	70.7	10.3	348.0	Y	-21.3	14.4	-15.3
J1026-19:S1	ESO568-G011	135.0	10.6	242.5	Y	-22.7	11.6	-15.5
J1026-19:S2	-	135.0	10.6	242.5	Y	-20.6	5.5	-14.1
J1039+01	UGC05797	7.8	7.7	47.8	Y	-15.5	14.7	-15.7
J1041-23	NGC3355	15.9	9.1	131.0	Y	-17.9	34.6	-16.4

Continued on next page

Table 3.1 – continued from previous page

Galaxy	Opt	D [Mpc]	M_{HI} [$M_\odot$]	W_{50} [km/s]	S	M_R [ABmag]	r_e [″]	$S_{H\alpha}$ [erg/s/cm^2]
1	2	3	4	5	6	7	8	9
J1042-23	E501-G080	13.2	9.1	141.8	Y	-17.9	28.3	-15.8
J1103-23:S1	NGC3511	14.2	9.6	265.2	Y	-20.8	72.1	-15.6
J1103-23:S2	NGC3513	14.2	9.6	265.2	Y	-20.0	36.4	-15.5
J1105-00	NGC3521	8.6	9.7	441.1	Y	-21.7	87.2	-15.2
J1107-17	-	11.9	8.3	110.0	Y	-15.7	11.9	-15.5
J1127-04	M01-29-023	10.6	8.2	76.9	Y	-15.1	19.0	-16.5
J1130-16	-	17.8	8.7	106.4	Y	-16.7	19.1	-16.8
J1136+00b	UGC06578	12.0	8.3	90.2	Y	-15.8	8.9	-14.5
J1145+02	-	10.2	8.1	-	Y	-13.2	18.9	-17.2
J1147-16	NGC3887	15.3	9.4	240.9	Y	-20.9	45.1	-15.4
J1157-15	-	20.2	8.7	66.4	Y	-17.1	15.7	-15.4
J1217+00	UGC07332	8.9	8.6	60.2	Y	-15.0	37.8	-16.9
J1247-03	NGC4691	11.8	8.2	64.8	Y	-20.2	33.1	-13.8
J1253-12	UGCA307	8.6	8.7	72.2	Y	-16.0	41.8	-15.7
J1255+00	UGC08041	15.3	9.1	188.4	Y	-19.1	46.5	-15.9
J1300-13:S1	NGC4897	39.0	10.0	239.4	Y	-21.7	25.4	-15.8
J1326+02A	-	12.2	8.8	-	N	-	-	-
J1338-09	DDO180	18.2	9.1	73.5	Y	-19.6	33.1	-15.6
J1403-06:S1	NGC5426	40.8	10.3	330.2	Y	-21.8	29.6	-15.4
J1403-06:S2	NGC5427	40.8	10.3	330.2	Y	-22.7	36.5	-15.1
J1423+01	UGC09215	22.5	9.5	222.1	Y	-19.4	36.7	-15.5
J1442-08	NGC5729	29.1	9.9	280.4	Y	-20.8	37.5	-15.4
J1447-17	UGCA394	33.5	10.0	212.4	Y	-20.8	44.0	-15.7
J1500+01	NGC5806	22.5	9.2	323.1	Y	-21.2	35.3	-15.7
J1509-11:S1	NGC5861	29.6	9.9	322.5	Y	-22.0	40.6	-15.2
J1609-04	MCG-01-41-006	13.5	8.5	71.9	Y	-16.5	12.7	-15.2
J1621-02	NGC6118	26.3	9.7	341.5	Y	-21.9	66.1	-15.9
J2025-24	NGC6907	47.9	10.4	285.4	Y	-23.5	40.7	-14.8
J2056-16	-	22.7	8.8	66.7	Y	-16.2	11.0	-16.0
J2102-16	IC5078	22.9	9.7	263.0	Y	-20.4	37.6	-16.3
J2142-06	-	19.8	8.6	62.7	Y	-16.9	14.0	-15.8
J2202-20:S1	NGC7184	38.6	10.1	524.6	Y	-23.1	61.1	-16.0
J2202-20:S2	-	38.6	10.1	524.6	Y	-16.0	8.4	-16.1
J2205-22	-	106.6	10.7	445.2	Y	-20.3	6.6	-15.4

Continued on next page

Table 3.1 – continued from previous page

Galaxy	Opt	D [Mpc]	M_{HI} [$M_\odot$]	W_{50} [km/s]	S	M_R [ABmag]	r_e [″]	$S_{H\alpha}$ [erg/s/cm^2]
1	2	3	4	5	6	7	8	9
J2234-04	-	14.1	8.7	92.9	Y	-16.6	27.1	-16.6
J2239-04	UGCA433	13.2	8.5	57.5	Y	-16.0	29.0	-17.0
J2242-06	-	14.1	8.1	62.6	Y	-15.6	11.4	-15.4

Comments: 1: SINGG galaxy name; 2: Optical identification from NED. ESO galaxies are denoted by "E" and MCG galaxies by "M". 3: HIPASS Distance (Meyer et al. 2004); 4: HIPASS logarithm of the H I mass (Meyer et al. 2004); 5: HIPASS H I linewidth: W_{50} (Meyer et al. 2004); 6: Presence of SINGG R-band and Hα observations (Y/N); 7: SINGG-derived R-band absolute magnitude; 8: SINGG-derived R-band effective radius (r_e); 9: SINGG logarithm of the Hα surface brightness.

Table 3.2: Observing Runs

Run	Date D/M/Y	N_d	N_f	Spec	Range [Å]	Disp [Å/pix]	Order	Obs
1	2	3	4	5	6	7	8	9
1	01/10/2004	2	9	BS	6505-6684	0.12	9	PMK
2	01/03/2005	2	8	BS	6505-6684	0.2	8	PMK,JF
3	20/03/2006	2	6	BS	6481-6895	0.2	8	PMK
4	24/02/2007	2	8	BS	6481-6895	0.2	8	PMK
5A	03/09/2007	2	16	BS	6481-6895	0.2	8	PMK,OIW
5B	17/09/2007	4	13	BS	6481-6895	0.2	8	PMK,JR
6	05/10/2008	2	14	STA1	6481-6895	0.2	8	PMK,GW
7	15/04/2009	2	8	STA1	6481-6895	0.2	8	PMK,GW
8	05/04/2010	2	23	STA1	6481-6895	0.2	8	PMK,KB
9	02/10/2010	2	13	STA1	6481-6895	0.2	8	PMK,KB
10	26/10/2011	2	18	STA1	6481-6895	0.2	8	PMK
11	16/03/2012	2	19	STA1	6481-6895	0.2	8	PMK,JP
12	05/04/2013	2	27	STA1	6481-6895	0.2	8	PMK,KB

Comments: 1: Run number; 2: Date; 3: Number of nights spent during the run; 4: Number of fields observed during the run; 5: Spectrograph used during observations : BS is the Bench Spectrograph and STA1 is the STA1 Spectrograph; 6: Wavelength range of spectra; 7: Dispersion of spectra; 8: Spectrum order; 9: Names of observers, PMK: P.M. Knezek, JF: J.Feldmeier, OIW: O.I. Wong, GW: G. Will, JP: J. Power, and KB: K. Butler)

Table 3.3: Observing details of the WIYN Sample.

Galaxy	Pointings	Exposure Time [s]	Run
1	2	3	4
J0019-22	3	1200	10
J0031-22	1	1200	9
J0034-08	4	600(R5A,R6), 1800(R1)	1,5A,6

Continued on next page

Table 3.3 – continued from previous page

Galaxy	Pointings	Exposure Time [s]	Run
1	2	3	4
J0039-14a	1	1800	1
J0040-13	4(1)	600	5A,5B.6
J0045-15	1	1800	1
J0112+00	3	600(R5A),1800(R1)	1,5A
J0130-22	3	600	5A
J0140-05:S1	1	1200	9
J0140-05:S2	1	1200	9
J0223-21	3	600	5A,5B
J0230-02:S1	2	600	5A
J0230-02:S2	1	600	5A
J0239-08	2	400	9
J0241-06	2	1200(R9), 600(R10)	9,10
J0246-07	2	400	9
J0249-02	1	1800	1
J0302-18	3	1200	10
J0335-24	3	600(R5B,R6), 1800(R6)	5B,6
J0404-02	3	1800(R1), 600 (R6)	1,6
J0441-02	7(1)	1800(R2,R5B), 600(R5B), 1200(R9,R10)	2,5B,9,10
J0504-16:S1	2	600(R4), 1200(R10)	4,10
J0935-05	1	1800	4
J0942+00	6(3)	400, 1200	11
J0943-05b	3	400	12
J1002-06	3	900(R7), 1800(R2,R7)	2,7
J1005-16:S1	3	400,1200	12
J1005-16:S2	3	400	12
J1005-16:S3	1	400	12
J1026-19:S1	1	1800	2
J1026-19:S2	1	600	4
J1039+01	1	1800	3
J1041-23	3	400,1200	8
J1042-23	3	400	8
J1103-23:S1	4	400, 1200	11
J1103-23:S2	2	400	11
J1105-00	5	900(R2), 400(R2,R5B,R9)	2,5B,9

Continued on next page

Table 3.3 – continued from previous page

Galaxy	Pointings	Exposure Time [s]	Run
1	2	3	4
J1107-17	1	600	4
J1127-04	1	1200	8
J1130-16	1	1200	12
J1136+00b	1	600	4
J1145+02	1	1800	4
J1147-16	1	400	3
J1157-15	1	400	12
J1217+00	3	1800(R3), 1200(R11)	3,11
J1247-03	1	1800	2
J1253-12	2	400,1200	12
J1255+00	3	1800(R3), 900	3,7
J1300-13:S1	4	1800(R3), 400(R11,R12), 600(R11)	3,11,12
J1326+02A	4	1800(R2,R3), 400(R11)	2,3,11
J1338-09	3	900(R3), 400(R8)	3,8
J1403-06:S1	4	600(R4,R8),400(R8)	4,8
J1403-06:S2	3	600(R4), 400(R8)	4,8
J1423+01	2	900(R7), 1200(R8)	7,8
J1442-08	6(2)	400, 1200	12
J1447-17	2	400	12
J1500+01	2	400, 1200	8
J1509-11:S1	2	400	12
J1609-04	1	1200	9
J1621-02	3	900(R7), 400(R8)	7,8
J2025-24	5	600, 1200(R9)	5B,6,9
J2056-16	1	1800	6
J2102-16	5(1)	1800(R1), 600(R5A), 400(R9), 1200(R9)	1,5A,9
J2142-06	1	1800	5B
J2202-20:S1	6	600(R6), 400(R10)	6,10
J2202-20:S2	1	1200	10
J2205-22	1	1200	10
J2234-04	1	1800	1
J2239-04	2	1800	1,5A
J2242-06	1	600	6

Comments: 1: SINGG galaxy name; 2: Number of pointings used in the data analysis (the number of duplicate pointings are shown in parentheses); 3: Exposure time (the associated observing run numbers are shown in parentheses where necessary); 4: Observing runs when pointings were observed.

Basic image reduction was performed using IRAF *. The spectra were bias subtracted and trimmed; cosmic ray removal was performed using LACosmic (van Dokkum, 2001): pixels containing cosmic rays were flagged on an individual frame basis using LACOSMIC, and flagged data were not used when combining and averaging pixels. For each pointing, the exposures (3 for a large majority of pointings) were co-added, and at each fiber position the median of the count values was taken as the final number of counts. The DOHYDRA package was used to reduce the resulting images (including: aperture identification, aperture fitting, flat-fielding, wavelength calibration). I find that the rms of the residuals of the wavelength calibration typically 0.02 Å ($\sim 0.9\,$km/s). Fibers that are not affected by galaxy emission were identified manually and the average spectrum of these "sky" spectra was subtracted from the calibrated spectra. A polynomial was fitted to the continuum of each spectrum and then subtracted.

I fitted single Gaussian profiles to the six lines covered by our observations (Hα: λ6562.8, $[N\,II]\lambda\lambda$6548.05, 6583.75, $[S\,II]\lambda\lambda$6716.44, 6730.82 and [He I]λ6678.15) to determine the central wavelength, linewidth and peak amplitude of the spectral lines. The systemic velocity of the source from the HIPASS database (in some cases optical spectroscopic velocities were used) was used to determine the initial guess for the position of each line, and lines within a 900 km/s window centered on the predicted velocity were attributed to this line and fitted. Each line was fitted individually using Levenberg-Marquardt optimization to determine the mean central wavelength λ_c, the continuum level F_{c0}, amplitude A, velocity dispersion σ from the Gaussian fit:

$$F_c = F_{c0} + A\,exp\left(\frac{(\lambda-\lambda_c)^2}{\sigma^2}\right) \tag{3.2}$$

(where F_{c0} is the observed number of counts and λ is the observed wavelength). The central wavelength was converted to a mean velocity $v = \frac{(\lambda-\lambda_o)}{\lambda_r}c$, where λ_o is the rest wavelength and the velocity dispersion to the FWHM: $w = 2\sigma\sqrt{2ln(2)}$. A second iteration was performed where the mean velocity is checked. A narrower window of $\sim 450\,$km/s centered on the fitted mean velocity from the initial fit was then used in the second fit. If the initial fitted mean velocity is outside the initial window a wider window than the initial one was used for the second fit. The uncertainty in the fitted mean wavelength e_λ was calculated as:

$$e_\lambda = \frac{\sqrt{\Delta\lambda w}\,e_f}{A[4\pi ln(2)]^{\frac{1}{4}}}, \tag{3.3}$$

*more specifically I used the PYRAF implementation. IRAF is distributed by the National Optical Astronomy Observatory, which is operated by the Association of Universities for Research in Astronomy (AURA) under a cooperative agreement with the National Science Foundation.

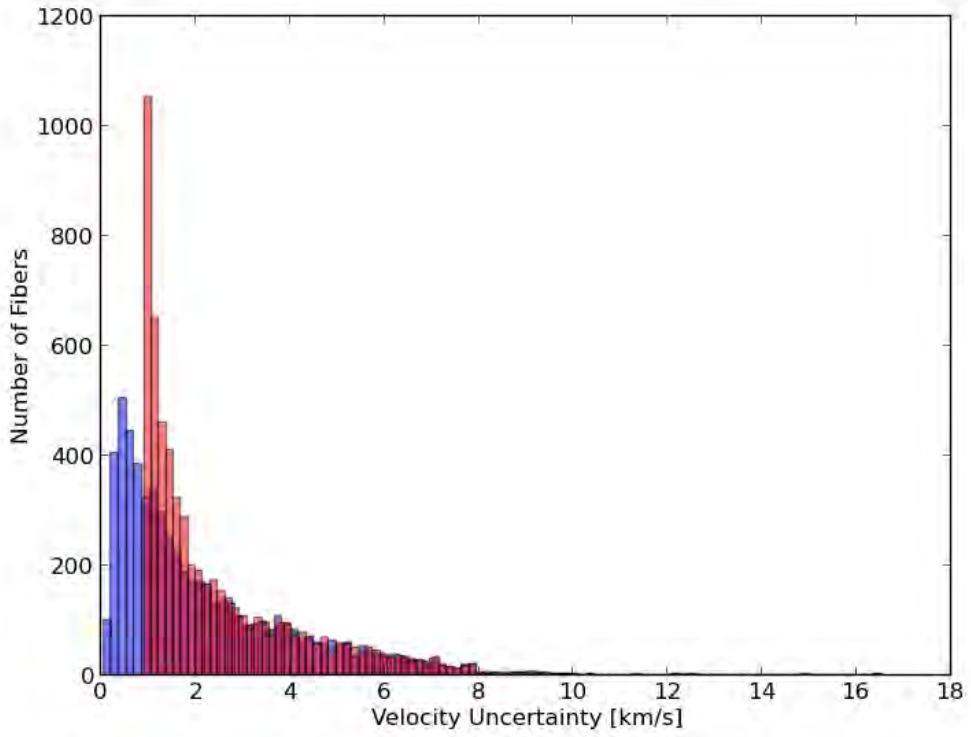

Figure 3.3: The distribution of fitted velocity uncertainties (blue histogram) and the distribution of the final velocity uncertainties (pink) after the wavelength calibration uncertainty was included. The fibers used in this figure were those above the detection threshold and those used for the final kinematic analysis.

determined from the covariance matrix, where e_f is the standard deviation of the difference between the fitted and measured flux within the wavelength window. The e_λ are converted into velocities at the λ_o. The final velocity uncertainty (e_v) was calculated by adding the uncertainty of the wavelength calibration to the original uncertainty (e_{vor}) in quadrature: $e_v = \sqrt{e_{vor}^2 + 0.9\mathrm{km/s}^2}$. The distribution of the fitted uncertainties e_f and the final velocity uncertainties is shown in Figure 3.3. In the kinematic analysis I only use the results for Hα. I rejected fits where w<26.85 km/s (this corresponds to 0.25Å) and for those with fitted velocities outside 200 km/s of the systemic velocity. This threshold was sufficient for removing noise, artefacts and spurious signals and it was above the wavelength spectral resolution (0.2Å) combined with the wavelength calibration uncertainty (0.02Å). A S/N ratio of 3 was used as a cut-off, where the S/N is the ratio between A and e_f. Exceptions were made for spectra having peak amplitudes below the S/N cut-off at similar velocities to neighbouring fibers or the galaxy as a whole. The velocity range cut-off was extended as needed for cases where the velocity

field was clearly truncated by the initial velocity range cut.

3.3 SINGG Observations

The SINGG team (see Hanish et al. 2006 and Meurer et al. 2006) provided me with radial flux profiles and axial ratios derived from their photometric analysis (private communication Meurer). I converted these to radial surface brightness profiles and then applied corrections determined by the SINGG team.

The observations for SINGG were made with the Cerro Tololo Inter-American Observatory (CTIO) 1.5m telescope and the CTIO Schmidt 0.9m telescope. Additional observations with the CTIO Curtis Schmidt telescope and Australian National University (ANU) 2.3m telescope were performed but will not be discussed here. The observing strategy and sample selection are detailed in Meurer et al. (2006). Hα and R-band observations were made for each galaxy. Narrowband filters were selected that covered redshifted Hα emission and R-band filters were used for R-band photometry for continuum subtraction of the Hα observations. Typically each CTIO 1.5m observation consisted of $3 \times 120\,s$ R-band exposures and $3 \times 600\,s$ narrowband exposures. Somewhat longer exposure times were used for CTIO 0.9m observations. The data from the observations was reduced using the IRAF package QUADPROC and fluxes were measured as specified in Meurer et al. (2006). Meurer et al. (2006) measured fluxes by summing the flux within apertures that have fluxes above the signal-to-noise threshold. The flux was combined with fluxes from regions outside of the apertures but within masks they created to include H II regions that could clearly be identified as H II regions but were very faint or surrounded by noisy regions. The Hα observations had their continuum subtracted using the R-band observations. Radial flux profiles and curve of growth (enclosed flux) profiles were made for each galaxy (for both Hα and R-band observations) using concentric elliptical apertures with constant shapes. The shapes and centers of these elliptical apertures were set interactively. I used these data to determine the Hα and R-band surface brightnesses for this analysis. The flux profiles received from the SINGG team needed to be corrected for dust and contamination. The corrections for each galaxy were calculated by the SINGG team and I applied them to the surface brightnesses I calculated. The corrections were determined as follows.

The filters used in the Hα observations were not narrow enough to exclude the 6548.04 Å and 6583.45 Å [N II] lines. The [N II] correction was the same as that used

by Helmboldt et al. (2004). Helmboldt et al. (2004) took spectroscopic data from the Nearby Field Galaxy Survey (NFGS, Jansen et al. 2000) and compared the ratio of Hα and [N II] emission ($w_{6583} = \frac{F_{[NII]6583}}{F_{H\alpha}}$) to the R-band luminosity of each galaxy. The fitted relation between these variables (in AB magnitudes) was :

$$\log(w_{6583}) = (-0.13 \pm 0.035)M'_R + (-3.30 \pm 0.98), \tag{3.4}$$

where M'_R is the uncorrected R-band absolute magnitude. This relation was used to determine the [N II] correction (for both [N II] lines). Meurer et al. (2006) corrected the SINGG Hα data for both [N II] lines.

Hα absorption present in the spectra reduces the measured Hα emission flux. Brinchmann et al. (2004) found that stellar absorption was $2\% - 6\%$ of the flux of the stellar emission (for SDSS). As mentioned before, to correct for this, the Hα fluxes of the SINGG galaxies were increased by 4%.

The foreground dust absorption correction was performed using reddening from the Schlegel et al. (1998) maps and the Cardelli et al. (1989) extinction law. The internal dust correction was based on work by Helmboldt et al. (2004). They used NFGS data to calculate the internal dust correction. Case B recombination and a mean temperature of 10^4 K (Osterbrock 1989) were assumed. The O'Donnell (1994) extinction curve and an $R_v = 3.1$ were also assumed. They determined the internal dust extinction by using the Balmer decrement (ratio of Hα and Hβ fluxes). The intrinsic Balmer decrement was assumed to be $H\alpha/H\beta = 2.85$. They then fitted the internal dust extinction as a function of the R-band absolute magnitude (M_R). The fit was used to determine the internal dust correction for a galaxy with a known R-band absolute magnitude. The internal dust absorption (in AB magnitudes) ($A_{H\alpha}$) relation was found to be:

$$\log(A_{H\alpha}) = -0.12(\pm 0.048)M'_R - 2.47(\pm 0.95). \tag{3.5}$$

The radiation that the dust absorbs is re-emited in the far-infrared, therefore larger dust correction corresponds to more emission in the FIR. This means that the correlation between the internal dust correction and M_R results in a FIR - M_R correlation. Meurer et al. (2006) used SINGG data and IRAS data to test the relation and they found that $F_{H\alpha}/F_{FIR}$ decreases with decreasing M_R. They used dust models to test whether that trend was similar to that found between the internal extinction and M_R. The analysis was able to adequately model the trends in the extinction for bright galaxies but had difficulty with predicting the total FIR emission. The galaxies were 2.7 to 4.8 brighter in the FIR than what was predicted by their models. After removing this

zero-point difference the models predict the $F_{H\alpha}/F_{FIR}$ ratio to a factor of 1.7 . The underprediction of F_{FIR} by the models was attributed to various possible causes including deficiencies in the stellar atmosphere models and errors in the assumed dust geometry which did not include completely obscured star formation. The method relies on optical H *alpha* emission escaping from star forming areas, but if the area where the stars form is completely hidden by gas and dust then there will be no detectable optical emission and therefore no Balmer decrement. This obscured star formation will therefore only be detectable in the infrared. The determination of the unobscured star formation to a factor of 1.7 was sufficient for studies that only involve the Hα such as this. The R-band surface brightnesses were also corrected for internal and external dust extinction similar to how the Hα values were corrected. Internal extinction has less of an effect on continuum observations such as R-band fluxes than it does for Hα and other Balmer lines (e.g., Fanelli et al. 1988, Calzetti et al. 1994). Therefore Meurer et al. (2006) used a lower internal dust correction factor for R-band surface brightnesses: $A_R = 0.5A_{H\alpha}$.

I calcualted the enclosed face-on surface brightness $S(r)$ within a radius r from enclosed flux profiles from the SINGG survey by the following:

$$S(r) = F(r)/(2\pi r^2) \tag{3.6}$$

where $F(r)$ is the total flux enclosed within the area described by an ellipse with a semi-major axis radius of r and a minor axis related to it by the photometric axis ratio. The foreground and internal dust extinction and [NII] corrections from the SINGG database were applied to the surface brightness values that were calculated. The R-band surface brightness S_R was calculated in the same way as the $S_{H\alpha}$ (in units of ergs/s/cm^2/arcsec^2/Å). I converted these to surface brightness units relative to frequency (i.e., Hz^{-1}) via the relation: $F_\nu = \frac{\lambda^2}{c} F_\lambda$ and these were converted to AB magnitudes (Oke & Gunn 1983) using the following formula:

$$m_{AB} = -2.5 \log_{10}(S_R) - 48.6, \tag{3.7}$$

where S_R is in units: ergs/s/cm^2/Hz. The R-band and Hα surface brightnesses were then converted to ergs/s/cm^2 (by multiplication with the central frequency of the observing bands) for use in further analysis. Surface brightness, luminosity and flux values in these units are sometimes denoted by the ν subscript.

3.4 WISE Observations

Jarrett (private communication) supplied me with WISE infrared surface brightness profiles, fluxes, masses and star formation rates derived for galaxies in our sample. I converted the surface brightness profiles to enclosed surface brightness profiles.

The Wide-field Infrared Explorer (WISE) is a 40 cm space-based infrared telescope that performed an all sky survey in bands centered at 3.4, 4.6, 12 and 22 μm bands, known as W1, W2, W3 and W4 bands respectively (Wright et al. 2010) . These are similar to the Spitzer Infrared Array Camera (IRAC) and Multiband Imaging Processor (MIPS) instrument bands. W1 and W2 are used to study the old stellar populations of galaxies, the W3 band is sensitive to PAH emission and W4 emission is analogous to Spitzer MIPS 24 μm and is sensitive to emission from hot dust that has been heated by hot young stars. The resolution of the original observations was $\sim 6''$ in the first 3 bands and $12''$ in W4, but Jarrett et al. (2012) and Jarrett et al. (2013) enhanced the resolution of nearby galaxies to $\sim 3''$ (for W1, W2 and W3) and $\sim 6''$ (for W4). Cutri et al. (2011) describes how WISE Atlas images and mosaics were made from the observations. Calibration, aperture correction, colour correction (correction values are in Wright et al. 2010) and the correction of the calibration discrepancy between blue and red stars are described by Jarrett et al. (2011). Source characterization was performed using an interactive pipeline developed using tools from the Two Micron All-Sky Survey (2MASS) Extended Source Catalog (XSC) pipeline (Jarrett et al. 2000) and the WISE Photometry System (Cutri et al. 2011). Azimuthally averaged elliptical surface brightness profiles were determined for annuli whose shapes were determined from the source characterization. The shape of the annuli used for the surface brightness profiles was fixed for all radii. The surface brightness profiles provided by the WISE team were determined from mean local surface brightness values in each annulus, I converted these to enclosed surface brightness profiles.

Table 3.4: WISE Vega to AB Magnitude offset: $\delta m = m_{AB} - m_{Vega}$

Band	δm
W1	2.699
W2	3.339
W3	5.174
W4	6.620

The surface brightnesses were converted from Vega magnitudes to monochromatic

AB magnitudes (Oke & Gunn 1983) using the conversion shown in Table 3.4 (Jarrett et al. 2011, Tokunaga & Vacca 2005). The surface brightness values were converted to the same final units as the Hα and R-band for use in further analysis.

3.5 Conclusion

The sample of galaxies was described and details given on how the spectroscopic data was observed and reduced. The kinematics used for this analysis will be determined using Hα emission and the velocity profiles of this emission line were fitted with single-Gaussian functions. Kinematic parameters fitted by the Gaussian fits will be used to determine the velocity fields, rotation curves and kinematic parameters required for this analysis. The SINGG and WISE observations of our sample of galaxies were described. The photometric data was reduced to interior surface brightness profiles, these will be used to determine the stellar surface densities and star formation surface densities.

Chapter 4

Measurements

4.1 Kinematics

4.1.1 Rotation Curves

Mean velocities of fibers with spectral lines that are above the detection thresholds were used to make velocity fields for each galaxy that had a Hα detection. Velocity fields are plots of the spatial position of fibers and the fitted central velocities of their spectra. An example of the velocity fields produced for each galaxy is shown in Figure 4.1. These velocity fields were used to extract kinematic information for each galaxy.

If I adopt the standard assumption that the dynamics of disk galaxies are dominated by circular orbits, then the observed line-of-sight velocity at the observed position (x,y) in a disk galaxy can be described in terms of the inclination i, position angle ϕ, systemic velocity V_{sys} and kinematic central position (x_0,y_0) of the disk galaxy and the rotation velocity V_c at the radius r of the particle. The x and y are defined such that increasing x corresponds to west and increasing y corresponds to north; and (0,0) is the central position of the first pointing. The position angle is that of the receding major axis and is measured from north to east. It should be noted that the assumption of dynamics dominated by circular orbits can break down inside galaxy bars, where non-circular motions are large. The effect of bars on the inner parts of rotation curves and our analysis is discussed in section 5.3 . Following Warner et al. (1973), the line-of-sight velocity can be described by the following equation:

$$V(x,y) = V_{sys} + V_c sin(i) cos(\theta), \tag{4.1}$$

where θ is the position angle with respect to the receding major axis in the plane of the galaxy. It is related to the position angle (ϕ) of the galaxy by:

$$cos(\theta) = \frac{-(x-x_0)sin(\phi) + (y-y_0)cos(\phi)}{r}, \tag{4.2}$$

$$sin(\theta) = \frac{-(x - x_0)cos(\phi) - (\mathrm{y} - \mathrm{y}_0)\sin(\phi)}{rcos(i)}. \tag{4.3}$$

Bars can have a large effect on inner galaxy dynamics by introducing non-circular motions. The resolution and sampling of our data does not allow for the accurate modeling of non-circular velocities induced by bars. The uncertainties due to not modeling bars will be discussed later. The geometric parameters are constant for symmetric, non-barred, non-warped and non-disturbed disk galaxies. If galaxy disks contract or expand there are inward or outward velocity components (perpendicular to the rotation velocity). Due to the sparse sampling I also assume for this kinematic analysis that our galaxies are undisturbed, symmetric, and non-warped disk galaxies with no expansion velocity.

The most important kinematic parameter I require for the dynamical star formation studies is the central gradient of the rotation curve. I use three methods to constrain the kinematic parameters. In order of increasing complexity of the fit they are the 3D plane model, DISKFIT (Spekkens & Sellwood 2007, Sellwood & Sanchez 2010) and ROTCUR (Begeman, 1987). The 3D plane model is the simplest model and I investigate where the model successfully fits the data better than the other two models. In cases where this model fits the data well and performs better than the other two models there is no need to derive a rotation curve for analysis that requires the rotation gradient.

I will test whether the 3D plane fit method can be used to determine velocity gradients of galaxies for which rotation curves could not be determined with the other methods. It will be used as an alternative in cases where ROTCUR and DISKFIT produce rotation curves that cannot be used for this analysis.

3D Plane

Tully et al. (1978), Broeils (1992) and Côté et al. (2000) showed that the rotation curves of dwarf galaxies rise slowly over most of their extent and often do not show indications of a turnover. Such cases can be approximated by a linearly rising rotation curve. Adopting the case of a galaxy with a linearly rising rotation curve centered at (0,0) and where the receding major axis lies on the x axis, the gradient of the rotation curve α can be described by:

$$\alpha = \frac{dV}{dr} = \frac{V_c}{r}, \tag{4.4}$$

and therefore:

$$V_c = \alpha r. \tag{4.5}$$

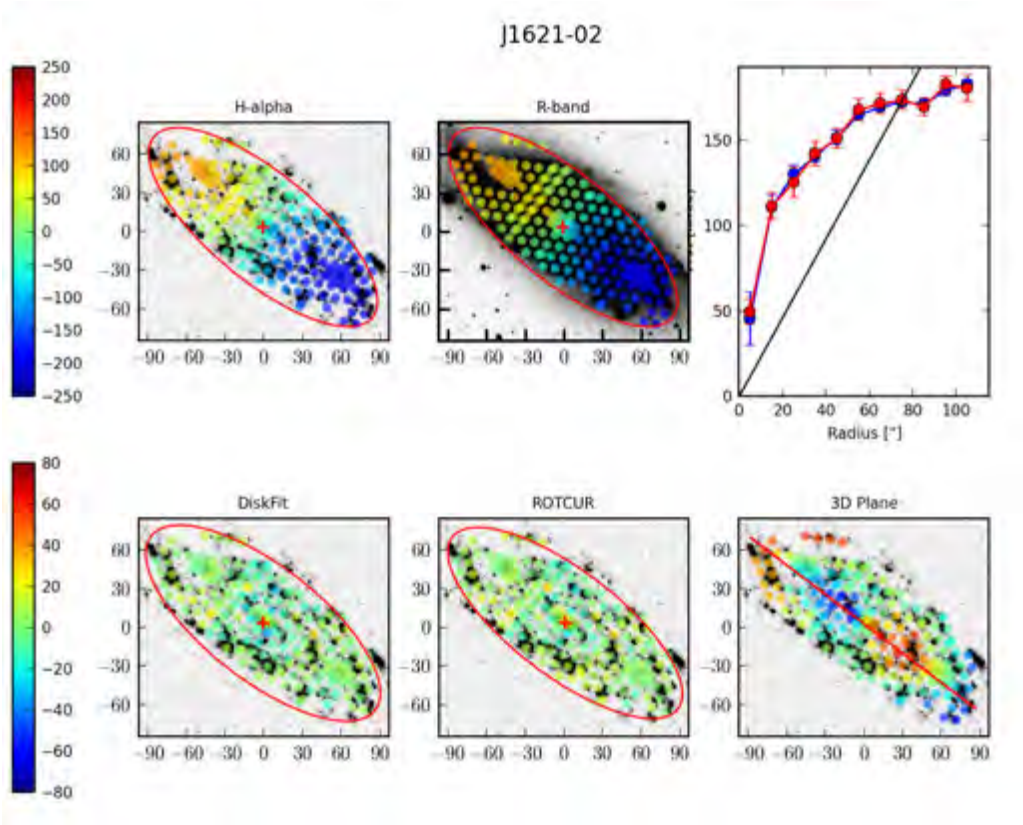

Figure 4.1: Velocity field and rotation curves of J0230-02:S1. The velocity field overlayed over Hα (top left) and R-band (top center) SINGG images. The rotation curves derived using DISKFIT (red) and ROTCUR (blue) are shown on the top right. The corresponding DISKFIT (bottom left), ROTCUR (bottom center) and 3D Plane (bottom right) residual velocity plots are overlayed over Hα images. Crosses are used to indicate the central position of galaxy. Red ellipses are used to indicate the photometric (in the Hα and R-band plots) and kinematic (in the DISKFIT and ROTCUR residual plots) i and ϕ, their sizes are determined by the radius of the largest radius used for DISKFIT fits (except in the ROTCUR sub-plot where the radius of the ellipse is the of radius last ring used in the ROTCUR fit). The red line in the 3D residual plot is used to indicate the ϕ_{3D}. The rotation velocities from the 3D plane model (assuming a photometric inclination) are plotted as a solid black line.

Equation 4.1 becomes:

$$V(x,y) = V_{sys} + \alpha sin(i) r cos(\theta). \tag{4.6}$$

Since $x = rcos(\theta)$ the observed velocity is:

$$V = V_{sys} + \alpha x sin(i). \tag{4.7}$$

There is no dependence on y and the x dependence is linear, so this is the equation for a plane. For arbitrary central positions and orientations, using these equations and Equations 4.2 - 4.3, I see that a simple model where velocity field is described as a tilted 3 dimensional plane can be used to fit the velocity field. The velocity field is parameterized as follows:

$$V = ax + by + c, \tag{4.8}$$

where a, b and c are the plane coefficients. These coefficients are related to the kinematic parameters via the following equations:

$$a = -\alpha sin(i) sin(\phi), \tag{4.9}$$

$$b = \alpha sin(i) cos(\phi), \tag{4.10}$$

and

$$c = V_{sys} + \alpha sin(i)(x_0 sin(\phi) - y_0 cos(\phi)). \tag{4.11}$$

Combining Equation 4.8 and Equation 4.1 allows us to determine the position angle:

$$\phi = arctan(-a/b). \tag{4.12}$$

The observations also provide a direct measurement of the *observed* velocity gradient $\alpha sin(i)$:

$$\alpha sin(i) = \sqrt{a^2 + b^2}. \tag{4.13}$$

The c coefficient is dependent on V_{sys}, x_0 and y_0, therefore the central position and systemic velocity of the galaxy are degenerate in this model. The only two kinematic parameters that I can extract from the plane fit are ϕ and $\alpha sin(i)$. The velocity gradient cannot be decoupled from the inclination so $\alpha sin(i)$ is the lower limit of the velocity gradient in the absence of other constraints on i. I can use photometric properties such as the axial ratios of isophotes to estimate i and thus constrain α. The position angle ϕ can be used to verify or as alternative initial parameters for the more complex rotation

curve derivation software.

I developed software to perform 3D plane fits to the velocity fields using the non-linear least-squares KMPFIT package from the Kapteyn Python* module (the package is derived from MPFIT(Moré 1978, Markwardt 2009)). The software fits each galaxy automatically. I performed fits over the entire velocity field of each galaxy.

DISKFIT

DISKFIT can fit axisymmetric and non-axisymmetric models to velocity fields and images (Spekkens & Sellwood 2007, Sellwood & Sanchez 2010 and Kuzio de Naray et al. 2012). It uses a harmonic decomposition of the velocities in the disk of a galaxy. It fits physically motivated models to the velocity field and uses the minimization technique described by Barnes & Sellwood (2003). Bootstrap realizations of the best fitting model are used to determine realistic estimates of the uncertainties on the parameters. Due to the sparse sampling and few data points DISKFIT was only used to fit axisymmetric non-warped disk models. Therefore the line of sight velocity (relative to an arbitrary center) of each particle in a galaxy can be described by Equation 4.1. I set the turbulent dispersion to 10 km/s and determined the fit uncertainties using 1000 bootstrap realizations. DISKFIT can provide fits of the systemic velocity, central position, inclination, and position angle of the entire disk, and the rotation velocity at specified radii. The fitting procedure consists of selecting input parameters and letting the program fit the data without any further inputs. If the fit is "unphysical" the input parameters are adjusted. Fits were "unphysical" when any one of the circular velocity, inclination or position angle were less than zero or when the rotation curve does not follow the standard shapes expected from disk galaxies. In cases when the rotation velocities and position angles were less than zero the input position angle was changed by 180° or 360°.

I used this fitting software because it determines the rotation curve of a velocity field, has successfully been used to determine the kinematics of galaxies like in the case of Kuzio de Naray et al. (2012), its fitting process is automated and uncertainties can determined for all the kinematic parameters and rotation velocities.

*Kapteyn Astronomical Institute, Terlouw, J.P. and Vogelaar, M.G.R., "Kapteyn Package, 2.3, March 2015, Groningen.

ROTCUR

ROTCUR uses tilted-ring rotation curve analysis (Begeman 1987). This analysis describes a galaxy as a set of concentric rings, each fully described with its own V_c, V_{sys}, (x_0,y_0), i and ϕ. These parameters are related by Equation 4.1. A ring size is chosen and the parameters can be determined for each ring (annulus). The optimization of each ring's parameters is done using a least-squares algorithm. The software has successfully been used to determine the rotation curves for many kinematic surveys (e.g., de Blok et al. 2008). Therefore it is used as the standard to compare the DISKFIT and 3D plane fits to. Most of its use has been for H I observations. The fiber observations result in incomplete sampling of the galaxies, the number of individual velocity measurements is far less than those of H I observations and there is irregular coverage of the velocity fields. NEMO is an extendible stellar dynamics toolbox with various programs used to analyze and visualize simulated and astronomical data. A NEMO implementation of ROTCUR is capable of handling this data format and incomplete sampling of a velocity field, therefore it was used for this analysis.

In order to improve fits ROTCUR allows exclusion of data at an angle (free angle) around the minor axis. The minor axis has the lowest projected rotation velocity relative to the observer and therefore uncertainties in the observed velocities and localized non-circular velocities dominate the observed velocities. Therefore points in this region can cause large uncertainties in the rotation curve derivation. A cosine weighting function was used to weight the least squared solution as a function of galactic angle away from the major axis. Due to the number of data points a free angle of 10° was used for most cases. This number was adjusted in cases when ROTCUR fits were bad (i.e., the fitted parameters were very different from what is expected from the photometry and from fits using other software or the derived rotation curve was not the expected shape) or in cases when I fitted the central kinematic position using ROTCUR. The central kinematic position was fitted for cases where the optical centers were clearly far from the kinematic values. A symptom of this is a slowly rising rotation curve at small radii (first few rings) followed by a sharp rise in the next few rings. This would imply a "hollow" mass distribution, which is unphysical.

The ROTCUR fitting process is similar to the method used by Carignan et al. (1988). I use 3 steps: initially I use large ring widths to get a good fit of the systemic velocity (and sometimes central position). Then the resultant fitted value is used as the fixed systemic velocity; the inclination and position angle are left as free parameters. The last step involves using small rings (generally $\sim 10''$), fixing all the geometric param-

eters and systemic velocity to values fitted in the previous steps and then fitting the rotation velocity for each ring. The mean of the fitted inclination and position angles of all the annuli was used as the fixed values in the final step. Fixing these values forces circular motions and thus assumes no warps or non-circular motions from structures such as bars (which can be described by changes in these parameters at different radii). The effects of bars on position and angles and inclinations is mentioned in the fitted inclination and position angle subsections.

In cases where fitted parameters were not found or were unphysical (i.e. i and ϕ are less than zero or very different from both the DISKFIT and photometric parameters, or the systemic velocity is very different from V_D and V_{HI}) after using the aforementioned procedure the galaxy was classified as not having a ROTCUR fit.

Rotation Curve Fitting

The initial parameters constrain the DISKFIT and ROTCUR fits. Photometric geometric parameters derived from Hα and R-band SINGG observations were used as initial parameters for the kinematic fitting, where possible, otherwise NED estimates of the inclination were used where possible to guide the initial parameters used in kinematic fits. Where possible, I used optically determined centers as input parameters to DISKFIT and ROTCUR and kept these fixed. The central positions (x_0,y_0) were derived from the SINGG photometric data. Accurate central positions are important for the determination of accurate rotation curves. In general these central positions are sufficiently accurate for this use, as seen in the shapes of the inner rotation curves of the galaxies in the sample. If the shapes of the velocity field and rotation curves indicate that there are large differences between the kinematic and photometric centers, they were determined using kinematic fits at the beginning of the fitting procedure (while i and ϕ are kept constant). The fitted central positions were kept constant for the rest of the fitting procedure. The other parameters: i, ϕ, V_{sys} and V_c were fitted. In DISKFIT, I choose to fit circular velocities about $10''$ intervals about two fiber diameters wide. Due to the higher number of free parameters used in ROTCUR, the initial fits for V_{sys} used rings that were $15''$ or $20''$ wide, the final V_c fits used annuli of $10''$ width.

In order to test the performance of each of the fitting methods I define a parameter

s^2 to calculate the goodness of fit. This parameter is calculated as follows:

$$s^2 = \sum \frac{\left(\frac{V-V_f}{e_v}\right)^2}{N_f - N_p}, \tag{4.14}$$

where V and V_f are the observed and fitted velocities; e_v is the uncertainty in the observed velocities and N_f and N_p are the number of points and number of fitted parameters used in the fit. While this equation is designed to be similar to the definition of χ^2m with $N_f - N_p$ meant to describe the number of degrees of freedom of the fit, in practice this quantity is difficult to determine with the method used in this analysis, at least in the cases of DISKFIT and ROTCUR. All data points in the velocity field are used to determine the geometric parameters i, ϕ and V_{sys}, whereas only the data in a narrow range of radii is used to determine each V_c value. Hence the true number of degrees of freedom is constant over the velocity field, for the geometric parameters, but varies with radius for V_c. There is an additional complication in the case of ROTCUR where each step in the fitting procedure involves keeping some parameters fixed while fitting for others, then fixing the fitted parameters in subsequent fitting iterations (this procedure was also used in cases where x_0 and y_0 were fitted). Here I am only concerned with defining a quantity to use to decide which of the three methods I use gives the best results, and so consider s^2 adequate for this purpose. The lowest s^2 value corresponds to the best fit. I adopt $N_p = 3$ (a,b,d) for the 3D plane model and $N_p = 4$ (i,ϕ,V_c,V_{sys}) for DISKFIT and ROTCUR.

There are instances where the data are fitted well but the resultant kinematic parameters or rotation curve are unphysical. The photometric geometric parameters allow us to estimate the parameters the galaxies should have. The rotation curves are expected to have an inner rising part which flattens off or slowly rises (sometimes declining) at large radii as expected from disk galaxies (e.g., Tully et al. 1978, Bosma 1981, Begeman 1987, Broeils 1992, Côté et al. 2000 and Swaters et al. 2009). In these cases the method whose results are closest to the expected rotation curve or geometric parameters will be chosen.

The galaxies in our sample are divided into 4 categories based on which method provides the best fit to the data:
Class 0 : None of the methods provide a reasonable fit (i.e., there is no 3D Plane fit and no DISKFIT fit or the DISKFIT fitted i or ϕ values are less than zero). This can occur if the data quality is very low or there is no observed rotation.
Class 1 : 3D Plane has the lowest s^2

Class 2 : DISKFIT has the lowest s^2
Class 3 : ROTCUR has the lowest s^2.
There were many galaxies with no ROTCUR fits and many Class 1 and Class 2 galaxies only had their 3D Plane and DISKFIT s^2 compared.

4.1.2 Rotation Curve Kinematic Analysis

General Properties

The aim of this section is to show the relationship between different observational and physical galaxy properties and their classification. In order to show this the Hα surface brightness ($S_{H\alpha}$), effective radius (r_e), R-band absolute magnitude (M_R), H I mass ($M_{\rm HI}$), photometric inclination (i_O) and H I line width W_{50} are plotted against each other and the different fitting classifications in Figure 4.2. $S_{H\alpha}$, r_e, M_R and i_O were determined from SINGG data (see Meurer et al. 2006). $M_{\rm HI}$ and W_{50} were calculated from the HIPASS H I spectrum (Meyer et al. 2004).

Not all the galaxies had SINGG Hα and R-band observations, the inclinations of galaxies with no SINGG observations were estimated using the axial ratios from NED. These estimates were used as initial parameters for the fits and as the photometric inclinations in the following plots. They were determined using: $i = arccos(\frac{b}{a})$, where a and b are the semi-major and semi-minor axes respectively. This is an approximation of the Hubble (1926) and Holmberg (1946, 1975) inclination axis ratio relation:

$$cos^2(i) = \frac{(b/a)^2 - f^2}{1 - f^2}, \tag{4.15}$$

where the flattening ratio f is often assumed to be 0.2 (e.g., Holmberg 1958, Haynes & Giovanelli 1984, Courteau et al. 1997, Courteau et al. 2007), but has been shown to range from 0.08-0.2 (e.g., Holmberg 1975, Giovanelli et al. 1994). I am effectively assuming $f = 0$. The large uncertainties, non-uniform methods used to calculate a and b, and the f approximation mean these can only be used as estimates and as initial parameters of the fits.

The M_R values for galaxies with no SINGG observations were determined from NED apparent magnitudes (m_R) and distances. The m_R for all but one of the galaxies were measured in the optical follow-up to HIPASS by Doyle et al. (2005). They were converted to absolute magnitudes. The M_R values are in AB magnitudes but the m_R values were in Johnson magnitudes, the AB R-band magnitude is 0.055 larger than the Johnson magnitude (based on αLyr, Frei & Gunn 1995). These were converted

to AB magnitudes and were used in the subsequent analysis when SINGG data was unavailable.

The Hα face-on effective surface brightness $S_{H\alpha}$ can be directly converted to star formation surface density ($\Sigma_{\rm SFR}$), with a unit conversion, dust absorption correction and specification of the initial mass function (IMF). It is an indicator of how well I can detect each galaxy; galaxies with low $S_{H\alpha}$ are faint and harder to detect than high surface brightness galaxies. Meurer et al. (1998) demonstrated that $\Sigma_{\rm SFR}$should be proportional to the central halo density, under the assumption that the disk stability parameter Q is constant. Lelli et al. (2013) showed that the R-band surface density (which is a tracer of the stellar surface density) is correlated with the gradient of the inner rotation curve (which traces the central potential well and therefore the halo density). The size of the galaxy is parameterized by r_e which should be indicative of how many fibers can be used to sample the galaxy. Low r_e can result in a poorly sampled rotation curve because the fibers may be too large to sample the rotation curve turnover or the turnover radius may be larger than the effective radius and therefore not detected in our observations. Low r_e also places a limit on the number of fiber detections and sampling of each galaxy, which affects how well the fitting software can constrain the kinematic parameters.

The top left panel of Figure 4.2 plots $S_{H\alpha}$ and r_e against each other. Most Class 1 galaxies have r_e<20$''$, independent of $S_{H\alpha}$. The dense central region of SparsePAK has a size of $39'' \times 24''$ (Bershady et al. 2004), therefore its major axis radius is $19.5''$. There are no galaxies with ROTCUR fits below this r_e, therefore only large galaxies with r_e extending beyond the central part of the fiber array have sufficient quality for ROTCUR fits. Galaxies that cover a small area in the sky tend to be fitted better by 3D Plane than the other methods, irrespective of their $S_{H\alpha}$. At low $S_{H\alpha}$ and r_e there are a mix of Class 1 and Class 2 galaxies. At large $S_{H\alpha}$ and r_e values, DISKFIT and ROTCUR perform better than 3D Plane. The galaxies with high $S_{H\alpha}$ and r_e are large, intensely star forming galaxies. Their rotation curves are likely to be well sampled and often flatten off. Their velocity fields are not well modeled using the 3D plane model. Instead the data usually has sufficient quality to allow good fits by ROTCUR and DISKFIT. Galaxy size has a greater effect on the fitting class of a galaxy than $S_{H\alpha}$, and velocity fields of most high $S_{H\alpha}$ galaxies with large r_e cannot be modeled with a linearly rising rotation curve with no turnover.

The absolute magnitude M_R is plotted against H I mass $M_{\rm HI}$ in the top right panel of Figure 4.2. M_R measures the luminosity of the stellar component of a galaxy. In disk galaxies it is proportional to $\log V_{max}$ via the Tully-Fisher relationship (TFR, Tully &

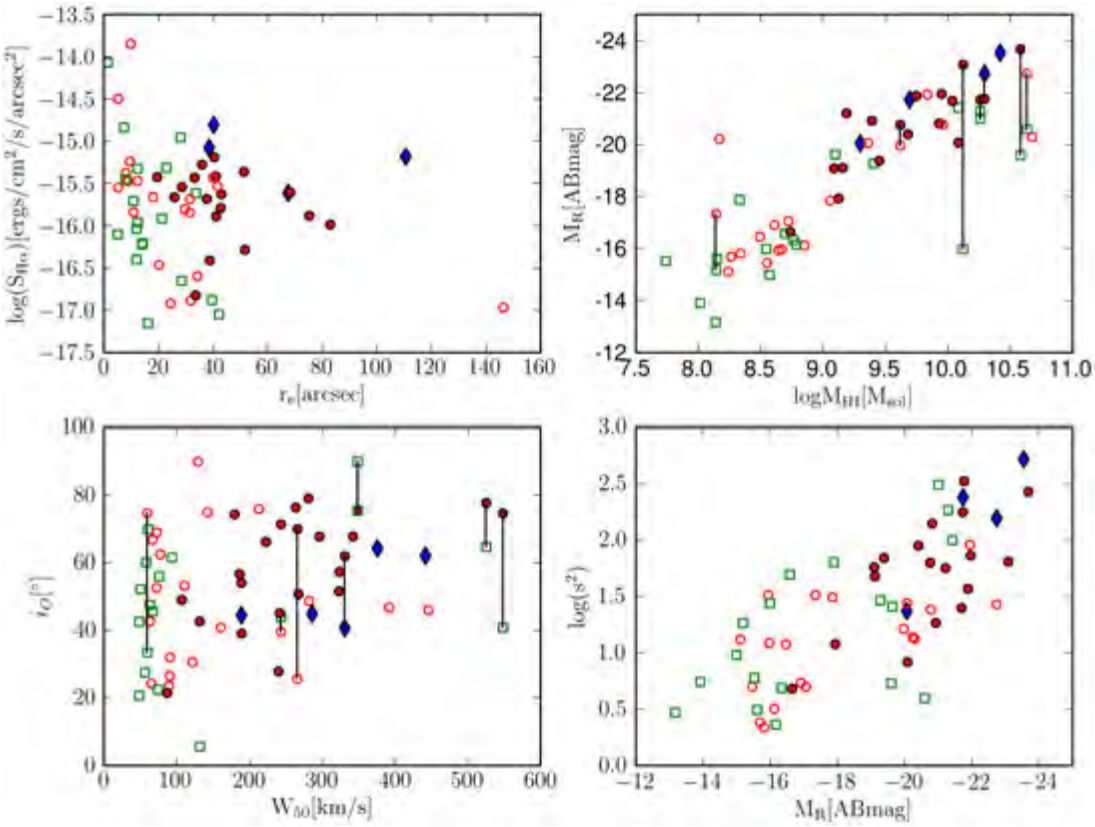

Figure 4.2: Comparisons of the properties of galaxies. Class 1 galaxies are shown as squares, Class 2 galaxies as circles and Class 3 galaxies are shown as diamonds. Filled symbols are used to show galaxies that have a ROTCUR rotation curve fit. *Top Left:* Hα surface brightness plotted against the effective radius. *Top Right:* R-band absolute magnitude plotted against the H I masses. *Bottom Left:* Photometric inclination plotted against H I W_{50}. *Bottom Right:* Log s^2 plotted against the H I M_R. Multiple sources belonging to one HIPASS source have the same HIPASS systemic velocities and are connected by a black line. The inclinations, Hα surface brightnesses, R-band absolute magnitudes and effective radii are derived from SINGG photometry; the H I masses and W_{50} values are from HIPASS.

Fisher 1977) and therefore the total mass of a galaxy. The H I mass is a measure of the gas content of a galaxy and it was used as the primary selection criteria for our sample of galaxies. The total gas content affects the rate of star formation in a galaxy (which affects the detectability of a galaxy in Hα). The total mass of a galaxy affects the dynamics of a galaxy (e.g., V_{max} and the steepness of the rotation curve). The figure shows that most Class 1 galaxies have low $M_{\rm HI}$ and M_R. These galaxies are dwarf galaxies, and hence have small r_e and slowly rising rotation curves with no turnovers. Dwarf galaxies are generally been defined by their small sizes, low luminosities and low V_{max} (e.g., Hodge 1971, Tamman 1980, Staveley-Smith et al. 1992, Tammann

(1994), Swaters et al. 2002, Lelli et al. 2014). Purely luminosity based definitions such as the $M_B > -16$ Tammann (1980) definition are problemmatic because of the large range in star formation rates and therefore luminosities (e.g., Gallagher & Hunter 1984, Staveley-Smith et al. 1992, Dunn 2010, Lelli et al. 2014). Definitions based on the V_{max} such as $V_{max} < 100\,\mathrm{km/s}$ by Lelli et al. (2014) are useful because they are purely based on the dynamical mass of the system. Most dwarf galaxies do satisfy this criterion (e.g., Swaters et al. 2002, 2009). This threshold is equivalent to $M_R > -19.1$, if I use the TFR from Wong et al. (2016). The most massive and H I rich galaxies are a mixture of the different classes but most are Class 2 and 3. All the Class 1 galaxies in this regime (e.g., J0230-02:S2, J1005-16:S2) are galaxies that are part of individual H I sources which consist of multiple optical galaxies. Their plotted H I masses are a combination of all galaxies within the H I source, therefore they are not accurate for the individual galaxies. Most of the massive and H I rich galaxies are Class 2 and 3. *This confirms that the 3D Plane model is most effective at fitting the velocity fields of dwarf galaxies and more massive galaxies have velocity fields that are better fitted by* ROTCUR *and* DISKFIT .

The bottom left panel of Figure 4.2 shows the photometric inclination i_O plotted against W_{50}. i_O quantifies how a galaxy is orientated with respect to the observer. The orientation (i.e., projection) of a galaxy affects how accurately its velocity can be measured and how effectively its rotation velocity can be derived from its velocity field. Face-on galaxies are problematic because their projected velocities are dominated by velocity dispersions and non-rotational velocities. This makes it difficult to determine their rotation velocities. Edge-on galaxies are also problematic because the long sight-lines through the galaxy disks cover a wide range of radii and projected velocities, making it difficult to determine the rotation velocity at the minimum projected radius. In observations such as Hα, dust obscuration can also affect the velocity profiles that I measure by attenuating the Hα emission. Determining photometric inclinations from axial ratios requires assumptions about the shape of galaxy and its flattening parameter (see earlier section). The W_{50} parameter is the profile width and it is a combination of the V_{max} and inclination of a galaxy. Therefore it is an indicator of the total mass of a galaxy and its inclination. The H I W_{50} compared to other wavelengths is particularly useful because it is unaffected by dust and H I disks extend much further out than the Hα-bright part of a galaxy does (e.g., Leroy et al. 2008).

In Figure 4.2 the Class 1 galaxies all have W_{50} <150 km/s. Most of the galaxies with W_{50} <150 km/s are Class 1, irrespective of their inclinations. This suggests that the mass of a galaxy has a greater effect on the fitting class than the inclination for

most inclinations. However, for very low i (i_O<25°) Class 2 galaxies have DISKFIT rotation curves that have large errorbars (J0504-16:S1) or their shapes do not match the expected shape of a rotation curve. Low inclination and low W_{50} galaxies tend to be better fitted by 3D plane. *This confirms along with the other panels that 3D plane fit performs best for low mass galaxies and those that cover a small area in the sky .*

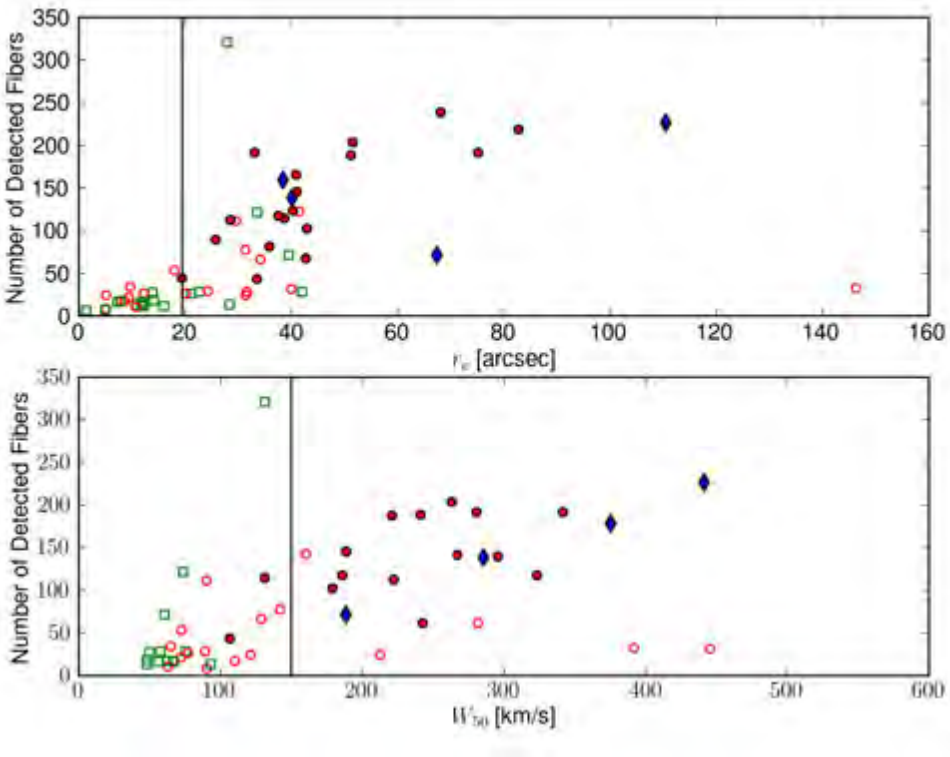

Figure 4.3: The number of fibers above the detection threshold used in each galaxy's kinematic fit plotted against the effective radius (*top*) and W_{50} (*bottom*). Galaxies where the s^2 from the 3D plane fit is the lowest are shown as squares, when the DISKFIT value is the lowest they are shown as circles and when the ROTCUR values are lowest they are shown as diamonds. Filled symbols are used to show galaxies that have a ROTCUR rotation curve fit. The effective radii are derived from SINGG photometry and the W_{50} values are from HIPASS. Vertical lines of $r_e = 19.5''$ (the radius of the semi-major axis of the inner fiber array) and $W_{50} = 150\,\mathrm{km/s}$ are shown in the top and bottom plots respectively.

I use s^2 as a goodness-of-fit parameter in our analysis. Analysis of s^2 with another parameter that can be used to differentiate the different fitting classes is useful

in order to study the absolute values of s^2 and its behaviour. I previously showed that M_R can be used to distinguish between Class 1 and Class 2-3 galaxies. Unlike the H I-derived parameters I can determine M_R for all the galaxies in our sample (i.e., even galaxies that are grouped into single HIPASS sources have their individual M_R values measured). The lowest s^2 values (i.e., the lowest value from the 3 methods) for each galaxy are plotted against M_R in the lower right panel of Figure 4.2. Below $W_{50} = 150\,\mathrm{km/s}$ there is a large range in s^2 and above it there is a smaller range in s^2 values. Faint M_R galaxies tend to have the lowest s^2 values. $s^2 = 1$ would occur for a model that perfectly fits the data. However, none of the methods produce s^2 values close to 1.0.This suggests that either the error model ($e_v = \sqrt{e_{vor}^2 + 0.9\,[\mathrm{km/s}]^2}$, see Chapter 2) underestimates the real velocity uncertainties or none of the models fully describe the velocity fields.

If I assume that some of the galaxies' velocity fields can be fully described by the models when the uncertainty includes the velocity dispersion, then I can estimate how much velocity dispersion is required to achieve $s^2 = 1$ for a galaxy that is fitted well by a model. This velocity dispersion is due to turbulence, thermal dispersion and other non-circular motion. J1621-02 has a regular velocity field and exhibits a prototypical spiral galaxy rotation curve, it is therefore the ideal case to determine this dispersion (ΔV). For a revised error model : $e_v = \sqrt{e_{vor}^2 + 0.9\,[\mathrm{km/s}]^2 + \Delta V^2}$, the required ΔV to get $s^2 = 1$ is $9.5\,\mathrm{km/s}$ for this galaxy. This value is slightly less than the velocity dispersion of H I but larger than that of CO (Mogotsi et al. 2016, Ianjamasimanana et al. 2012), and it is comparable to the Δ_{ISM} value I used in the DISKFIT fits.

As mentioned before, most of the Class 1 galaxies have r_e<20″ and W_{50}<150 km/s and I partly attributed this to lower data quality (i.e., few detected fibers covering the galaxy) in these regimes. The number of fibers in the velocity field of each galaxy is plotted against r_e and W_{50} in Figure 4.3 in order to verify this. Figure 4.3 shows that galaxies with low r_e and W_{50} tend to have fewer fiber detections than the galaxies with high r_e and W_{50}. For reference, inner fiber array has 17 tightly packed fibers and the radius of its semi-major axis is 19.5″. All the galaxies with r_e<20″ have fewer than 55 detected fibers. J0504-16:S1 is the only galaxy that has a ROTCUR fit that has $r_e < 20$". The plots confirm that most galaxies that have low r_e and W_{50} tend to have a lower quantity of data than the larger galaxies.

Systemic Velocity

The systemic velocity provides the zero point for rotation velocity measurements. It is very sensitive to the central position of a galaxy. It affects the rotational velocity amplitude and therefore the V_{max} of a galaxy. Determining the kinematic V_{sys} is useful in order to determine whether galaxies that are part of the same HIPASS source are part of the same group. Due to the large HIPASS beam the H I V_{sys} values for multiple systems are not necessarily the same as the V_{sys} values of individual members of the system. In individual systems the systemic velocities are expected to be similar to the HIPASS values. H I systemic velocities are flux-weighted and therefore some differences are expected between them and the kinematic values, but the kinematic V_{sys} should be within the H I profile of the system/ galaxy. The H I and kinematic V_{sys} values from DISKFIT and ROTCUR are plotted in Figure 4.4, and diagonal lines are used to show the range of profile width (W_{50}) around V_{sys}.

Hα emission is more concentrated in the central regions of disk galaxies (except in early type spirals with strong bulges) due to the higher star formation surface densities. H I is more extended than the stellar disk (e.g., Leroy et al. 2008); the outer parts of H I disks are often warped (e.g., Burke 1957, Kerr 1957, Sancisi 1976, Rogstad & Shostak 1971, Bosma 1981a,b) and asymmetric or lopsided (e.g., Matthews et al. 1999, Hayes et al. 1998, Swaters et al. 1999). Therefore I expect that the kinematic center and systemic velocity is better determined in Hα. In order to analyze the systemic velocity fits I determined weighted systemic velocities for the integrated Hα profiles of each galaxy ($V_{H\alpha}$). Profiles of each fiber that were above the detection threshold and not in the outer "sky" fiber part of the fiber bundle were co-added. Profiles from fibers that were not in the central bundle were weighted 3 times higher than those from the central regions to offset the effect of lower filling factor and decreased sensitivity in the outer regions. The flux-weighted mean velocities were determined for these integrated profiles. Comparisons between these velocities, ROTCUR (V_R), DISKFIT (V_D) and HIPASS systemic velocities (V_{HI}) are shown in Figure 4.4 .

In general the $V_{H\alpha}$ values are similar to V_{HI}, the standard deviation for the Hα velocities was 54.3 (km/s) (standard error 7.8 km/s), but there are many galaxies with large differences between them. The $V_{H\alpha}$ velocities are problematic because the fiber distribution is not uniform across galaxies, there are gaps between fibers, and the Hα emission is not uniform across galaxies. Most of the large differences between $V_{H\alpha}$ and V_{HI} are due to this.

Most of the HIPASS multi-sources have V_{sys} values within the H I W_{50} of the source

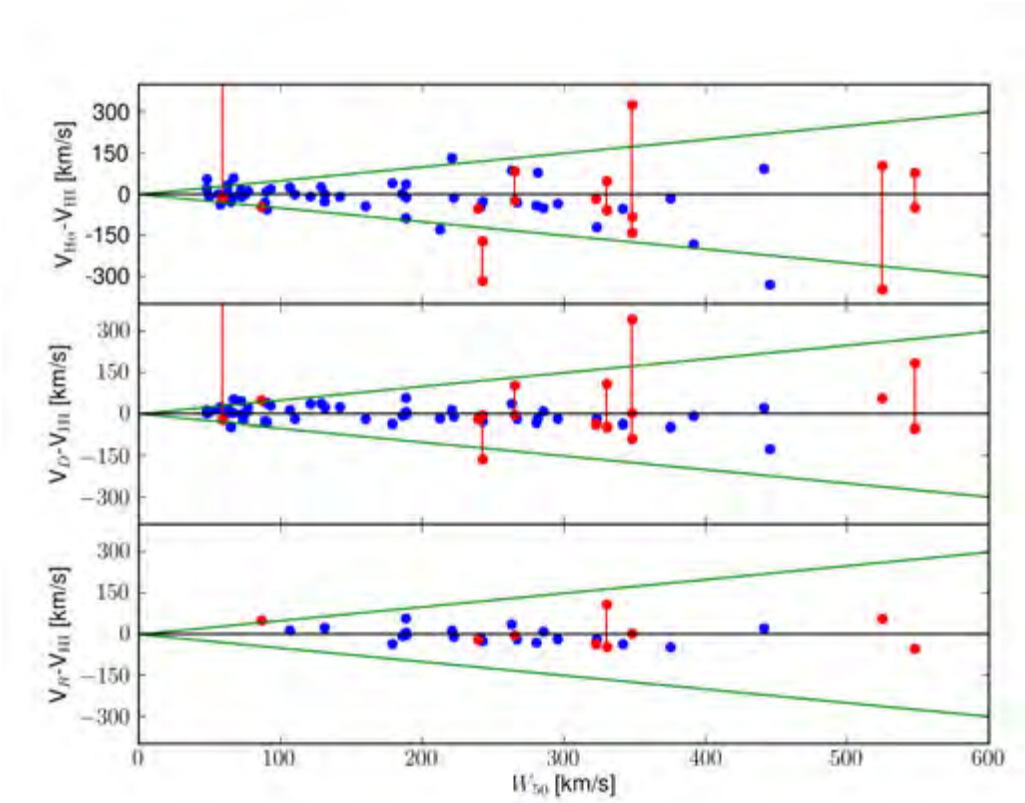

Figure 4.4: Comparisons between systemic velocities plotted against W_{50}. Galaxies that are part of multiple-source individual HIPASS detections source are shown in red. Multiple sources belonging to one HIPASS source have the same HIPASS systemic velocities and are connected by a red line. Green lines of $\pm 0.5\,(W_{50})$ are plotted too. *Top:* the difference between the integrated profile systemic velocities ($V_{H\alpha}$) and HIPASS (V_{HI}) plotted against the H I profile width (W_{50}). *Middle:* the difference between the HIPASS systemic velocities and DISKFIT systemic velocities plotted against W_{50}. *Bottom:* the difference between HIPASS systemic velocities and ROTCUR systemic velocities plotted against W_{50}. The red lines that extend beyond the plot range in the top and middle panels correspond to J0140-05:S2, which is outside the scale of the plot and is discussed in the text.

and are therefore likely to be group members or interacting with other galaxies that are covered by the profile. However J0140-05:S2 has $V_{H\alpha}$ and V_D values that are 788 km/s larger than V_{HI} and J0140-05:S1's systemic velocities. Therefore J0140-05:S1 and J0140-05:S2 are not part of the same group.

Most of the individual galaxies have kinematic V_{sys} within 50 km/s of V_{HI}. The standard deviations of the differences between them are: DISKFIT 25.4 km/s and ROTCUR

is 26.7 km/s . This indicates that the Hα dynamical center correlates well with the H I. Large differences indicate cases where the disks may be lopsided or have undergone some form of interaction.

Inclination

The inclination of a galaxy affects how the intrinsic rotation velocities of the galaxy are projected to the observed line-of-sight velocities. The i_O values for each galaxy are determined by comparing the photometric axial ratios. Comparisons between photometric and kinematic inclinations (i_K) are important as diagnostics for ROTCUR and DISKFIT fits. Differences between i_O and i_K either indicate some form of interaction or that they were not well constrained or fitted. They can also be due to non-circular motions due to structures like bars.

Figure 4.5 shows comparisons between the photometric i_O, DISKFIT i_D and ROTCUR i_R inclinations. The top panel compares i_O and i_D, the middle panel i_R and i_O and the bottom panel compares i_D and i_R. The i_D and i_O are mostly within 20° of each other (see Figure 4.5). The differences between them increase for faint M_R values (M_R >-20.5), where the fraction of Class 1 galaxies and galaxies with no ROTCUR fits is high. The difference $i_D - i_O$ has a standard deviation of 17.6° for $M_R>-17$, 15.2° for $M_R>-20.5$ and 5.4° for $M_R<-20.5$. Of the different galaxy classes, Class 1 galaxies have the largest differences between i_O and i_D. Class 1 galaxies tend to be the least luminous and most irregular in shape, hence i_O is more difficult to estimate. In addition to this the least luminous galaxies tend to have thicker disks (e.g., Roychowdhury et al. 2013) than large high luminosity galaxies, this results in rounder isophotes which make determining i_O difficult. The largest uncertainties in i_D tend to be from galaxies with the lowest luminosities, those with no ROTCUR fits.

Most of the low luminosity galaxies have small angular size and therefore few detected fibers. Many of them are Class 1 galaxies and have unreliable DISKFIT fits (the parameters are not well-constrained or are very different from the values expected from photometric data). If the galaxies' velocity fields can be approximated by a 3D plane, the kinematic fits are insensitive to inclination. This can result in the large DISKFIT uncertainties and bad i_D fits that I see in some of these galaxies. These faint M_R dwarf galaxies are typically irregular galaxies, their shapes are difficult to determine (e.g., Hodge & Hitchcock 1966, Staveley-Smith 1992, Binggeli & Popescu 1995, Sung et al. 1998, Sánchez-Janssen et al. 2010) and some of them have non-ellipsoidal shapes. Even for dwarfs that are not irregulars, the photometric major and minor axes were defined by eye and this is very difficult to do for small galaxies. Dwarf galaxies have thicker disks than regular spirals (e.g., Staveley-Smith et al. 1992, Hodge & Hitchcock

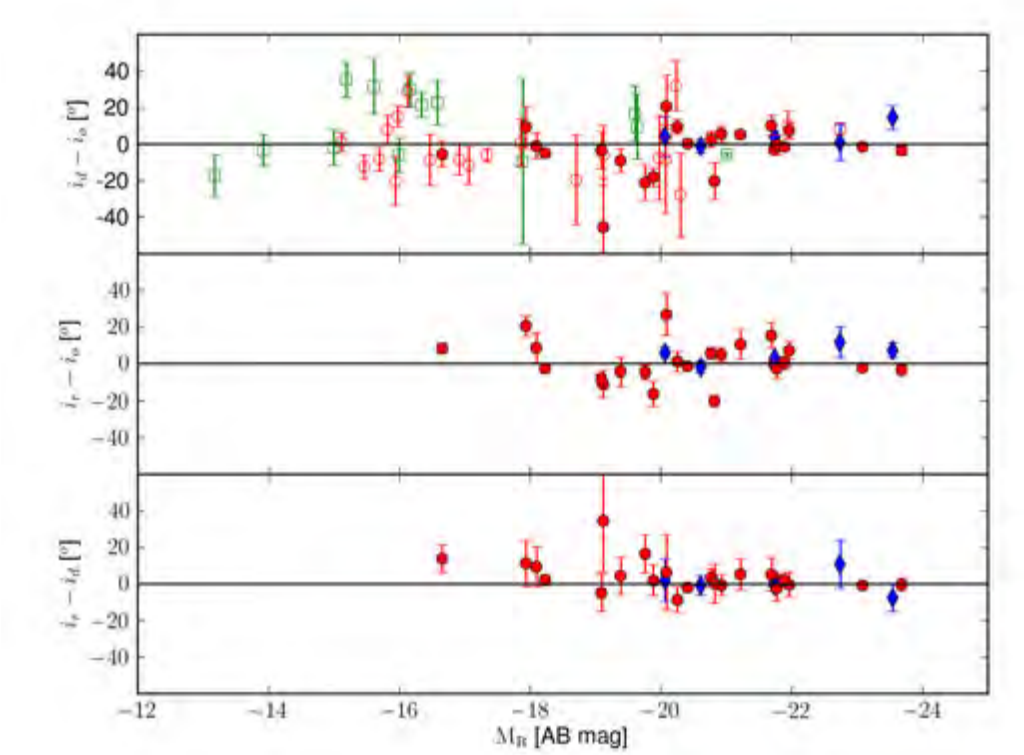

Figure 4.5: Plots of the comparisons between inclinations plotted against M_R. Galaxies where the s^2 from the 3D plane fit is the lowest are shown as squares, when the DISKFIT value is the lowest they are shown as circles and when the ROTCUR values are lowest they are shown as diamonds. Filled symbols are used to show galaxies that have a ROTCUR rotation curve fit. *Top:* the difference between the DISKFIT (i_D) and photometric (i_O) inclinations plotted against M_R. *Middle:* the difference between the ROTCUR (i_R) inclination and i_O plotted against M_R. *Bottom:* the difference between i_R and i_D plotted against M_R.

1966, Roychowdhury et al. 2013). The flatness parameter required to determine i_O from the major and minor axes ratios may not be constant for all the galaxies. For i_O calculations, we assumed zero disk thickness, therefore thicker disks have larger differences between the real inclination and i_O values used in this analysis. These factors can result in inaccurate i_O values at faint M_R causing large differences between i_O and i_D.

The i_R values are typically similar to the optical values, however there is a lack of galaxies with ROTCUR fits with faint M_R. But there there are galaxies with M_R >-20.5 that have ROTCUR fits and there are larger differences between i_R and i_O for

these galaxies than those with brighter M_R. For galaxies with $M_R < -20.5$, the standard deviations for $i_R - i_O$ and $i_D - i_O$ are 5.8° and 5.4° respectively. The similarity of i_D and i_R is confirmed in the lower panel where $i_R - i_D$ the standard deviation is 2.3° for galaxies with $M_R < -20.5$. Therefore galaxies with ROTCUR fits have high luminosities and they tend to be massive galaxies with many fiber detections and for the brightest of these galaxies i_D and i_R are very similar.

The galaxy with the highest differences between i_D and i_O is J0404-02 ($\Delta i = 45.6°$, Figure A20). Only J0302-18 (Figure A18) and J0404-02 (Figure A20) had differences between i_R and i_D greater than 15°. In both cases i_R values are closer to i_O than i_D is. These galaxies are Class 2, however their ROTCUR kinematic parameters will be used in further analysis because they are closer to what is expected based on the galaxies' photometry.

Position Angle

The position angle refers to the receding major axis of a rotating disk galaxy. It can be used as useful diagnostic of a simple rotating disk. Mismatches between the kinematic and photometric position angles can be due to problems with the measurements of one of these position angles. Photometric position angles are difficult to measure for galaxies that are face-on (or with low axial ratios), those that have ill-defined shapes or those with distortions in their light distributions. Misalignments can be due to an event that has disturbed the dynamics of the galaxy such as an interaction with another galaxy (e.g., García-Lorenzo et . 2014, Barrera-Balleseros et al. 2014). Structures which cause departures from pure disk rotation such as bars can also cause large differences between the photometric and kinematic position angles (e.g., García-Lorenzo et al. 2014, Barrera-Balleseros et al. 2014). Comparisons between kinematic and photometric i and ϕ values are useful for diagnosing whether the ROTCUR and DISKFIT fits are good and whether the disk is purely rotating.

Comparisons between the ϕ values derived by different methods are shown in Figure 4.6. The top left plot shows the differences between kinematic ϕ and photometric position angles ϕ_O plotted against H I W_{50}. The resistant mean [†] values and the corresponding mean errors of the ϕ differences from each method (in 50 km/s bins) are shown in the plot. The greatest differences between the kinematic ϕ and ϕ_O are at low W_{50} values, these differences decrease with increasing W_{50}. For $W_{50} > 150$ km/s the

[†]This is a robust mean which is determined by calculating the mean for all data points that have values within 2 standard deviations of the mean.

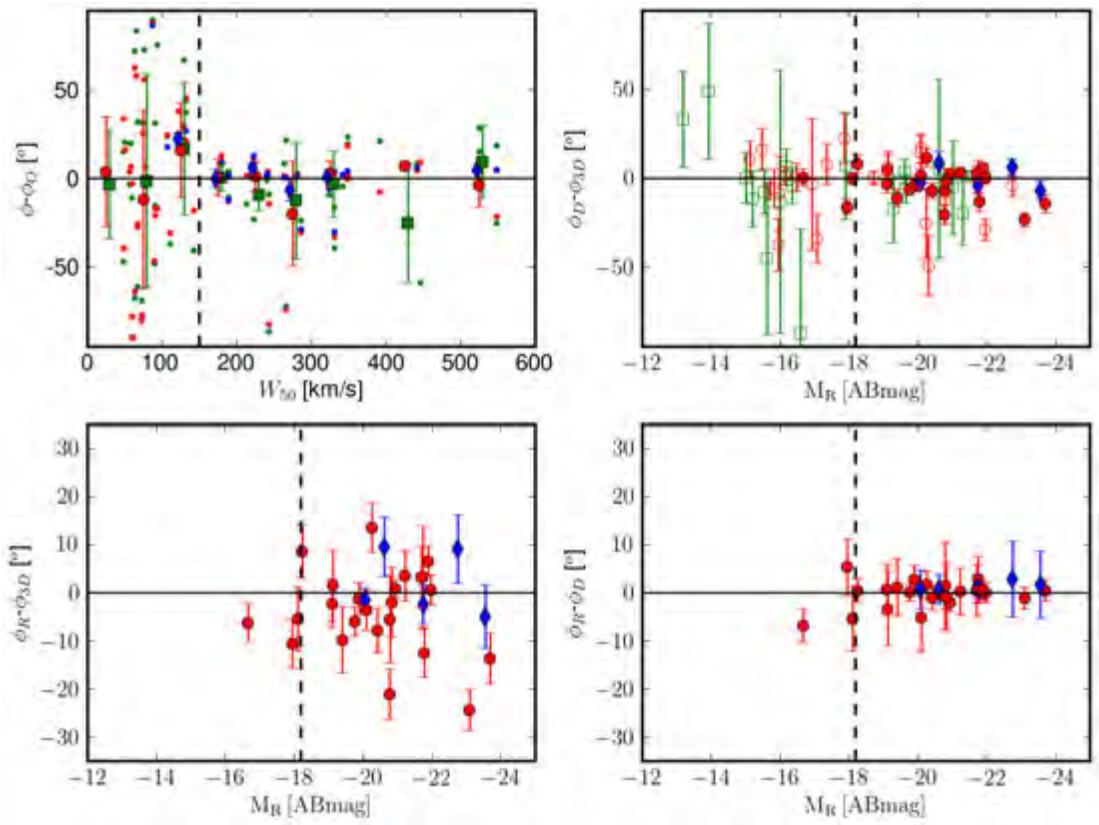

Figure 4.6: Plots of the comparisons between photometric and kinematic position angles plotted against W_{50} and M_R. *Top Left:* the difference between 3D plane (green), DISKFIT (red) and ROTCUR (blue) and photometric position angles plotted against W_{50}. The mean ϕ values of each 50 km/s W_{50} bin are plotted with errorbars being standard deviation. Class 1 galaxies are shown as squares, Class 2 galaxies as circles and Class 3 galaxies are shown as diamonds. *Top Right:* the difference between the DISKFIT (ϕ_D) and 3D plane (ϕ_{3D}) position angles plotted against M_R. *Bottom Left:* the difference between the ROTCUR (ϕ_R) position angle and ϕ_{3D} plotted against M_R. *Bottom Right:* the difference between ϕ_R and ϕ_D plotted against M_R. In the top right and bottom plots filled symbols are used to show galaxies that have a ROTCUR rotation curve fit. $W_{50} = 150$ km/sis indicated by the dotted line in the *top panel*, and the equivalent M_R value (-18.19, which was calculated by TFR fits from Wong et al. 2016) for 90° inclined galaxies is plotted as dotted line in the other panels.

difference between the kinematic and photometric ϕ values is close to zero and there is a smaller variance in the mean ϕ compared to galaxies at lower W_{50}. 3D plane ϕ values (ϕ_{3D}) differ from ϕ_O more than the DISKFIT (ϕ_D) and ROTCUR (ϕ_R) values do. Galaxies like J0504-16:S1 (Figure A22), J1103-23:S2 (Figure A36), J1247- 03 (Figure A46) and J1609-04 (Figure A58) have large differences between kinematic and photo-

metric ϕ. In some cases (e.g., J1247-03) the differences are due to bad velocity fields, or the velocity field is not aligned with the optical position angle (e.g., J0504-16:S1, J1103-23:S2 and J1609-04). J0504-16:S1 and J1103-23:S2 have low axial ratios and the i_O derived from these are 22° and 26° respectively. It is difficult to define the ϕ in such nearly face-on systems. Both galaxies are also in multiple systems and could therefore be interacting with their neighbouring galaxies resulting. Galaxies with ROTCUR fits have similar kinematic ϕ, there are large differences in galaxies with no ROTCUR fits.

The top right panel of Figure 4.6 shows $\phi_D - \phi_{3D}$ plotted against M_R. $\phi_R - \phi_{3D}$ and $\phi_R - \phi_D$ are plotted against M_R in the lower right and lower left panels respectively. These compare the different kinematic ϕ values and show where the largest differences between methods occur. The largest differences between ϕ_D and ϕ_{3D} values are for low-luminosity galaxies. Low luminosity galaxies also have the largest uncertainties in ϕ_D. As mentioned before, many of these galaxies are dwarf galaxies and the high uncertainties are due to the difficulty of measuring geometric parameters for such galaxies - due to their larger thickness, rounder or ill-defined shapes and small sizes. They have low rotational velocities (e.g., Swaters et al. 2009) and non-circular motions have a greater effect on our measurements than they would for larger galaxies. Turbulence, outflows, inflows, winds, bars and interactions can all cause non-circular motions that affect the determination of ϕ.

The TFR is used to relate the profile width and absolute magnitude of a galaxy therefore I can determine the equivalent M_R value of the W_{50} threshold. I plotted the W_{50}<150 km/s and its equivalent M_R value in Figure 4.6. Wong et al. (2016) measured the TFR for the SINGG sample of galaxies. The sample they used to fit the relation had moderately inclined galaxies, and the V_{max} values of the galaxies were derived from HIPASS W_{50} and they corrected the linewidths for inclination, turbulence, relativistic broadening (broadening due to the Hubble flow) and instrumental resolution (Meurer et al. 2006, Meyer et al. 2008). Their fitted relation was: $M_R = -3.9 - 7.622 \log(V_{max})$, where V_{max} can be calculated from W_{50}. I therefore used these fitted parameters to estimate the M_R, which I found to be −18.19. Galaxies may deviate from the TFR due to measurement uncertainties in W_{50} or M_R as well as due to intrinsic scatter in the TFR. The W_{50} of each galaxy depends on the profile width, inclination and peak flux. The H I W_{50} values are not corrected for inclination and the conversion assumes an inclination of 90°. Therefore lower inclination galaxies will have underestimated W_{50} values compared to M_R. The greatest uncertainties are due to W_{50} measurements. The M_R can also be enhanced due to starbursts, but this will only have a minor effect on the value of M_R. Despite the uncertainties in the W_{50}, most of the Class 1 galaxies have M_R >−18.19 and W_{50} <150 km/s , therefore these thresholds can be used interchange-

ably. As mentioned before, the largest density of Class 1 galaxies is in the regime: M_R >-17, using the same formula this corresponds to $W_{50} = 104.6\,\mathrm{km/s}$. This confirms that these galaxies are primarily small dwarf galaxies.

For $M_R>-17.0$ galaxies, $\phi_D - \phi_{3D}$ has a standard deviation of 29.5° and for more luminous galaxies the standard deviation is much smaller: 11.8°. Therefore for larger and more massive galaxies there is greater agreement between the ϕ_D and ϕ_{3D} and this is due to larger fiber detections and the non-circular motions having a smaller effect on the our observations and the kinematic fits. For $M_R <-17.0$, $\phi_D - \phi_{3D}$ (standard deviation: 11.8°) has a larger scatter than $\phi_R - \phi_{3D}$ (standard deviation: 8.8°). Part of the reason for the larger scatter is due to galaxies with no ROTCUR fits being included in the $\phi_D - \phi_{3D}$ plot. These galaxies have no ROTCUR fits because of insufficient data quality/number of detected fibers or low inclinations. Most of the galaxies with ROTCUR fits have ϕ differences less than 20°. The ROTCUR and scdiskfit ϕ values are very similar to each other and $\phi_R - \phi_D$ has a standard deviation of 2.0° for $M_R <-17.0$. The small differences between the two methods is expected because ROTCUR and DISKFIT fit the same kinematic parameters and both assume a constant ϕ and i throughout a disk that has no warp, bar, inflow or outflow, therefore they should produce the similar results when fitting high quality data. Kinematic ϕ values for galaxies with $M_R <-17.0$ are very similar when all three fitting methods can fit the data. Therefore the kinematic ϕ is well constrained for high quality data and it is more difficult to constrain it at low W_{50}.

Table 4.1: Kinematic Parameters of the Sample.

Galaxy		Vsys [km/s]		Inclination [Degrees]			Position Angle [Degrees]			
SINGG	H I	D	R	Opt	D	R	Opt	D	R	3DP
1	2	3	4	5	6	7	8	9	10	11
J0019-22	669.6	705.9	-	30.7	18.2	-	117.1	335.3	-	319.0
J0031-22	539.2	552.9	-	42.6	39.1	-	31.0	357.0	-	226.4
J0034-08	1651.8	1665.7	1644.6	-	53.2	56.4	-	221.4	222.9	228.4
J0039-14a	1451.9	1458.5	-	56.1	18.2	-	10.9	314.9	-	143.0
J0040-13	1636.1	1618.3	-	48.7	54.5	-	-	350.4	-	333.1
J0045-15	941.3	946.4	-	27.6	25.2	-	49.5	189.3	-	204.7
J0112+00	1151.9	1132.5	-	40.9	34.7	-	-	113.6	-	107.4
J0130-22	1627.6	1609.1	1609.0	50.8	60.2	51.8	-	282.1	283.8	270.2

Continued on next page

Table 4.1 – continued from previous page

Galaxy		Vsys [km/s]		Inclination [Degrees]			Position Angle [Degrees]			
SINGG	HI	D	R	Opt	D	R	Opt	D	R	3DP
1	2	3	4	5	6	7	8	9	10	11
J0140-05:S1	1283.7	1262.6	-	33.5	68.7	-	130.3	28.1	-	39.6
J0140-05:S2	1283.7	2108.8	-	74.8	68.9	-	168.1	165.4	-	157.4
J0223-21	1507.5	1460.8	1477.1	64.3	63.1	62.4	-	251.9	252.7	243.1
J0230-02:S1	5739.0	5686.9	5692.2	74.7	71.4	71.2	5.4	10.0	10.6	24.2
J0230-02:S2	5739.0	5923.6	-	40.9	57.8	-	147.2	126.0	-	122.2
J0239-08	1245.9	1220.6	1220.5	71.4	66.6	68.7	-	145.7	146.2	137.6
J0241-06	1294.3	1287.9	1287.7	56.7	55.7	65.3	-	49.7	44.4	49.8
J0246-07	1405.4	1387.3	1383.7	67.8	49.6	51.6	-	211.3	214.1	215.3
J0249-02	1092.0	1066.4	-	23.7	52.5	-	140.1	93.8	-	92.2
J0302-18	1777.2	1774.2	1772.6	39.1	18.2	34.7	-	53.6	53.8	59.8
J0335-24	1462.9	1455.0	-	46.8	57.3	-	135.2	127.7	-	156.6
J0404-02	861.3	826.3	816.5	74.4	28.8	63.4	12.3	205.3	202.0	200.5
J0441-02	716.1	774.1	775.1	44.6	48.5	50.5	38.2	205.5	206.3	207.7
J0504-16:S1	3341.7	3391.0	3393.0	21.5	64.6	48.3	47.1	321.1	313.8	317.7
J0935-05	1495.3	1500.7	-	52.3	73.8	-	93.9	110.4	-	114.6
J0942+00	1894.0	1916.7	-	5.7	-	-	82.3	307.9	-	306.5
J0943-05b	2026.2	2066.9	-	26.6	18.2	-	22.8	186.1	-	171.4
J1002-06	661.4	699.5	-	90.0	69.6	-	14.9	44.7	-	82.0
J1005-16:S1	4676.4	4678.8	4683.2	75.7	72.5	75.6	167.2	349.0	351.7	348.3
J1005-16:S2	4676.4	5020.7	-	90.0	84.2	-	48.6	67.3	-	72.3
J1005-16:S3	4676.4	4589.0	-	75.5	-	-	50.3	50.3	-	70.0
J1026-19:S1	9094.1	9088.5	-	39.6	47.8	-	151.8	233.9	-	238.1
J1026-19:S2	9094.1	8932.0	-	44.0	-	-	172.9	187.1	-	181.6
J1039+01	708.5	710.9	-	20.7	-	-	153.0	185.1	-	228.5
J1041-23	1195.3	1219.0	1222.3	42.7	52.0	63.3	36.7	58.4	63.8	74.3
J1042-23	1044.6	1069.4	-	75.1	75.8	-	108.2	90.3	-	67.8
J1103-23:S1	1113.9	1109.6	1109.3	70.1	72.3	75.6	76.5	257.8	257.1	278.2
J1103-23:S2	1113.9	1217.4	-	25.7	18.2	-	83.4	189.4	-	191.3
J1105-00	797.8	819.6	819.0	62.2	66.0	65.1	160.3	345.1	346.4	348.8
J1107-17	993.5	-	-	53.3	-	-	157.7	-	-	194.5
J1127-04	966.6	988.5	-	62.6	63.5	-	167.1	174.1	-	163.2
J1130-16	1315.2	1329.5	1329.8	49.1	43.6	57.5	79.7	104.5	97.7	103.8
J1136+00b	1102.6	1072.5	-	32.1	20.7	-	162.0	162.2	-	159.1

Continued on next page

Table 4.1 – continued from previous page

Galaxy	Vsys [km/s]			Inclination [Degrees]			Position Angle [Degrees]			
SINGG	H I	D	R	Opt	D	R	Opt	D	R	3DP
1	2	3	4	5	6	7	8	9	10	11
J1145+02	-	990.7	-	52.2	34.7	-	136.6	210.6	-	177.1
J1147-16	1206.5	1196.0	1194.7	45.2	50.6	50.1	9.3	193.4	191.4	190.5
J1157-15	1432.2	1435.8	-	66.8	55.0	-	153.9	180.9	-	214.7
J1217+00	935.2	925.4	-	69.9	67.9	-	93.1	183.4	-	182.9
J1247-03	1124.7	1079.7	-	24.3	56.3	-	66.9	305.0	-	330.4
J1253-12	824.2	823.0	-	69.1	84.2	-	138.9	61.9	-	70.2
J1255+00	1321.5	1328.7	1323.5	54.1	50.5	45.8	164.0	345.2	346.0	348.2
J1300-13:S1	2554.0	2534.5	2535.1	27.9	38.2	43.5	145.9	148.1	148.6	145.2
J1326+02A	-	1071.7	-	37.9	18.2	-	-	308.8	-	308.4
J1338-09	1298.2	1276.7	-	22.5	31.9	-	97.1	303.0	-	308.7
J1403-06:S1	2591.0	2544.8	2548.0	62.0	61.5	59.4	171.7	175.0	175.6	188.1
J1403-06:S2	2591.0	2700.1	2701.3	40.8	41.5	52.4	85.7	52.8	55.7	46.5
J1423+01	1386.8	1377.1	1378.8	66.2	57.2	62.0	157.5	169.3	170.5	180.3
J1442-08	1818.8	1788.8	1789.1	79.1	58.9	59.1	166.0	348.0	347.2	349.1
J1447-17	2198.8	2182.5	-	76.0	80.2	-	168.6	170.3	-	182.8
J1500+01	1357.4	1339.7	1334.4	57.4	62.7	67.8	171.6	165.9	166.2	162.6
J1509-11:S1	1866.1	1830.6	1831.9	51.7	59.1	59.0	148.5	328.1	328.2	327.5
J1609-04	830.5	877.5	-	52.6	44.0	-	118.5	18.6	-	17.9
J1621-02	1569.2	1533.5	1535.1	67.9	66.3	68.1	50.5	52.3	53.0	46.3
J2025-24	3182.0	3191.7	3198.6	45.0	59.4	52.1	82.9	232.7	234.5	239.4
J2056-16	1451.9	1505.4	-	45.7	75.5	-	29.7	184.1	-	177.5
J2102-16	1471.6	1508.0	1508.7	76.4	76.7	74.8	83.7	85.4	84.5	92.3
J2142-06	1262.7	1273.0	-	42.7	34.3	-	137.7	21.4	-	24.9
J2202-20:S1	2620.6	2677.1	2682.7	77.8	76.2	75.4	59.7	65.1	64.0	88.4
J2202-20:S2	2620.6	-	-	64.8	-	-	145.0	-	-	340.4
J2205-22	7416.2	7291.2	-	46.1	18.2	-	162.4	171.9	-	221.0
J2234-04	889.3	918.4	-	61.6	84.4	-	96.7	79.8	-	172.3
J2239-04	829.0	852.9	-	60.2	54.1	-	77.1	264.2	-	277.1
J2242-06	900.3	919.6	-	47.6	79.1	-	41.6	104.2	-	149.4

Comments: Column 1: Galaxy name; Column 2: Systemic Velocities from HIPASS H I data; Column 3: Systemic Velocities from DISKFIT; Column 4: Systemic Velocities from ROTCUR; Column 5: Inclinations from optical data; Column 6: Inclinations from DISKFIT; Column 7: Inclinations from ROTCUR; Column 8: Position angles from optical data; Column 9: Position angles from DISKFIT; Column 10: Position angles from ROTCUR; Column 11: Position angles from 3D plane fit.

Comments about General Properties

The largest uncertainties in the fitted kinematic parameters are for Class 1 galaxies. Most Class 1 galaxies and other galaxies with large uncertainties in their kinematic parameters have W_{50}<150 km/s which corresponds to $M_R > -18.19$. When I examine M_R, the highest fraction of these galaxies has $M_R > -17.0$ which corresponds to W_{50} <16.8 km/s , these are dwarf galaxies. Dwarf galaxies are difficult to fit rotation curves to due to their few detectable fibers, poor data quality (due to weak emission), thicker disks (larger velocity dispersion relative to rotation velocity), small rotation amplitude, poor sampling of the rotation curve and lack of or inability to observe the turnover radius of the rotation curve. As expected the 3D plane model performs better for these galaxies than it does for the large galaxies. It outperforms DISKFIT and ROTCUR for a larger fraction of these galaxies than it does for the more massive galaxies. Despite low s^2 values and 3D plane being able to fit these galaxies, their ϕ uncertainties are very high. ROTCUR can only be used to successfully fit massive galaxies with moderate to high inclinations and many fiber detections (i.e., good data quality). DISKFIT and ROTCUR perform best for these galaxies and their i and ϕ values generally agree with the photometric values and with each other. DISKFIT successfully fits parameters over the largest range of galaxies, but is outperformed by 3D plane for the faintest and smallest galaxies.

Due to the large differences between V_{sys} and V_{HI} for J0140-05:S2, it is not in a group with J0140-05:S1. Therefore I use its V_{sys} value instead of V_{HI} as its recession velocity and this is the value used to calculate its Hubble flow distance. J0302-18 and J0504-16:S1 are Class 2 galaxies, however their ROTCUR derived kinematic properties are much more similar to the photometric properties than the DISKFIT derived properties and the shapes of their ROTCUR rotation curves match what is expected from a disk galaxy's rotation curve. Therefore these were re-classified as Class 3 galaxies for the surface brightness - kinematics analysis.

4.1.3 Velocity Gradient Measurement

Linear Approximations and 3D Plane

The 3D plane model fits the velocity gradient directly from the velocity field. Since the inclination cannot be determined using the 3D plane model, therefore I cannot independently decouple the i and α. The output from 3D plane model fits is: $\alpha sin(i)$. i_O can be used to determine α from the $\alpha sin(i)$ fitted in the 3D plane model. How-

ever, it should be noted that many Class 1 galaxies are dwarf galaxies and their i_O values can be difficult to determine accurately. There are also additional uncertainties introduced by using parameters determined by different methods. DISKFIT and ROTCUR were used to model velocity fields with a rotation curve that has constant i and ϕ. α can be determined directly from their rotation curves. The i and α derived from these methods can then be used to calculate $\alpha sin(i)$ in order to compare with what is found using 3D plane, without using i_O or making additional assumptions.

In order to determine whether the gradients determined from the 3D plane model are reliable, they are compared to DISKFIT gradients in Figure 4.7. DISKFIT is used because there are more galaxies that have DISKFIT fits than those with ROTCUR fits. Due to the different effectiveness of each method for galaxies with different properties I only make comparisons between galaxies where DISKFIT and 3D plane s^2 values are similar (within 50% of each other) and low (below $s^2 = 30$). This is done to compare velocity gradients where both methods fit the data reasonably well and have similar effectiveness. The gradients from both methods should be similar for these cases. This comparison is not ideal because the cases where 3D plane fits the data well is where the rotation curve has no turnover and DISKFIT struggles to fit the data, and conversely when there is a clear turnover DISKFIT is expected to perform well while 3D plane struggles to fit the data. The galaxies that have ($s^2 < 30$ and s^2 values within 50% of each other) will be those that are intermediate between these two cases.

There are different ways to determine velocity gradients from rotation curves. In the kinematics and star formation analysis I aim to study the inner rotation gradient and compare it to the star formation density therefore in the top two panels of the Figure 4.7 I compare the inner DISKFIT rotation gradient to the 3D plane gradient. In the top panel I calculated the DISKFIT gradient by using the first non-zero point of its rotation curve, and in the middle panel I calculated the gradient by using the second point of its rotation curve. The gradients were calculated as follows: $\alpha_1 = V_1/R_1$ (top panel) and $\alpha_2 = V_2/R_2$ (middle panel), where the subscripts indicate the sequence of points on the DISKFIT rotation curve (ordered by increasing radius starting from $r = 0''$).

In the top panel most of the galaxies have gradient ratios (DISKFIT/3D plane) between 0.7 and 2; the mean gradient ratio is 1.35 (with a standard deviation of 0.77). There is less scatter in the middle plot, the mean of the ratios in that plot is 1.25 (standard deviation: 0.38). The DISKFIT gradients tend to be larger than those from the 3D plane method. This is because the gradients determined from the DISKFIT rotation curves are for the inner part of the galaxy (typically of radii $20''$ and lower). J0040-13, J0943-05b, J2142-06 are the only galaxies with gradient ratios larger than 2.0 in the α_1

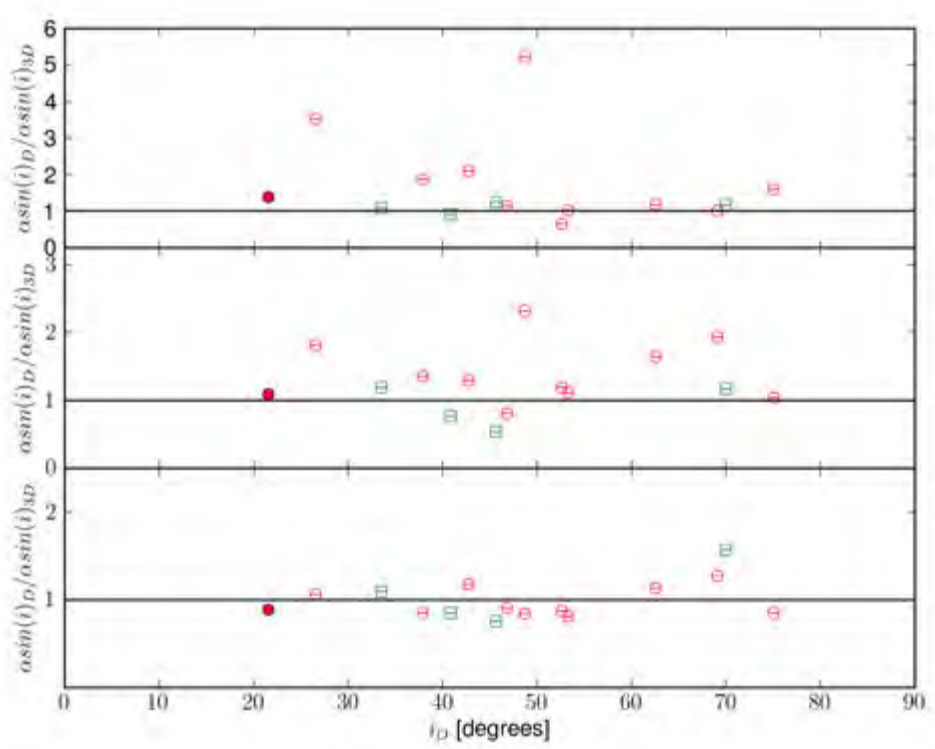

Figure 4.7: Ratios of the DISKFIT and 3D plane velocity gradients ($\alpha sin(i)$) plotted against i_O. These were plotted for galaxies with 3D plane and DISKFIT s^2 values within 50% of each other and with s^2 values below 30. The different panels show DISKFIT α values calculated in different ways. Top: α was determined by using the first non-zero value of the rotation curve. Middle: α was determined by assuming a constant linear rise to the second non-zero value of the rotation curve (this was the only value used in the fit). Bottom: α was calculated by a linear fit to the DISKFIT rotation curve.

comparison plot. J0040-13 (see Figure A5) and J0943-05b (Figure A25) have rotation curves that have turnover radii lower than the first points of their rotation curves - their rotation curves appear roughly flat. J2142-06 has a turnover at 10″. Therefore in these galaxies the gradients determined from the 3D plane fit, which are calculated over the entire galaxy, will be much lower than the DISKFIT inner gradients. Galaxies where gradients are similar such as J0140-05:S1 and J0230-02:S2 have no observed turnover, therefore their velocity fields can be fitted to a 3D plane and their rotation curves are close to linear. Many of these galaxies have very low rotation amplitudes, few fiber detections and therefore have large uncertainties in their fitted rotation velocities. In some galaxies such as J2056-16 and J0045-15, the DISKFIT fits to the velocity field are not good despite the low s^2 values of the fits, resulting in unphysical rotation curves.

Since the 3D plane model fits the entire velocity field I also compared the gradient determined from it with the gradient of the entire DISKFIT rotation curve. That gradient was determined by fitting a line to the entire rotation curve. There is a much tighter correlation between this gradient and the 3D plane than with the gradients calculated using the inner points. The mean gradient ratio is 0.97 (standard deviation: 0.15). There is no bias towards large gradient ratios. The tighter correlation and mean close to one is because the 3D plane fits model the entire velocity field and assumes that the rotation curve can be approximated by a constant gradient line with no turnover. The large differences are an indicator of galaxies with rotation curves that have a turnover. When there rotation curve turns over then fitting a line or performing a 3D plane fit result in poor fits to the data. Some galaxies have large differences between the top and bottom plot. The tight correlation in the bottom plot indicates that the 3D plane gradients do match DISKFIT gradients when both methods fit the data equally well. This indicates that the 3D plane α measures the gradients as expected.

I used alternative methods to determine the inner velocity gradients from the DISKFIT and ROTCUR rotation curves. These methods involve parameterizing and fitting the rotation curves. In order to do this the shape of the rotation curve must be assumed, and due to the sparse sampling only simple parameterizations can be used. The following subsections show the different methods that were tested. The other source of uncertainty arises from the definition of the inner gradient. The inner gradient can either be the innermost gradient or the gradient of the rising part of the rotation curve. Both of these definitions are considered in this analysis. An important consideration in these gradient definitions is that they need to be matched to surface densities that cover the same radius that they are defined at.

Diagonal Step Function

As mentioned before, rotation curves of disk galaxies have a rising inner part that flattens at large radii. This shape can be parameterized into a diagonal step function which consists of a linear rising inner part with a gradient larger than zero and a flat (gradient = 0) line at larger radii which has V_c equal to the maximum velocity of the flat part of the rotation curve (V_{max}). The two lines intersect at the turnover radius (r_{ts}, in the case of the diagonal step function). The biggest problem with using this parameterization is having to estimate r_{ts} (or V_{max}). I attempted to estimate r_{ts} by visual inspection, however this method is fraught with uncertainty. I developed software to try the following automated methods of determining r_t.

The H I W_{50} was used to estimate V_{max}, by assuming that $V_{max} = \frac{W_{50}}{2sin(i)}$. This is

a reasonable assumption because the H I extends further out and is more symmetric than the Hα emission. Therefore it is more likely to reach the flat part of the rotation curve in galaxies that have slowly rising rotation curves. And since the emission is symmetric, half of the width of the total profile should equal V_{max}. However, the i has to be decoupled from W_{50} in order to extract V_{max}, and this introduces additional uncertainties. The use of W_{50} is also problematic because it means that the gradients will not be determined purely from the Hα observations. Another problem with the use of this method was that in some cases ($S1, S2, S3$... galaxies) multiple galaxies had the same H I profile, therefore the W_{50} represents their combined width and cannot be used to determine V_{max} for the individual galaxies.

Another method was to determine when the rotation curve is flat by iteratively moving through the rotation curve and selecting the points where the difference between consecutive points was below a particular threshold. Thresholds were determined by using the uncertainties of the V_c points. However many of the DISKFIT rotation curves had large uncertainties, rendering the thresholds determined with their uncertainties ineffective. And very few galaxies had smooth rotation curves that flattened out completely and could be described by the step function. Therefore gradients, r_{ts}, V_{max} determined by using this parameterization were not very accurate. To improve the r_t and V_{max} fits I fitted smooth and more complex functions to the rotation curves. Figure 4.8 shows an example of how the different methods of fitting the diagonal step function compare to one of the other functions I fitted to the rotation curve for a galaxy that is closer to the ideal than most of our sample.

arctan

The arctan function has been used to model rotation curves (e.g., Courteau 1997). And it is a useful parameterization that captures a sharp to gradual rise in a rotation curve that flattens off at large radii. I fitted an arctan function (using KMPFIT) to the DISKFIT and ROTCUR rotation curves using this formulation:

$$V_c = a_0 \, arctan\left(\frac{r}{r_{tt}}\right), \tag{4.16}$$

where r_{tt} is the turnover radius fitted by the arctan function and a_0 is the constant that can be used as an estimate of V_{max}. Initially, fitting this function to the data proved largely unsuccessful due to bad initial parameters. The fitted turnover radii for most of the galaxies was less than $1''$, which is unphysical. The outputs of the diagonal step function were then used as initial parameters and they proved to be good enough estimates to improve the fits and I was able to get reasonable fits for many galaxies.

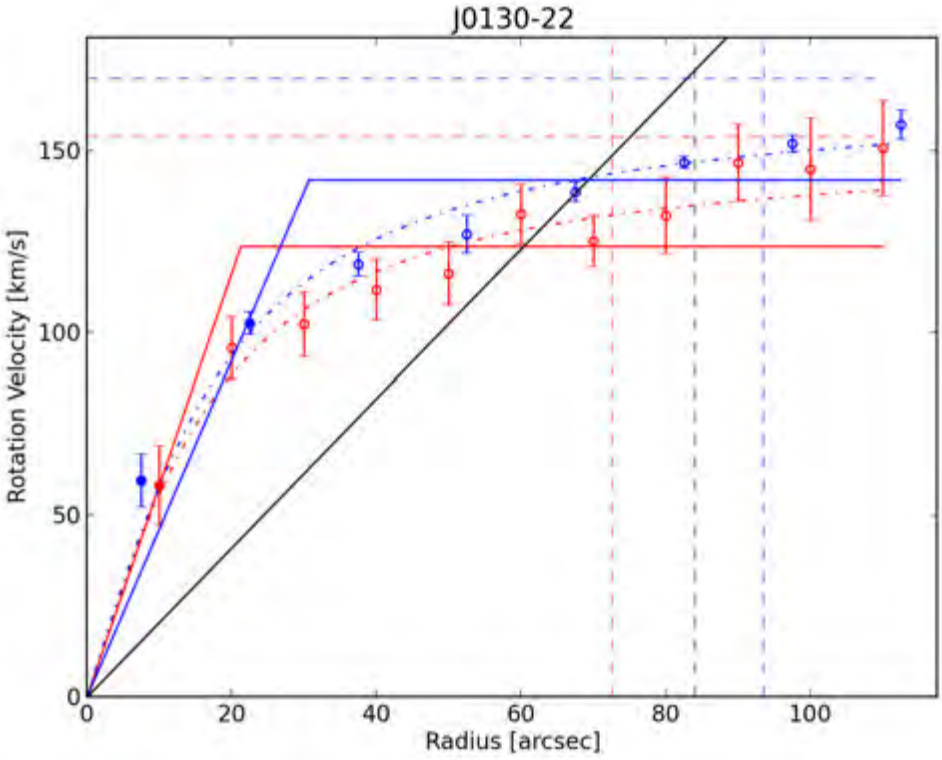

Figure 4.8: The DISFKIT (red) and ROTCUR (blue) rotation curves of J0130-22. The solid lines are the diagonal step function fits determined using a V_{max} defined by where the rotation curve flattens, the dashed lines are V_{max} and r_t values determined from the H I profile (r_{ts}), and the dashed-dot lines are from the arctan fits (r_{tt}. The solid black line is the 3D Plane gradient line (using i_O).

Figure 4.8 shows an example of the arctan fit.

If V_{max} is defined as $V_{max} = \frac{\pi}{2} a_0$,then r_{tt} is the value of r when $V = 0.5 V_{max}$. The gradient of the arctan function is:

$$\frac{dV}{dr} = \frac{a_0 r_{tt}}{r_{tt}^2 + r^2}. \tag{4.17}$$

The arctan model is relatively simple, therefore I tried to fit a more complex alternative to it in the following section.

Courteau Multi-Parameter Model

Courteau (1997) used a phenomenological parameterization of the rotation curve they called the multi-parameter function. Schlegel (1995), Rix et al. (1997) and Kravtsov et al. (1998) developed similar formulations to theirs. This function is more complex

than the arctan function, it takes into account a wider variety of shapes and distortions in the rotation curve than the arctan model does. I fitted the following form of the function to the rotation curves (using KMPFIT):

$$V_c = \frac{V_{max}\,(1 + (r_{tm}/r))^{b_0}}{(1 + (r_{tm}/r)^{b_1})^{1/b_1}}, \tag{4.18}$$

where b_0 is a parameter that models the drop-off or rise of the outer rotation curve and b_1 models the sharpness of the turnover. In their analysis, Courteau (1997) set b_0 to zero for most of their galaxies. This more complex parameterization was designed to fit the commonly found shapes and distortions in the shapes of rotation curves. For $b_0 = 0$, r_{tm} is related to r_{tt} via the following relation: $r_{tt} = r_{rm}/(2^{b_1} - 1)^{1/b_1}$. Therefore $r_{tt} = r_{tm}$ when $b_1 = 1$. The multi-parameter function reduces to solid body rotation when r_{tm} is much larger than r, and to a flat rotation curve when r_{tm} is much smaller than r.

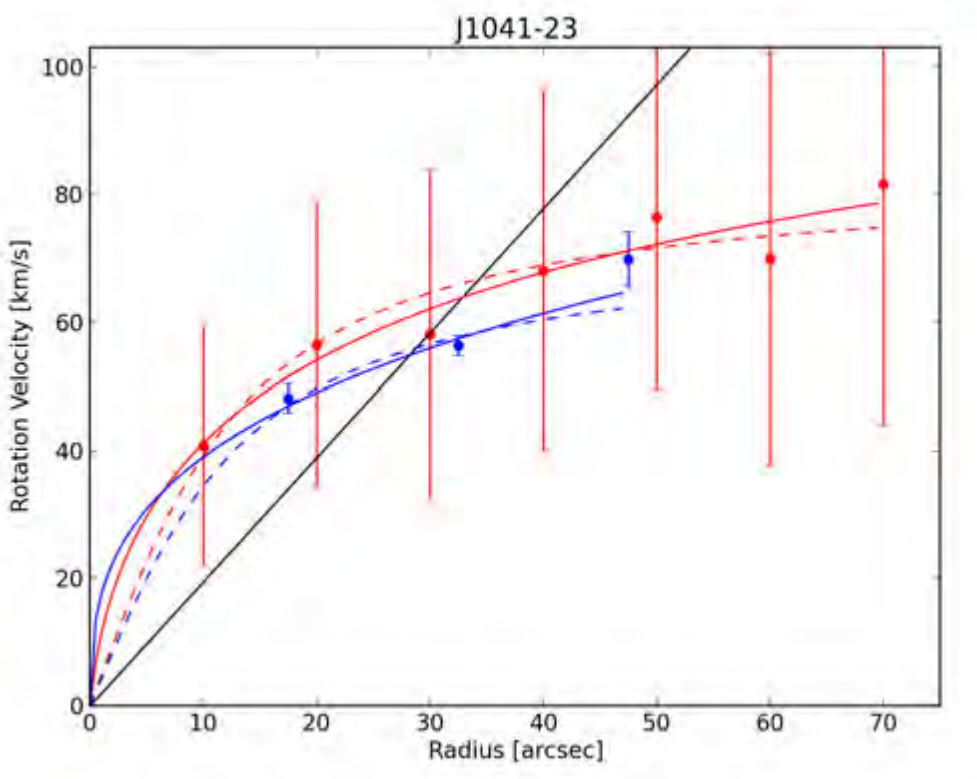

Figure 4.9: The DISFKIT (red) and ROTCUR (blue) rotation curves of J1041-23. The dashed lines are from the arctan fits, and the solid lines are the multi-parameter fits. The solid black line is the 3D Plane gradient line (using i_O).

After testing fits where I set b_0 as free parameter, I found that it resulted in many unphysical fits and overfitting of the rotation curves, therefore I fixed b_0 to zero. There

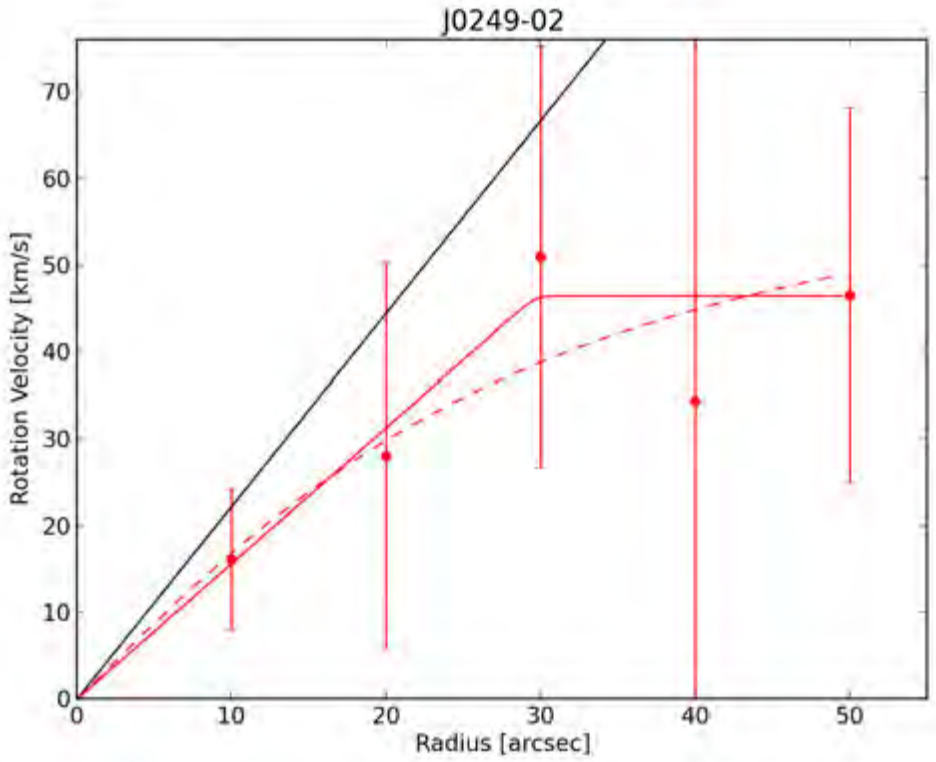

Figure 4.10: The DISFKIT (red) rotation curve of J0249-02. The dashed lines are from the arctan fits, and the solid lines are the multi-parameter fits. The solid black line is the 3D Plane gradient line (using i_O).

were only two free parameters: b_1 and r_{tm} in the final fits. A typical example of a multi-parameter function fit compared to an arctan fit is shown in Figure 4.9. In most cases the fits are similar, but the multi-parameter fits often have a steeper inner region than the arctan fit. The multi-parameter fit is able to fit rotation curves with sharp changes in velocity better than the arctan function, which does not perform well in those cases (unless the r_t is very small and unsampled, when both models seem to work equally well), an example of this is shown in Figure 4.10. The multi-parameter fits tend to have sharper turnovers than the arctan fits (e.g., Figure 4.10 and 4.11). I was able to fit more galaxies using the arctan function than with the multi- parameter fit due to the simpler form of the arctan function. It should also be noted that both functions are approximations and both of them are sensitive to the turnover radius and not the inner gradient. Therefore they are more useful for determining gradients close to the turnover radius rather than the center.

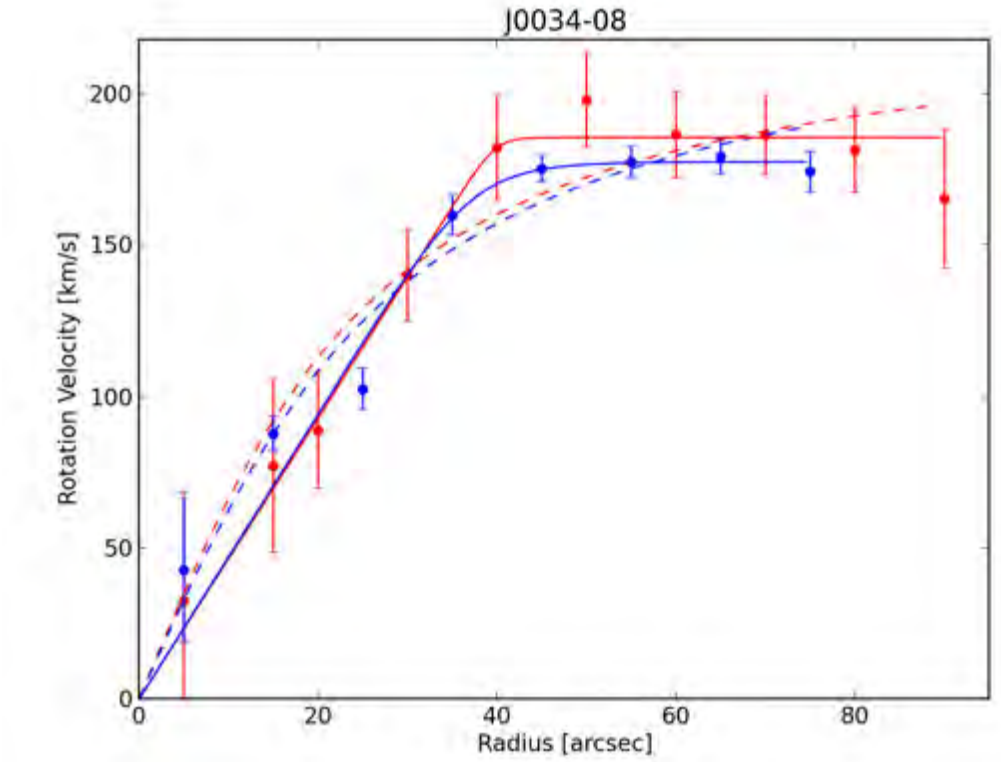

Figure 4.11: The DISFKIT (red) and scrotcur (blue) rotation curves of J0034-08. The dashed lines are from the arctan fits, and the solid lines are the multi-parameter fits. The solid black line is the 3D Plane gradient line (using i_O).

When the r_t calculated by the arctan and the multi-parameter fits from DISKFIT rotation curves are compared in Figure 4.12 I see that the r_{tt} and t_{tm} are similar for many galaxies. For most cases $r_{tt} > r_{tm}$. However, there are many cases where the ratio between them is very small (i.e., r_{tt} is very small or r_{tm} is very large). To eliminate cases where r_{tt} or r_{tm} are unphysically large (or they indicate that the rotation curve does not flatten off) r_t values greater than twice the radial extent of the rotation curve were not used in this analysis. This was done to remove galaxies with slowly rising rotation curves (typically dwarf galaxies). In addition to these unphysical turnover radii, in some cases the functions have unphysically steep inner rotation curves. Therefore turnover radii less than $0.1''$ were rejected from the analysis. The arctan fits worked in more cases and resulted in more r_t values that are usable than the multi-parameter fit. The turnover radii from the arctan fit were also compared to those determined by using the diagonal step function in Figure 4.13. The turnover calculated using the diagonal step function r_{ts} are larger than r_{tt}. Part of the reason is that r_{tt} values are the radius when $V = 0.5V_{max}$ in the arctan function, whereas r_{ts} values are when $V = V_{max}$ in for

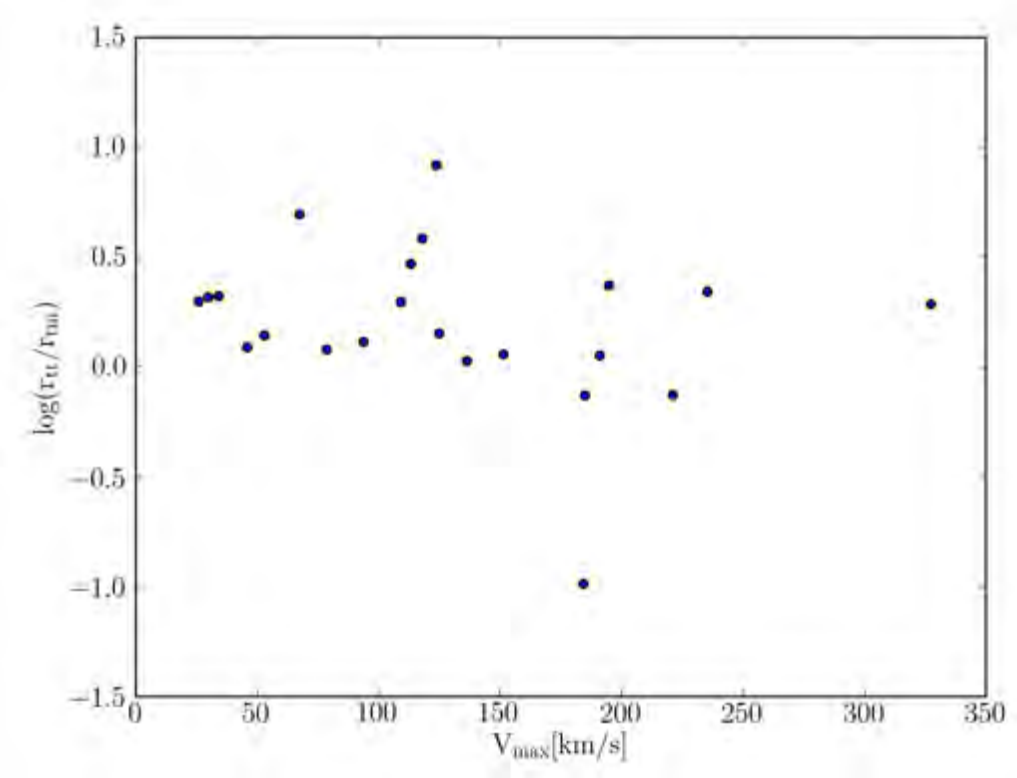

Figure 4.12: The logarithm of the ratio between r_{tt} and r_{tm} values (arctan and multi-parameter fitted turnover radii) plotted against V_{max} calculated using the diagonal step-function.

the diagonal step function. The ratio of r_{tt} to r_{ts} decreases with increasing V_{max}. The arctan function can fit the non-linearity in the rotation curve for radii where $V < V_{max}$ therefore it is potentially more useful in analysis of turnover radii and gradients at those radii. **Therefore the arctan function is the preferred function for data analysis for radii less than the radius when $V = V_{max}$.**

Gradients at Turnover Radius and Effective Radius

The surface brightness values calculated in the SINGG surveys and the WISE observations were all determined out to radii beyond r_e. Ideally I would compare the gradients and surface brightnesses on the same scales and locations of the galaxies. r_e are well defined and measured for the SINGG galaxies, however these are photometric properties. The turnover radii (r_t) are determined by the galaxy dynamics and are good reference points where the gradient relations can be made. r_e values were shown to be

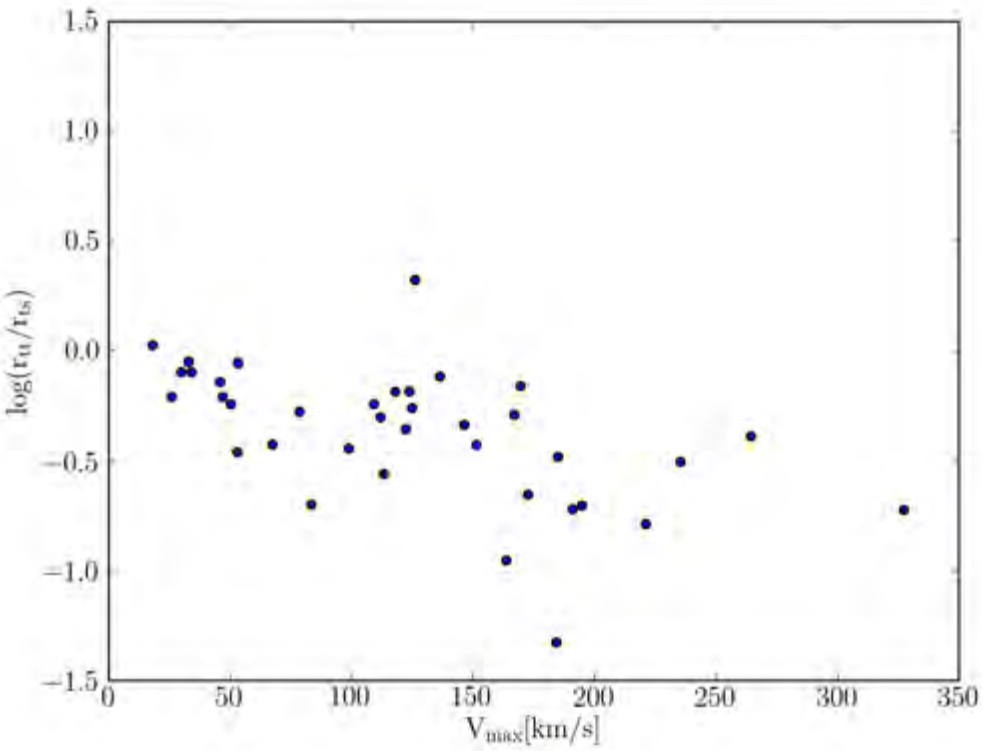

Figure 4.13: The logarithm of the ratio between r_{tt} and r_{ts} values (arctan and diagonal step function fitted turnover radii) plotted against V_{max} calculated using the diagonal step-function.

related to the turnover radii of starburst galaxies by Lehnert & Heckman (1996). I determined the r_t values from the diagonal step, arctan and multi-parameter fits and then tested whether these are similar to r_e. The r_t values were converted from arcseconds to physical units by using HIPASS distances. Figure 4.14 compares r_{ts} with Hα r_e. The r_{ts} values are in general greater than r_e, and correlated with r_e. Figure 4.15 shows a similar but less tight correlation between r_{tt} and Hα r_e. The r_{tt} are more similar to r_e compared to r_{ts}, but there is a large variation in these values with differences between r_e and r_{tt} reaching as high as $\sim$ 0.6 dex. The multi-parameter r_t values are plotted against Hα r_e in Figure 4.16. There much fewer r_{tm} values that were acceptable for the plot compared to the number of galaxies used for the other two fitting methods. Most of the t_{tm} values are lower than their corresponding r_e values and do not show a strong correlation. The diagonal step and arctan fitted r_t are correlated with r_e and confirm the results found by Lehnert & Heckman (1996). This shows that there is a connection between the size of the region that rotates similarly to a solid body and the region of Hα emission. Therefore the larger the part of the galaxy that obeys solid body rotation the

larger the region that emits Hα emission is (i.e., the star forming region). This can be extended by comparisons between r_t and the Hα effective surface brightness. Plots of r_{tt} and r_{ts} against $S_{H\alpha}$ are in Figures 4.17 and 4.18. The low surface brightness galaxies in the figures tend to also have low r_t, while galaxies with high $S_{H\alpha}$ can have high r_t. The Spearman's and Person's correlation coefficients between log r_{ts} and log $S_{H\alpha}$ are $\zeta_S = 0.47$, $\zeta_P = 0.53$ respectively and the standard deviation of a linear fit of the data is $\sigma_{fit} = 0.25$. The Spearman's and Person's correlation coefficients between log r_{tt} and log $S_{H\alpha}$ are $\zeta_S = 0.24$, $\zeta_P = 0.27$ respectively and the standard deviation of a linear fit of the data is $\sigma_{fit} = 0.31$. Therefore the size of the part of the galaxy whose dynamics match solid body rotation is at-best weakly correlated to the $S_{H\alpha}$. I will further study the relationshiop between the dynamics of the regions with solid body rotation and star formation surface density. This will be further studied and tested in Chapter 6.

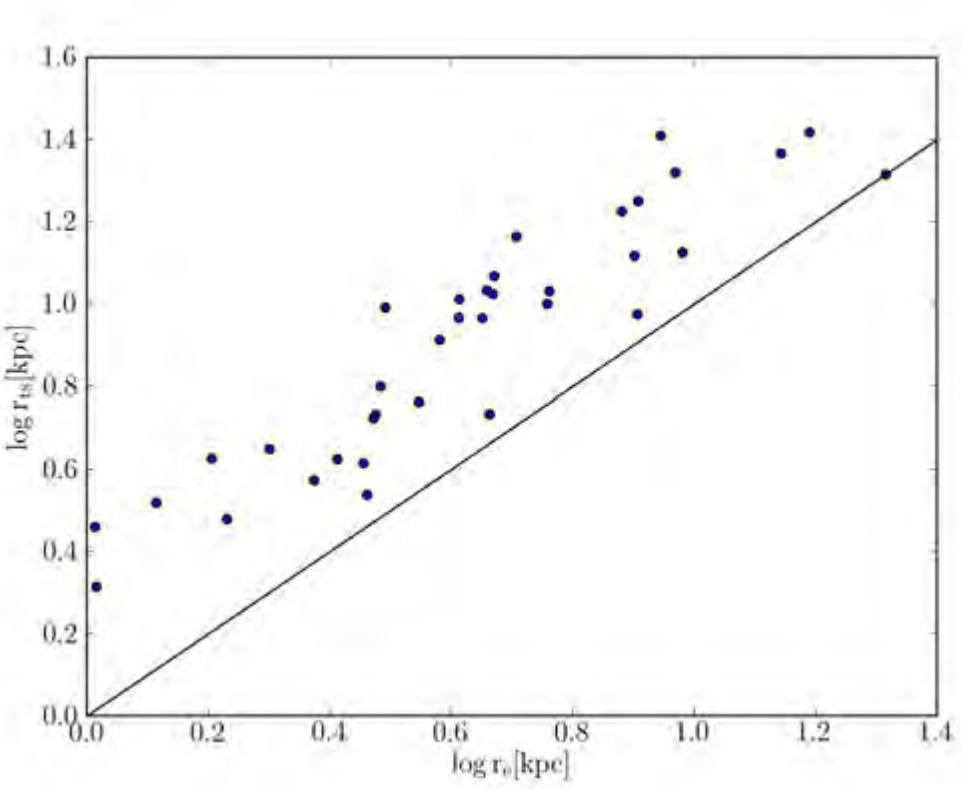

Figure 4.14: Comparison between the diagonal step turnover radius r_{ts} and the Hα effective radius. A black line of unity is shown.

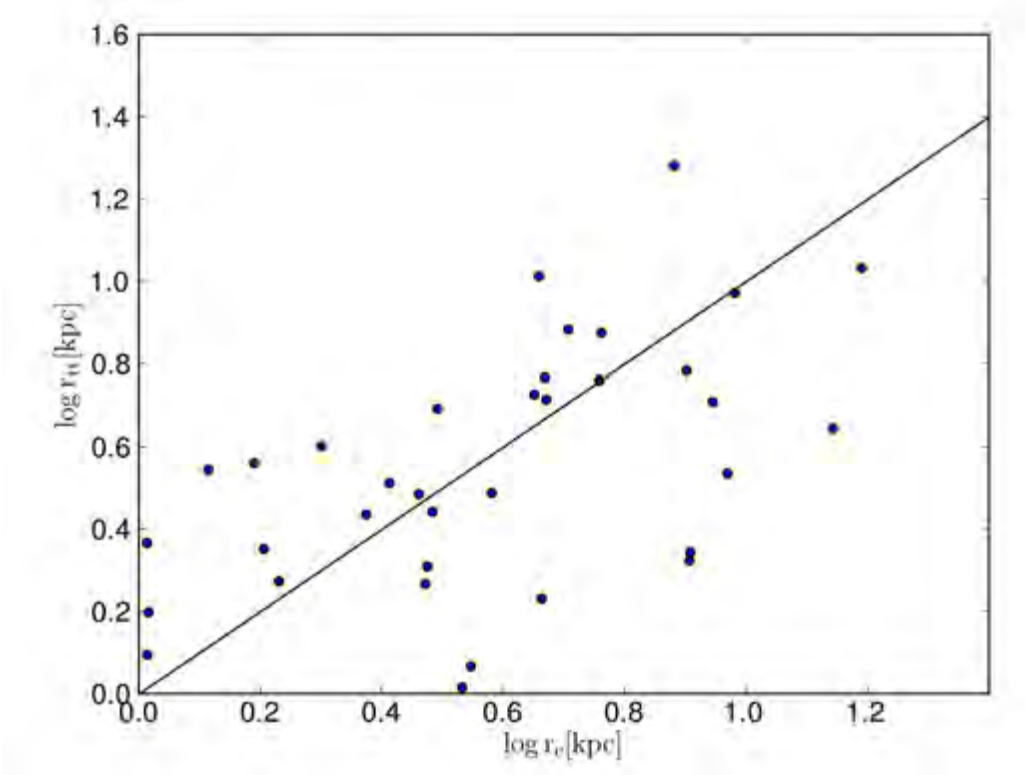

Figure 4.15: Comparison between the arctan turnover radius r_{tt} and the Hα effective radius. A black line of unity is shown.

Inner Gradients and the Multi-Polynomial Method

Lelli et al. (2013) determined the velocity gradients by fitting different order polynomials to the rotation curves and using the linear part of the polynomial fit as the inner gradient. I performed similar analysis on the rotation curves using KMPFIT for the fitting. I fitted 1st to 6th order polynomials (with the velocity at $r = 0''$ fixed to 0 km/s) to each rotation curve and selected the fit with the reduced χ^2 closest to 1. The higher order polynomials overfit the data often, this is why I select the polynomial order with the reduced χ^2 closest to 1 as the best fit. The linear part of the polynomial with the best fit was used as the inner velocity gradient of the rotation curve. This method provides a more systematic and unbiased way to determine the inner gradient from the rotation curve than fitting lines to the first few points of a rotation curve. An example of the polynomial fit is shown in Figure 4.19. Unlike the multi-parameter and arctan fits it is only used to fit the inner gradient, it is not used to characterize the rest of the rotation curve.

The inner gradients determined from using the multi-polynomial method are from

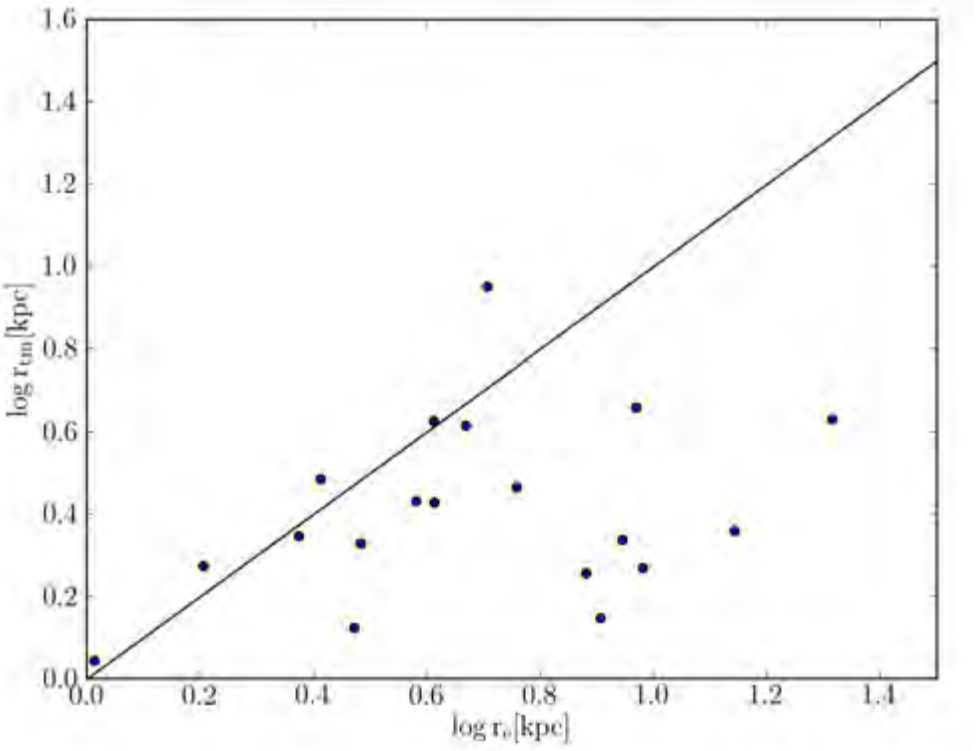

Figure 4.16: Comparison between the multi-parameter turnover radius r_{tt} and the Hα effective radius. A black line of unity is shown.

their linear component. This makes them comparable to the gradients determined from the 3D plane method. However, the 3D plane fit relies on the assumption that the entire rotation curve is linear, while the multi-polynomial method can fit a non-linear rotation curve. The multi-polynomial method can be tested by comparing them with 3D plane gradients of galaxies with rotation curves that are well fitted by 3D plane (and are therefore reasonably described by linear rotation curves). The gradients determined with this method (for DISKFIT rotation curves) were compared to 3D Plane gradients in the top panel of Figure 4.20 for galaxies with 3D Plane and DISKFIT s^2 values that are similar and below 20. There is a large scatter in the points and the values are only similar for 3 cases. This is an indication that the 3D plane or DISKFIT fits for some galaxies can be unreliable even when the s^2 values of the fits are low and the s^2 fit should be used in conjunction with visual inspection and inspection of the fitted parameters in order to establish whether the gradients of the fit should be used in this analysis.

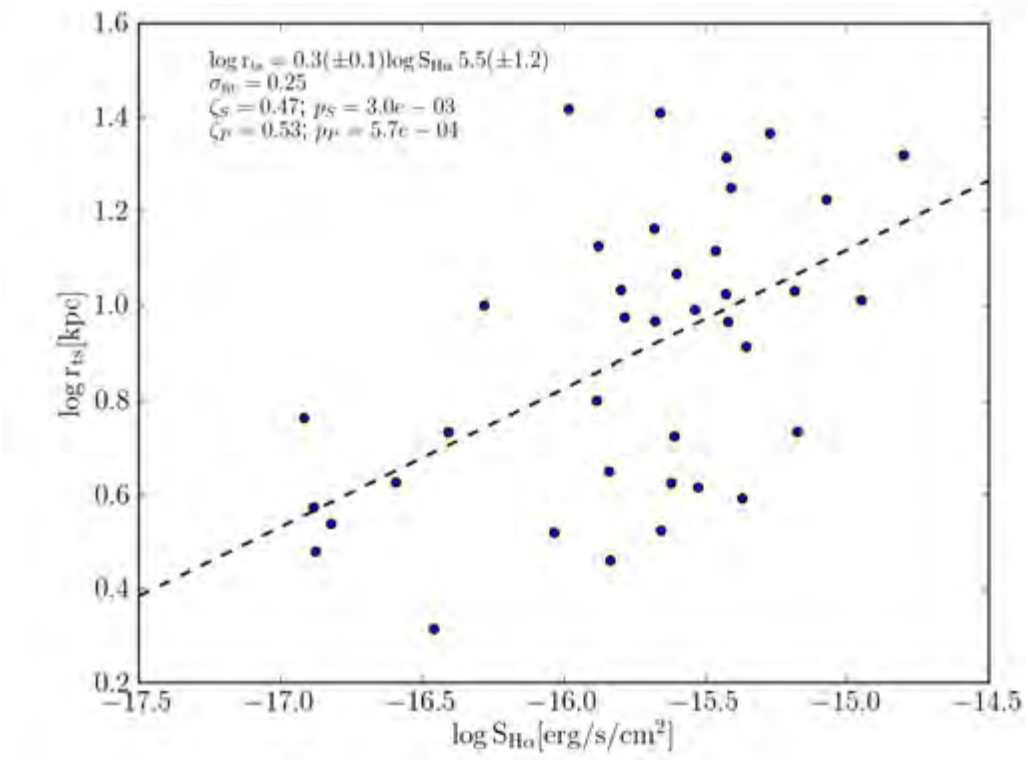

Figure 4.17: Comparison between the diagonal step turnover radius r_{ts} and the Hα effective surface brightness. The dashed line represents the best linear fit to the data.

I also tested how similar the inner gradients are for ROTCUR and DISKFIT rotation curves. This comparison is shown in the bottom panel of Figure 4.20. In this panel ROTCUR and DISKFIT inner velocity gradients are calculated by using the multi-polynomial method are compared to each other and are found to be very similar to each other. This confirms that the shapes of ROTCUR and DISKFIT rotation curves are similar and either can be used in calculations.

I compare the arctan and multi-polynomial fits of inner rotation curves by determining the mean χ^2 values of both methods for data points in the inner DISKFIT rotation curves. In order to determine which method had χ^2 values closest to 1 (ideal fit to the data), I calculated the mean log χ^2 values (such that zero corresponds with the ideal fit) of all their fits. The mean log χ^2 values from the arctan fits are -0.9 ± 1.1 (for data points within r_{tt}) and -1.3 ± 1.1 (for the first non-zero point of the rotation curve). The mean log χ^2 values from the multi-polynomial fits are 0.2 ± 1.4 (for data points within r_{tt}) and 0 ± 1.3 (for the first non-zero point of the rotation curve). Therefore multi-polynomial fits perform better in inner rotation curves. It should be noted

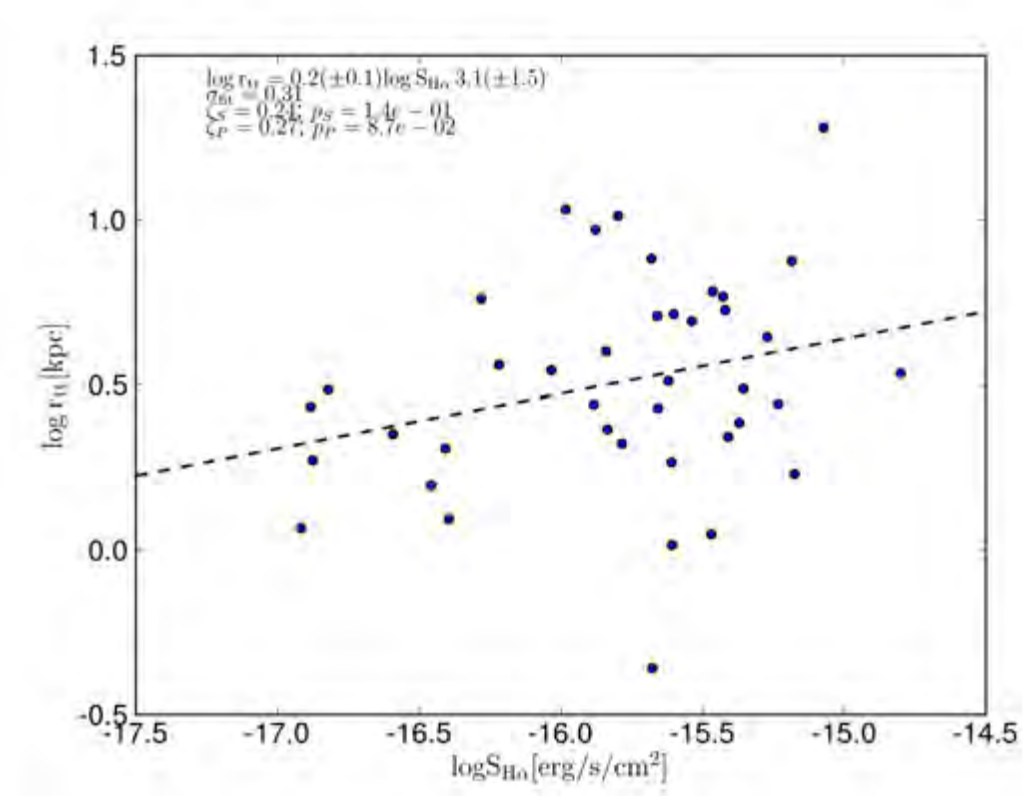

Figure 4.18: Comparison between the arctan turnover radius r_{tt} and the Hα effective surface brightness. The dashed line represents the best linear fit to the data.

that the multi-parameter fit method has values further from 1 than both methods. I compare how well arctan fits reproduce the central velocity gradient compared to the multi-polynomial fits in Figures 4.21 and 4.22 for different sampling of the rotation curve. High resolution and well sampled ($\sim 1-3''$) rotation curves from de Blok et al. (2001) were chosen for this comparison. Two galaxies with typical rotation curves were selected: F571-8 (Figure 4.21) and U11748 (Figure 4.22). They represent a slowly rising rotation curve with intermediate V_{max} and a quickly rising rotation curves with high V_{max} respectively. Multi-polynomial and arctan fits were made for the rotation curves and the central gradients derived from these were compared. The rotation curves were down-sampled by reducing the number of points sampled in the inner region of the rotation curve to simulate the sampling and resolution of the rotation curves or removing those at large radii to simulate galaxies whose rotation curves do not flatten out completely. These down-sampled rotation curves were also fitted with the arctan function and using the multi-polynomial fit, the derived central gradients from these fits were then compared to the gradient of the first point of the original rotation curve. The results of these and the down-sampled rotation curves are shown in the panels

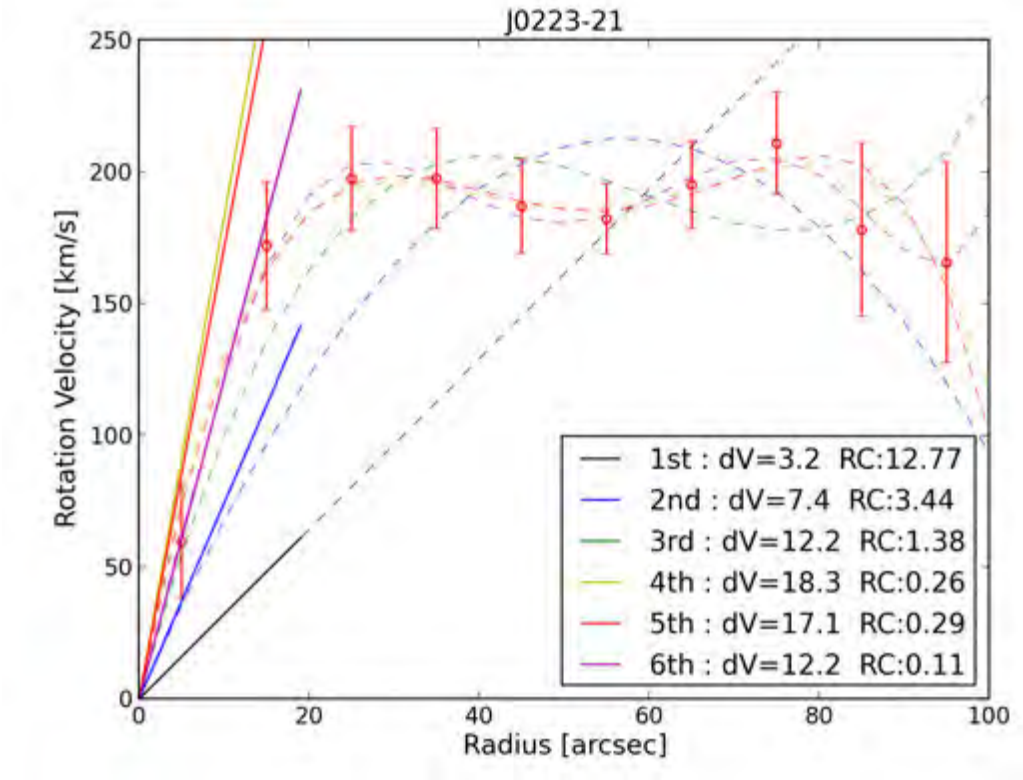

Figure 4.19: The multi-poloynomial fit for the DISKFIT rotation curve of J0223-21. The points of the DISKFIT rotation curve are in red. The multi-oder polynomial fits are shown as dashed lines (first order: black, second order: blue, third order: green, fourth order: yellow, fifth order: red, sixth order: purple). The first order of the polynomials (which are used to determine the inner gradients) are shown as solid lines of their respective colours). The legend shows the inner gradients (denoted as dV) and reduced χ^2 (denoted as RC) values for each polynomial fit.

of Figures 4.21 and 4.22. At high sample rates of the inner rotation curves (e.g., 1″ and 3″) the multi-polynomial and arctan fits produce similar results. For the steeply rising rotation curve, the multi-polynomial method is closer to the gradient of first point of the rotation curve than gradient from the arctan fit. When the sampling is reduced for the slowly rising rotation curve the multi-polynomial method and arctan fits have similar gradients that underestimate the gradient. For the quickly rising rotation curve down-sampling the arctan fit greatly overestimates the gradient and the multi-polynomial gradient is closer to the real gradient. Therefore arctan and multi-polynomial fits are similarly effective at determining the inner rotation gradient for slowly rising rotation curves. But the multi-polynomial method provides better fits for the inner gradient in steeply rising rotation curves and those that have low rota-

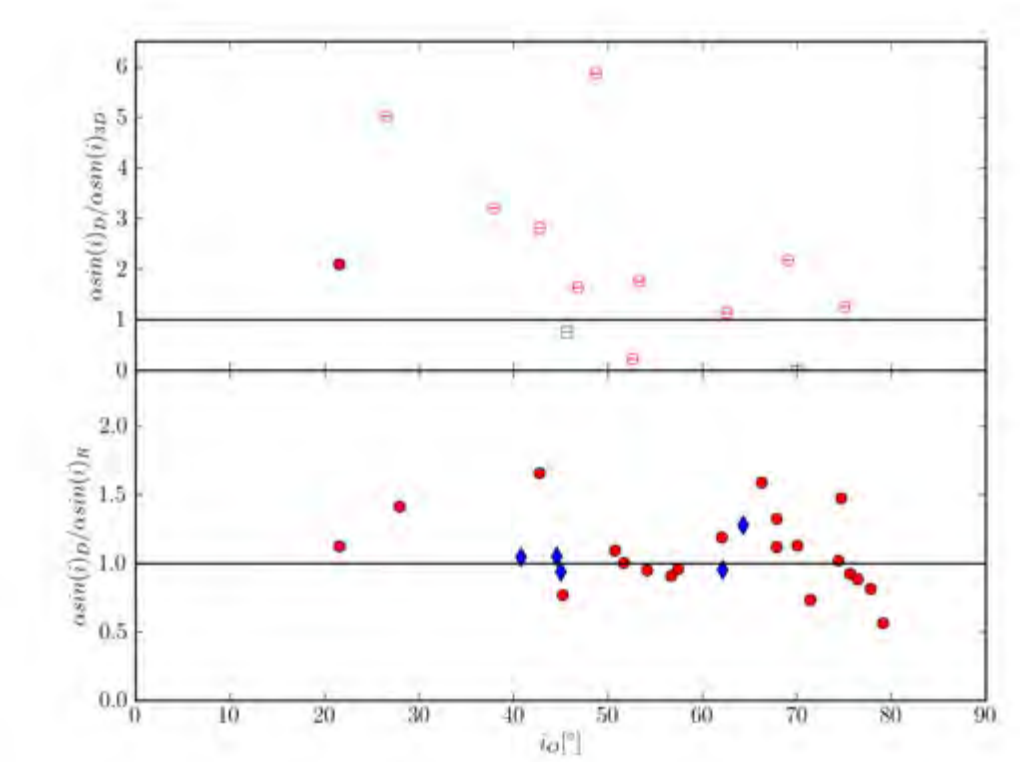

Figure 4.20: Top: Ratios of the DISKFIT and 3D plane velocity gradients ($\alpha sin(i)$) plotted against i_O. These were plotted for galaxies with 3D plane and DISKFIT s^2 values within 50% of each other and with s^2 values below 20. The DISKFIT velocity gradients were calculated using the multi-order polynomial fit method. Bottom: Ratios of the DISKFIT and ROTCUR velocity gradients ($\alpha sin(i)$) plotted against i_O. These were plotted for galaxies with DISKFIT and ROTCUR s^2 values within 50% of each other. The DISKFIT and ROTCUR velocity gradients were calculated using the multi-order polynomial fit method.

tion curve sampling. **Therefore I use the multi-polynomial fit that Lelli et al. (2013) used for the central gradient analyses, and the arctan fit for analyses at the turnover radius**.

It should be noted that J0019-22, J0031-22, J0039-14a, J0045-15, J0335-24, J1145+02, J2242-06 and J2239-04 were not used for further analysis due to the inability to determine accurate inner velocity gradients for these galaxies, or that they have unphysical rotation curves, or that their gradients and kinematic parameters do not match what is expected based on their velocity fields or photometry.

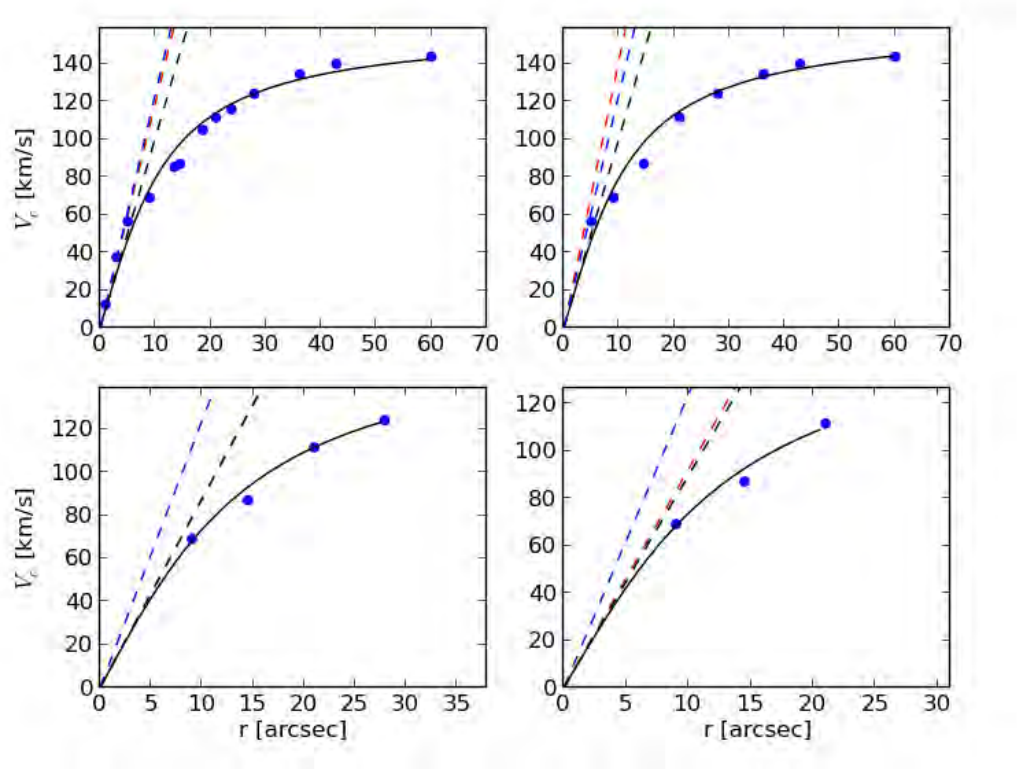

Figure 4.21: Rotation curve of F571-8 and the arctan fit (black line), the central gradient of the arctan fit (black dashed line), the central gradient determined by the multi-polynomial fit (red dashed line) and the gradient of the first non-zero point of the rotation curve (blue dashed line). The top left panel is the full sampling of the rotation curve (de Blok et al. 2001), and the other panel have rotation curves with worse sampling than the original rotation curve.

Gradient Uncertainty

The Hα emission lines were fitted with Gaussian functions. If the profiles shapes are warped then Hermite polynomials can better fit the data than Gaussians. The focus of this study is on inner rotation gradients. High velocity gradients, high inclinations, low spatial resolution and weak emission can result in velocity profiles that are asymmetric due to effects such as beam smearing and multiple profiles in the line-of-sight. Hermite polynomials can be fitted to these profiles to determine more robust rotation velocities (e.g., de Blok et al. 2008). Representative Hα velocity profiles are showed in Figures 4.23 to 4.25, these are profiles of innermost diamond of fibers (Fibers 26, 31, 43, 46, 52 (central fiber), 65 and 47 (not shown)). These normally represent fibers of the inner parts of the rotation curves and would show the largest profile distortions due to beam smearing effects. The Gaussian and Hermite $h3$ fits to the velocity profiles are plotted

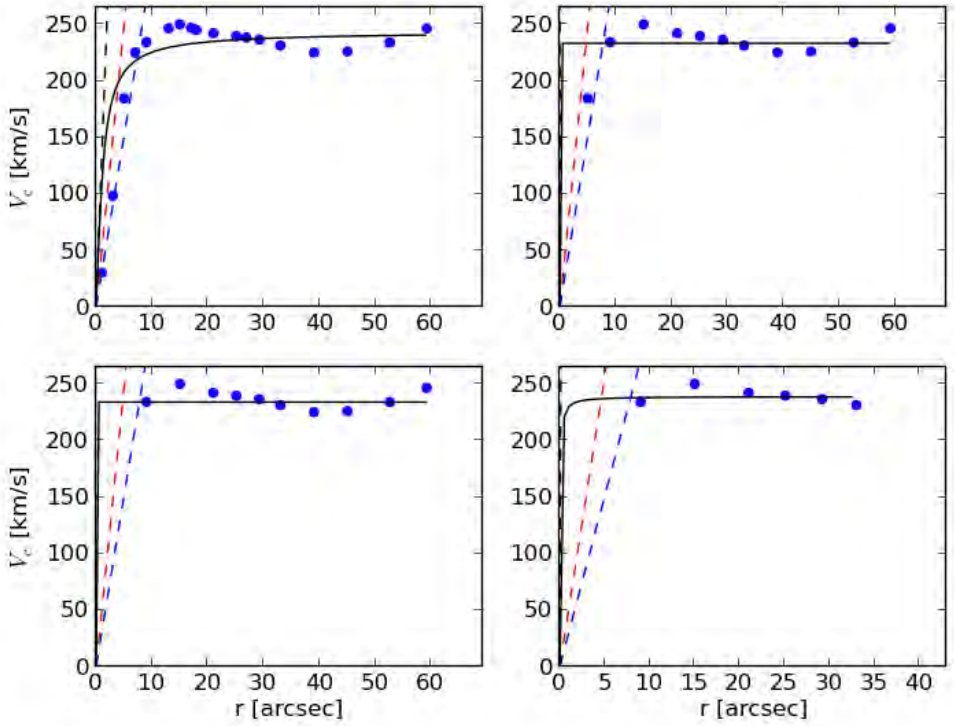

Figure 4.22: Rotation curve of U11748 and the arctan fit (black line), the central gradient of the arctan fit (black dashed line), the central gradient determined by the multi-polynomial fit (red dashed line) and the gradient of the first non-zero point of the rotation curve (blue dashed line). The top left panel is the full sampling of the rotation curve (de Blok et al. 2001), and the other panel have rotation curves with worse sampling than the original rotation curve.

in these figures and their fitted mean velocities are also displayed. Figures 4.23(a) to 4.23(f) are for J0230-02:S1, which has $i_D = 71.4°$ and is at distance of 80 Mpc. Figures 4.24(a) to 4.24(f) are for J2056-16, which has $i_D = 44°$, $W_{50} = 66.7$ km/s and is at a distance of 22.7 Mpc. Figures 4.25(a) to 4.25(f) are for J1005-16:S2, which has $i_D = 85.2°$ and is at a distance of 70.8 Mpc. These galaxies cover a range of highly inclined (J1005-15:S2), high rotation gradient and low spatial resolution (J0230-02:S1) galaxies, and a dwarf galaxy with low rotation amplitude (J2056-16). These are the extreme cases where very asymmetric profiles are expected and where the Hermite fit is expected to fit the data better than a Gaussian fit (e.g., de Blok et al. 2008). The plots show that even for these galaxies, the central velocity profiles can be successfully fitted by Gaussians. Gaussian and Hermite fits produce similar mean velocities for most profiles. Cases of very warped profiles where the difference in the mean velocities

is high are rare and even in these cases the most extreme has a difference of 6 km/s . The predominance of profiles that are fitted well by Gaussians and where the difference between Gaussian and Hermite velocity profiles shows that the use of Hermite polynomial fits to the velocity profiles would only have had a minor effect on the fitted velocity gradients.

The uncertainty in α (e_α) is related to the uncertainties in the rotation curve gradient fit, inclination and distance. The distance estimates used in this analysis are based on HIPASS data. The greatest uncertainties in the distances are due to peculiar velocities. These are non-Hubble flow velocities due to gravitational effects by nearby galaxies, groups and clusters. Meurer et al. (2006) estimated that the uncertainty at the median distance of the SINGG survey is 10%. They assumed a peculiar velocity dispersion of 125 km/s (Willick et al. 1997, Willick & Strauss 1998), and this velocity dispersion results in a 10% uncertainty of the velocity at the median distance of the sample. Our sample has a similar median distance to the SINGG sample and I use a more conservative 15% uncertainty for our galaxies in order to account for the higher uncertainties at low distances (due to greater contributions of the peculiar velocities to the measured expansion velocity). In order to determine the α uncertainties I use the equation provided by Lelli et al. (2013):

$$e_\alpha = \sqrt{e_{\alpha,f}^2 + \left(\alpha \frac{e_i}{tan(i)}\right)^2 + \left(\alpha \frac{e_D}{D}\right)^2}, \tag{4.19}$$

where the $e_{\alpha,f}$ is the fitted uncertainty in α, e_i is the uncertainty in the rotation curve fitted i, D is the distance and e_D is the uncertainty in the distance.

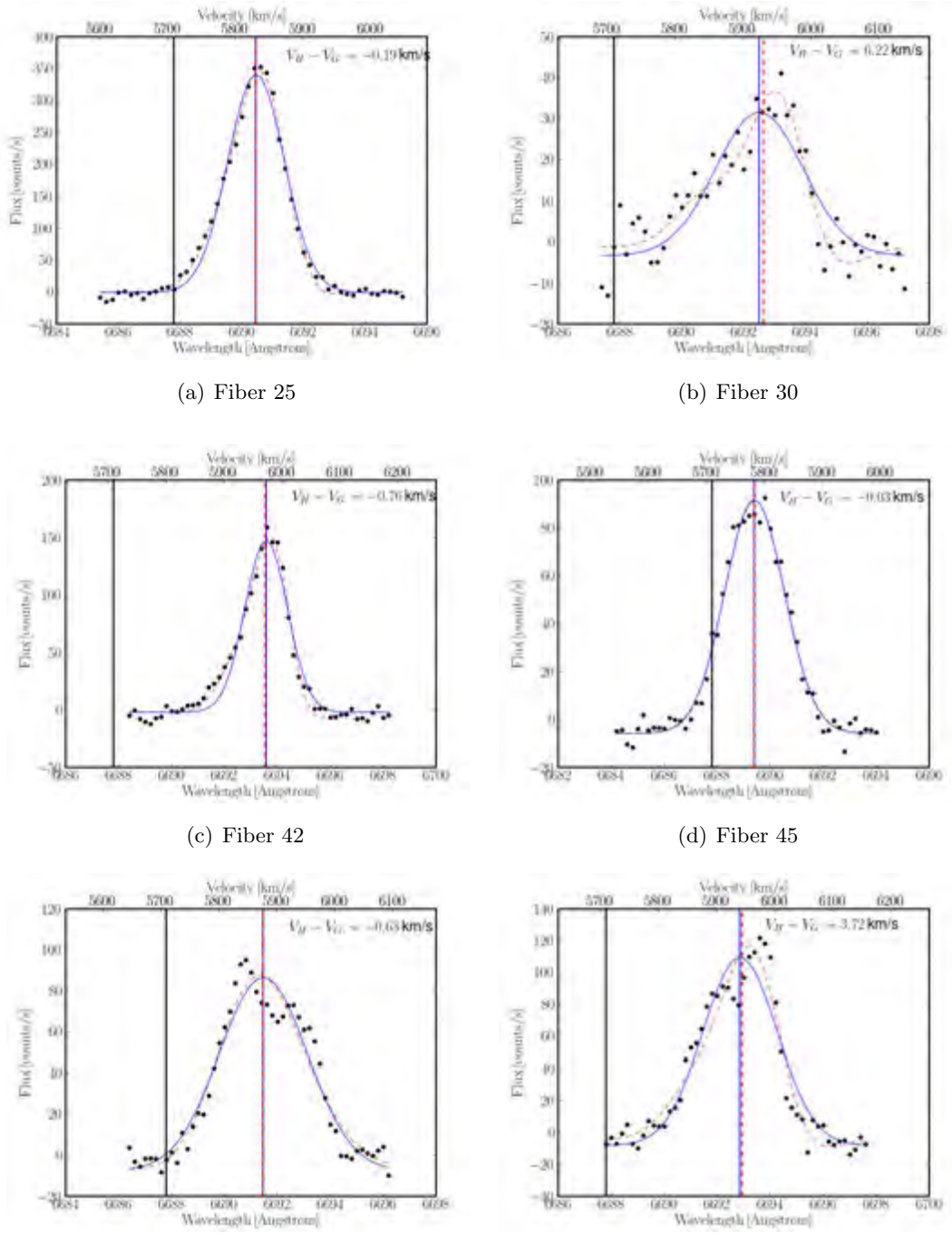

(a) Fiber 25

(b) Fiber 30

(c) Fiber 42

(d) Fiber 45

(e) Fiber 51

(f) Fiber 65

Figure 4.23: Plots of the Hα velocity profiles (black circles), overlayed with a Gaussian (blue blue curve) and Hermite $h3$ polynomial fit (red dashed curve) for the central fibers in J0230-02:S1's first pointing. The DISKFIT systemic velocity is shown as a solid black vertical line, vertical blue line represents the fitted Gaussian mean velocity and the Hermite $h3$ velocity is represented by a vertical red dashed line.

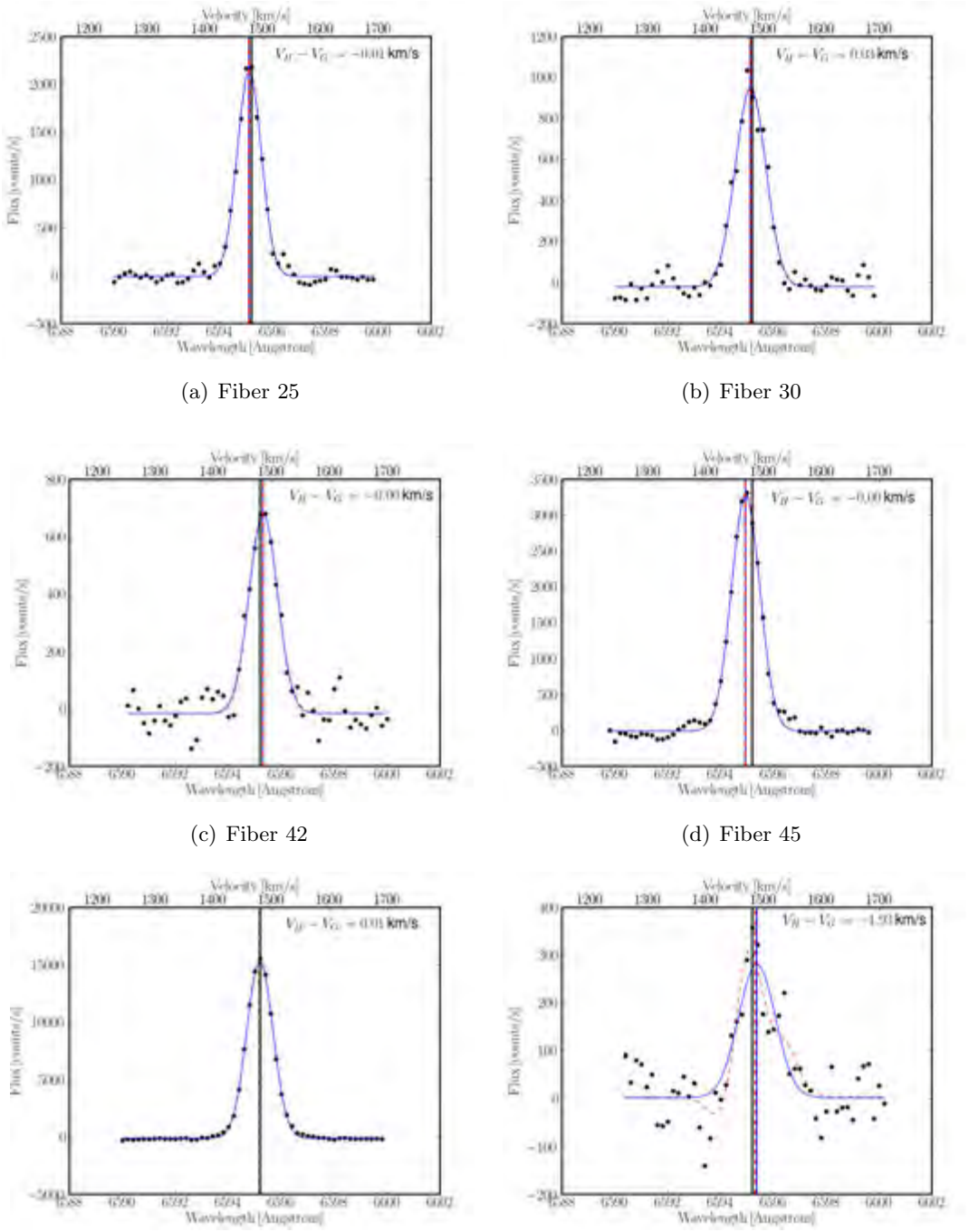

(a) Fiber 25 (b) Fiber 30

(c) Fiber 42 (d) Fiber 45

(e) Fiber 51 (f) Fiber 65

Figure 4.24: Plots of the Hα velocity profiles (black circles), overlayed with a Gaussian (blue blue curve) and Hermite $h3$ polynomial fit (red dashed curve) for the central fibers in J2056-16's first pointing. The DISKFIT systemic velocity is shown as a solid black vertical line, vertical blue line represents the fitted Gaussian mean velocity and the Hermite $h3$ velocity is represented by a vertical red dashed line.

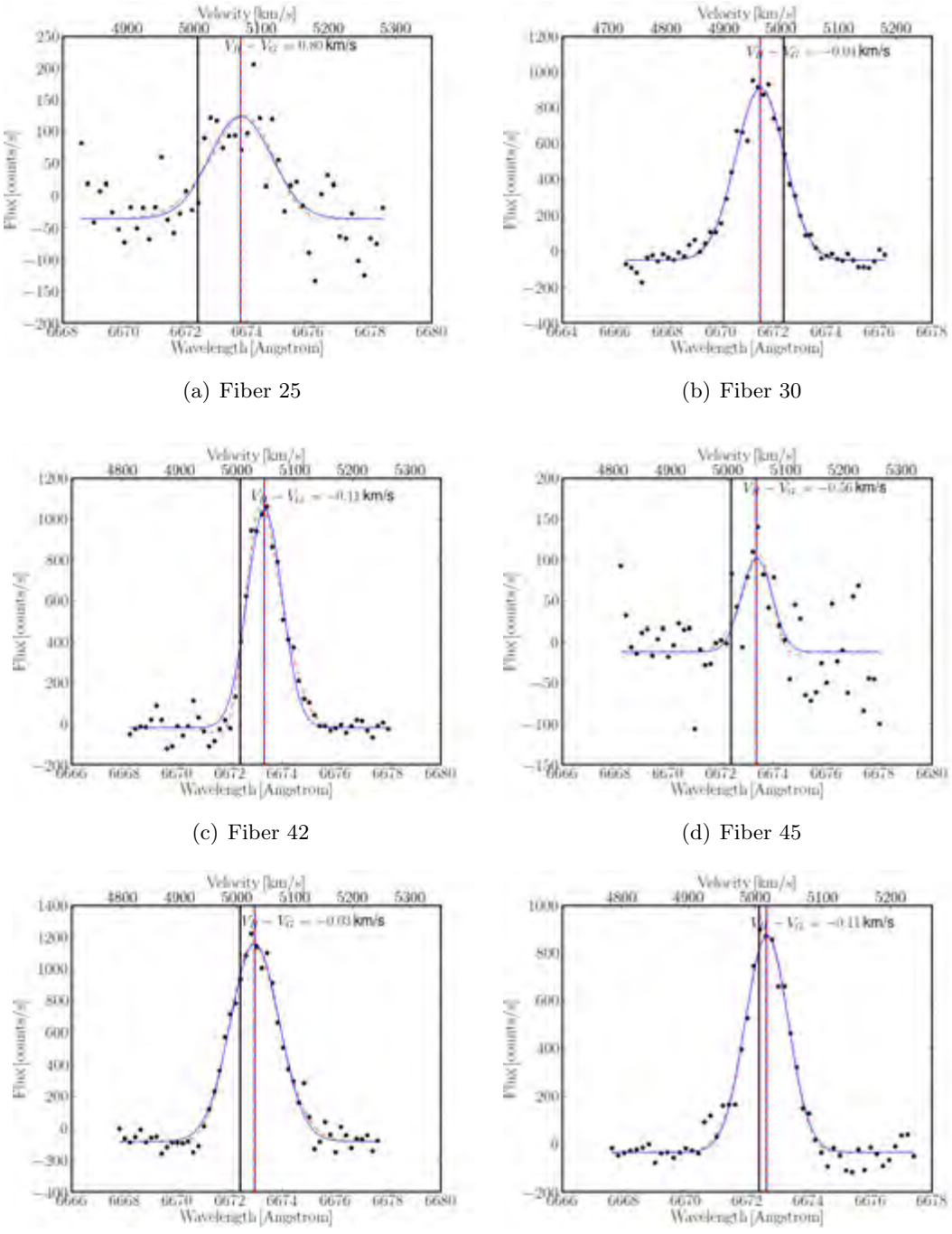

(a) Fiber 25

(b) Fiber 30

(c) Fiber 42

(d) Fiber 45

(e) Fiber 51

(f) Fiber 65

Figure 4.25: Plots of the Hα velocity profiles (black circles), overlayed with a Gaussian (blue blue curve) and Hermite $h3$ polynomial fit (red dashed curve) for the central fibers in J1005-16:S2's first pointing. The DISKFIT systemic velocity is shown as a solid black vertical line, vertical blue line represents the fitted Gaussian mean velocity and the Hermite $h3$ velocity is represented by a vertical red dashed line.

4.2 Surface Brightness Calculation

The average interior surface brightness profiles (hereafter referred to as the surface brightness profiles) were used to determine the surface brightnesses at $r = 0$ and r_t. The interior surface brightnesses are preferred over the local surface brightnesses because in this analysis I test relations between surface brightnesses and α. As shown in Chapter 2, α is a proxy for the slope of the gravitational potential well and is dependent on the interior mass density. Surface brightnesses at r_t were calculated by linearly interpolating the surface brightnesses between the data points that the r_t data point lies between. Lelli et al. (2013) found that for late type galaxies the central surface brightness is close to the surface brightness at $\sim 1''$ and that a linear extrapolation was sufficient for these galaxies. In order to determine the most accurate central surface brightnesses I considered extrapolating from the innermost 2-5 points of the surface brightness profiles. The fewer the number of points used the more susceptible to spurious points the extrapolations were. However I decided to calculate the central surface surface density by determining the surface brightness at $r = 5''$. This value was chosen because the first non-zero data point of the best sampled rotation curves in the analysis is at $r = 5''$. Each fiber has a diameter of $4.58''$, therefore the velocity measurements cannot be made over smaller angular distances. The innermost data point in the rotation curves and velocity fields sets the minimum distance over which the velocity gradient is constant (because of the limitations in the data) in the analysis. Determining surface brightness values at $r = 5''$ ensures that we match the scales that central velocity gradient and surface brightness vales are measured at. The nature of the surface inner surface density profiles of is discussed in later chapters.

The $S_{H\alpha}$ values were converted to luminosities (using the distance values determined from HIPASS velocities by Meurer et al. 2006) which were converted to $\Sigma_{\rm SFR}$ using the relation used in Hanish et al. (2006) and Kennicutt et al. (1994) :

$$SFR[M_\odot/yr] = L_{H\alpha}[ergs/s]/1.26 \times 10^{41}. \tag{4.20}$$

This assumes a single power-law initial mass function (IMF) that ranges from 0.1 to $100\,M_\odot$ and has a Salpeter (1995) slope. This SFR relation was used because it was the standard adopted for the SINGG analysis (Hanish et al. 2006).

The $\Sigma_{\rm SFR}$ values were calculated from S_{W4} by converting them to luminosities and using the Jarrett et al. (2013) SFR relation:

$$SFR[M_\odot/yr] = 7.5 \times 10^{-10} L_{\nu 22\mu m}[L_\odot]. \tag{4.21}$$

S_{W3} luminosities were converted to $\Sigma_{\rm SFR}$ by using:

$$SFR[M_\odot/yr] = 4.91 \times 10^{-10} L_{\nu 12\mu m}[L_\odot]. \quad (4.22)$$

They are based on the Rieke et al. (2009) relations between mid-infrared emission and the total infrared star formation. Their star formation rate calibrations are in agreement with star formation rates derived using Kroupa (2002) and Chabrier (2003) IMFs. They found that the star formation rate calibrations derived assuming these IMFs are a factor of 0.66 times the star formation rates determined assuming a single power-law Salpeter IMF. Therefore in order to compare Hα $\Sigma_{\rm SFR,0}$ to mid-infrared $\Sigma_{\rm SFR,0}$ observations the Hα star formation rates calculated by Equation 4.20 are adjusted by 0.66 such that:

$$SFR[M_\odot/yr] = 0.66 L_{H\alpha}[ergs/s]/1.26 \times 10^{41}. \quad (4.23)$$

The surface densities and star formation rate surface densities calculated in this manner were used in the following analysis of the relationships between α, S_R and $\Sigma_{\rm SFR}$ and the star formation models.

4.3 Conclusion

Different methods of determining kinematic parameters were described and used, and inspection of the fitted parameters and s^2 were used to determine which method worked best. The 3D Plane method was successfully used to determine α and ϕ in galaxies where DISKFIT and ROTCUR did not provide reasonable fits to the data. Most of the galaxies where 3D Plane outperformed the other methods are faint dwarf galaxies, which is expected due to the lower amount fibers with detectable emission, slowly rising rotation curves and lack of a rotation curve turnovers in these galaxies. Comparisons between the kinematic parameter outputs of each method were made and these were compared to photometrically determined geometric parameters. Different fitting functions were tested for characterizing the rotation curves, the arctan function was selected to characterize the turnover radius. The analysis also showed that there is a correlation between the turnover radius and the effective radius. The multi-polynomial method will be used to determine central α from DISKFIT and ROTCUR rotation curves that will be used for further analyses. Central surface brightnesses and star formation surface densities will be determined from surface brightness profiles by interpolating the surface brightness profiles to $r = 5''$.

Chapter 5

Stellar Surface Densities and the Inner Dynamics of Galaxies

I need to determine which mass component dominates the inner dynamics of galaxies in order to determine the relationship between star formation surface density and galaxy dynamics in the inner parts of galaxies. To do this I will test whether the stellar surface density is the dominant component of the inner parts of galaxies. The model presented in Chapter 2 predicts that:

$$\alpha = \sqrt{\frac{2\pi G m_s}{3\Delta z f_b}}\sqrt{\Sigma_s}, \tag{5.1}$$

which in terms of the surface brightness S_s is:

$$\alpha = \sqrt{\frac{2\pi G m_s (M_b/L)}{3\Delta z f_b}}\sqrt{S_s}, \tag{5.2}$$

where α is the velocity gradient, m_s is the geometric mass distribution parameter, M_b/L is the baryonic mass-to-light ratio, Δz is half of the characteristic width of the disk, f_b is the baryonic fraction and Σ_s is the stellar surface density. Therefore $\alpha \propto \Sigma_s^{0.5}$ if we assume that $\frac{2\pi G m_s}{3\Delta z f_b}$ is constant and independent of Σ_s. This is assumed for this analysis, and the validity of this will also be tested. Σ_s (in solar masses per unit area) is related to the surface density (measured in solar luminosities per area) by $S_s = \frac{\Sigma_s}{M_b/L}$, where M_b/L is the mass-to-light ratio. The following relation :

$$\log \alpha = -0.2\mu - 0.2C_\mu - 0.5 \log\left(\frac{2\pi G m_s (M_b/L)}{3\Delta z f_b}\right). \tag{5.3}$$

was derived for surface brightnesses measured in the AB magnitude system μ. It will be used to test the $\alpha \propto \Sigma_s^{0.5}$ relation in the central regions of galaxies using optical R-band and WISE near-infrared W1 and W2 observations. This will be done by plotting central velocity gradient α_0 against the central surface densities $\mu_{R,0}$ and $\mu_{W1,0}$ (in

$[ABmag/arcsec^2]$), where the subscripts "R" and "$W1$" represent the observing bands and the "0" subscript indicates that these are the central values. S_R and S_{W1} denote the linear surface densities (in $[L_\odot/pc^2]$ units). These surface brightnesses will be converted to central stellar surface densities $\Sigma_{s,0}$ (in $[M_\odot/pc^2]$ units) in order to test the relation and to constraint the baryonic fractions in the central regions of galaxies. Central velocity gradients are measured using the multi-polynomial method. Central surface densities are measured by interpolating to the interior surface brightness at $5''$, which is the close to the width of IFU fiber ($4.58''$) and radius of the first non-zero points of the DISKFIT and ROTCUR rotation curves (usually $5''$). All fits to the data are performed using the KMPFIT package. The models will be tested using both R-band and W1 observations in order to see the effects of optical versus NIR tracers or the relation. The chapter is ordered as follows: Section 5.1 will deal with testing the relation using SINGG R-band observations, Section 5.2 will focus on tests of the relation using WISE W1 observations and the final section will be relations with other parameters.

5.1 Optical R-band Stellar Surface Density and Velocity Gradient Comparison

Different structures in the inner parts of galaxies can affect the measured $S_{R,0}$ of galaxies and cause non-exponential behaviour in the S_R profiles. Central concentrations in the form of stellar bulges, pseudo-bulges and bars result in central surface brightnesses that are higher than expected from a purely exponential stellar disk (e.g., Freeman 1970, Kormendy & Kennicutt 2004). Starburst activity or high star formation rates can also cause excesses in the inner S_R profiles (e.g., Marlowe et al. 1999, Lian et al. 2016). There can also be central light depressions that result in lower surface brightnesses than expected from a purely exponential disk. Dust obscuration can also cause lower than expected S_R values in the inner parts of galaxies. In this study I am interested in the relationship between the total central stellar mass density and the gravitational potential of the galaxy, therefore I use the total $S_{R,0}$, this includes effects of the aforementioned structures. The Lelli et al. (2013) scaling relation between $\mu_{R,0}$ and α_0 was found using the total stellar surface brightness. For the remainder of this analysis the total surface density will be referred to as the surface density.

The relation in Equation 5.3 is tested in Figure 5.1, where $\log \alpha_0$ is plotted against $\mu_{R,0}$. Equation 5.3 can be rewritten in the form :

$$\log \alpha_0 = C_1 \mu_0 + C_2, \tag{5.4}$$

where C_1 is the slope which I expect to be -0.2 and the y-intercept of the plot is C_2,

Table 5.1: Best fit linear ($\log \alpha_0 = C_1 \mu_0 + C_2$) parameters and correlation coefficients for the R band data in Figure 5.2.

Source	N	C_1	C_2	$\lvert\zeta_S\rvert$	$\lvert\zeta_P\rvert$	$\sigma_{\rm fit}$
1	2	3	4	5	6	7
WIYN	44	-0.18 ± 0.03	5.5 ± 0.6	0.69	0.69	0.31
Lelli et al. (2013, 2014)	112	-0.19 ± 0.01	5.7 ± 0.2	0.81	0.89	0.23
Erroz-Ferrer et al. (2016)	29	-0.12 ± 0.03	4.3 ± 0.6	0.62	0.65	0.29
All	185	-0.17 ± 0.01	5.3 ± 0.2	0.81	0.84	0.26

Comments: Column 1: Origin of data; Column 2: Number of galaxies used in the fit; Column 3: Gradient of linear fit; Column 4: y-intercept of linear fit; Column 5: Absolute value of Spearman correlation coefficient; Column 6: Absolute value of Pearson correlation coefficient; Column 7: Dispersion of the linear fit;

which is expected to be:

$$C_2 = \left(\frac{2G\pi m_s (M_b/L)}{3\Delta z f_b} \right) - 9.72. \tag{5.5}$$

A linear fit was made to the data is shown in the figure. In my analysis the result of the linear fit to the data in Figure 5.1 is $C_1 = -0.18 \pm 0.03$. This slope is consistent (within its uncertainty) with but lower than the value predicted by the model. The dispersion around the linear fit ($\sigma_{\rm fit}$) is 0.30. The Spearman and Pearson's correlation coefficients for the variables are $|\zeta_S| = 0.69$ and $|\zeta_P| = 0.69$ respectively and the probability of a null hypothesis (p_S and p_P respectively) is $\sim 2 \times 10^{-7}$. This indicates that there is a correlation between α_0 and $S_{R,0}$, which suggests that α_0 is correlated with $\Sigma_{s,0}$. The fitted power-law index of the relationship is close to the expected value, therefore the model can adequately describe the data.

Lelli et al. (2013) studied a sample of galaxies going from dwarf irregular galaxies to late type spirals to early type spiral galaxies (Sa/S0 galaxies from Noordermeer et al. 2007) and found that C_1 varied between -0.15 and -0.25 depending on how they measured their α_0 and $S_{R,0}$. They settled on a value of -0.22 ± 0.2 for C_1 and $C_2 = 6.28 \pm 0.4$. Lelli et al. (2014) performed a further study of the inner dynamics of a sample of dwarf galaxies and found that there is a correlation between the inner α and μ_R values in their galaxies. Erroz-Ferrer et al. (2016) studied a wide range of galaxies (from dwarf galaxies to early type spirals) also found a correlation between α_0 and $\mu_{R,0}$. Our data are compared to Lelli et al. (2013, 2014) and Erroz-Ferrer et al. (2016) in Figure 5.2 in order to test whether the measurements are in agreement with theirs. I made linear fits to each dataset and the combined data. The results

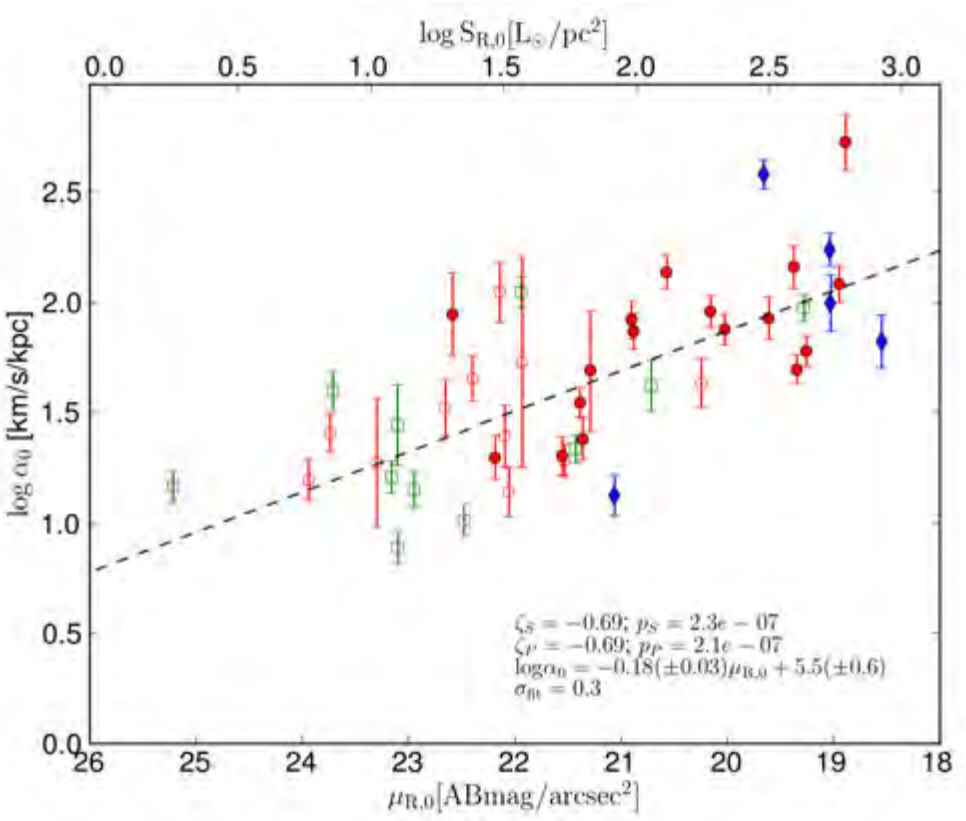

Figure 5.1: Central velocity gradient plotted against the central R-band surface brightness. The central R-band surface brightness values were extrapolated from R-band radial profiles. Symbols are the same as Figure 4.2. The Class 2 and 3 galaxy gradients were calculated using the multi-polynomial method and Class 1 galaxies' gradients were determined by the 3D Plane fit and using photometric inclinations. The best linear fit to the data is shown as a dashed line.

of the fits are shown in Table 5.1. The Lelli et al. (2013, 2014) fitted value of C_1 is closest to the theoretical value. For $26 > \mu_{R,0} > 17$ (where our data lies), the data are consistent with Lelli et al. (2013, 2014) and Erroz-Ferrer et al. (2016) data and the slopes of the relations found in this analysis are similar. The Lelli et al. (2013,2014) and Erroz-Ferrer et al. (2016) data extends to higher $S_{R,0}$ than our data: $\mu_{R,0} < 17$. Most of the high $S_{R,0}$ galaxies are bulge-dominated early type spirals (Sb or earlier). Lelli et al. (2013, 2014) data has the strongest correlation between α_0 and $\mu_{R,0}$, and they have better constraints on their α_0 values than I do. Unlike Lelli et al. (2013), I have access to infrared data which allows us to more accurately determine $\Sigma_{s,0}$ and I use it to estimate f_b and to test the constant-Q star formation models in Chapter 6. As shown in Table 5.1, if all the data are fitted the slope is: $C_1 = -0.17$ $pm0.01$, $\sigma_{\rm fit} = 0.26$, the correlation coefficients are $|\zeta_S| = 0.81$ and $|\zeta_P| = 0.84$ respectively.

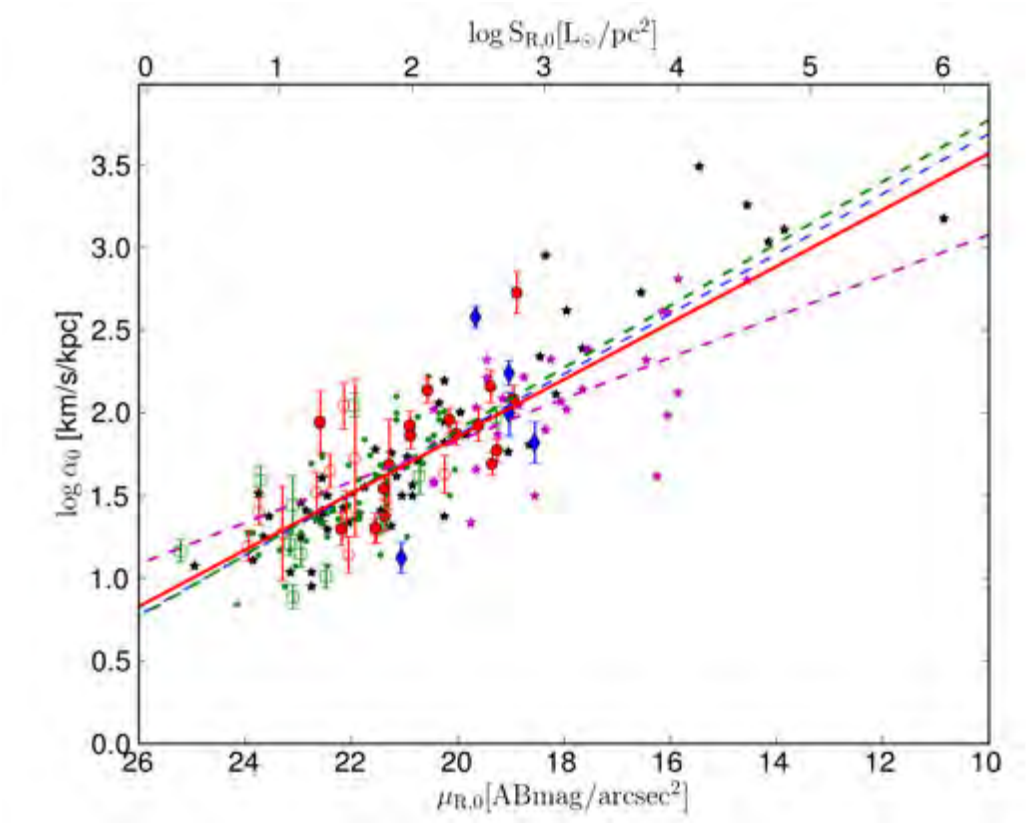

Figure 5.2: Same as Figure 5.1 but data from Lelli et al. (2013, 2014) and Erroz-Ferrer et al. (2016) are also plotted. Data from Lelli et al. (2013) are shown as black stars, Lelli et al. (2014) data are shown as green dots and data from Erroz-Ferrer et al. (2016) are shown as magenta stars. The best fit line to the data is shown as a blue dashed line. Best fit lines from other studies are also shown; Lelli et al. (2013, 2014): green dashed line, Erroz-Ferrer et al. (2016): magenta dashed line and the solid red line is the best linear fit for all the data.

Analysis by Lelli et al. (2013, 2014) and Erroz-Ferrer et al. (2015) lead them to suggest that the correlation between α_0 and $S_{R,0}$ indicates that f_b is high in the inner regions of galaxies. In other words, there is very little dark matter compared to baryonic material in the central regions of galaxies. I now use this analysis to constrain f_b.

Equation 5.2 can be expanded in log form to:

$$\log \alpha = 0.5 \log S_s + 0.5 \log \left(\frac{2\pi G m_s M_b / L}{3 \Delta z f_b} \right). \tag{5.6}$$

The y-intercept of the relation is $0.5 \log(\frac{2G\pi m_s (M_b/L)}{3\Delta z f_b})$. The correlation between α_0 and $\mu_{R,0}$ (therefore S_s) and power law similar to what is expected from the model

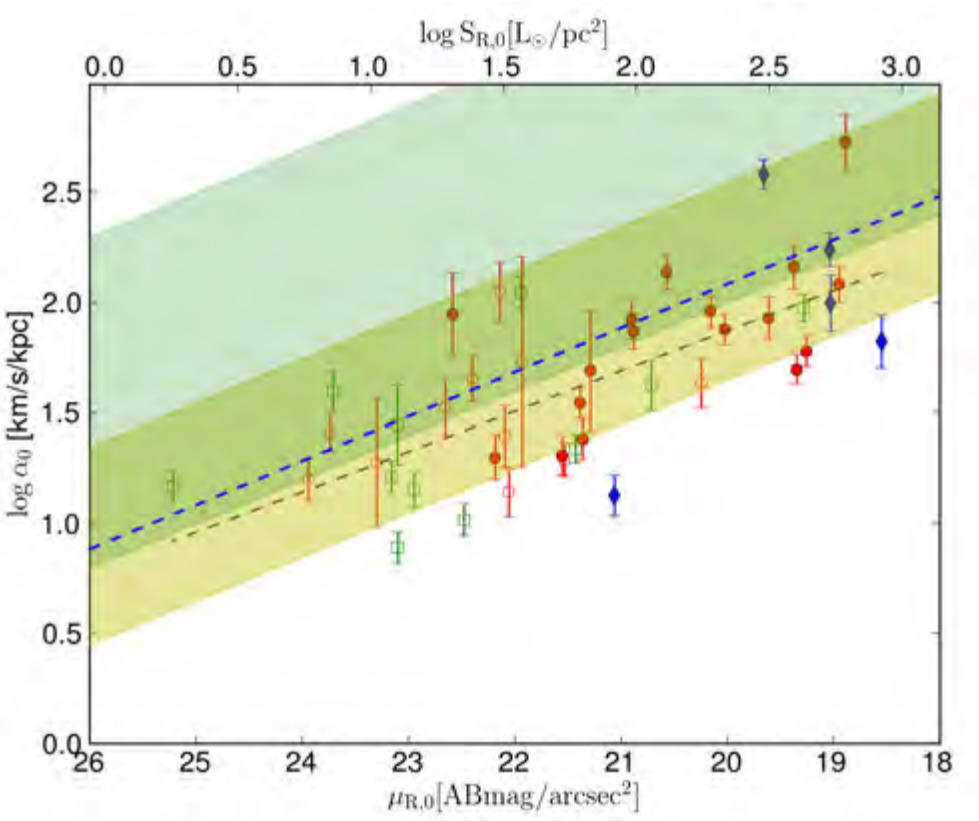

Figure 5.3: Data and symbols are the same as Figure 5.1. The yellow shaded regions show a model where Υ_s^R ranges from 1 to 5, Δz ranges from 100 pc to 500 pc, m_s ranges from 0.5 to 1.0 and f_b ranges from 0.8 to 1.0. The cyan shaded region is the same except that f_b ranges from 0.2 to 0.01. The green shaded region is where both models overlap. The blue dashed line shows the intermediate model where $\Upsilon_s^R = 2.0$, $\Delta z = 250$ pc, $m_s = 0.75$ and $f_b = 1.0$. The best fit line to the data (same as in Figure 5.1) is shown as a dashed grey line.

indicate that the term is constant, therefore $m_s M_b/L$ is proportional to $1/\Delta_z f_b$. I can use the y-intercept to constrain the values of these parameters. Of particular interest is the baryonic fraction. The correlation between α and $S_{R,0}$ suggests that the stellar surface density and the central potential well of galaxies (traced by α_0) are closely tied together. If the dark matter dominates the mass density of galaxy centers then the relation shows that the distribution and concentration of stars is driven by the dark matter. If the stars dominate the mass density then they are responsible for the inner potential well. Constraining the baryonic fraction will allow us to determine how much the stars dominate the potential well. This can be done by substituting typical values for M_b/L, Δz and m_s into Equation 5.6 and varying f_b. For this analysis I assume that the stellar mass is the dominant baryonic mass in the central parts of our galaxies,

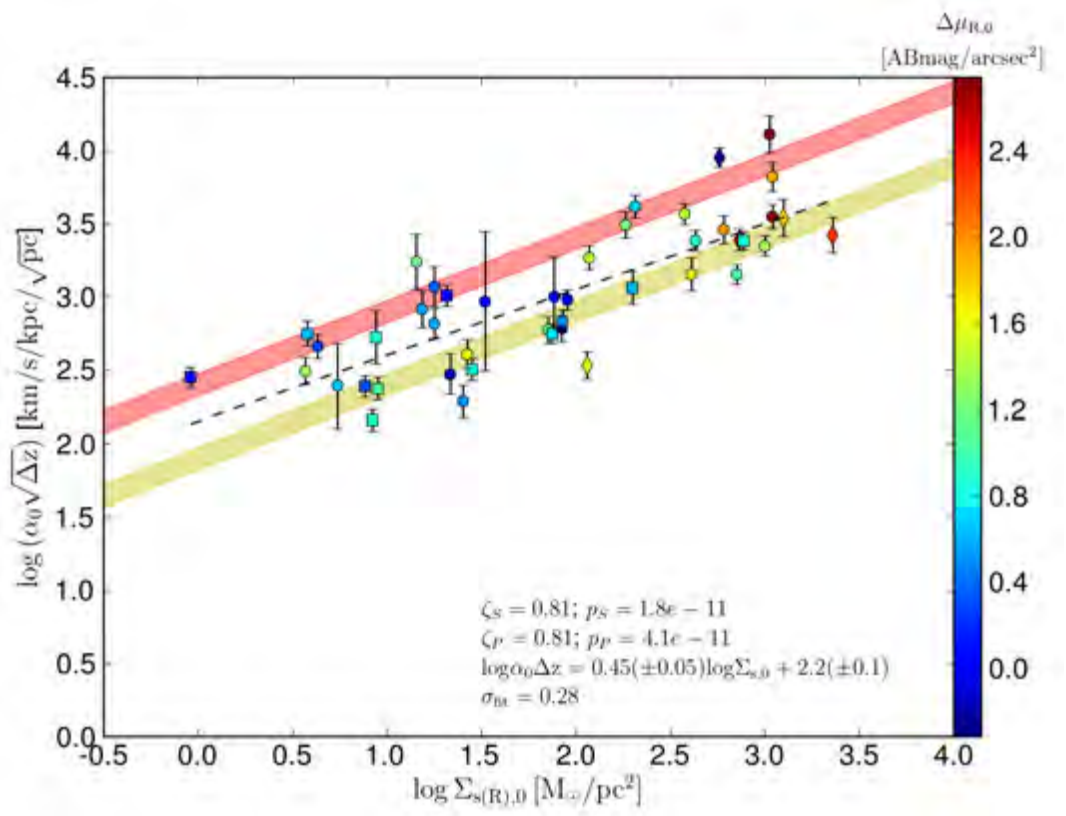

Figure 5.4: Product of $\sqrt{\Delta z}$ and the central velocity gradient plotted against the central stellar surface brightness (calculated from R-band observations). The symbols, dashed line and how the α_0 values were calculated are the same as Figure 5.1. The data points are colour-coded according to their central light excesses ($\Delta\mu_{R,0} = \mu_{R,0}\,(\text{outer}) - \mu_{R,0}\,(\text{inner})$). The yellow shaded region shows a model where m_s ranges from 0.5 to 1.0 and $f_b = 1$. The red shaded region shows a model where m_s ranges from 0.5 to 1.0 and $f_b = 0.1$.

this is supported by rotation curve and mass model analyses such as those of Puche & Carignan (1991) and de Blok et al. (2008) who found this to be the case for most of the galaxies they studied. Therefore I use the stellar mass-to-light ratio (M_s/L or more conveniently Υ_s) for the rest of the analysis. The Υ_s estimated using optical bands ranges from $3-7$ in the bluest optical bands (B-band having the largest values and uncertainty) (Bell & de Jong 2001) and down to $0.7-3$ in the I-band near-infrared (Bell & de Jong 2001, Portinari et al. 2003). Bell & de Jong (2001) determined this using a scaled down Salpeter IMF (it was scaled down by 0.7 to fit maximum disk models, see Fukugita et al. 1998 for more details) from 0.1 $M_\odot$ to 125 $M_\odot$, stellar population synthesis models from Bruzual & Charlot (2001). They tested their results for various IMFs and star formation histories (see Bell & de Jong 2001 for more details). For the

R-band I use a range between these bands but closer to the I-band, I consider Υ_s^R ranging from 1 to 5. As previously mentioned m_s varies between 0.5 and 1.0. Δz is taken to be the scale height (h_s) and can be estimated from the scale length (l_s) by using the $l_s/h_s = 7.3$ (Kregel et al. 2002) relation and the scale length can be determined from effective radius using the $r_e = 1.678 l_s$ (Erroz-Ferrer et al. 2016, Ciotti 1991) approximation. Using these, I find that for our sample most galaxies have h_s values ranging between 100 pc and 450 pc (median: $h_s = 239$ pc). This is a simplification and assumes a simple pure exponential thin disk, departures from this behaviour are discussed later in this chapter. α_0 and $\Sigma_{s,0}$ were calculated for these ranges in parameters and the results are overplotted over the data in Figure 5.3. The model where f_b is between 0.8 and 1.0 covers more galaxies than the model with lower f_b. There are many galaxies with lower α_0 values than the range that the models cover. Even the high f_b model when $f_b = 1$ has higher α_0 than the lowest α_0 galaxies. In order to explain this either $\Delta z > 500$ pc, $\Upsilon_s^R < 1$ for these galaxies or their α_0 values could be underestimated.

Better constraints on Υ_s and Δz can be used to better determine the typical baryonic fractions in the central parts of galaxies. Most of the Υ_s calibrations in the optical are done using colours, however the SINGG wideband optical observations were only performed using the R-band filter. Wong et al. (2016) fitted a relationship between Υ_s^R and M_R for typical SUNGG galaxies. They determined the relationship using the Bell et al. (2003) stellar population synthesis models, which assume a 'diet Salpeter' IMF. Their fitted relationship is:

$$\log(\Upsilon_s^R) = -1.578 - 0.856 M_R. \tag{5.7}$$

Υ_s^R is the R-band stellar mass-to-light ratio and is measured in solar units. It should be noted that this is a crude relationship that assumes that the galaxies are in the middle of the star forming sequence. This star forming sequence is the blue cloud of the observed bimodality of the galaxy population (e.g., Strateva et al. 2001, Baldry et al. 2004). I used this relation to determine Σ_s values for our galaxies. Directly using Σ_s reduces the number of free parameters in the model. I used the aforementioned relation to calculate Δz from l_s for each galaxy. The exponential scale lengths l_s were calculated by making exponential fits to the outer part of the radial μ_R profiles (where $r > r_e$). $\log(\alpha_0\sqrt{\Delta z})$ is plotted against $\log \Sigma_{s,0}$ in Figure 5.4. The velocity gradients, surface brightnesses, mass surface densities and scale lengths used in this analysis are listed in Table 5.2. The Υ_s^R of the galaxies used in the plot range from 0.5 to 2.9, with a mean of 1.3. The correlation coefficients for the parameters in the plot are $\zeta_P = 0.81$ and $\zeta_S = 0.81$ and the probability of the null hypothesis is $p \leq 5 \times 10^{-11}$. These show that there there is a better correlation between the parameters in the plot than when

$\log \alpha_0$ is plotted against $\log S_{R,0}$. The slope of the relation is 0.45 ± 0.05, which is close to the theoretical value (0.5). This indicates that the model is a reasonable description of the data. The tighter correlation is expected because the constants in the intercept were calculated for each individual galaxy and the only free parameters left in the model are m_s and f_b. Most of the galaxies are consistent with models that have f_b that range from 0.1 to 1. About half (22/44) of the galaxies are consistent with a model that has $f_b = 1$ and 14/44 were consistent with a model that has $f_b = 0.1$. The fitted linear relation is mostly consistent with a model with f_b between 1.0 and 0.1, and that f_b increases with increasing $\Sigma_{s,0}$. The dispersion of the linear fit is 0.28 and does not constrain this much and there are many galaxies at low $\Sigma_{s,0}$ values that are consistent with f_b models. Some galaxies have $\log(\alpha_0\sqrt{\Delta z})$ values less than the $f_b = 1$ model, this suggests that their Δz values were underestimated or their Υ_s^R are overestimated. This could therefore be the case for the other galaxies which are consistent with the model. The Δz values are based on assumptions that the disk is purely exponential, in hydrostatic equilibrium and isothermal in the vertical direction. If the galaxies are bulge dominated the exponential disk approximation used for Δz breaks down and the central values of Δz are more uncertain, these galaxies would have higher Δz values than predicted by the relations I used.

The excess central light (compared to that expected from an exponential disk) was quantified in order to study how the presence or lack of bulges affects galaxy centers in Figure 5.4 . Exponential functions were fitted to the outer part of the S_R profiles ($r > r_e$) and the $\mu_{R,0}$ values determined from these fits were compared to $\mu_{R,0}$ values determined from linear extrapolations of the inner S_R values. $\Delta\mu_{R,0} = \mu_{R,0}\,(\text{outer}) - \mu_{R,0}\,(\text{inner})$ was used to quantify the excess light. The excess light is usually due to the presence of bulges, pseudo-bulges, bars, or starbursts with the highest concentrations being found in bulge-dominated galaxies. In Figure 5.4 I see that the highest surface brightness galaxies tend to have much more pronounced increases in $\mu_{R,0}$ compared to what is expected from a purely exponential stellar disk. This is similar to what Lelli et al. (2013) found in their analysis. This indicates that galaxies with the brightest central regions tend to have the higher α_0 values and more pronounced bulges than galaxies with fainter central regions. Erroz-Ferrer et al. (2016) found that galaxies in their sample that have the most massive bulges and highest bulge-to-disk ratios tend to have the highest α_0 values. They found that for bulge masses less than $10^9\, M_\odot/pc^2$ increasing bulge masses did not result in increasing α_0 values. Galaxies with high α_0 values ($\alpha_0 > 110\,\text{km/s/kpc}$) tend to have have bulge masses greater than $10^9\, M_\odot/pc^2$ (and bulge-to-total light ratios greater than 0.1).

In our sample, most galaxies with $\Sigma_{s,0} > 10^{2.5}\, M_{\odot}/pc^2$ have excess light concentrations and most of them have $\Delta\mu_{R,0} > 0.5\,\mathrm{mag/arcsec^2}$. Structures that result in greater $\Delta\mu_{R,0}$ increase the inner $\Sigma_{s,0}$, and the increase in their mass and concentration with increasing α_0 shows that there is correlation between $\Sigma_{s,0}$ and the steepness of the inner potential well. However, galaxies that have lower $\alpha_0\sqrt{\Delta z}$ values than predicted by the $f_b = 1$ model have a wide range of $\Delta\mu_{R,0}$ values. Most of them have $\Delta\mu_{R,0} > 0$ and therefore have excess central light concentrations from structures like bulges or bars. For these galaxies and other galaxies with bright central concentrations the Δz determined from the l_s assuming an exponential disk underestimates the real value of Δz (except if the central concentrations are pseudo-bulges, which are thinner and more disk-like than classical bulges, e.g., Kormendy & Kennicutt 2004). The conversion from l_s and then to h_s is for an exponential disk and a central excess means that the disk is not purely exponential. Underestimated Δz values could also be due to the central regions of these galaxies to be thicker expected. The effect of higher disk thickness is discussed later in this section. Some of the galaxies with low $\alpha_0\Delta z$ values have $\Delta\mu_{R,0} < 1$, this could be due to dust absorption.

Uncertainties in the Υ_s calibration for R-band data could be responsible for some of the departures from the model. Υ_s calculations using optical bands have been shown to have large uncertainties (Bell & de Jong 2001). Υ_s^R values were calculated from a relationship that was fitted to globally averaged parameters, but this analysis is focused on the inner regions of galaxies, therefore variations within galaxies would increase the uncertainty. The Wong et al. (2016) relation was calculated for galaxies that are in the middle of the star forming sequence and due to the scatter in the sequence the relation has its own intrinsic scatter. Our galaxies cover a wide range of masses, galaxy types and star formation rates, hence they do not all lie in the middle of the star forming sequence. Therefore relation may not hold for the entire sample. Wong et al. (2016) used a variant of the surface-density luminosity relation (e.g., Disney & Phillipps 1985, Kauffmann et al. 2003), therefore the M_R - Υ_s^R relation can be converted to a S_R - Υ_s^R relation. This indicates that the Υ_s^R values are related to the S_R. The nature of the relation, its scatter and the dependence of Υ_s^R on S_R increase the uncertainty of the conclusions of this analysis. The plots suggest that $\sim 50\%$ of galaxy centers are consistent with central f_b values close to 1, but there are large ranges in f_b between galaxies and some have central f_b values closer to 0.1 . A more accurate method to determine the Σ_s is necessary in order to confirm these results. Better constraints of the central disk thicknesses and Υ_s values are required in order to test this model further and to calculate accurate f_b using this method.

Analysis of the R-band data shows that there is a good correlation between α_0 and $\Sigma_{s,0}$, and that the R-band observations are effective at tracing the stellar component of galaxies. The relation between the central light excess and $\alpha_0\sqrt{\Delta z}$ along with the correlation between α_0 and $\Sigma_{s,0}$ indicate that the stellar mass constitutes a large fraction of the central mass of many galaxies in our sample. $\sim 50\%$ galaxies have centers that are described by a model with f_b values close to 1, there is a large variation in f_b between the galaxies and better constraints on Δz and Υ_s^R are essential in order to better constrain f_b.

5.2 WISE Infrared Stellar Surface Density and Velocity Gradient Comparison

In the previous section I used the R-band as a tracer of the stellar surface density, but NIR bands are more ideal tracers of the stellar surface density. NIR observations are less affected by dust extinction and minor recent star formation events than optical observations (e.g., Into et al. 2013). Therefore better constraints have been made for Υ_s in NIR bands than in the optical (e.g., Bell & de Jong 2001, Portinari et al. 2003, Into et al. 2013). I used infrared data from WISE by using the W1 and W2 bands to study the relationship between α and Σ_s. The WISE W1 and W2 NIR band data was available for the galaxies in our sample, and they provide an alternative and in principle more accurate method of studying the relationship between α_0 and $\Sigma_{s,0}$ than optical studies such as the R-bands analysis and that of Lelli et al. (2013, 2014). In this section I perform similar analysis as done for the R-band in order to study the relationship and the baryonic fractions in the inner parts of galaxies and then compare with the R-band analysis.

The central velocity gradient α_0 is plotted against $\mu_{W1,0}$ in Figure 5.5. The data used includes that from galaxies which had no R-band observations, therefore the total number of galaxies used for this fit is 57 (compared to 44 used in the R-band analysis). The best fitted slope of the relation between $\log \alpha_0$ and $\mu_{W1,0}$ is -0.16 ± 0.02. This is lower but still consistent with what was found for $\mu_{R,0}$. The correlation coefficients are $|\zeta_S| = 0.71$ and $|\zeta_P| = 0.72$, and $\sigma_{\rm fit} = 0.29$ for the linear fit. The probability of the null hypothesis is $p < 5 \times 10^{-10}$. This is a slightly better correlation between the variables and a lower $\sigma_{\rm fit}$ than was found in the $\mu_{R,0}$ case. Some of the galaxies are brighter relative to other galaxies when their relative $\mu_{W1,0}$ values are compared to their $\mu_{R,0}$ values, which suggests that their $\mu_{R,0}$ values are affected by dust obscuration. The fit

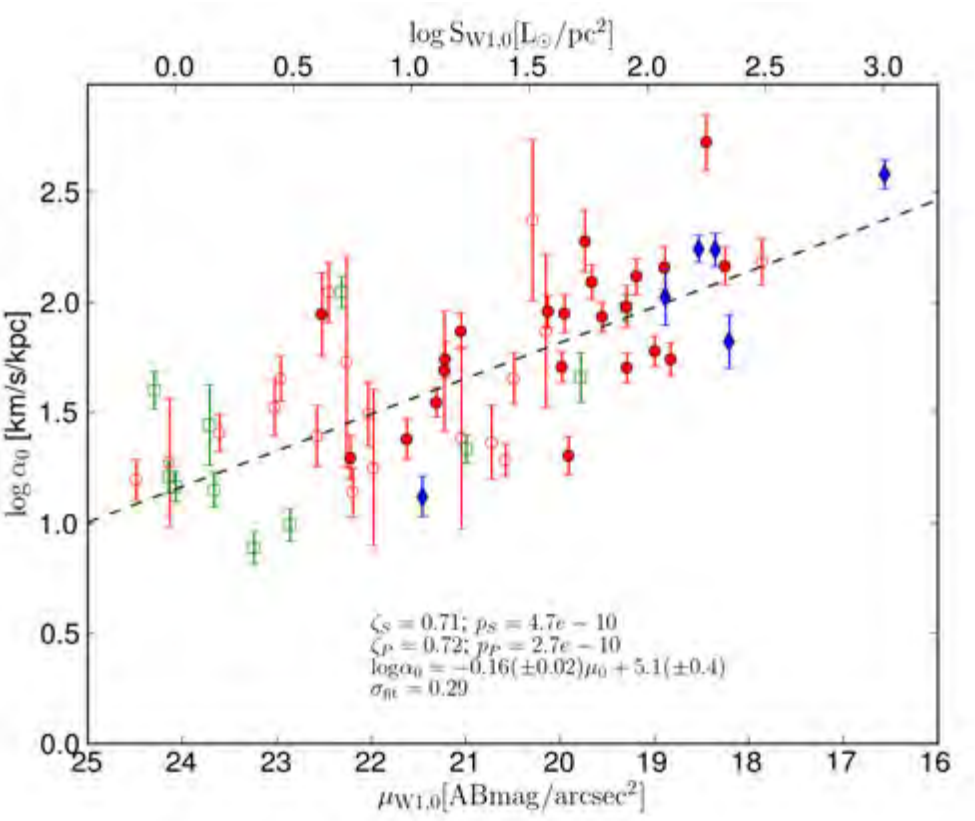

Figure 5.5: Same as Figure 5.1, but WISE W1 surface brightnesses are plotted.

results predict a power law index of the relation is lower than the predicted value. The similarity between the μ_R and μ_{W1} gradients shows that the R-band is a reasonable tracer to use for such studies. The better correlation between the parameters is expected because $W1$ is less affected by dust absorption and star formation history than the R-band is. The results of the fit and correlation between parameters indicates that there is a correlation between $\Sigma_{s,0}$ and the steepness of the potential well in the central regions of galaxies.

I can also use $W1$ observations to constrain the baryonic fraction in the inner parts of galaxies. This is done in Figure 5.6, where $\log(\alpha_0 \Delta z)$ is plotted against $\Sigma_{s,0}$. $\Sigma_{s,0}$ was calculated from $S_{W1,0}$ using the Υ_s^{W1} relation for WISE determined by Cluver et al. (2014). The relation is based on findings by Jarrett et al. (2013) that the mass-to-light ratio is linearly related to the W1-W2 and W2-W3 colours. Cluver et al. (2014) fitted the relation by using stellar masses estimated by Talyor et al. (2011). They estimated the stellar masses using a Chabrier (2003) IMF and Bruzual & Charlot (2003) synthetic stellar population models. The Cluver et al. (2014) relation relates W1-W2 colours to

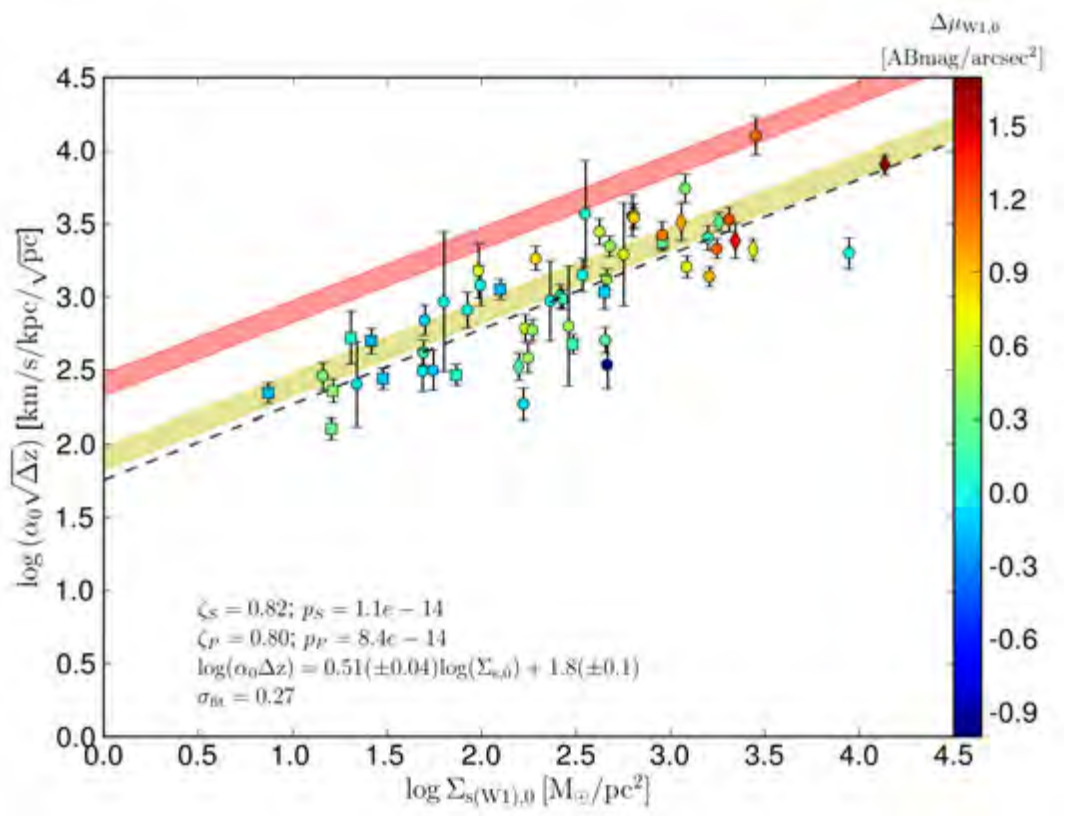

Figure 5.6: Product of $\sqrt{\Delta z}$ and the central velocity gradient plotted against the central stellar surface brightness (calculated from W1 observations). The symbols, dashed line and how the α_0 values were calculated are the same as Figure 5.1. The data points are colour-coded according to their central light excesses ($\Delta\mu_{W1,0}$ = $\mu_{W1,0}$ (outer) $-\mu_{W1,0}$ (inner)). The best fit line to the data is shown as a black dashed dashed line. The yellow shaded region shows a model where m_s ranges from 0.5 to 1.0 and $f_b = 1$. The red shaded region shows a model where m_s ranges from 0.5 to 1.0 and $f_b = 0.1$.

the stellar-mass-to-light ratio as follows:

$$\log(\Upsilon_s^{W1}) = -1.96(W1 - W2) - 0.03, \tag{5.8}$$

where Υ_s^{W1} is the stellar mass-to-light ratio calculated by using $W1$ and $W2$ photometry. This relation was fitted by Cluver et al. (2014) using "in-band luminosities" (see Jarrett et al. 2013). To convert the W1 νL_{nu} to its in-band equivalent I scale it up by a factor of 22.883 (Jarrett et al. 2013). This conversion was applied to the $S_{W1,0}$ measurements in order to calculate Σ_s using the Cluver et al. (2014) Υ_s^{W1} relation. The Υ_s^{W1} values calculated for the galaxies in the plot range from 0.2 to 0.9 and the mean is 0.47. The Δz values for each galaxy were calculated in the same

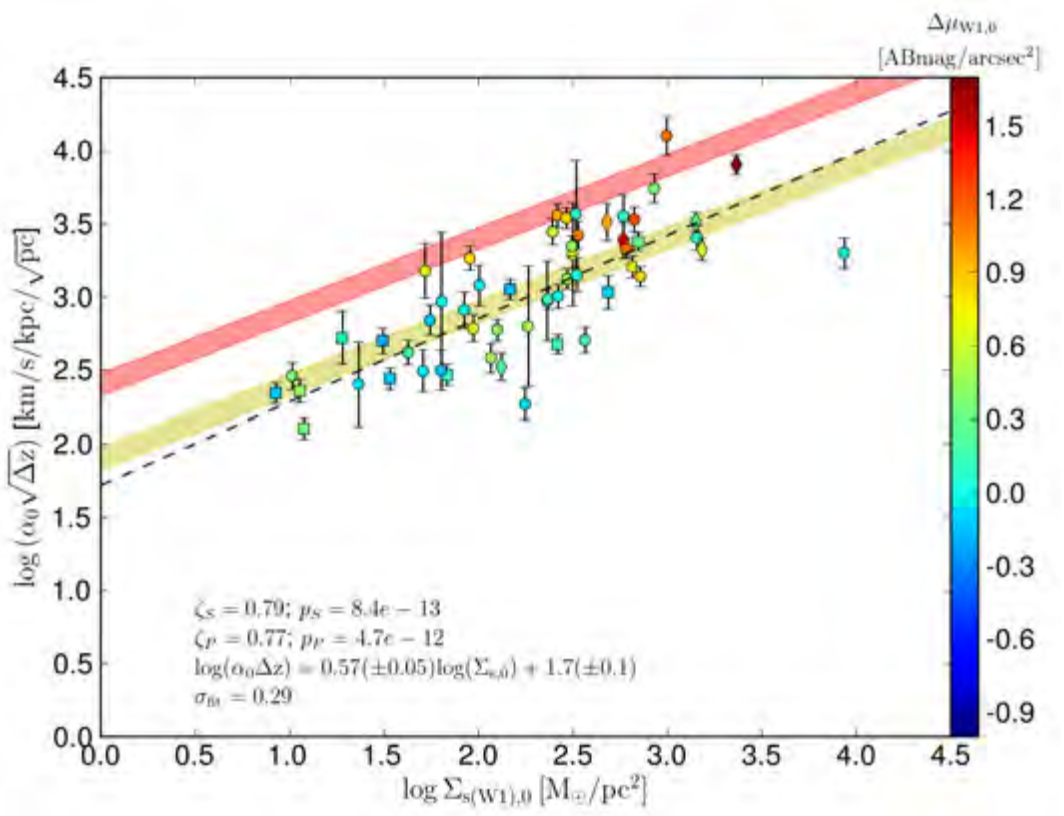

Figure 5.7: Product of $\sqrt{\Delta z}$ and the central velocity gradient plotted against the exponential central stellar surface density (calculated from W1 observations). The symbols, dashed line and how the α_0 values were calculated are the same as Figure 5.1. The data points are colour-coded according to their central light excesses ($\Delta\mu_{W1,0} = \mu_{W1,0}\,(\text{outer}) - \mu_{W1,0}\,(\text{inner})$). The best fit line to the data is shown as a black dashed dashed line. The yellow shaded region shows a model where m_s ranges from 0.5 to 1.0 and $f_b = 1$. The red shaded region shows a model where m_s ranges from 0.5 to 1.0 and $f_b = 0.1$.

way as in the R-band analysis, except that the l_s values were derived from μ_{W1} radial profiles. In order to directly compare with the R-band results the Υ_s^{W1} values were adjusted to the same IMF used to determine Υ_s^R. The conversion from a Chabrier (2003) IMF to a diet Salpeter is done by adding 0.19 dex (Wiegel et al. 2016, Bell et al. 2013). The surface brightnesses, mass surface densities and scale lengths used in this analysis are listed in Table 5.2. Figure 5.6 shows that many galaxies in the sample are consistent with a model with $f_b = 1$, however there are many galaxies that have lower $\log(\alpha_0\Delta z)$ than what the $f_b = 1$ model predicts. The best linear fit to the data is: $\log(\alpha_0\Delta z) = 0.51(\pm0.04)\log(\Sigma_{s,0}) + 1.8(\pm0.1)$. The fitted line to the data has $\log(\alpha_0\Delta z)$ lower than the model predicts. When these parameters are plotted there is a

much better correlation between $\log(\alpha_0 \Delta z)$ and $\log(\Sigma_{s,0})$ than what is found in Figure 5.5. The slope of the relationship in Figure 5.6 is 0.51 ± 0.04, this is consistent with the expected value from the model: 0.5. The linear fit has $\sigma_{\rm fit} = 0.26$, which is smaller than what was found for the linear fit in the $\Sigma_{R,0}$ plot. The slope of the fitted relation is more consistent with the model compared to the linear fit to the $\Sigma_{R,0}$ plot. The tighter correlation and better match to the model confirms that WISE W1 emission is a good tracer of Σ_s (better than the optical R-band) and that the observed α_0 and $\Sigma_{s,0}$ follow the relationship that is predicted by the model.

The relationship between $\Delta\mu_{R,0}$ and $\alpha_0\sqrt{\Delta z}$ is confirmed in the W1 band showing that the central light excess is higher for greater $\alpha_0\Delta_z$. And I see that galaxies that have lower than expected $\alpha_0\Delta z$ values are not necessarily bulge-dominated, therefore the Δz needs to be better constrained in future analysis. Most of the galaxies with high $\Delta\mu_{W1,0}$ and $\Delta\mu_{R,0}$ would not lie on the expected relation if only their exponential disk $S_{R,0}$ values were used in Figure 5.4 and Figure 5.6. I tested this by recreating Figure 5.6 but using $\Sigma_{s,0}$ values calculated using $\mu_{W1,0}$ values extrapolated from exponential fits of the outer parts ($r > r_e$) of the μ_{W1} radial profiles. These values represent the exponential disk component of the central stellar surface density. This data are plotted in Figure 5.7. This figure shows that the linear fit to the exponential component of $\Sigma_{s,0}$ has a steeper gradient (0.57 ± 0.05) than the total $\Sigma_{s,0}$. In this plot galaxies with high $\Delta\mu$ are off the original relation and many of them are now described by models with $f_b < 1$. These galaxies also have high $\Sigma_{s,0}$ compared to the rest of the sample, but the are lower than when the non-exponential fit method is used to determine their $\Sigma_{s,0}$. Their decreased $\Sigma_{s,0}$ values cause the relation to have a steeper gradient. The plot confirms that the relation in the model between $\log\alpha_0$ and $\Sigma_{s,0}$ is for the total stellar content. This was also suggested by results from Lelli et al. (2013). It indicates that the presence of structures that increase the central light (and stellar) density are important in determining the central dynamics and hence in setting the relation between $\Sigma_{s,0}$ and α_0 at high $\Sigma_{s,0}$ and α_0.

The y-intercept of the best fit line in the R-band case is 2.2, while in the W1 case the y-intercept is 1.8. In order to directly compare values from the W1 and R-band analyses the $\Sigma_{s,0}$ values must be calibrated correctly. The R-band analysis was done using a "diet" Salpeter IMF (Bell et al. 2003), but the W1 analysis was performed assuming a Chabrier (2003) IMF. The logarithm of mass-to-light ratios calculated using the Chabrier IMF are 0.19 dex lower than those calculated using a diet Salpeter IMF (Bell et al. 2003, Wiegel et al. 2016). If I convert from Chabrier W1 values

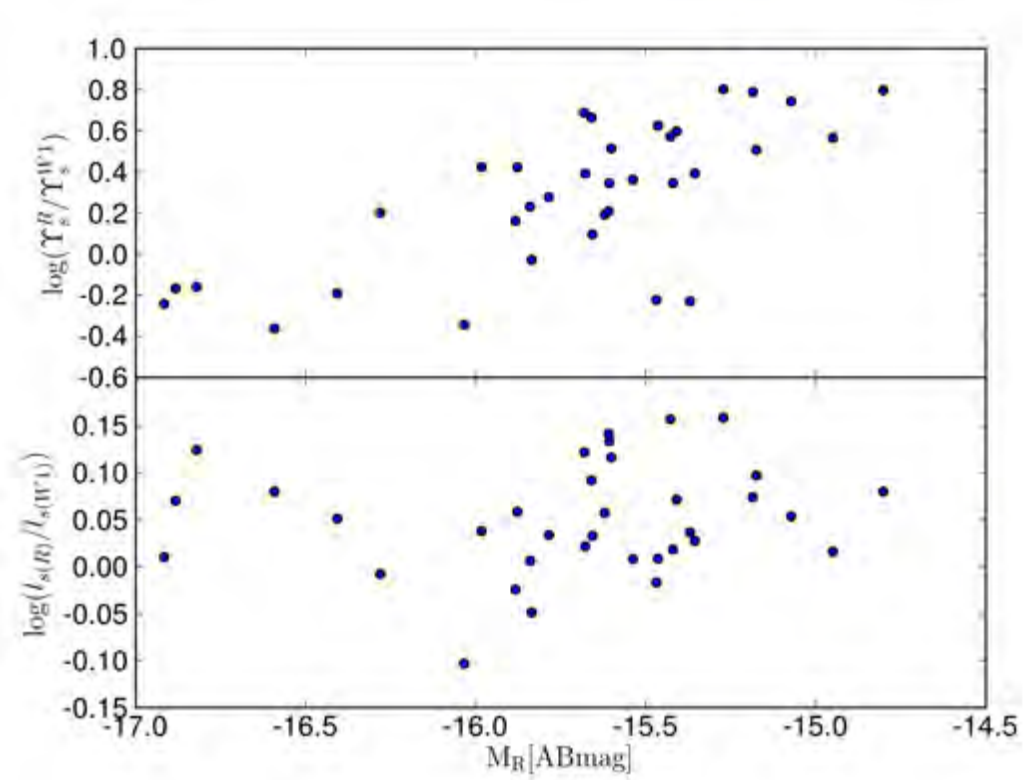

Figure 5.8: *Top :* Ratio between Υ_s^R and Υ_s^{W1} mass-to-light ratios plotted against the M_R. *Bottom :* Ratio of the R-band and W1 l_s ($l_{s(R)}/l_{s(W1)}$) plotted against M_R.

to diet Salpeter values the $\log \Sigma_{s,0}$ values are all increased by 0.19 dex. This would result in an even greater difference between the R-band and W1 values. The f_b values of the galaxies (mostly $f_b \geq 1$) are in general higher what was found for the R-band observations ($f_b \sim 1$). This is due to differences between the M/L or differences in the Δz for the R-band and W1. Δz is assumed to be h_s, which is calculated from l_s. Comparisons between the Υ_s and l_s calculated from R-band and W1 observations are shown in Figure 5.8. The figure shows that most l_s values determined from R-band observations range from 0.8 to 1.5 times those determined from W1 observations. There is a large spread of ratios across all M_R. High luminosity galaxies have mean ratios that are higher than low luminosity galaxies. For galaxies with $M_R < 16$ the most massive galaxies have increasingly larger l_s determined from the optical R-band observations relative to the near infrared W1 observations. For most galaxies l_s determined from R-band observations are greater than those determined from W1 observations. The higher R-band l_s result in higher $\log(\alpha_0 \Delta z)$ values because Δz is calculated from l_s. The differences between the R-band and W1 r_e are small and not enough to fully account for the differences in the $\log(\alpha_0 \Delta z)$ versus $\log \Sigma_{s,0}$ plots. The Υ_s^R values are

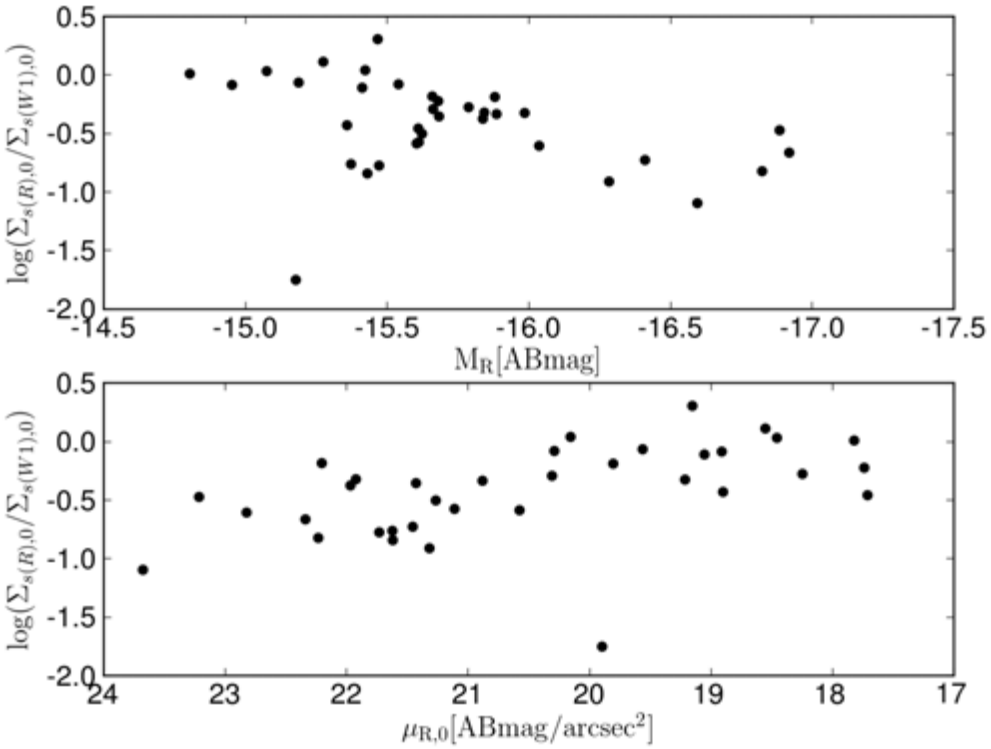

Figure 5.9: Ratio between $\Sigma_{s,0}$ calculated using the R-band ($\Sigma_{s(R),0}$) and W1 observations ($\Sigma_{s(W1),0}$) against M_R (*top*) and $\mu_{R,0}$ (*bottom*).

up to 6 times larger than Υ_s^{W1}, the difference between them increases as the R-band luminosities increase. The large differences between them are evident in the different $\Sigma_{s,0}$ values determined by using each of them.

For most of the galaxies $\Sigma_{s,0}$ values calculated using Υ_s^{W1} are higher than those calculated by using Υ_s^R. The ratios of $\Sigma_{s,0}$ calculated using the different tracers plotted against M_R and $\mu_{R,0}$ in Figure 5.9. The difference in $\Sigma_{s,0}$ values can be up to 1.0 dex. The difference in calculated $\Sigma_{s,0}$ is the reason why R-band data matches models with higher f_b than what the W1-derived $\Sigma_{s,0}$ data does. The R-W1 ratio of stellar mass densities decreases as the galaxy luminosity increases, and it increases as the R-band surface brightness increases. Both R-band and W1 $\Sigma_{s,0}$ determined values are plotted against M_R and $\mu_{R,0}$ in Figure 5.10. Figure 5.10 shows that $\Sigma_{s,0}$ behaves the same way that the ratio between the R-band and W1 derived $\Sigma_{s,0}$ does. The largest differences between R-band and W1 $\Sigma_{s,0}$ is for the lowest surface density galaxy centers. These plots show that the large differences between Υ_s^R and Υ_s^{W1}, the increase of the differ-

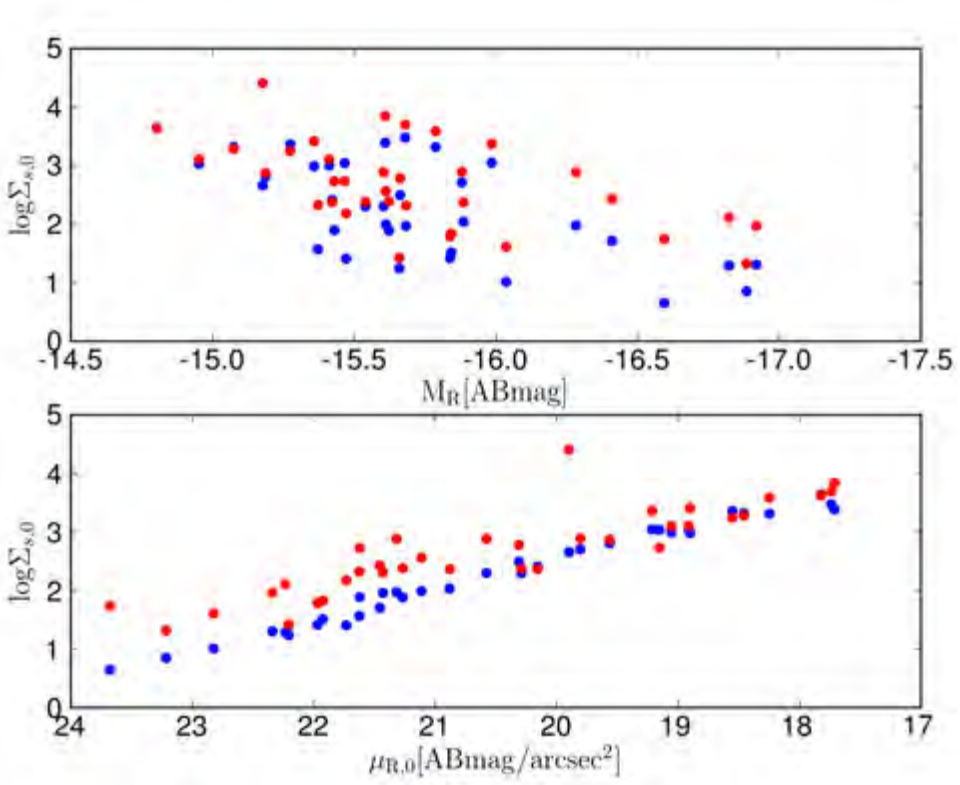

Figure 5.10: Comparison between $\Sigma_{s,0}$ calculated using the R-band ($\Sigma_{s(R),0}$) and W1 observations ($\Sigma_{s(W1),0}$) against M_R (*top*) and $\mu_{R,0}$ (*bottom*). The R-band data are plotted in blue and the W1 data are plotted in red .

ences with increasing M_R and to a lesser degree the differences between l_e calculated from the R-band and W1 contribute a large amount to the differences seen in the predicted f_b.

Both the R-band and W1 analyses show that there are many galaxies which have $\alpha_0\Delta z$ values lower than the $f_b = 1$ model. Overestimation of Υ_s and underestimation of Δz can cause these differences. Uncertainties in the optical Υ_s^R have been mentioned, and I noted that Υ_s^{W1} values are much higher than Υ_s^R. Υ_s calibrations are affected by variations in the initial mass function, star formation history, age of the stellar population, metallicity, dust extinction, emission from AGB stars and nuclear activity (Jarrett et al. 2013). W1 photometry (hence the Υ_s^{W1} calibration) is less sensitive to dust obscuration and more sensitive to the low surface density emission than shorter wavelengths (Jarrett et al. 2013). However, near-infrared tracers overestimate the real M/L ratio because dust emission from star formation and AGB stars contribute more

to this wavelength band (e.g., Meidt et al. 2012) thereby causing an overestimation of the flux attributed to the low mass stars (which W1 traces). Meidt et al. (2012) found that emission due to hot dust and PAHs can contribute on average 20% of the 3.6 mum flux in star forming regions and intermediate-age AGB or RSG stars contribute more than 50% of 3.6 mum flux in some star forming knots.

The h_s value used to determine Δz in Figures 5.4 and 5.6 were determined with the Kregel et al. (2002) relation : $h_s = l_s/7.3$, which is based on their analysis of 34 edge on spiral galaxies. Based on the Freeman (1970) exponential disk model Bottema (1993) determined that the l_s/h_s should range from 12 to 4, with most of galaxies with values between 8 and 4. Studies of large samples of edge-on galaxies (≥ 153) by Bizyaev & Mitronova (2002, 2009), Mosenkov et al. (2010) and Bizyaev et al. (2014) found l_s/h_s ranging between 2.5 and 4.8. In their analysis of more than 5700 edge-on SDSS galaxies Bizyaev et al. (2014) found that the median l_s/h_s in the r band was 3.4 (peak of the distribution was at 2.5) and in 3.3 for the i band. Using $h_s = l_s/2.5$ results in an increase in the $\alpha_0 \Delta z$; the fitted y-intercept in Figure 5.6 increases from 1.8 to 2.0 and a higher fraction of galaxies is consistent with the models than when the Kregel et al. (2002) relation is used. This indicates that use of more realistic values of Δz do result in better consistency with the models. That combined with more accurate Υ_s values may improve agreement between our data and the models.

High f_b values are expected from studies of the dynamical contributions the stellar disks that have been determined by rotation curve decomposition and mass model analysis such as that made by Puche & Carignan (1991) and de Blok (2008). Work by Corradi & Capaccioli (1990) showed that the inner dynamics of spiral galaxies are dominated by visible matter. Stellar kinematics and dipsersion analysis by Bottema (1993, 1997) showed that the stellar disk contributes $63 \pm 10\%$ of V_{max}. Work by Courteau & Rix (1999) supports this and Bottema & Verheijen (2002) found similar results using rotation curve mass-decomposition. All these studies show that even if the maximum-disc hypothesis (Kalnajs 1983, van Albada et al. 1985, Carignan & Freeman 1985, and van Albada & Sancisi 1986), where the contribution is up to 90% (Sancisi 2004), is false the inner regions of galaxies still have large amaounts of baryonic matter and it dominates over the dark matter. Even low surface brightness galaxies which are expected to be dominated by dark matter, both Verheijen (1997) and Swaters (1999) found that models of disks with high mass contributions from the disk can be used to fit the inner parts of these galaxies. However, Bershady et al. (2011) determined that in disk galaxies baryons contribute 15% to 30% of the total mass within $2.2l_s$ by

independently measuring the dynamical mass and baryonic masses of disk galaxies.

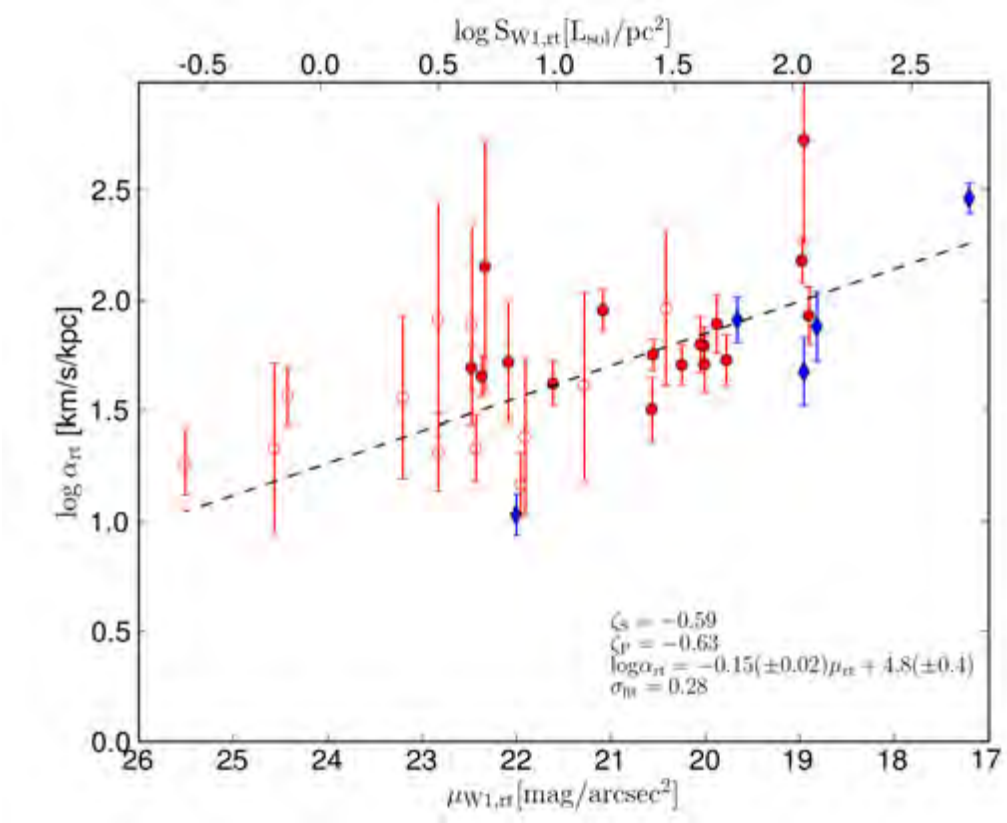

Figure 5.11: The velocity gradient plotted against the W1 surface brightness at r_t. The W1 surface brightness values at r_t were extrapolated from W1 radial profiles. Symbols are the same as Figure 5.1. The Class 2 and 3 galaxy gradients were calculated using the multi-polynomial method. The best linear fit to the data is shown as a dashed line.

The stellar density decreases as the radius increases, therefore the effect of the stellar disk on the gravitational potential well decreases with increasing radius. I studied the relationship between α and Σ_s at larger radii. The same analysis performed for data at $r = 0$ was performed at $r = r_t$ to determine whether the relationship between α and Σ_s still holds and what the f_b is. As mentioned before, α_{rt} values were determined from arctan fits of the rotation curves. Interpolations of the interior surface brightness profiles were used to determine the surface brightness at r_t. Interior surface brightnesses were used because in the model I am testing the velocity gradient is set by the total mass interior to the radius at which it is measured. The interior surface brightness traces the interior mass density which can be used to calculate the total mass within the radius at which the measurement is made. α_{rt} is calculated by assuming a linearly

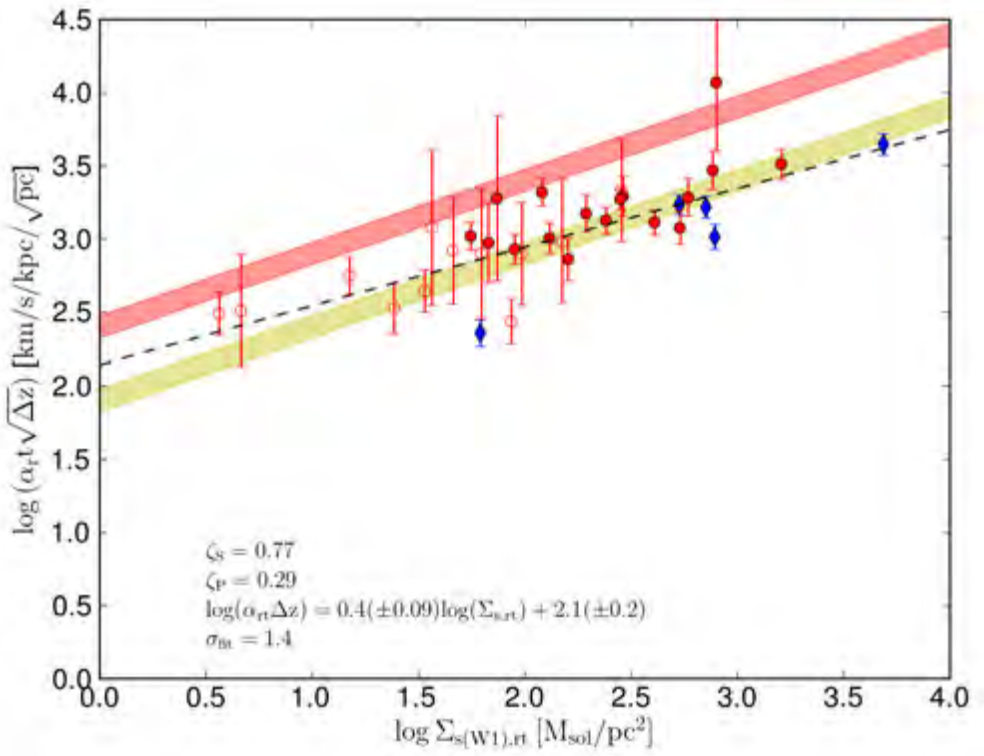

Figure 5.12: Product of $\sqrt{\Delta z}$ and the velocity gradient plotted against the stellar surface density (calculated from W1 observations) at r_t. Symbols are the same as Figure 5.1. The Class 2 and 3 galaxy gradients were calculated using the multi-polynomial method. The best linear fit to the data is shown as a black dashed line. The yellow shaded region shows a model where m_s ranges from 0.5 to 1.0 and $f_b = 1$. The red shaded region shows a model where m_s ranges from 0.5 to 1.0 and $f_b = 0.1$.

rising rotation curve to r_t. This is chosen because the model assumes a linearly rising rotation curve.

A plot of $\log \alpha_{rt}$ and $\mu_{W1,rt}$ is shown in Figure 5.11. From it I see that the slope of the linear fit to the data is -0.15 ± 0.02, $\sigma_{fit} = 0.28$, and the correlation coefficients are $|\zeta_S| = 0.59$ and $|\zeta_P|$=0.63. The fitted linear relation has a slope similar to the slope found for the data measured at $r = 0$ and the σ_{fit} values are similar. The correlation between the parameters is slightly weaker than at $r = 0$. Hence the α versus Σ_{W1} correlation holds at the turnover radius with a power law index somewhat lower than predicted by the model but similar to that found at $r = 0$. The relation was tested at larger radii and at $3r_t$, the slope is close to zero while the correlation between α and

S_{W1} is much weaker than it is at low radii. Figure 5.6 was re-made for parameters measured at $r = r_t$ and the result is shown in Figure 5.12. The slope of the relation is lower and the correlation coefficients weaker than for parameters measured at $r = 0$. At r_t the galaxies in our sample are consistent with models that have $f_b = 1$ to $f_b = 0.1$, this is lower than what was found at $r = 0''$. Σ_s is lower and more weakly correlated with the gravitational potential well at r_t than it is at $r = 0$.

Table 5.2: Stellar Surface Densities of the Sample.

Galaxy	RC	α_0	R-band			W1		
			$\mu_{R,0}$	$\Sigma_{s,0}$	l_s	$\mu_{W1,0}$	$\Sigma_{s,0}$	l_s
1	2	3	4	5	6	7	8	9
J0034-08	2	55.08 (10.41)	-	-	-	18.83	3.09	6.24
J0040-13	2	153.92 (42.19)	-	-	-	17.87	3.94	1.22
J0112+00	2	23.25 (10.81)	-	-	-	20.73	2.67	1.60
J0130-22	2	50.80 (8.73)	-	-	-	19.98	2.66	4.96
J0140-05:S1	1	39.96 (8.86)	23.71	0.58	1.46	24.30	1.42	1.17
J0140-05:S2	2	33.33 (11.09)	22.66	1.19	4.45	23.02	1.92	4.34
J0223-21	3	175.35 (26.86)	-	-	-	18.53	3.25	2.51
J0230-02:S1	2	143.68 (36.33)	19.38	3.04	15.22	18.89	3.08	10.56
J0230-02:S2	1	9.87 (1.80)	22.48	1.45	6.88	22.86	1.86	5.81
J0239-08	2	189.45 (73.39)	-	-	-	19.74	2.80	2.62
J0241-06	2	54.98 (11.52)	-	-	-	21.22	2.42	2.45
J0246-07	2	146.45 (31.46)	-	-	-	18.26	3.20	2.18
J0249-02	2	15.79 (3.75)	23.94	0.57	2.85	24.49	1.16	2.43
J0404-02	2	49.06 (42.78)	21.29	1.88	3.03	21.23	2.36	2.65
J0441-02	3	173.38 (32.68)	19.04	2.87	1.47	18.36	3.44	1.08
J0504-16:S1	3	13.26 (3.18)	21.06	2.06	4.71	21.46	2.20	4.51
J0935-05	1	7.76 (1.41)	23.10	0.92	2.53	23.24	1.20	1.96
J0942+00	1	94.36 (14.33)	19.28	2.88	4.81	19.30	2.96	4.63
J0943-05b	2	24.42 (38.29)	-	-	-	21.05	2.46	4.86
J1002-06	2	25.67 (5.43)	23.74	0.63	2.32	23.61	1.69	1.93
J1005-16:S1	2	89.21 (19.91)	20.90	2.26	10.04	19.96	2.62	8.12
J1005-16:S3	1	45.57 (13.72)	20.72	2.30	5.50	19.78	2.65	4.78
J1026-19:S1	2	45.03 (13.56)	20.25	2.61	8.04	20.49	2.53	7.87
J1039+01	1	111.38 (19.87)	21.94	1.31	0.61	22.32	2.10	0.75

Continued on next page

Table 5.2 – continued from previous page

Galaxy	RC	α_0	R-band			W1		
			$\mu_{R,0}$	$\Sigma_{s,0}$	l_s	$\mu_{W1,0}$	$\Sigma_{s,0}$	l_s
1	2	3	4	5	6	7	8	9
J1041-23	2	19.94 (5.20)	22.19	1.42	3.00	22.22	2.24	2.66
J1042-23	2	53.89 (107.25)	21.93	1.52	2.18	22.26	1.80	2.15
J1103-23:S1	2	123.79 (24.77)	20.57	2.31	6.62	19.66	2.81	5.06
J1103-23:S2	2	73.98 (91.90)	-	-	-	20.15	2.75	3.43
J1105-00	3	381.24 (63.70)	19.66	2.76	4.01	16.57	4.13	3.21
J1107-17	2	110.97 (41.26)	22.14	1.25	0.82	22.45	1.99	0.85
J1127-04	2	18.88 (17.73)	23.30	0.74	1.25	24.14	1.34	1.31
J1130-16	2	88.37 (48.06)	22.59	1.15	2.82	22.52	1.98	2.12
J1147-16	2	59.90 (10.20)	19.26	2.85	4.14	19.00	3.21	3.88
J1157-15	2	13.87 (3.99)	22.06	1.40	1.42	22.19	2.22	1.31
J1217+00	1	14.75 (2.51)	25.22	-0.04	2.66	24.07	0.87	1.63
J1253-12	1	14.23 (2.83)	22.95	0.95	2.01	23.66	1.21	1.87
J1255+00	2	24.08 (5.63)	21.36	1.85	4.43	21.63	2.23	4.69
J1300-13:S1	2	131.10 (27.54)	18.95	3.04	6.20	19.20	3.31	5.73
J1326+02A	2	236.86 (313.18)	-	-	-	20.29	2.55	1.76
J1338-09	1	21.77 (3.48)	21.43	1.87	4.82	20.99	2.48	3.47
J1403-06:S1	2	95.70 (23.59)	19.61	2.78	8.41	19.30	2.95	7.13
J1403-06:S2	3	105.63 (36.34)	19.03	3.10	8.89	18.89	3.06	7.85
J1423+01	2	73.84 (15.28)	20.88	2.07	4.58	21.05	2.29	4.49
J1442-08	2	20.33 (4.58)	21.55	1.92	6.50	19.91	2.65	4.52
J1447-17	2	19.37 (3.58)	21.53	1.93	9.05	20.58	2.27	6.83
J1500+01	2	533.09 (181.08)	18.89	3.02	4.27	18.46	3.45	4.06
J1509-11:S1	2	85.74 (14.74)	20.03	2.63	7.58	19.56	2.68	6.38
J1609-04	2	24.79 (9.23)	22.10	1.33	1.04	22.58	1.74	1.18
J1621-02	2	90.70 (16.53)	20.16	2.57	12.05	20.13	2.81	10.52
J2025-24	3	66.45 (21.63)	18.55	3.36	11.60	18.21	3.34	9.64
J2056-16	1	16.24 (2.94)	23.16	0.88	1.66	24.15	1.48	2.10
J2102-16	2	35.13 (5.88)	21.39	1.95	5.40	21.31	2.43	5.50
J2142-06	2	44.98 (12.05)	22.40	1.25	1.56	22.96	1.70	1.74
J2202-20:S1	2	50.41 (8.35)	19.35	3.00	14.82	19.29	3.24	13.57
J2205-22	2	17.88 (22.27)	-	-	-	-	-	-
J2234-04	1	27.84 (14.40)	23.11	0.94	2.63	23.71	1.31	2.60

Comments: 1: SINGG galaxy name; 2: Galaxy Class; 3: Central velocity gradient in [km/s/kpc] units, with uncertainty in parentheses; 4: R-band central surface brightness in [ABmag/arcsec^2] units; 5: R-band central stellar surface density in [$M_\odot$/pc^2] units; 6: R-band scale length in [kpc] units; 7: W1 central surface brightness in [ABmag/arcsec^2] units; 8: W1 central stellar surface density in [$M_\odot$/pc^2] units; 9: W1 scale length in [kpc] units.

5.3 Rotation Curve Uncertainties

One of the limitations for the analysis is the rotation curve sampling. Sampling of the rotation curve is limited by the fiber size and the coverage of the fibers. The best sampled rotation curves have 5″ sampling. Most of the galaxies in the sample are at distances between 10 Mpc to 25 Mpc. 5″ sampling for galaxies at these distances is a physical distance of 0.24 kpc - 0.6 kpc. Most of this analysis is on the inner gradients of the rotation curves, these are where the rise of the rotation curve is steepest. Good sampling of the rising part of the rotation curve is very important in order to obtain accurate gradients despite the large changes in velocity. In some cases the rise is so steep and the turnover radius so small that the rise is only sampled by a single point or none. Therefore the inner gradients can have large uncertainties and can be highly dependent on the assumed shape of the rotation curve. In the extreme case where there are no points that sample the rising part of the rotation curve, the gradient determined from the fit is a lower limit of the actual gradient. If they are treated only as lower limits then the real power law index of the α and μ relation is likely higher than what was fitted in the analysis. In cases when the rising part of the rotation curve is sampled by multiple data points and part of the rotation curve that flattens out its shape can be well-approximated and fit by the arctan function (and the multi-parameter function). Gradients measured at large radii are much less dependent on the assumed shapes of the rotation curve. Therefore the gradients determined at the turnover radius and larger radii are the best constrained and their real uncertainties are closer to the uncertainties of the fits. In the inner regions the uncertainties diverge from the fitting uncertainties due to the sampling used and the reliance on assumed rotation curve shapes. However, α values measured at the turnover radius are also affected by rotation curve sampling and whether the rotation curve fully flattens off. Many of our galaxies do not flatten off completely and therefore their turnover radii are not well-constrained. The α_0 values used in the analysis are calculated using the multi-polynomial fit which assumes a linear rise in the inner part of the rotation curve. The method was shown to perform better than the arctan fit in galaxies with steeply rising rotation curves but similar in galaxies with slowly rising rotation curves which are well sampled. This linear assumption is good enough for this analysis and has been used by the similar studies of Lelli et al. (2013) and Erroz-Ferrer et al. (2016).

Galaxies with weak emission, low inclinations, low rotation amplitudes and patchy emission are also problematic because they have large uncertainties in the rotation

velocities or have very erratic (i.e., have large increases and decreases in velocity as the radius changes) rotation curves. These result in large uncertainties in the fits and velocity gradients. Most of the galaxies that are strongly affected by this are dwarf galaxies which have low $S_{H\alpha}$ and $S_{R,0}$ values. This is the same part of the parameter space where Class 1 galaxies dominate, therefore faint Class 1 galaxies tend to have low α values compared to the Class 2 and 3 galaxies with similar $S_{H\alpha}$ values. Distance uncertainties can result in large uncertainties in the velocity gradients, this mostly affects the nearest galaxies in our sample. I therefore used a conservative 15% uncertainty in the distances. More accurate distance measurements and better constraints on the distance uncertainties would help to improve my tests of the model.

The rotation curve analysis assumes that the gas moves in circular orbits, however observations of the gas of galaxies show that non-circular motions are prevalent within galaxies (e.g., Trachternach et al. 2008). Star formation and heating of gas from stars injects kinetic energy into the ISM and this results in non-circular motions. Structures such as bars and spiral arms cause non-circular motions within galaxies (Swaters et al. 2003). Non-circular motions add uncertainties to the rotation curves of galaxies (e.g., Swaters et al. 2003, Trachternach et al. 2008, Oh et al. 2008). The high rates of star formation, presence of bars and low rotational velocities at small radii mean that non-circular motions can have a large effect on inner rotation curves (Swaters et al. 2003). Kinematic studies have been made to isolate and correct for such effects (e.g., Trachternach et al. 2008 and Oh et al. 2008). The non-circular motions and effects due to star formation feedback are difficult to model in central regions. These analysis were performed on observations with fully sampled velocity fields with velocity resolution higher than in this study. Bars are found in the inner regions of galaxies, cause streaming motions in the gas and can be the source of large scale non-circular motions in the inner parts of galaxies. Software such as DISKFIT can be used to model them (e.g., Kuzio de Naray et al. 2012), however, the fiber sampling is too sparse to allow for accurate modeling of non-circular motions due to bars with DISKFIT. The effect of a bar on the inner rotation curve depends on its strength and orientation (e.g., Sellwood & Sánchez 2010, Randriamampandry et al. 2015, 2016). Randriamampandry et al. (2015, 2016) showed that the bar orientation relative to the kinematic major axis can cause either over or underestimation of the circular velocities measured by rotation curve software. Bars that are aligned with the major or minor axes have the greatest effect on the observed rotation velocities. They found that tilted ring analysis using ROTCUR could underestimate or overestimate inner rotation velocities in barred galaxies by up to 40% for the aforementioned bar orientations and that even DISKFIT is unable to realistically model bars in these orientations (Randriamampandry et al.

2016). About ∼20 galaxies in Figure 5.1 have been identified as having bars. Modeling and studying bars and their effects on rotation curves is beyond the scope of this analysis. The bars in the inner regions can cause increases or decreases in the observed α_0, however most of the galaxies with bars are close to the best fit relation in Figure 5.1 and 5.5.

The interactions between gas clouds result in non-circular motions that affect the observed line of sight velocities and measured velocity dispersion of the Hα (Binney & Tremaine 2008). This results in lower circular velocities than isolated particles would have if they were under the same gravitational potential (Binney & Tremaine 2008). Assuming galaxies with cylindrical isotropic rotation, constant scale height and Sérsic profile (Sérsic 1963) the asymmetric drift corrected velocity was shown to be :

$$V^2 = V_{un}^2 + \sigma_{obs}^2 \left(\frac{b_n}{n} \left(\frac{r}{r_e} \right)^{1/n} - 2 \frac{d\, ln(\sigma_{gr})}{d\, ln(r)} \right), \tag{5.9}$$

by Lelli et al. (2014); where V_{un} is the uncorrected velocity, σ_{obs} is the velocity dispersion, n is the Sérsic index, and b_n is a constant that depends on n (Ciotti 1991, Ciotti & Bertin 1999). For galaxies with exponential surface brightness profiles $n = 1$ and $b_1 = 1.678$. For a constant σ_{gr} (physical dispersion) the asymmetric drift-corrected velocity reduces to:

$$V^2 = V_{un}^2 + {\sigma_{gr}}^2 (r/l_s), \tag{5.10}$$

where $l_s = 1.678 r_e$. Therefore these corrections are radius and dispersion dependent. The dispersion used in this calculation is the dispersion that is due to the gravitational interactions and pressure due to turbulence, temperature gradients and other sources. Therefore the observed σ_{obs} must be corrected for instrumental broadening to become σ_{gr} before usage in the calculations. Due to the radial dependence the correction is smallest at small radii and most of the analysis is performed at $r \sim 0$, therefore the corrections are relatively small. Furthermore Erroz-Ferrer et al. (2016) showed that the resulting rotation curves after the correction was made were very similar to the uncorrected rotation curves. The typical maximum correction velocities for galaxies in their sample were $\sim 3 - 6\,\mathrm{km/s}$, these were at l_s which is much larger than the typical radii I study. And therefore these corrections would not have a large effect on the conclusions. It should be noted that small dwarf or irregular galaxies can have large dispersion values relative to their rotation velocities, and they can have thick disks, both which result in higher pressures and larger asymmetric drift (relative to the rotation velocity) compared to large galaxies. Therefore the velocity gradients of low mass galaxies have larger uncertainties due to such effects.

5.4 Stellar Surface Density Correlation with Mass

Tully et al. (1978), Broeils (1992), Côté et al. (2000) and Swaters et al. (2009) showed that the rotation curves of different kinds of galaxies have different shapes and that dwarf galaxies tend to have shallow and slowly rising rotation curves. In this study I have explored the relation between the slope of the central potential well and the central stellar surface density. If dwarf galaxies tend to have shallow rotation curves and more massive galaxies have steeply rising rotation curves, as seen in the aforementioned studies and others such as Erroz-Ferrer et al. (2016), this suggests that the total masses of galaxies and the central mass distributions of galaxies are linked. This is a complex relationship (e.g., Burstein & Rubin 1985) and Erroz-Ferrer et al. (2016) suggest that the relation they (and Lelli et al. 2013) find may be due to the relationship between total stellar mass and bulge mass. In this section I study the relationship between the inner potential well and the global properties of galaxies by comparing α_0 and other global properties of galaxies.

As mentioned before, W_{50} can be used as a proxy for the total mass of a galaxy through the TFR, however care should be taken because it needs to be corrected for the galaxy inclination. The HIPASS W_{50} values were corrected for relativistic broadening, instrumental broadening and smoothing and turbulent motion according to the procedure outlined in Meyer et al. (2008). I plotted $\log \alpha_0$ against W_{50} in Figure 5.13. $W50$ in the plots is corrected for inclination by dividing the uncorrected value by $sin(i)$, where i_O is used for Class 1 galaxies and i_D and i_R are used for Class 2 and 3 galaxies respectively. Galaxies in multiple systems were not included in the plot because they share a single HIPASS H I profile with other galaxies so their W_{50} values are not representative of their individual mass. The plot shows that α_0 correlates with W_{50}. The correlation coefficients for the plot are: $\zeta_S = 0.56$ and $\zeta_P = 0.23$, the probabilities of a null hypothesis are: $p_S = 0.00018$ and $p_R = 0.16$ respectively. There are similar results when $\log \alpha_0$ is plotted against V_{max}, but there was much larger scatter than found in the W_{50} plot and therefore the relation is less clear. The correlation is better than the W_{50} plot: $\zeta_S = 0.60$, $p_S = 9.72 \times 10^{-7}$, $\zeta_P = 0.58$ and $p_R = 2.52 \times 10^{-6}$. Measuring V_{max} for many of the galaxies in the sample can be problematic because many of them do not have rotation curves that completely flatten off due to the Hα emission being faint and having low filling factors at large radii. The rough increase in α_0 with increasing total mass is in agreement with dwarf galaxies having shallower

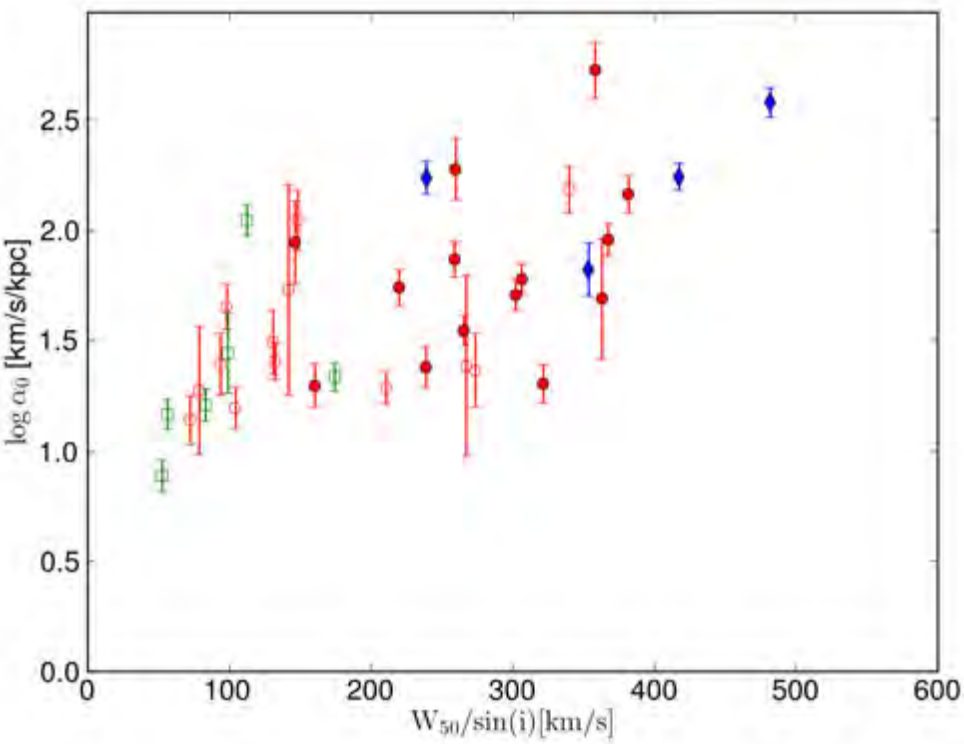

Figure 5.13: Central velocity gradient plotted against the inclination corrected W_{50}. Symbols are the same as in Figure 5.1.

velocity profiles than more massive galaxies.

It would be interesting to test whether the α_0 is correlated to the different mass components of galaxies. To test whether the mass-inner potential relation holds for different components of mass in galaxies here I plot α_0 is against H I mass in Figure 5.14 (as before HIPASS galaxies that are multiples are excluded) and stellar mass in Figure 5.15. There is no correlation between H I mass and α_0; the correlation coefficients and null hypothesis probabilities are: $\zeta_S = 0.20$, $p_S = 0.20$, $\zeta_P = 0.15$ and $p_R = 0.36$. The total stellar mass derived from W1 and W2 observations (using the relations from Cluver et al. 2014) is plotted against α_0 in Figure 5.15. The correlation coefficients null hypothesis probabilities for the plot are: $\zeta_S = 0.54$, $p_S = 2.13 \times 10^{-5}$, $\zeta_P = 0.50$ and $p_R = 9.30 \times 10^{-5}$. The plots show that there is a weak correlation between the total stellar mass and α_0. The highest density of stars is found in the inner parts of galaxies and the correlation with total stellar mass confirms and extends the results of the α_0, μ_0 and μ_{rt} plots to the entire stellar disk. Dwarf galaxies are expected to be dark-matter

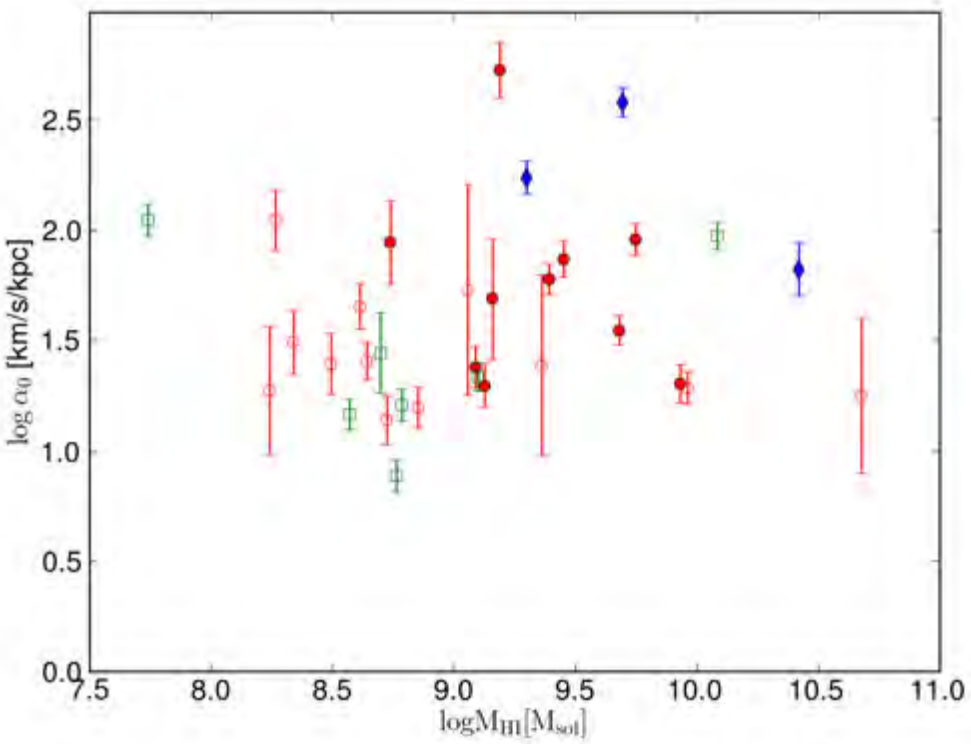

Figure 5.14: Central velocity gradient plotted against the H I mass. Symbols are the same as in Figure 5.1 and the gradients were calculated in the same way.

dominated therefore Figure 5.4 was re-plotted but with the data points colour-coded according to their total stellar masses in Figure 5.16. The plot shows that there is no correlation between the total stellar mass of a galaxy and its baryonic fraction. It is important to note that these are baryonic fractions of the galaxy center. This suggests that even in dwarf galaxies the central baryonic fractions can be very high. Oh et al. (2011) found that the baryonic fractions of the dwarf galaxies from their sample have roughly constant baryonic fractions for most of the disk, each galaxy having very different f_{bar} values ranging from 0.8 to 0.1. The f_{bar} values of these galaxies decline at low radii. Therefore our analysis of the central regions could be an extension of this trend, therefore leading to higher f_{bar} values in these galaxies than seen in Oh et al. (2011,2015).

5.5 Conclusion

There is a good correlation between Σ_s and α in the central regions of

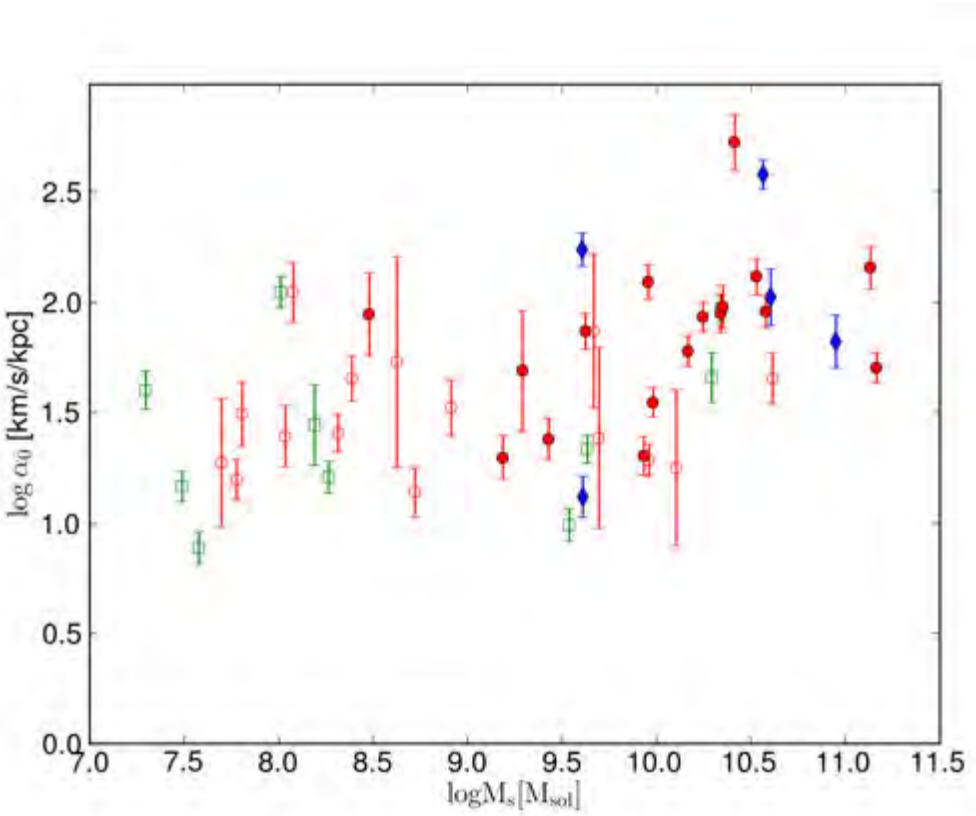

Figure 5.15: Central velocity gradient plotted against the stellar mass. Symbols are the same as in Figure 5.1 and the gradients were calculated in the same way.

galaxies and the power law index is close to 0.5, which is the theoretically expected value. The $W1$ values have a tighter correlation and are closer to the theoretical values than the R-band observations, good correlations using both bands confirm that the R-band is a good tracer of the stellar surface density. The product of the velocity gradient and square root of the galaxy scale height is tightly correlated to the stellar surface density. **The correlations suggest that the stellar surface density has a strong effect on the inner gravitational potential well**. I found that most galaxies have baryonic fractions that range from 0.1 to 1 in their central regions. The central f_b values are not very well constrained but **a large fraction of galaxy centers can be modeled by f_b values close to 1** and **the f_{bar} are not correlated with $\Sigma_{s,0}$ or the total stellar mass**. Baryonic fractions are higher when W1 observations are used, differences between the M/L calculations in the different bands are a large contributing factor to the differences in f_b. For the W1 analysis many galaxies have lower $\alpha_0 \Delta z$ than can be explained by the model, this is likely due to overestimation of Υ_s and underestimation of Δz. The correlation between Σ_s and α weakens with increasing radius and the power law index decreases. This is expected

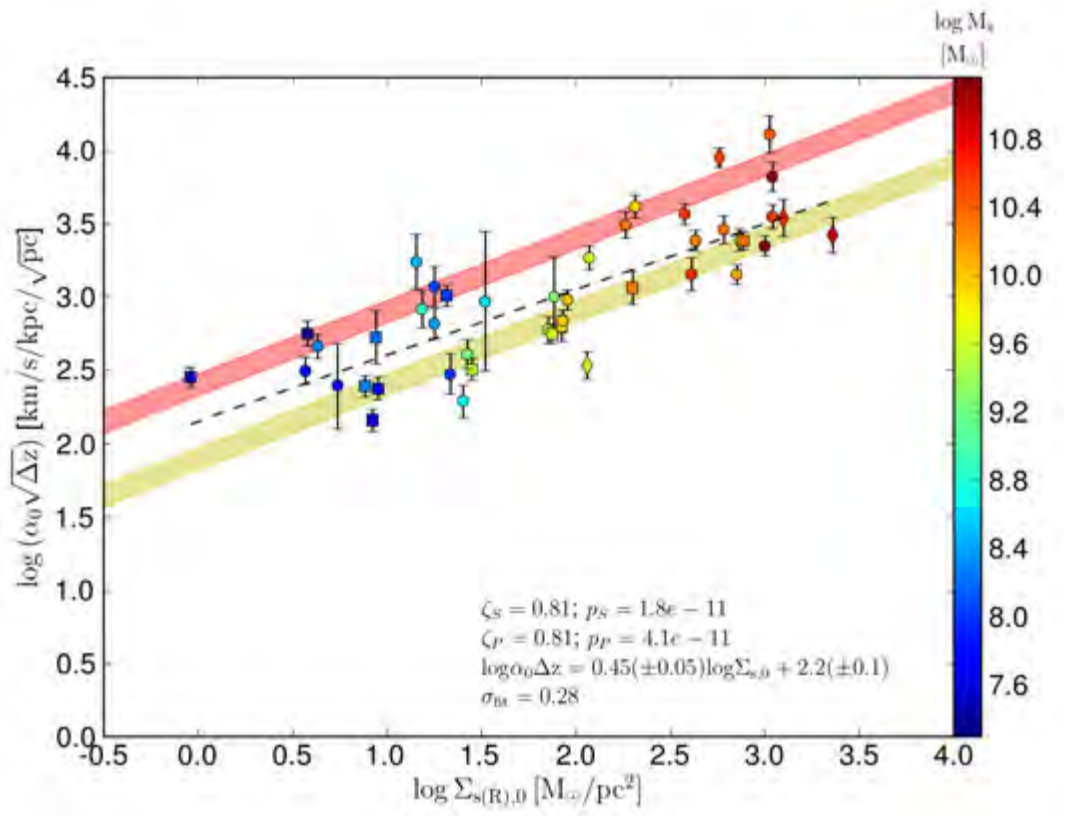

Figure 5.16: Product of $\sqrt{\Delta z}$ and the central velocity gradient plotted against the central stellar surface brightness (calculated from R-band observations). The symbols, dashed line and how the α_0 values were calculated are the same as Figure 5.1. The data points are colour-coded according to their stellar masses. The yellow shaded region shows a model where m_s ranges from 0.5 to 1.0 and $f_b = 1$. The red shaded region shows a model where m_s ranges from 0.5 to 1.0 and $f_b = 0.1$.

and is due to the increasing fraction of dark matter at larger radii. Better constraints on α, Δz and M/L will help to improve the constraints on f_b as the f_b values are still largely unconstrained. Galaxies with steep inner potential wells tend to be more massive and have larger stellar masses than galaxies with shallow potential wells. This indicates that the processes that shape the inner potential well are affected by or affect the total stellar mass and the mass of the dark matter halo of the galaxy. This may be due to more massive galaxies having more massive bulges which cause steeper inner potential wells, this disagrees with what Burstein & Rubin (1985) found but it agrees with studies such as Corradi & Capaccioli (1990), Casertano & van Gorkom (1991), Broelis (1992), Verheijen (1997), Swaters (1999), Lelli et al. (2013) and Erroz-Ferrer et al. (2016).

Chapter 6

The Link Between Star Formation and Galaxy Dynamics

For a galaxy with a purely gaseous disk (i.e., where the single fluid disk stability parameter Q_g applies) with a constant stability parameter Q_g, a linearly rising rotation curve and whose star formation follows the Kennicutt (1998) $\Sigma_{\rm SFR} \propto \Sigma_g/t_{orb}$ star formation law, its central star formation surface density $\Sigma_{\rm SFR,0}$ can be described by the following relation:

$$\Sigma_{\rm SFR} = \frac{\epsilon_{orb}\sigma_g}{\pi^2 G Q_g}\alpha^2. \tag{6.1}$$

where α_0 is the central velocity gradient, ϵ_{orb} is the orbital timescale and σ_g is the velocity dispersion of the gas. Equation 6.1 can be linearized to:

$$\log \Sigma_{SFR} = C_3 \log \alpha + C_4, \tag{6.2}$$

where $C_3 = 2.0$ and $C_4 = \log\left(\frac{\epsilon_{orb}\sigma_g}{\pi^2 G Q_g}\right)$, and C_3 is constant. For this analysis we assume that ϵ_{orb}, Q_g and σ_g are constant, therefore C_4 is assumed to be constant. The relation will be tested using different star formation tracers : Hα, 22 μm , and a combination of these two. The 22 μm is measured by the WISE W4 band and arises from dust re-emitting UV radiation from hot stars. The W3 band which is centered at 8 μm is dominated by emission from polycyclic aromatic hydrocarbons (PAHs) and will also be used to study the near-infrared based star formation. As before the central velocity gradients of the Class 2 and Class 3 galaxies are determined using the multi-polynomial method, whilst the Class 1 velocity gradients are determined from the 3D Plane fit and using optical photometric inclinations. The central surface brightnesses are determined by interpolating the interior surface brightness profiles to $r = 5''$ and all fits in this chapter are performed with the KMPFIT package. The star formation recipes used to convert central Hα and 22 μm surface densities ($S_{H\alpha,0}$ and $S_{W4,0}$ respectively)

into $\Sigma_{\rm SFR,0}$ are scaled to the same initial mass function and are described in Chapter 4. The Q_g is tested using the different tracers in Section 6.1, and the differences found between them are discussed. Velocity gradient - star formation relations from models that use stability parameters derived from both the gas and stellar disks Q_{WS} were also developed. These models relate α_0 to $\Sigma_{\rm SFR,0}$, $\Sigma_{s,0}$ and l_s and are tested in Section 6.2.

6.1 Single Fluid Q

6.1.1 Optical Hα $\Sigma_{\rm SFR}$ Analysis

The constant Q_g star formation model for a single fluid gas disk with a constant σ_g and ϵ_{orb} predicts that $\Sigma_{\rm SFR} \propto \alpha^2$. The relation will be tested in the central regions of galaxies. In this subsection Hα emission will be used to test the relation. The Hα observations were made as a part of the SINGG survey. Hα is used as a tracer of SFR and Equation 4.20 is used to calculate $\Sigma_{\rm SFR}$ from $S_{H\alpha}$. A description of the Hα data and how the surface densities were calculated and converted in to $\Sigma_{\rm SFR,0}$ values is found in Chapter 4. In order to test the relation the central velocity gradient α_0 is plotted against the central $S_{H\alpha}$ ($S_{H\alpha,0}$) in Figure 6.1. The equivalent $\Sigma_{\rm SFR,0}$ values are shown in the plot. The Spearman and Pearson's correlations between $\log \alpha_0$ and $\log\Sigma_{\rm SFR,0}$ ($S_{\alpha,0}$) and their associated probabilities for a null hypothesis were also calculated. The correlation coefficients between $\log \alpha$ and $\log\Sigma_{\rm SFR}$ are: $\zeta_S = 0.40$ and $\zeta_P = 0.44$, the associated probabilities of a null hypothesis are $p_S = 7.6 \times 10^{-3}$ and $p_P = 2.9 \times 10^{-3}$. Equation 6.2 was fitted to the data. Fitting the equation results in a direct fit of the power law index for the relation and the y-intercept provides a method to determine the values of Q_g, σ_g and η_{orb}. A tight correlation between α_0 and $\Sigma_{\rm SFR}$ would indicate that the parameters are constant as assumed in the model. The linear fit yielded $C_3 = 5.1 \pm 1.6$ and $C_4 = -16.3 \pm 5.6$ and $\sigma_{\rm fit} = 1.7$. The correlation coefficients are weak and the fitted C_3 is much higher than the theoretical value: 2 from our constant Q_g, t_{orb} star formation model. J1103-23:S1 has the highest $\Sigma_{\rm SFR,0}$ of any galaxy in Figure 6.1, it is discussed further in Section 6.1.4. If this galaxy is removed from the analysis a linear fit to the data yields $C_3 = 4.1 \pm 1.4$, $\sigma_{\rm fit} = 1.4$, but lower correlation coefficients.

Hα SFR uncertainties

$S_{H\alpha,0}$ values are determined by interpolation to $5''$ in the interior surface brightness profiles, therefore the behaviour of the inner surface density profiles have a large effect

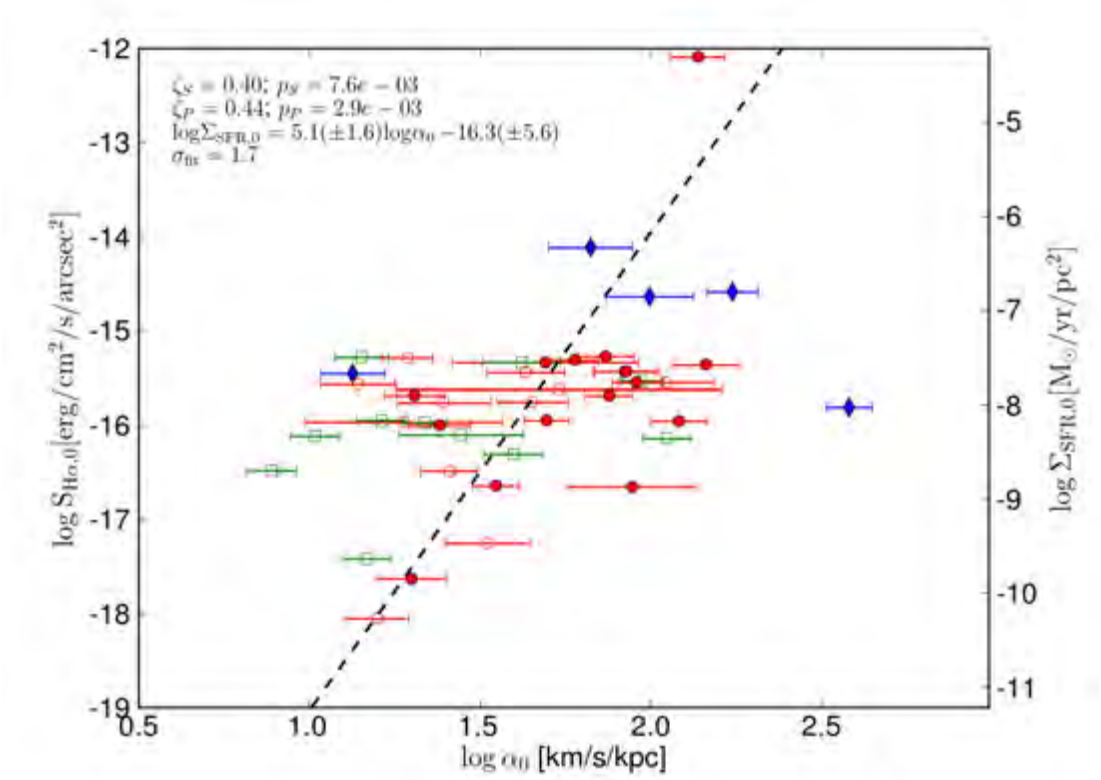

Figure 6.1: Central Hα surface brightness and $\Sigma_{\rm SFR}$ plotted against the central velocity gradient. Symbols are the same as Figure 4.2. The best linear fit to the data is shown as a dashed line.

Table 6.1: Best fit linear ($\log\Sigma_{SFR} = C_3\log\alpha + C_4$) parameters and correlation coefficients for the data of different star formation tracers.

Source	No. of gals	C_3	C_4	ζ_S	ζ_P	$\sigma_{\rm fit}$
Hα: WIYN	43	5.1 ± 1.6	-16.3 ± 5.6	0.40	0.44	1.7
W4: WIYN	53	3.7 ± 0.8	-14.5 ± 3.6	0.49	0.53	1.2
W3: WIYN	53	3.4 ± 0.7	-14.0 ± 3.3	0.54	0.56	1.1
Hα + W4: WIYN	43	3.9 ± 1.0	-14.4 ± 4.1	0.51	0.52	1.3

on $S_{H\alpha,0}$. Hα profiles show more variation than R-band surface brightness profiles. Examples of $S_{H\alpha}$ and S_R profiles are shown in Figures 6.2 to 6.5, these are plots of $S_{H\alpha}$ versus the semi-major axis radius. The figures show the different behaviours of $S_{H\alpha}$ that are seen in our galaxy sample. The variations in $S_{H\alpha}$ mostly occur in the inner parts of galaxies, as shown in the case of J1500+01 (Figure 6.5) and J1338-09 (Figure 6.3). If the changes in $S_{H\alpha}$ are sharp (i.e., large changes in $S_{H\alpha}$ over a small

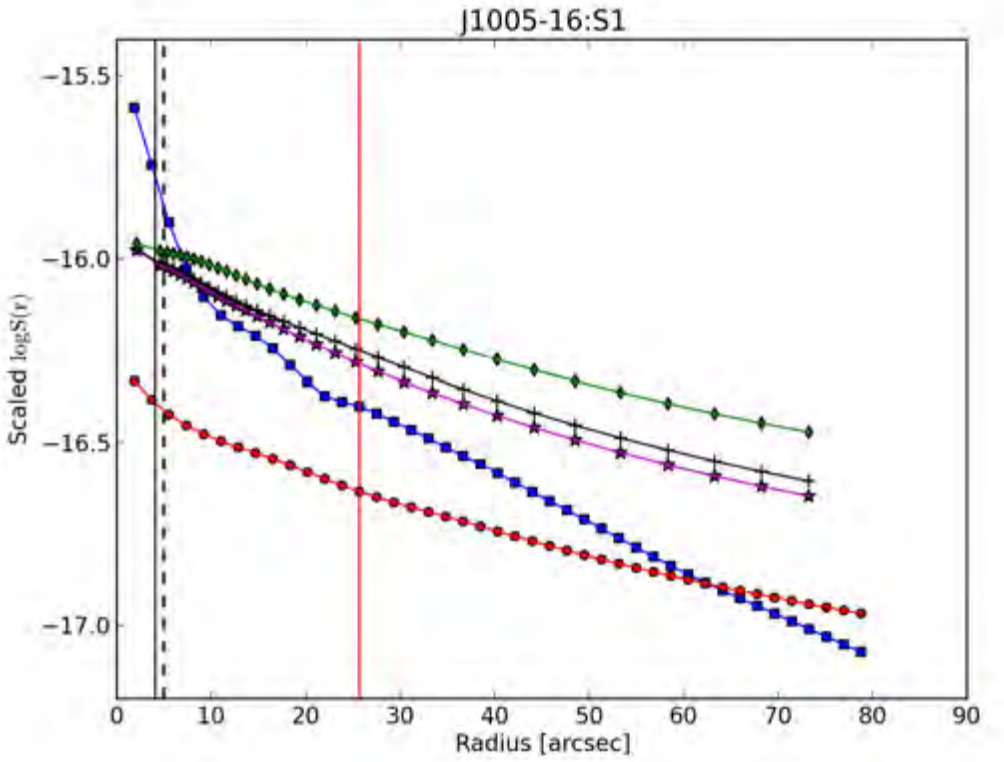

Figure 6.2: Radial interior surface brightness profiles of J1005-16:S1. The different observing bands are depicted as follows: $S_{H\alpha}$: blue squares , S_R: red circles, S_{W1}: magenta stars, S_{W3}: black crosses and S_{W4}: green diamonds. The red vertical line is r_e,the black vertical line is the r_t and the black vertical dashed line is $r = 5''$.

range in r) and they occur over the innermost few points ($r < 5''$) they can have a large effect on the interior $S_{H\alpha}$ at $r = 5''$. The magnitude of the $S_{H\alpha}$ decreases and the radii where the sharp decreases begin vary greatly across the sample. These variations contribute to the weakness of correlation between α_0 and $S_{H\alpha,0}$. Some galaxies have sharp increases in $S_{H\alpha}$ with decreasing r in their inner regions. The outer parts of the disk have smooth $S_{H\alpha}$ profiles and are more representative of an exponential disk than the inner parts. Some galaxies have large variations in $S_{H\alpha}$ throughout the disk (e.g., J1338-08, Figure 6.3). In most cases where there are large $S_{H\alpha}$ variations they occur in the inner regions of the optical disk. In order to test how much the sharp variations in the inner regions increase the non-correlation the following was done: $S_{H\alpha,0}$ was determined by linearly fitting and extrapolating from the outer part of the $\log S_{H\alpha}$ profile to $r = 0$". This was done for $r > r_e$ to avoid most of the large variations and departures from exponential disk behaviour. These $S_{H\alpha,0}$ values were plotted against α_0 in Figure 6.7. The plot has higher correlation coefficients than Figure 6.1: $\zeta_S = 0.51$

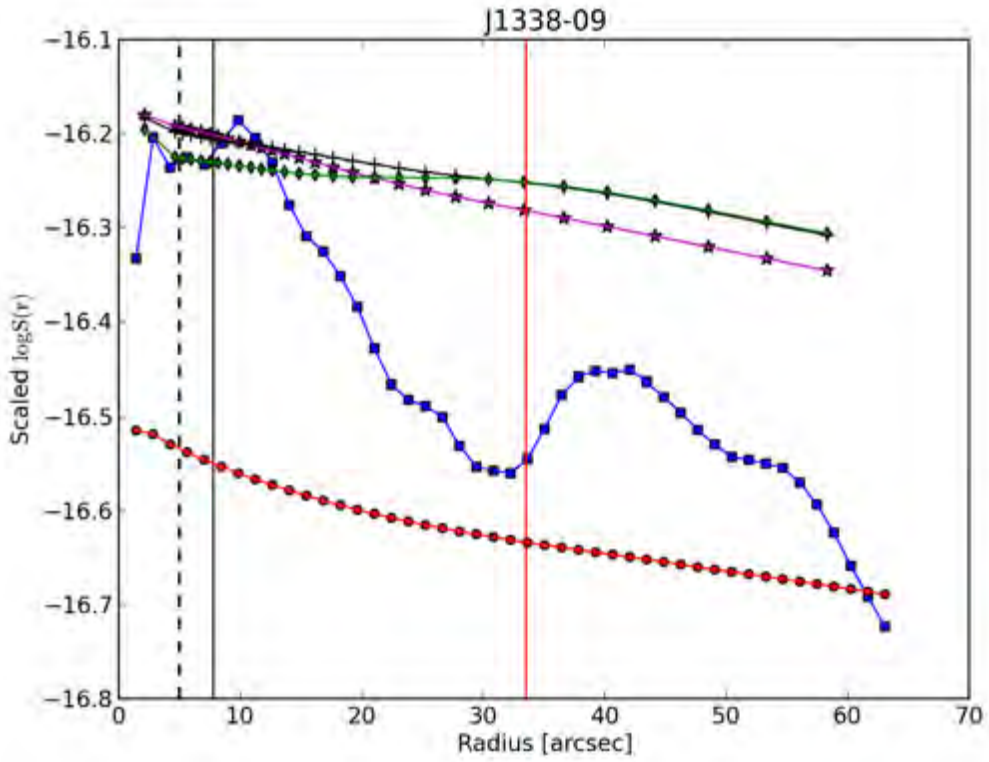

Figure 6.3: Radial interior surface brightness profiles of J1338-09. The different observing bands are depicted as follows: $S_{H\alpha}$: blue squares , S_R: red circles, S_{W1}: magenta stars, S_{W3}: black crosses and S_{W4}: green diamonds. The red vertical line is r_e,the black vertical line is the r_t and the black vertical dashed line is $r = 5''$.

and $\zeta_P = 0.46$. The slope of the best fit linear relation is $C_3 = 3.1 \pm 0.07$. This is closer to the slope predicted by the model than found when $\Sigma_{\mathrm{SFR},0}$ is determined by extrapolation from the inner points. The dispersion of the linear fit is $\sigma_{fit} = 1.0$, which is much smaller than when inner profile data are used. Therefore departures from exponential behaviour in the $S_{H\alpha}$ profiles contribute to weakening the correlation between α_0 and $S_{H\alpha}$ and they contribute to the high fitted power law index of the relationship. However it is clear from the surface density profiles that the exponential behaviour breaks down in the inner regions. These results indicate that if the inner regions follow the same exponential behaviour as the outer disk there is a better correlation between $S_{H\alpha,0}$ and α_0.

If smaller radii are used to measure $S_{H\alpha,0}$ then $S_{H\alpha,0}$ would be even more sensitive to the sharp variations at small radii and if larger radii are used the values would be less sensitive to the variations. Figure 6.8 shows the effect of determining $S_{H\alpha,0}$ at $r = 15''$.

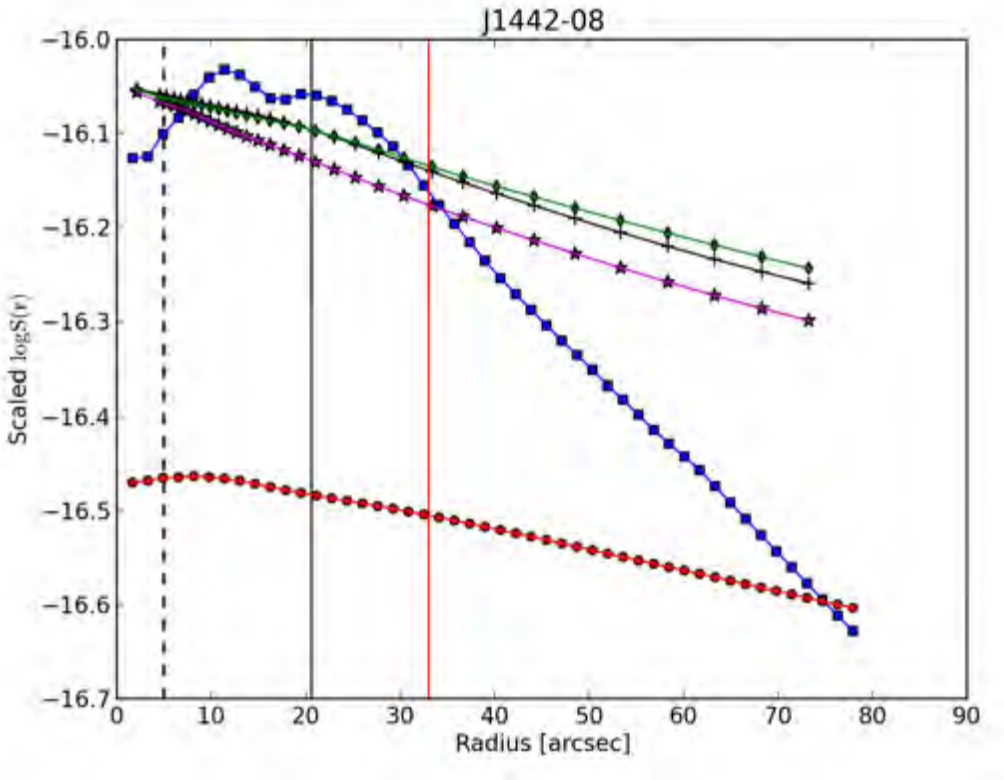

Figure 6.4: Radial interior surface brightness profiles of J1442-08. The different observing bands are depicted as follows: $S_{H\alpha}$: blue squares , S_R: red circles, S_{W1}: magenta stars, S_{W3}: black crosses and S_{W4}: green diamonds. The red vertical line is r_e,the black vertical line is the r_t and the black vertical dashed line is $r = 5''$.

That radius was chosen because it is ~ 3 times the width of a WIYN fiber and is the radius of the third point in the best sampled rotation curves. The slope of the best fit relation in the plot is $C_3 = 4.0 \pm 1.1$ and the correlation coefficients are $\zeta_S = 0.52$ and $\zeta_P = 0.47$. The tighter correlation and slope closer to the slope of the model than when compared to $S_{H\alpha,0}$ determined at smaller radii confirms that using larger radii reduces the effect of large $S_{H\alpha}$ variations. However, the linearly rising rotation curve assumption fails at large r for galaxies whose rotation curves have a turnover, therefore $S_{H\alpha,0}$ is calculated $r = 5''$. It is apparent from the figures that there are still some Hα variations at larger radii, which indicates that effects such as dust extinction are likely still important here. Much lower and more ″patchy″ star formation (e.g., spiral arms are patchier and more spread out) also contribute to the variation. These variations are smaller than the ones found in the inner regions due to the lower overall star formation rate in the outer regions.

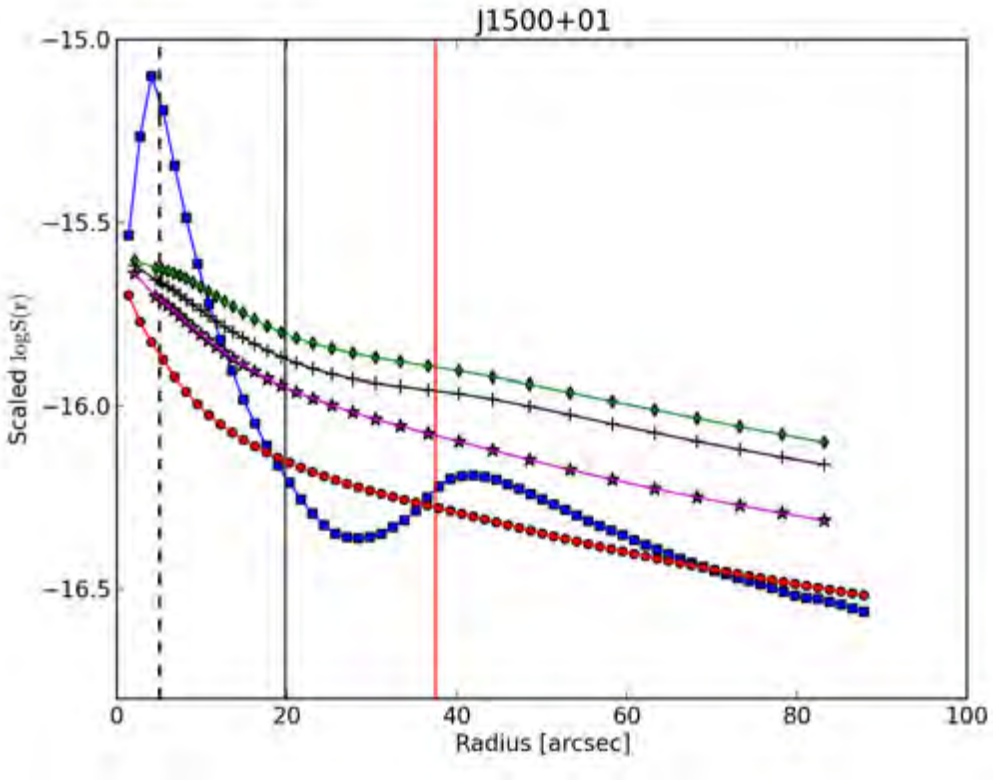

Figure 6.5: Radial interior surface brightness profiles of J1500+01. The different observing bands are depicted as follows: $S_{H\alpha}$: blue squares , S_R: red circles, S_{W1}: magenta stars, S_{W3}: black crosses and S_{W4}: green diamonds. The red vertical line is r_e,the black vertical line is the r_t and the black vertical dashed line is $r = 5''$.

The stability parameter Q_g is proportional to the velocity gradient and inversely proportional to the gas surface density Σ_g and is related to them by the following equation:

$$Q_g = \frac{2\sigma_g \alpha}{\pi G \Sigma_g}. \tag{6.3}$$

The surface brightness in Hα decreases in the inner regions of many of the galaxies and is below what is expected if the exponential behaviour of the outer disk extends to $r = 0''$. If Q_g is constant in these regions regions the decreases (with no concurrent decreases in α_0) suggest that the gas surface density decreases. Decreases in the gas surface density are likely an indicator that the gas transport is not high enough to fuel the star formation rates required to keep Q_g constant in these regions. If the fraction of gas used up in star formation remains constant the low gas transport would result in a Q_g that is not constant in these regions. The sharp increases in $S_{H\alpha}$ that occur in the inner parts of the surface brightness profiles indicate enhanced star formation, this would be caused by increased efficiency of star formation (i.e., fraction of gas converted

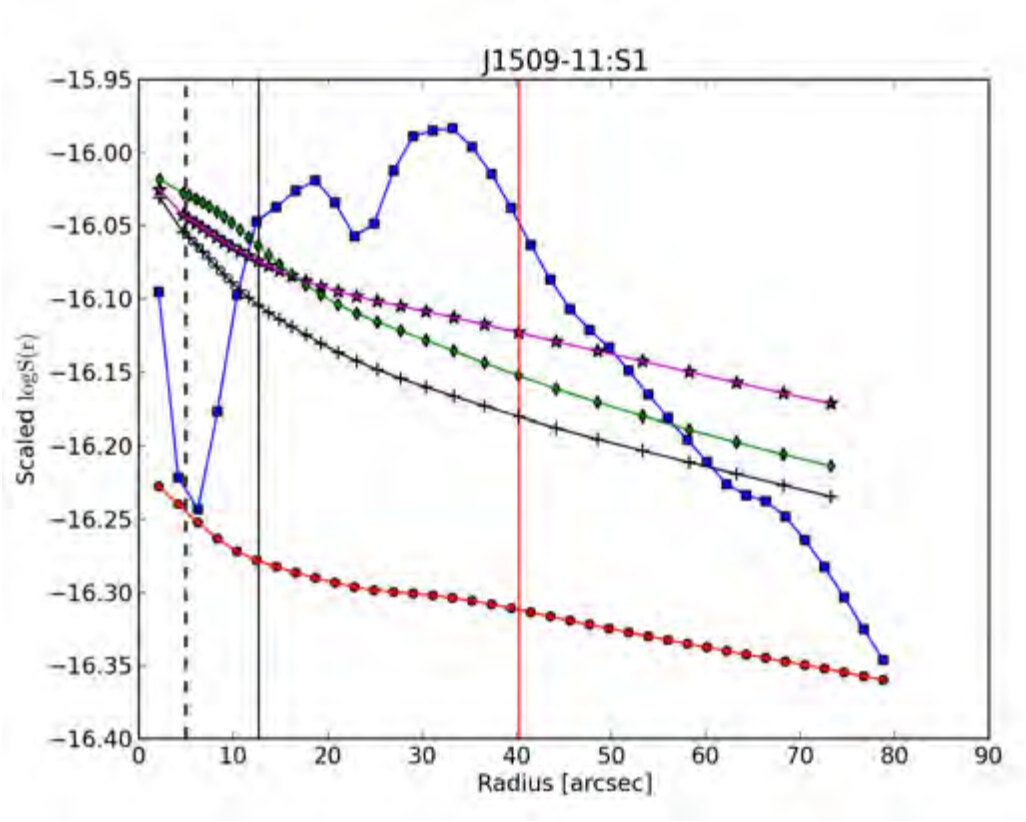

Figure 6.6: Radial interior surface brightness profiles of J1509-11:S1. The different observing bands are depicted as follows: $S_{H\alpha}$: blue squares , S_R: red circles, S_{W1}: magenta stars, S_{W3}: black crosses and S_{W4}: green diamonds. The red vertical line is r_e,the black vertical line is the r_t and the black vertical dashed line is $r = 5''$.

to stars) or more efficient gas transport into the galaxy centers. Q_g could remain constant while textbf$\Sigma_{\rm SFR}$ decreases if the star formation efficiency decreases, however as will be discussed later this does not seem likely. The large variations (increases and decreases) show that there are various dynamical processes that affect the distribution of star formation and their effects differ between galaxies. These variations could be due to feedback from ongoing star formation (e.g., McKee & Ostriker 1977, Dekel & Silk 1986, Dib 2011, Dib et al. 2013, Melioli et al. 2015), galaxy interactions (e.g., Hopkins et al. 2013), starbursts (e.g., Melioli & de Gouveia 2015) , efficient gas transport through bars or lack of efficient gas transport to the central regions of galaxies (e.g., Sheth et al. 2005, Saintonge et al. 2012). There are high densities of dust in the inner regions of galaxies, therefore dust obscuration can play a large role in the changes seen in the observed $S_{H\alpha}$ and could cause some of the apparent decreases in star formation measured by $H\alpha$ emission.

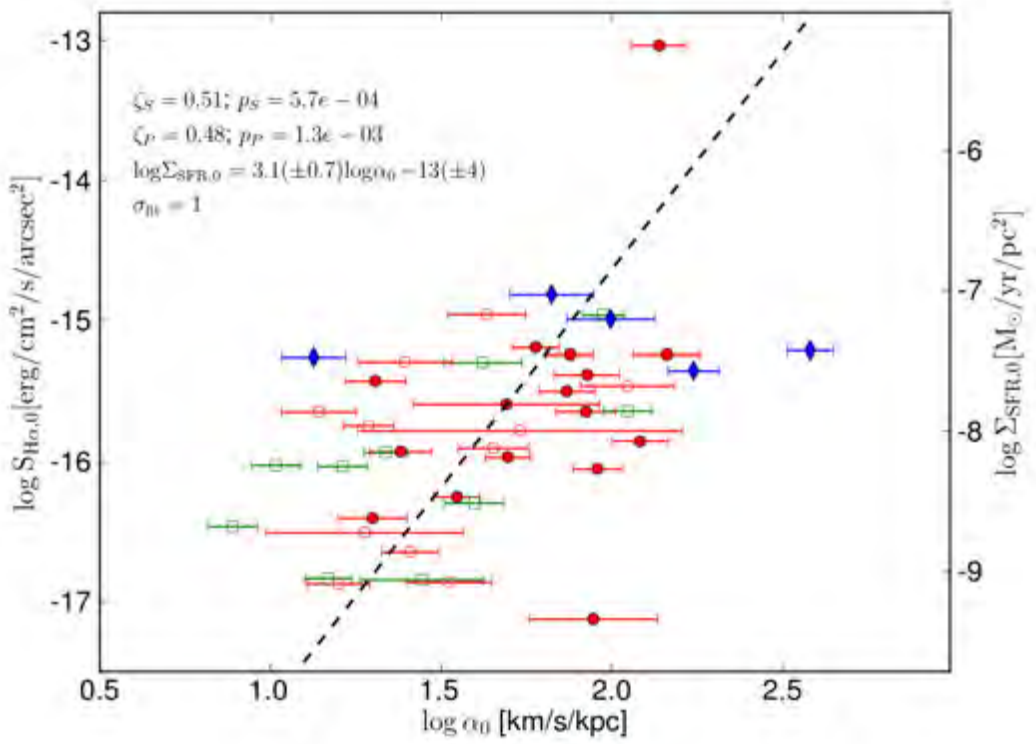

Figure 6.7: Same as Figure 6.1 but the central Hα surface brightness values were extrapolated from the outer ($r > r_e$) parts of the $S_{H\alpha}$ radial profiles.

As mentioned before, $S_{H\alpha}$ observations were corrected for dust obscuration by fitting the Balmer decrement as a function of the absolute magnitude (Helmboldt et al. 2004), and the corrections were tested by comparing the corrected values to FIR emission (Meurer et al. 2006). They results were broadly consistent with the FIR but there were some discrepancies between the FIR and the Hα. The FIR-Hα discrepancies are dependent on galaxy mass, and are greatest for dwarf galaxies. The dust correction applied to the Hα flux assumed a constant Balmer decrement and that all ionizing flux from the stars is captured by the surrounding H II. These assumptions can break down in regions with high dust obscuration, low metallicities and other ISM conditions that that are poorly modeled by the dust models used in assessing and determining the dust corrections. Therefore I also tested the model using mid-infrared star formation tracers which better trace star formation that is surrounded by dust.

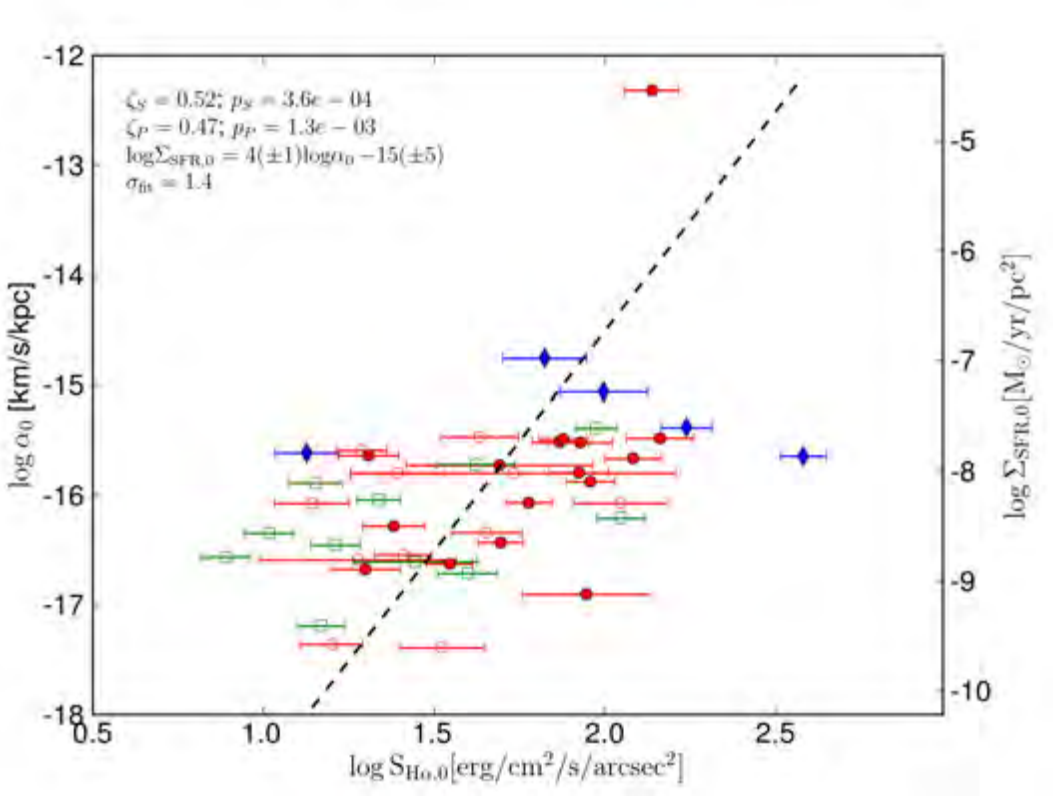

Figure 6.8: Central Hα surface brightness and $\Sigma_{\rm SFR}$ plotted against the central velocity gradient. The central surface brightnesses are calculated at $r = 10''$. Symbols are the same as Figure 4.2. The best linear fit to the data is shown as a dashed line.

6.1.2 WISE Mid-Infrared $\Sigma_{\rm SFR}$ Analysis

Ultraviolet emission emitted from hot young stars is absorbed by and heats up the surrounding dust. This dust re-emits the radiation at infrared wavelengths. The reprocessed light from the hot dust is a good tracer of star formation. Mid-infrared 22 μm dust emission is reprocessed light from hot young stars formed during high-mass star formation and can therefore be used as an indicator of star formation that is hidden by dust in star forming regions. In regions of high optical extinction this obscured star formation is not detected by using Hα and UV emission. The emission from hot young stars excites PAHs which emit mid-infrared radiation which is detectable via the $W3$ band. 11.3 μm PAH emission dominates this band and it is due to PAH excitation from UV radiation from hot young stars and radiation from older and more evolved stars. Cluver et al. (2013), Houck et al. (2007) and Farrah et al. (2007) showed how PAHs can be used to estimate star formation.

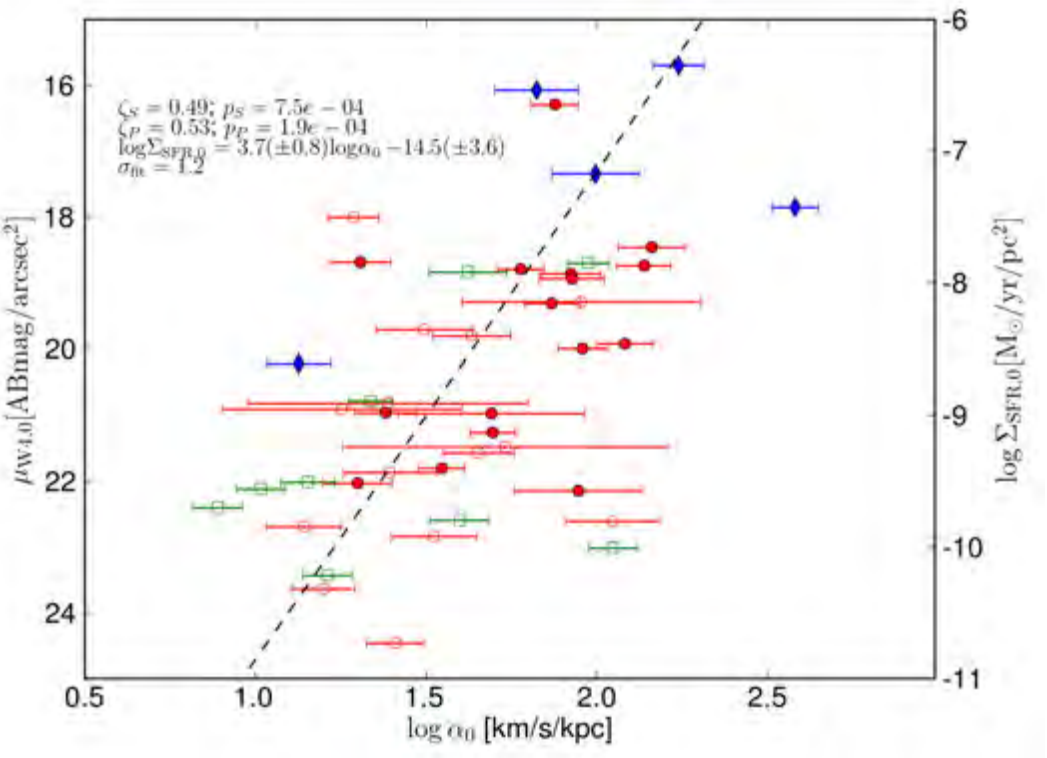

Figure 6.9: Central $W4$ surface brightnes (and $\Sigma_{\mathrm{SFR},0}$) plotted against the central velocity gradient in the same manner as Figure 6.1.

The internal dust correction which was fitted and implemented for Hα emission is based on a simple model which assumes a foreground screen (Helmboldt et al. 2004). When the model was tested by Meurer (2006) using FIR emission they found that the corrected Hα underestimated the FIR fluxes by a factor of 3-5. They attributed this difference to totally obscured star formation and bad stellar population models. A single dust correction value is used for an entire galaxy but there are large variations in conditions within galaxies. The fraction of obscured star formation varies within a galaxy and does not only depend on the stellar mass of a galaxy (whose proxy is M_R); the amount of dust in a galaxy is also related to the metallicity (e.g., Burstein & Heiles 1982, Skibba et al. 2011, Cortese et al. 2016). The observed Balmer decrement that was used in the Hα dust correction has been shown to not be constant in galaxies and is dependent on the stellar mass, stellar mass surface density, metallicity and the dust geometry (Wijesinghe et al. 2011, Boselli et al. 2013). Hα emission underestimates the total amount of star formation, and the fraction of obscured star formation that Hα emission is insensitive to is dependent on the amount of dust in star forming regions and its properties. The obscured star formation can be determined by studying the

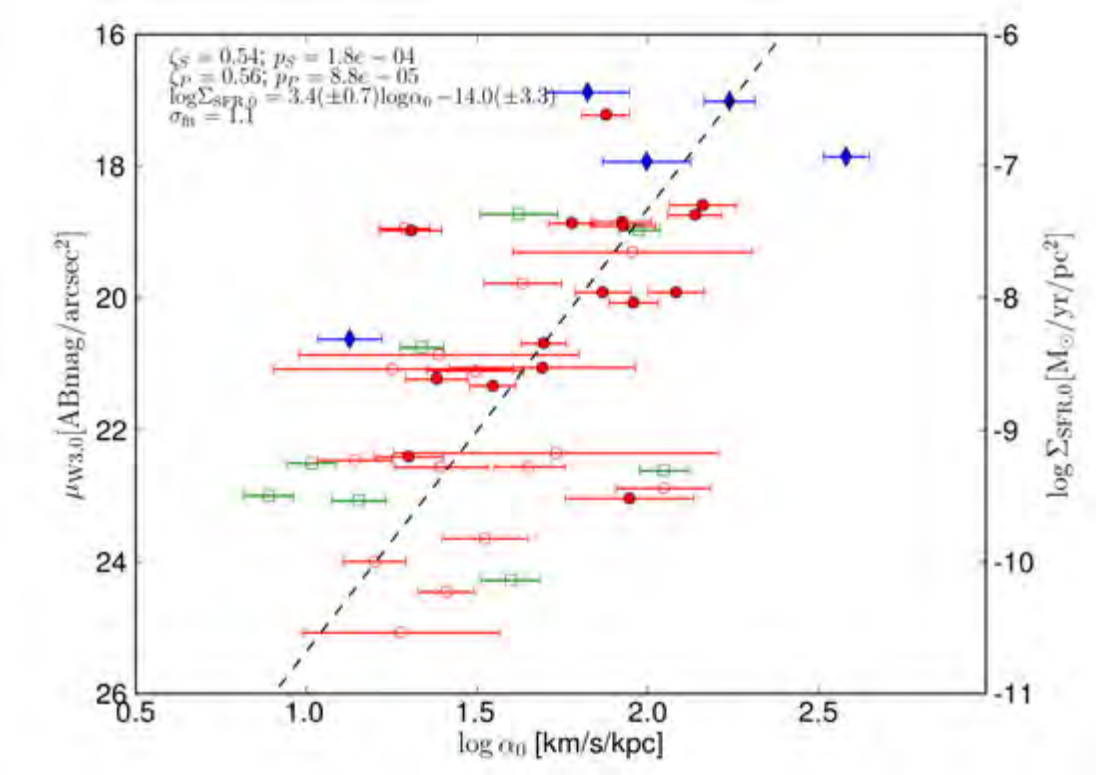

Figure 6.10: Central $W3$ surface brightness (and $\Sigma_{\rm SFR,0}$) plotted against the central velocity gradient in the same manner as Figure 6.1.

mid-infrared emission. W3 and W4 observations will be used to probe the obscured star formation and hence to test whether the α - $\Sigma_{\rm SFR}$ relation holds and whether the lack of a strong correlation correlation seen in Hα is due to dust obscuration.

Figure 6.9 is the equivalent of Figure 6.1 for $S_{W4,0}$ and $\Sigma_{\rm SFR}$ derived from W4 emission. Table 6.1.1 shows a comparison of the fitted values of the $S_{H\alpha,0}$ plots and that of WISE emission. The slope of the $\log\alpha_0$ and W4 derived $\Sigma_{\rm SFR,0}$ relation is 3.5 ± 0.06, and this is closer to the theoretical slope (2) than was found for the Hα. The fitted intercept is $C_4 = -14.4 \pm 3.0$. The correlation coefficients for the parameters are $\zeta_S = 0.55$ and $\zeta_P = 0.56$; the associated probabilities of a null hypothesis are $p_S = 1.7 \times 10^{-5}$ and $p_P = 1.1 \times 10^{-5}$. Therefore there is a tighter correlation and the power-law index is closer to the theoretical value than it was for the Hα. Star formation rates based on Hα emission are more adversely affected by extinction than those based on W4 emission. Therefore the weaker Hα correlation is in part due to dust obscuration in the inner parts of our galaxies.

The radial profiles of S_{W4} are smoother and less variable than $S_{H\alpha}$, part of the smoothness is due to the lower resolution of the W4 observations. But even in cases where there are large changes in $S_{H\alpha}$ over large radii the S_{W4} do not vary much. Examples of $S_{H\alpha}$ and S_{W4} profiles are shown in Figures 6.2 - 6.6. These show how little S_{W4} varies compared to $S_{H\alpha}$, this indicates that the large variations in $S_{H\alpha}$ are likely due to different amounts of dust obscuration within galaxy disks. The higher resolution in $S_{H\alpha}$ means that smaller local structures have greater effect on the $S_{H\alpha}$ profile than the case for S_{W4}. Dust obscuration generally varies on small scales such as over parts of giant molecular clouds, these can cause small scale variation in highly extinction-sensitive observations such as those of Hα and UV radiation.

Observations of the W3 band have better spatial resolution than the W4 observations ($3.5''$ versus $5.5''$) and can also be used to trace the star formation. Even though the W3 band has better spatial resolution and higher sensitivity (Jarrett et al. 2012), it does not trace star formation as well as W4 observations (Jarrett et al. 2013, Cluver et al. 2014). The 3.5" resolution of the $W3$ observations is closer to the seeing-limited resolution of the Hα, and like $W4$ the band is not strongly affected by dust extinction. The central velocity gradient is plotted against the W3-derived $\Sigma_{\rm SFR,0}$ in Figure 6.10. The slope of the relation is: 3.2 ± 0.5. The slope closer to the model value and lower but still consistent with the fitted slope found using the W4 band. The W3 data are slightly better correlated (e.g., $\zeta_S = 0.6$ compared to $\zeta_S = 0.5$) and the probability of null hypothesis are lower than for W4 data. J1103-23:S1 has the highest $\Sigma_{\rm SFR,0}$ of any galaxy in Figure 6.1, it is discussed further in Section 6.1.4 . If this galaxy is removed from the analysis a linear fit to the data yields $C_3 = 4.1 \pm 1.4$, $\sigma_{\rm fit} = 1.4$, but lower correlation coefficients. W3 and W4 emission being a good tracers of SFR and being relatively insensitive to dust extinction result in a slope in the relation that is closer to the theoretical value than Hα, and the lower resolution might contribute to the lower slope in the relation by averaging over local changes in the star forming regions.

Old evolved and unevolved stars also heat the dust and cause mid-IR dust emission (e.g., Hirashita et al. 2003, Kaneda et al. 2008, Buat et al. 2011). This contaminates IR star formation measurements because part of the flux that is assumed to be from star formation originates from dust heated by old evolved stars. Therefore the IR-calculated star formation rates overestimate the amount of star formation. The fraction of L_{IR} due to these old stars is still very uncertain and likely depends on the type of galaxy

and its star formation history, studies have found that it ranges from 0.17 (Buat et al. 2011) to 0.4 (Hirashita et al. 2003). Leroy et al. (2012) also performed a study to try to constrain the effect on non-star formation related dust heating on the star formation determined from 24 μm emission. They found that for $\Sigma_{\rm SFR} < 10^{-8}\, M_{\odot}/yr/pc^2$ more than half the 24 μm emission can be due to non-star formation processes. W3 generally suffers from more contamination issues than the W4 band because there are more bright spectral lines in the band (Cluver et al. 2013), emission from the destruction and fragmentation of PAHs (Boulanger et al. 1988, 1990; Houck et al. 2004, Pety et al. 2005) or emission from the galactic radiation field (Li & Draine 2002, Bosselli et al. 2004, Mattioda et al. 2005). Due to the higher contamination W4 will be used as the preferred mid-infrared star formation tracer. The relationship between 24μm emission and star formation is non-linear at high $L_{24\mu}$ (Li & Draine 2001, Draine & Li 2002, Calzetti et al. 2007) and for low metallicity and opacity regions (Helou 1988, Walter 2007, Calzetti et al. 2007); and similar trends are expected for the W4 band. More studies of the dust and star formation properties of galaxies will help improve star formation recipes. Despite these uncertainties W3 and W4 prove to be useful star formation tracers and play and important role in quantifying the obscured star formation in galaxies.

Mid-infrared results show that the correlation between α_0 and $\Sigma_{\rm SFR,0}$ is weak (but better than for Hα). Fitted power law indexes of the W3 and W4 data range between 3.4 and 3.7, while the model predicts a slope of 2. The dispersions around the linear fits to the W3 and W4 data are $\sim$ 1.1 dex, these confirm the poor match to the model. Therefore the constant Q_g and α_0 - $\Sigma_{\rm SFR,0}$ model does not fully describe galaxy centers in the sample.

6.1.3 Hybrid Star Formation Tracer Analysis

The discussion of the shortcomings of using Hα and W4 as star formation tracers has shown the limitations of only using a single tracer in such studies. In general Hα and W4 become ideal tracers in opposite conditions. Using Hα with no dust correction leads to underestimation of the star formation hidden in high extinction regions, the available dust corrections do not accurately model the dust extinction. Mid-infrared tracers rely on the presence of dust or PAHs in order to be detectable. A hybrid star formation recipe that uses both of these can trace both the exposed/unobscured star formation and the star formation that is hidden behind areas of high dust extinction. Using both components will allow for a more complete picture of how α_0 is related

to $\Sigma_{\rm SFR,0}$. Calzetti et al. (2007) performed a study of different tracers of SFR and calibrated a relationship between the Hα and 24 μm emission. This star formation recipe was successfully used by authors such as Bigiel et al. (2008), Leroy et al. (2008) and Schruba et al. (2012); whose studies I am using as a basis for some of this analysis (and comparing my results to). The uncertainties in star formation recipes (see Leroy et al. 2012, and later in this chapter) are so large that selecting this over other recipes will not affect our conclusions. WISE W4 has a mean frequency of 22 μm and traces the same warm dust continuum emission as the 24 μm MIPS band, and they have similar bandpasses. Jarrett et al. (2013) showed that the W4 - MIPS 24 flux ratio for galaxies ranges between $\sim$ 0.9 and $\sim$ 1.1. Rieke et al. (2009) calibrated 24 μm emission to infrared SFR (this is star formation determined from the total infrared light that was re-emitted by dust that was irradiated by hot young stars), and found the calibration to be:

$$SFR_{IR}[M_{\odot}/yr] = 1.12 \times 10^{-9} - 1.23 \times 10^{-9} L_{24\mu m}[L_{\odot}], \tag{6.4}$$

where $L_{24\mu m}$ is the luminosity of the 24 μm emission (defined as νL_{ν}). Jarrett et al. (2013) determined the relation between 22 μm W4 emission to the infrared SFR, the fit of their relation was:

$$SFR_{IR}[M_{\odot}/yr] = 7.5(\pm 0.07) \times 10^{-10} L_{22\mu m}[L_{\odot}], \tag{6.5}$$

where where $L_{22\mu m}$ is the luminosity of the 22 μm emission defined similarly to $L_{24\mu m}$. These are very similar to each other, the 22 μm:24 μm - SFR_{IR} conversion ratio is 1.5. The Calzetti et al. (2007) calibration of the unobscured and obscured SFR using Hα and 24 μm emission is:

$$SFR[M_{\odot}/yr] = 5.3 \times 10^{-42} (L_{H\alpha} + 0.031 L_{24\mu m})[ergs/s] \tag{6.6}$$

where $L_{22\mu m}$ is defined as before. This can be altered for 22 μm emission leading to a formula for total SFR that is as follows:

$$SFR[M_{\odot}/yr] = 5.3 \times 10^{-42} (L_{H\alpha} + 0.046 L_{22\mu m})[ergs/s]. \tag{6.7}$$

$L_{H\alpha}$ is the $H\alpha$ luminosity that is not corrected for internal dust absorption. This formula was used to calculate the total $\Sigma_{\rm SFR,0}$ for our sample of galaxies (surface brightnesses are used instead of luminosities in order to determine $\Sigma_{\rm SFR}$ instead of SFR and these relations are scaled to the $S_{H\alpha,0}$ and $S_{W1,0}$ values of our sample). The star formation surface densities of the galaxies in our sample determined using different star formation tracers are listed in Table 6.2.

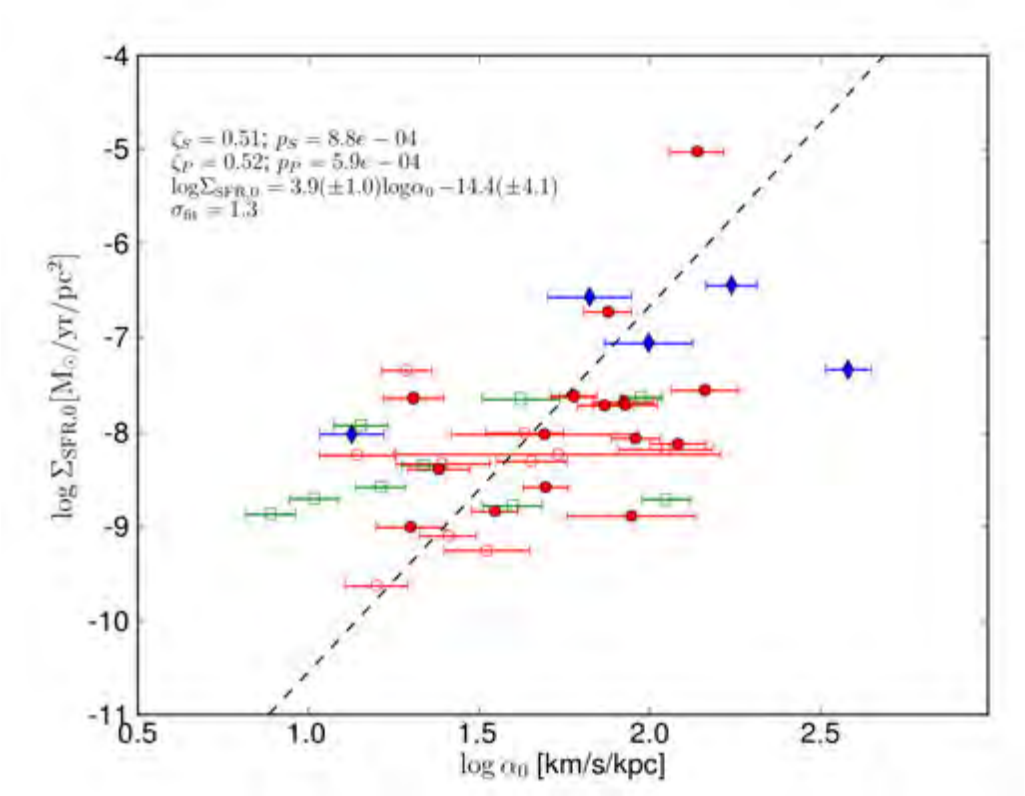

Figure 6.11: The total $\Sigma_{SFR,0}$ plotted against the central velocity gradient. Total $\Sigma_{SFR,0}$ was calculated by using the obscured (W4 component) and unobscured (Hα) SFR components. Symbols are defined the same as those in Figure 6.1.

Analysis using the total star formation removes the effects of dust obscuration on the measured Σ_{SFR}, and this allows us to perform studies of other parameters that affect the α_0 - $\Sigma_{SFR,0}$ relation. $\log \alpha_0$ is plotted against the total $\log \Sigma_{SFR,0}$ in Figure 6.11. The correlation coefficients for the plot are $\zeta_S = 0.51$ and $\zeta_P = 0.52$; the dispersion of the fit is $\sigma_{fit} = 1.3$ and the slope of the relation is 3.9 ± 1.0. The fit results are closer to the model when Hα is used, but not as close as W3 and W4; correlation between the parameters is better than the Hα but not as good and tight as for W3 and W4.

I used a Hα – 22 μm hybrid star formation rate recipe based on the Hα – 24 μm calibration determined by Calzetti et al. (2007). Authors such as Calzetti et al. (2007, 2009), Kennicutt et al. (2007, 2009), Zhu et al. (2008) and Leroy et al. (2012) have all determined star formation indicator recipes that combine the $H\alpha$ and 24 μm emission. There are large uncertainties associated with these recipes from the uncertainties of

each tracer and how they are calibrated and combined together to calculate a total star formation rate. Leroy et al. (2012) showed that Hα recipes can have intrinsic uncertainties of up to ~ 0.3 dex in the case where the galaxy or region has a single stellar population. They found that below $\Sigma_{\rm SFR}= 10^{-9}\,M_{\odot}/yr/pc^2$ the tracers are highly uncertain and the $24\,\mu$m part of the hybrid tracers is uncertain by up to a factor of ~ 2.

Most of the galaxy centers in our sample have $\Sigma_{\rm SFR}> 10^{-9}\,M_{\odot}/yr/pc^2$, hence the hybrid tracer is a reasonable star formation tracer. This confirms the results of the Hα and $W4$ analyses. **Different star formation tracers all confirm that there is a weak correlation between α_0 and $\Sigma_{\rm SFR,0}$ and the data does not fit the constant Q_g star formation model well (the power law index ranges from ~ 3.4 to 5.1 and $\sigma_{\rm fit}$ ranges between 1.1 and 1.7 dex). The tightest correlations and best fits to the data are found when using mid-infrared star formation tracers.** The weak correlation and higher than expected power law indexe are likely due to the effects of a non-constant Q_g or that the star formation law used does not hold in these central regions. This will be investigated by studying the constants in the star formation model and Kennicutt (1998) t_{orb} star formation law.

Table 6.2: Star Formation Surface Densities of the Sample

Galaxy	Hα		W3		W4		Hα+ W4
	$S_{H\alpha,0}$	$\Sigma_{\rm SFR,0}$	$\mu_{W3,0}$	$\Sigma_{\rm SFR,0}$	$\mu_{W4,0}$	$\Sigma_{\rm SFR,0}$	$\Sigma_{\rm SFR,0}$
1	2	3	4	5	6	7	8
J0034-08	-	-	18.16	-7.49	17.72	-7.40	-
J0040-13	-	-	18.85	-7.77	19.26	-8.01	-
J0112+00	-	-	21.36	-8.77	21.05	-8.73	-
J0130-22	-	-	19.11	-7.87	18.87	-7.86	-
J0140-05:S1	-16.71	-8.93	24.27	-9.94	22.59	-9.34	-8.72
J0140-05:S2	-17.39	-9.61	23.64	-9.68	22.84	-9.44	-9.22
J0223-21	-	-	18.01	-7.43	17.62	-7.36	-
J0230-02:S1	-15.48	-7.70	18.59	-7.66	18.46	-7.69	-7.43
J0230-02:S2	-16.35	-8.56	22.50	-9.23	22.11	-9.15	-8.53
J0239-08	-	-	18.60	-7.67	18.59	-7.74	-
J0241-06	-	-	21.44	-8.81	21.53	-8.92	-
J0246-07	-	-	17.11	-7.07	16.45	-6.89	-
J0249-02	-17.36	-9.57	23.99	-9.82	23.63	-9.76	-9.62

Continued on next page

Table 6.2 – continued from previous page

Galaxy	Hα		W3		W4		Hα+ W4
	$S_{H\alpha,0}$	$\Sigma_{\mathrm{SFR},0}$	$\mu_{W3,0}$	$\Sigma_{\mathrm{SFR},0}$	$\mu_{W4,0}$	$\Sigma_{\mathrm{SFR},0}$	$\Sigma_{\mathrm{SFR},0}$
1	2	3	4	5	6	7	8
J0404-02	-15.73	-7.94	21.06	-8.65	20.97	-8.69	-7.83
J0441-02	-15.38	-7.60	17.01	-7.03	15.69	-6.58	-6.40
J0504-16:S1	-15.61	-7.83	20.63	-8.48	20.22	-8.39	-7.84
J0935-05	-16.56	-8.78	22.99	-9.42	22.40	-9.27	-8.80
J0942+00	-15.39	-7.61	18.97	-7.82	18.70	-7.79	-7.55
J0943-05b	-	-	20.87	-8.57	20.82	-8.63	-
J1002-06	-16.54	-8.76	24.45	-10.01	24.46	-10.09	-9.00
J1005-16:S1	-15.79	-8.01	18.85	-7.77	18.86	-7.85	-7.56
J1005-16:S3	-15.72	-7.93	18.73	-7.72	18.84	-7.84	-7.52
J1026-19:S1	-15.47	-7.68	19.78	-8.14	19.81	-8.23	-7.77
J1039+01	-16.21	-8.42	22.61	-9.27	23.01	-9.51	-8.63
J1041-23	-16.67	-8.89	22.40	-9.19	22.03	-9.12	-9.00
J1042-23	-15.80	-8.01	22.34	-9.16	21.48	-8.90	-8.09
J1103-23:S1	-12.32	-4.53	18.74	-7.72	18.74	-7.80	-4.66
J1103-23:S2	-	-	19.30	-7.95	19.29	-8.02	-
J1105-00	-15.64	-7.86	17.85	-7.37	17.85	-7.45	-7.31
J1107-17	-16.07	-8.29	22.88	-9.38	22.60	-9.35	-8.09
J1127-04	-16.59	-8.80	25.07	-10.26	-	-	-
J1130-16	-16.90	-9.12	23.03	-9.44	22.14	-9.16	-8.84
J1147-16	-16.07	-8.28	18.87	-7.77	18.80	-7.82	-7.50
J1157-15	-16.07	-8.29	22.45	-9.21	22.69	-9.38	-8.11
J1217+00	-17.19	-9.41	-	-	-	-	-
J1253-12	-15.89	-8.10	23.07	-9.45	22.01	-9.11	-7.82
J1255+00	-16.28	-8.49	21.22	-8.72	20.96	-8.69	-8.28
J1300-13:S1	-15.67	-7.88	19.91	-8.19	19.92	-8.28	-8.02
J1326+02A	-	-	20.01	-8.23	19.75	-8.21	-
J1338-09	-16.04	-8.26	20.75	-8.53	20.78	-8.62	-8.23
J1403-06:S1	-15.52	-7.74	18.91	-7.79	18.93	-7.88	-7.58
J1403-06:S2	-15.06	-7.28	17.93	-7.40	17.34	-7.24	-6.88
J1423+01	-15.51	-7.73	19.92	-8.19	19.31	-8.03	-7.59
J1442-08	-15.64	-7.85	18.97	-7.82	18.68	-7.78	-7.58
J1447-17	-15.59	-7.81	18.95	-7.81	18.00	-7.51	-7.28
J1500+01	-15.62	-7.83	18.52	-7.64	18.30	-7.63	-
J1509-11:S1	-15.49	-7.70	17.22	-7.12	16.29	-6.82	-6.72

Continued on next page

Table 6.2 – continued from previous page

Galaxy	Hα		W3		W4		Hα+ W4
	$S_{H\alpha,0}$	$\Sigma_{\rm SFR,0}$	$\mu_{W3,0}$	$\Sigma_{\rm SFR,0}$	$\mu_{W4,0}$	$\Sigma_{\rm SFR,0}$	$\Sigma_{\rm SFR,0}$
1	2	3	4	5	6	7	8
J1609-04	-15.80	-8.02	22.56	-9.25	21.86	-9.05	-8.24
J1621-02	-15.87	-8.09	20.07	-8.26	20.00	-8.31	-7.86
J2025-24	-14.76	-6.98	16.88	-6.98	16.07	-6.74	-6.36
J2056-16	-16.45	-8.67	-	-	23.43	-9.68	-8.48
J2102-16	-16.62	-8.84	21.32	-8.76	21.80	-9.03	-8.75
J2142-06	-16.34	-8.56	22.55	-9.25	21.57	-8.93	-8.20
J2202-20:S1	-16.43	-8.65	20.69	-8.50	21.26	-8.81	-8.30
J2205-22	-	-	21.08	-8.66	20.90	-8.67	-
J2234-04	-16.60	-8.82	-	-	-	-	-

Comments: 1: SINGG galaxy name; 2: Logarithm of the Hα central surface brightness in [erg/s/cm^2] units; 3: Logarithm of Hα-based $\Sigma_{\rm SFR,0}$ in [$M_\odot$/yr/pc^2] units; 4: The W3 central surface brightness in [ABmag/arcsec^2] units; 5: Logarithm of W3-based $\Sigma_{\rm SFR,0}$ in [$M_\odot$/yr/pc^2] units; 6: The W4 central surface brightness in [ABmag/arcsec^2] units; 7: Logarithm of W4-based $\Sigma_{\rm SFR,0}$ in [$M_\odot$/yr/pc^2] units; 8: Logarithm of hybrid $\Sigma_{\rm SFR,0}$ in [$M_\odot$/yr/pc^2] units.

6.1.4 Star Formation Model and Law Parameters

The aim of this subsection is to test whether the results of the models imply a constant Q or that the Kennicutt (1998) t_{orb} star formation law holds. The results of the fits imply that at least some of the assumptions breaks down. The first step in performing these tests is to identify which star formation tracer to use for this analysis. I will compare the different tracers to each other and how their relationships change with changes in different galaxy parameters. Then the validity of the constant Q assumption and t_{orb} star formation law will be tested. They will be tested by determining the model values for each of those parameters (for variations that have been found in the literature used as inputs into the model) and determining whether the results are consistent with other studies that find varying Q and ϵ_{orb}. There is still a lot of uncertainty about star formation laws and Q measurements in the inner parts of galaxies. It is important to note that this excercise is useful to determine whether the variations are consistent with other work but is limited due to the lack of direct measurements of the gas density,

this does not allow for studies of the degeneracies between these parameters.

Star Formation Tracer Analysis

The first step in the tracer analysis will be to compare two different star formation recipes used to determine star formation rates from $W4$ emission. The star formation tracer recipe used to convert $S_{W4,0}$ and $S_{W3,0}$ to $\Sigma_{\rm SFR,0}$ values were from the Jarrett et al. (2012). This study only used 17 galaxies and the calibration was determined by using comparisons to similar mid-IR Spitzer bands. Donoso et al. (2012) used $> 96,000$ galaxies to fit a W3-SFR conversion using optical emission lines. Cluver et al. (2014) used a large sample ($> 25,000$ with $W4$ detections with S/N> 2) of galaxies to derive their own conversions based on Hα derived star formation rates. The conversion factors derived by Jarrett et al. (2013) and Cluver et al. (2014) were both determined from globally averaged parameters and they diverge at low $L_{\nu\,22\mu m}$ ($L_{\nu\,22\mu m} < 10^{7.5}\,{\rm L}_{\odot}$). For this analysis I assumed that the relations extend to lower luminosities. I used surface brightnesses instead of luminosities in order to determine $\Sigma_{\rm SFR}$ values. Most of our galaxies have $S_{W4,0}$ below this value and the resultant differences between the Cluver et al. (2014) and Jarrett et al. (2013) $\Sigma_{\rm SFR,0}$ conversions can be as large as dex ~ 2 for our faintest galaxy centers.

The ratio of the Cluver et al. (2014) $W4$ - derived $\Sigma_{\rm SFR,0}$ to the Hα-derived $\Sigma_{\rm SFR,0}$ is plotted against the stellar mass in Figure 6.12 . The stellar masses are calculated using $W1$ and $W2$ observations and fitted relations determined by Cluver et al. (2014). The $W4$-derived $\Sigma_{\rm SFR,0}$ are higher than those determined from Hα for all but one galaxy (J1103-23:S1). The mean ratio is 1.24 dex, and some galaxy centers have rations greater than $10^{2.5}$. These differences are very high and imply that either the Hα dust corrections severely underestimate the obscured star formation rate or that the Cluver et al. (2014) conversion underestimates the star formation rate. Meurer et al. (2006) found that the dust corrected Hα star formation underestimated the infrared emission by a factor of up to 5. The ratios found using the Cluver et al. (2014) are much higher than that for most of the sample. The version of the plot that uses the Jarrett et al. (2013) conversion to determine $\Sigma_{\rm SFR,0}$ is shown in Figure 6.13. The $W4$ $\Sigma_{\rm SFR,0}$ tend to be lower than the Hα $\Sigma_{\rm SFR,0}$, however the mean ratio between them is -0.52 dex. There is much better agreement between $W4$ and Hα derived $\Sigma_{\rm SFR,0}$ when the Jarrett et al. (2014) conversion is used. J1103-23:S1 is an outlier in both plots and has a very high $S_{H\alpha,0}$ compared to $S_{W4,0}$ (due to this behaviour it is not used in the Section 6.2 analysis). It has a $S_{H\alpha}$ that rises sharply in at low radii (see Figure 6.14). When either conversion is used the ratios increase with increasing stellar mass. Therefore high stellar mass galaxies have the highest ratio of W4 to $H\alpha$ central sur-

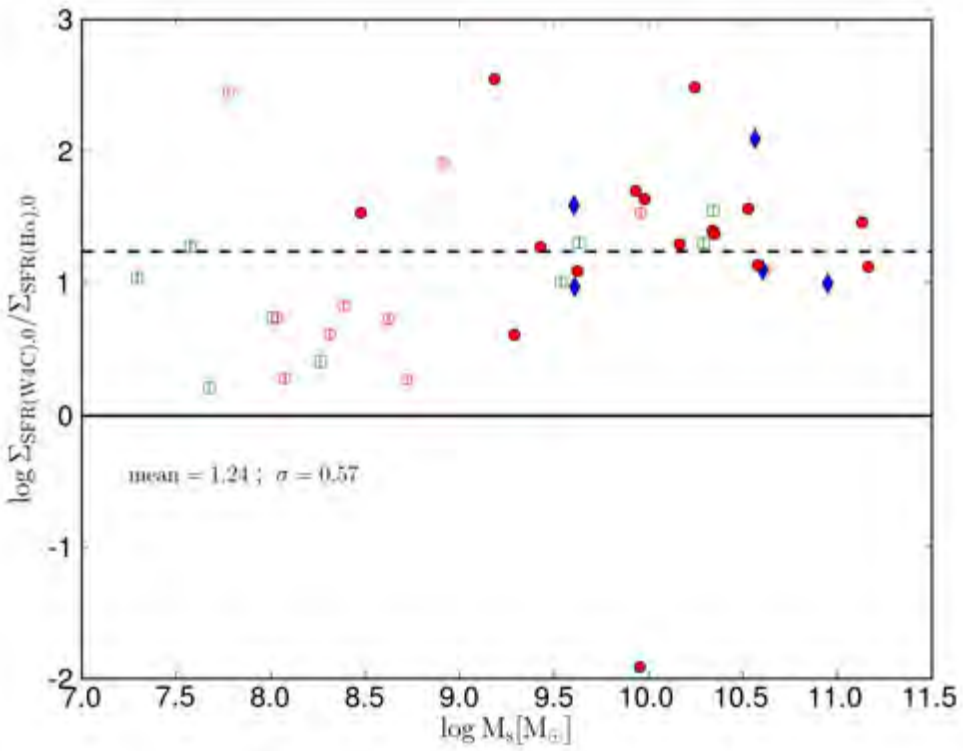

Figure 6.12: Ratio of the $W4$-derived $\Sigma_{\rm SFR,0}$ to the Hα-derived $\Sigma_{\rm SFR,0}$ plotted against the total stellar mass. The $W4$-derived $\Sigma_{\rm SFR,0}$ values were determined using the Cluver et al. (2014) conversion factor. Symbols are the same as those in Figure 6.1.

face brightnesses. I use the Jarrett et al. (2013) conversions because their sample has galaxies that has lower luminosities than the Cluver et al. (2014) sample, their recipes were calibrated using 24μm and related IR relations, and they are in better agreement with the Hα-derived $\Sigma_{\rm SFR,0}$.

The ratio of the hybrid $\Sigma_{\rm SFR,0}$ to the Hα $\Sigma_{\rm SFR,0}$ plotted in Figure 6.15. It is important to note that the obscured part of the hybrid star formation recipe is Hα that is not corrected for dust, whilst the Hα $\Sigma_{\rm SFR}$ is corrected for dust. As expected the addition of a dust component to $H\alpha$ in the hybrid star formation recipe results in higher $\Sigma_{\rm SFR,0}$ than those derived from the Hα. The trend of increasing ratios with increasing stellar mass is confirmed in Figure 6.15. The mean ratio (0.34 dex) and the dispersion around the mean (0.43 dex) is smaller than the ratios of the $W4$ $\Sigma_{\rm SFR,0}$. The low mean, dispersion and its inclusion of an unobscured and obscured component makes leads me to use the hybrid star formation recipe for further star formation analysis.

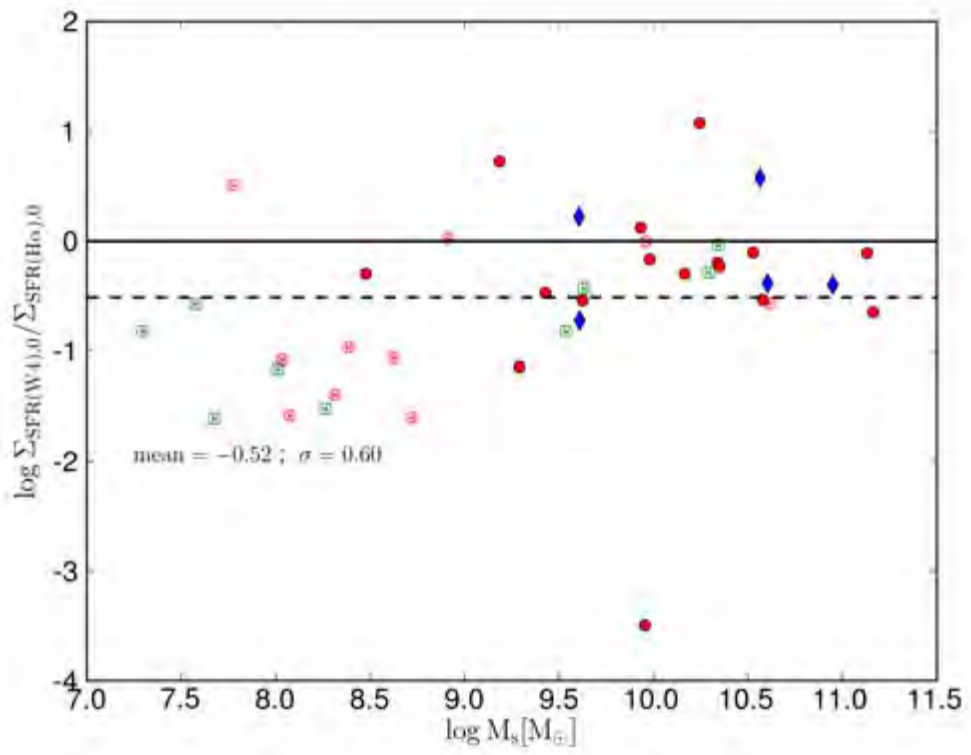

Figure 6.13: Ratio of the $W4$-derived $\Sigma_{\mathrm{SFR},0}$ to the Hα-derived $\Sigma_{\mathrm{SFR},0}$ plotted against the total stellar mass. The $W4$-derived $\Sigma_{\mathrm{SFR},0}$ values were determined using the Jarrett et al. (2013) conversion factor. Symbols are the same as those used in Figure 6.1.

It is important to note other uncertainties of using these star formation recipes. $\Sigma_{\mathrm{SFR},0}$ values calculated from $S_{H\alpha,0}$ are sensitive to the amount of dust obscuration. The conversions from $S_{H\alpha,0}$, $S_{W4,0}$ and $S_{W3,0}$ to $\Sigma_{\mathrm{SFR},0}$ assume a single conversion constant for all galaxies and these conversion constants were determined from globally averaged measurements. Local conditions vary greatly within and between galaxies, therefore small scale factors like the presence of starburst regions, bars, rings, AGN, dark molecular clouds, the leakage of flux between separate star forming regions, outflows can result in deviations from the globally averaged conversion factors. Differences in metallicities, IMFs and the assumed stellar populations and length of star formation can also cause variations in the conversion factors. Our analysis showed the difference between a transparent (unobscured) tracer of star formation like Hα and tracers of the obscured star formation such as W3 and W4 emission. Hα does a good job of tracing star formation but since this study focuses on the inner parts of galaxies where the

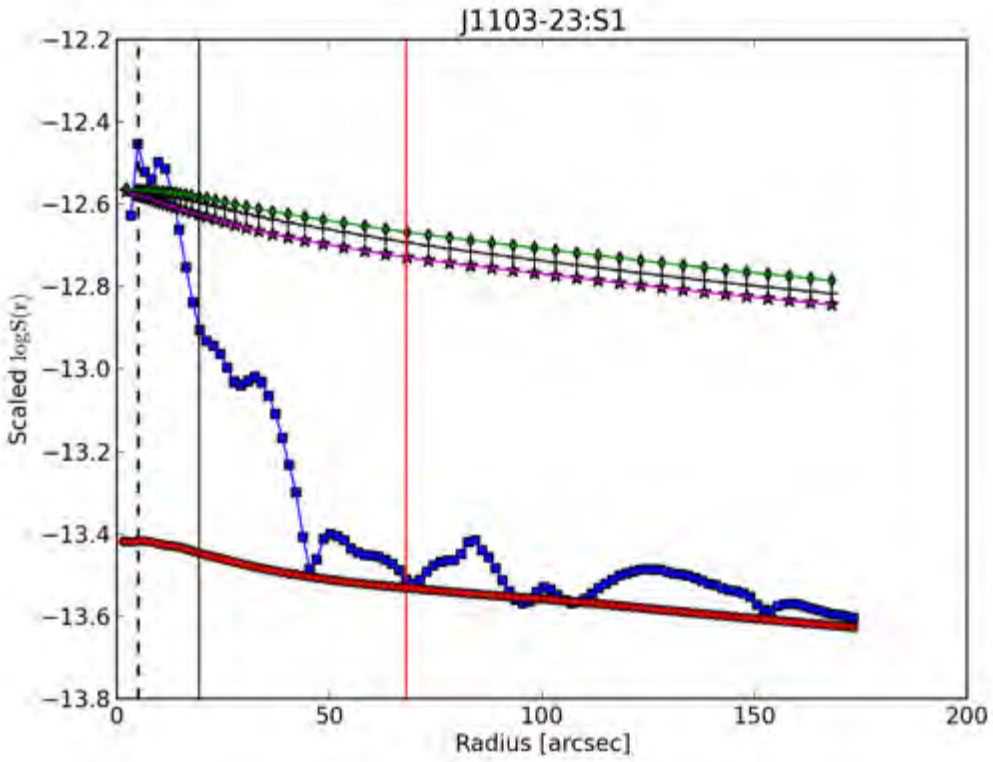

Figure 6.14: Radial interior surface brightness profiles of J1103-23:S1. The different observing bands are depicted as follows: $S_{H\alpha}$: blue squares , S_R: red circles, S_{W1}: magenta stars, S_{W3}: black crosses and S_{W4}: green diamonds. The red vertical line is r_e,the black vertical line is the r_t and the black vertical dashed line is $r = 5''$.

amount of dust and star formation are high, dust obscuration can have a significant effect on the Hα-based $\Sigma_{\mathrm{SFR},0}$ values (even when an internal dust correction is applied to the data).

The use of the hybrid star formation recipe allows the dissection of the total star formation into an obscured and unobscured component. The ratio of the obscured and unobscured components of $\Sigma_{\mathrm{SFR},0}$ is plotted against the total stellar mass of a galaxy in Figure 6.16 and it confirms that the ratio of obscured to unobscured $\Sigma_{\mathrm{SFR},0}$ increases with increasing stellar mass. Most galaxies with stellar masses below $10^9\,M_\odot$ have higher unobscured $\Sigma_{\mathrm{SFR},0}$ than obscured $\Sigma_{\mathrm{SFR},0}$.

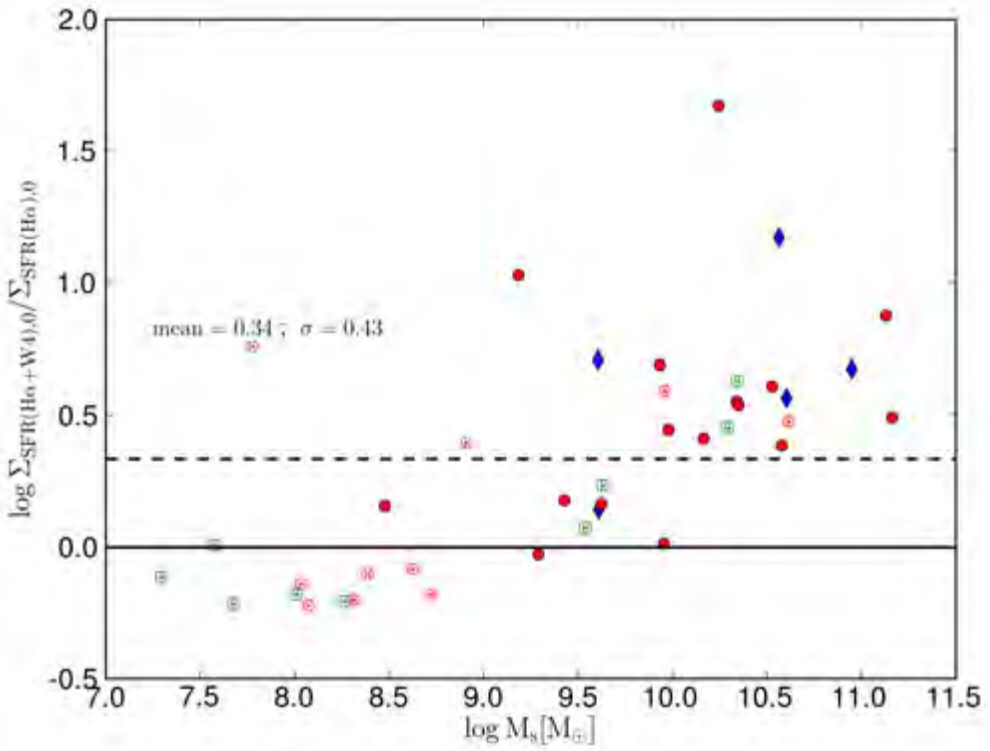

Figure 6.15: Ratio of the hybrid $\Sigma_{\rm SFR,0}$ to the Hα-derived $\Sigma_{\rm SFR,0}$ plotted against the total stellar mass. Symbols are the same as those in Figure 6.1.

Orbital Efficiencies

One of the assumptions of the α - $\Sigma_{\rm SFR}$ model is that the $\Sigma_{\rm SFR}$-t_{orb} star formation law holds. If I assume that our model is correct I can plot $\log \alpha_0$ and $\log \Sigma_{\rm SFR}$ for different values of ϵ_{orb} in order to determine the ϵ_{orb} of the centers of our galaxies and whether their ϵ_{orb} values are the same as what was found by Kennicutt (1998). Lines of constant ϵ_{orb} (assuming this model) are overplotted over the α_0 and $\Sigma_{\rm SFR}$ data in Figure 6.17. Different lines are drawn for different assumed Q_g values. Q_g values of 4 and 2 were used in order to show the typical Q_g that Leroy et al. (2008) found in their analysis and $Q_g = 1$ is the threshold value for disk stability The figure shows that the central regions of the galaxies in our sample have a wide range of ϵ_{orb} values. All but 9 of the galaxies in Figure 6.17 have $\epsilon_{orb} < 0.11$ (at $Q_g = 4$), and most can be modelled by ϵ_{orb} ranging from ~ 0.01 to ~ 0.11 with varying Q_g. Galaxies with high $\Sigma_{\rm SFR,0}$ and ϵ_{orb} have $S_{H\alpha}$ values that increase sharply in their inner regions. There are galaxies with very low ϵ_{orb} values ($\epsilon_{orb} \sim 0.001$), the majority of these galaxies have $S_{H\alpha}$ profiles that decrease in their inner regions. The galaxies with enhanced $\Sigma_{\rm SFR}$ in their inner regions are able to consume their gas much more quickly per orbital timescale than the other

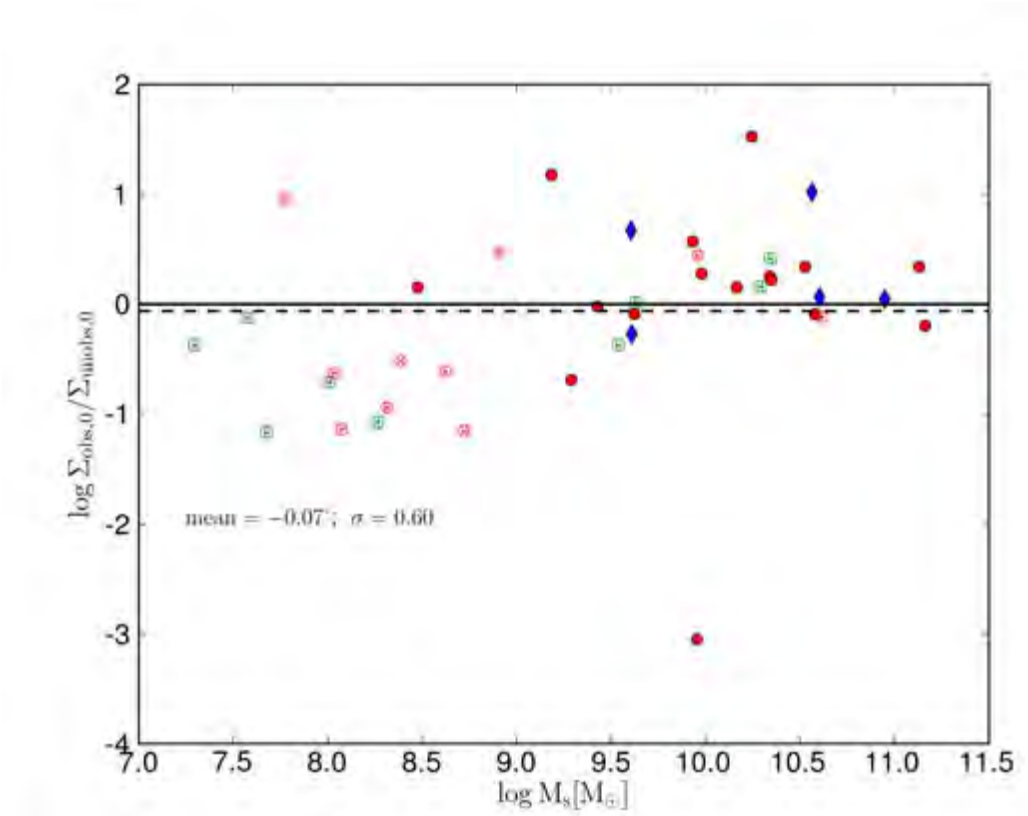

Figure 6.16: Ratio of the obscured $\Sigma_{\rm SFR,0}$ to the unobscured $\Sigma_{\rm SFR,0}$ derived from the hybrid star formation recipe plotted against the total stellar mass. Symbols are the same as those in Figure 6.1.

galaxies. Galaxies with $\Sigma_{\rm SFR}$ that decreases in the inner regions and those that have low $\Sigma_{\rm SFR}$ use up very little of their gas per orbital timescale. The large range in ϵ_{orb} values shows that the model does not describe the data well.

Kennicutt (1998) found that $\epsilon_{orb} = 0.11$, but most of our galaxies have lower ϵ_{orb} than their value. If I assume $Q_g = 4.0$ then the difference between our ϵ_{orb} vules and the Kennicutt (1998) value is even much larger. Leroy et al. (2008) and Meurer et al. (2013) found that at very small radii Q_g can be larger than 10. Therefore using more realistic values of Q_g (based on previous studies) confirms that ϵ_{orb} is not constant between galaxy centers and it is lower than what Kennicut (1998) found in their analysis. In order to have a constant ϵ_{orb} between the galaxier in our sample Q_g would have to vary by more than 3 orders of magnitude, such large Q_g values are not supported by previous Q_g studies. Daddi et al. (2010) also found that ϵ_{orb} was constant among their sample of nearby disk galaxies and starbursts, their best fit value was $\epsilon_{orb} = 0.24$.

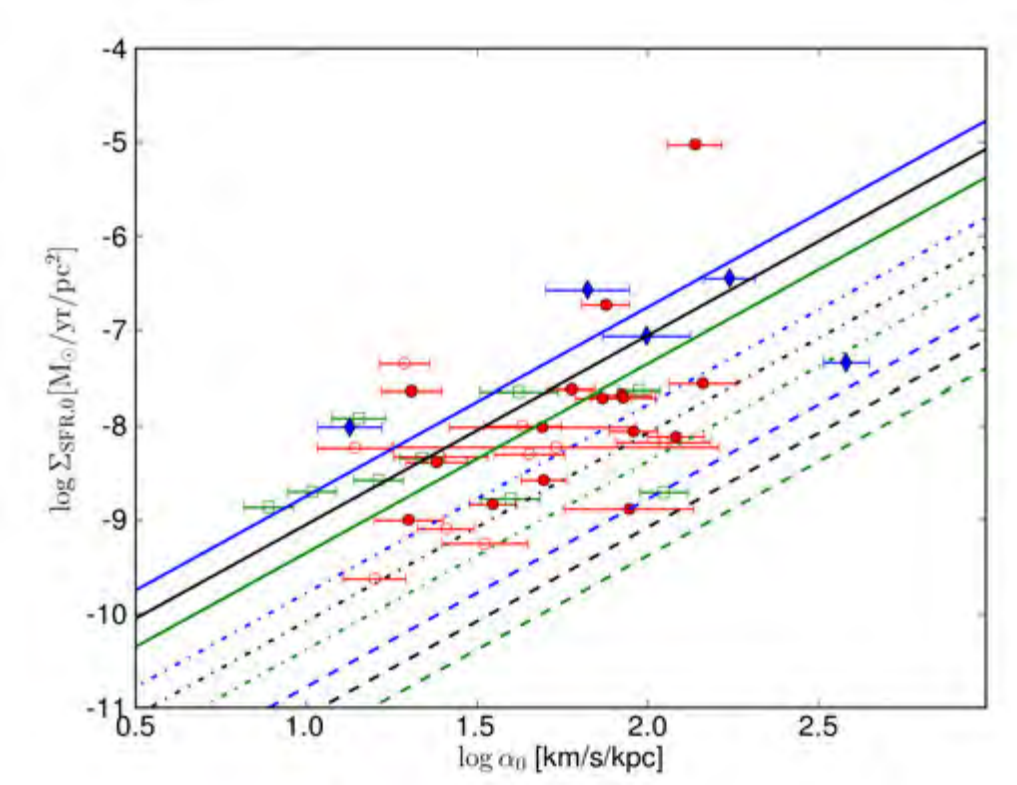

Figure 6.17: Same as Figure 6.11. The diagonal lines are lines of constant orbital efficiency : $\epsilon_{orb} = 0.11$ is shown by a solid line, $\epsilon_{orb} = 0.01$ is shown by a dash-dot line and $\epsilon_{orb} = 0.001$ by the dashed line. The black lines are for $Q_g = 2$, green lines $Q_g = 1$ and blue lines $Q_g = 4$. The symbols are the same as for Figure 6.11.

Daddi et al. (2010) and Genzel et al. (2010) showed that starbursts and high redshift highly star forming galaxies can have $\epsilon_{orb} > 0.11$. All these studies studies were of globally averaged parameters. Krumholz et al. (2012) showed that azimuthally averaged studies of nearby galaxies (e.g., Bigiel et al. 2008 and Leroy et al. 2008) give different results for the Σ_{SFR} and Σ_g/t_{orb} relationship than the unresolved and globally averaged values. Studies using azimuthally averaged values have lower power law indexes (shallower slope in the star formation relations) than the global studies. Their ϵ_{orb} is lower than the Kennicutt (1998) and Daddi et al. (2010) values. Lelli et al. (2014) studied the inner regions of dwarf galaxies ($r < r_t$) and found that $\epsilon_{orb} < 0.11$. Our ϵ_{orb} values are consistent with what Lelli et al. (2014) and Krumholz et al. (2012) found in their inner dwarf galaxy study and azimuthally averaged study respectively. This indicates that ϵ_{orb} tends to be lower in the central regions of galaxies than when calculated over large scales or in the outer parts of galaxies. This is still uncertain due to the lack of high quality studies of the star formation and kinematics of the inner

regions of galaxies. If there are lower efficiencies, they likely due to the gas transport inefficiency or that the triggering of star formation in the central regions is not dominated by structures that follow the orbital timescale, which result in the breakdown of the Kennicutt (1998) relation.

Kennicutt (1998) showed that the $\Sigma_{\rm SFR}$-t_{orb} relationship holds for globally averaged nearby bright galaxies. However they found that the fitted power law index of the relation was 0.9 rather than the predicted 1.0. Daddi et al. (2010) found that the relationship holds even for high redshift starburst galaxies, albeit with a power-law index of 1.1. Krumholz et al. (2012) show that the correlation between Σ_{SFR} and Σ_g/t_{orb} is different for globally averaged values than it is for values measured within galaxies. Krumholz et al. (2012) showed that the power-law index is lower for azimuthally averaged measurements than it is for global measurements in nearby large spirals. They found a power-law index less than what Kennicutt (1998) found in their global analysis (index $\sim 0.9 - 1.0$) and a value similar to the Kennicutt (1998) value when they considered unresolved galaxies. When they studied local molecular clouds from studies by Heiderman et al. (2010) and Lada et al. (2010), Krumholz et al. (2012) they found that the power law index and ϵ_{orb} of these were very different from the extragalactic scale observations. Therefore the resolution of the observations and scales being studied seems to affect the validity and parameters of the $\Sigma_{\rm SFR}$-t_{orb} relation. The aforementioned studies suggest that the smaller the scales being studied the greater the departure from the original Kennicut et al. (1998) parameters. Our study is of the central regions at the hundreds of parsec to kiloparsec scales, therefore the relation will be expected to deviate from what Kennicutt (1998) and Daddi et al. (2010) found. Due to the lack of direct Σ_g observations in the analysis no firm conclusions can be made about the relation by using this analysis. However, the study does suggest that there is variation in ϵ_{orb}, and this is supported by Lelli et al. (2014) who directly observe the gas density.

Gas Densities and Depletion Times

Leroy et al. (2008) showed that the molecular gas star formation efficiency ($SFE \equiv \Sigma_{SFR}/\Sigma_g$, i.e., the inverse of the gas depletion time t_{dep}) is constant in the inner molecular-gas dominated regions of nearby disk galaxies. They found that the molecular $t_{dep} = 1.9\,\mathrm{Gyr}$ in the molecular-gas dominated regions of galaxies. Bigiel et al. (2008) showed that the total gas (H I combined with molecular gas) efficiency within galaxies is not constant and varies greatly for different Σ_g. For samples of nearby bright

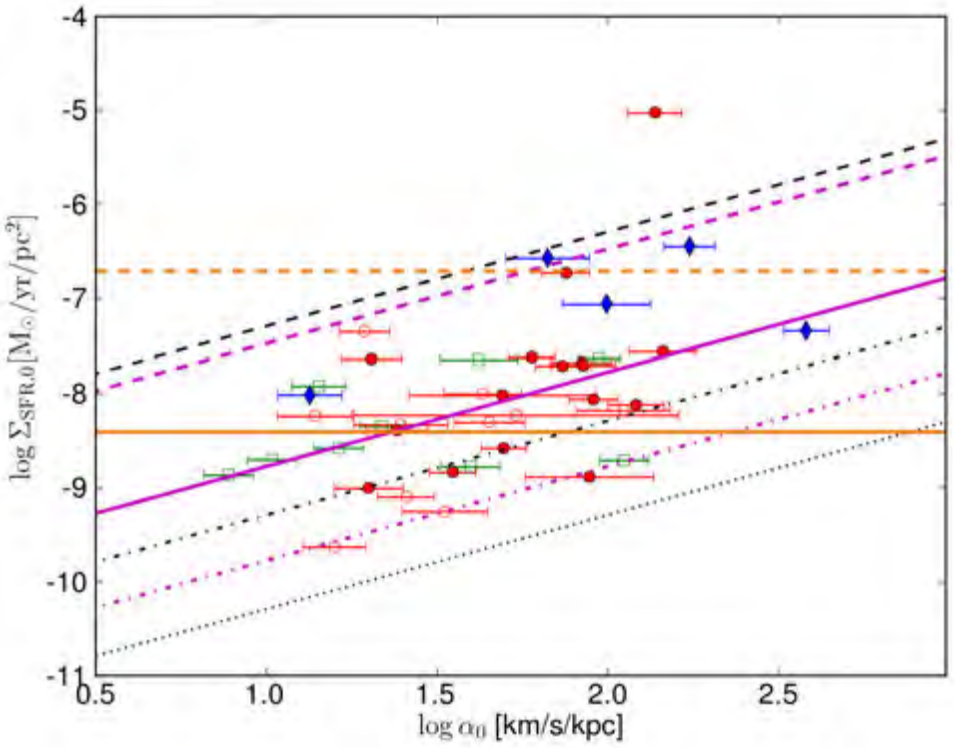

Figure 6.18: Same as Figure 6.11. The diagonal lines are lines of constant gas depletion time (t_{dep}) : $t_{dep} = 2\,\mathrm{Gyr}$ is the solid line, $t_{dep} = 100\,\mathrm{Gyr}$ is a dotted line, $t_{dep} = 10\,\mathrm{Gyr}$ is a dash-dot line and $t_{dep} = 0.1\,\mathrm{Gyr}$ is depicted by the dashed line. They were calculated for $Q_g = 2$. The magenta diagonal lines are lines of constant Σ_g, these were calculated by using the Kennicutt (1998) t_{orb} star formation law. The dashed line shows $\Sigma_g = 200\,M_\odot/pc^2$, the solid line: $\Sigma_g = 10\,M_\odot/pc^2$ and the dash-dot line shows $\Sigma_g = 1\,M_\odot/pc^2$. The horizontal yellow lines are lines of constant Σ_g determined using the fit of the $\Sigma_{\mathrm{SFR}} \propto \Sigma_g$ by Krumholz et al. (2012), the line styles and the Σ_g they represent are the same as those of the magenta lines.

disk galaxies the t_{dep} in the inner regions ranged between ~ 1 – $10\,\mathrm{Gyr}$ (Leroy et al. 2008). Bigiel et al. (2008), Daddi et al. (2010), Genzel et al. (2010) and Krumholz et al. (2012) showed that starburst and high redshift sub-mm galaxies have lower t_{dep} than nearby disk galaxies, most have t_{dep} that range between 2 – 0.1 Gyr.

With our data I can estimate Σ_g from α, if I assume a constant Q_g. This Σ_g can be used to estimate the total t_{dep} in the central regions of our galaxies. The total gas t_{dep} is calculated as follows: $t_{dep} = \frac{2\alpha_0\sigma_g}{\pi Q G \Sigma_{SFR}}$. These central t_{dep} values can be compared to

the globally averaged and azimuthally averaged values from other studies. I assumed a constant Q of 1.6 and plotted lines of constant t_{dep} over our α_0 and $\Sigma_{\rm SFR}$ data in Figure 6.18. The central regions of our galaxies show a wide range in t_{dep}: ~ 0.1 to 100 Gyr. Most of the galaxies have t_{dep} values that range between 0.5 Gyr and 10 Gyr, and many the have $t_{depl} \sim 2$ Gyr. This is similar to what Bigiel et al. (2008) and Leroy et al. (2008) found in regions where molecular gas is dominant ($\Sigma_g > 9\,M_\odot/pc^2$) and even in the inner regions of galaxies which were not dominated by molecular gas. H I becomes saturated at around $\Sigma_g \sim 10\,M_\odot/pc^2$ (Schaye et al. 2001, Wong & Blitz 2002, Bigiel et al. 2008) and gas above this density is in the form of molecular gas for nearby spiral galaxies. The galaxies that have $t_{dep} = 2$ Gyr are likely to have central regions where molecular gas is the dominant gas component and $\Sigma_g \sim 9$–$200\,M_\odot/pc^2$. If I assume that the gas is molecular-dominated and has a constant $t_{dep} = 2$ Gyr then there is a large variation in the implied Q_g values required to model our galaxy centers. In this case the large range in Q_g values is not enough to explain the α_0 and $\Sigma_{\rm SFR,0}$ values of our sample. Leroy et al. (2008) also found that H I dominated dwarf galaxies can have $t_{dep} = 1$ Gyr in their central regions. There is a greater range in the central t_{dep} values for these galaxies than for molecular gas dominated disk galaxies, their t_{dep} values range from 1 Gyr to 10 Gyr (Leroy et al. 2008). Our sample consists of a wide range of galaxies. Most galaxies that are fit by models with high t_{dep} (~ 100 Gyr) have $S_{H\alpha}$ profiles that decrease at low r, therefore they behave like the low $\Sigma_{\rm SFR}$ and Σ_g regimes shown in Bigiel et al. (2008). Low metallicity dwarf galaxies that have not undergone recent starbursts or mergers can have very large t_{dep}. Filho et al. (2016) found that some of their low metallicity dwarf galaxies had t_{dep} up to 1000 Gyr. The low efficiencies I find in the central regions of some of our galaxies are representative of these conditions. Lelli et al. (2014) found that their inner (they measured values within the optical disk) t_{dep} varied from $\sim$ 1–100 Gyr for their dwarf galaxy sample.

Figure 6.18 has lines of constant Σ_g, these were calculated using the Kennicutt (1998) t_{orb} star formation law, assuming $\epsilon_{orb} = 0.11$ (which was what they found in their fit). Therefore if I assume a constant ϵ_{orb} that is equal to what Kennicutt (1998) found, the galaxies with $t_{dep} \sim 0.1$ Gyr have gas densities greater than $200\,M_\odot/pc^2$. These galaxies have $\epsilon_{orb} \sim 0.1$, therefore the Σ_g values derived from assuming $\epsilon_{orb} = 0.11$ are reasonable estimates. Lines of constant Σ_g (10 and $200\,M_\odot/pc^2$) calculated from the $\Sigma_{\rm SFR}$ using fits of the Schmidt Law by Krumholz et al. (2012) and these were also plotted in Figure 6.18 to compare with those calculated from the t_{orb} star formation law. Even if I use this parameterization of the star formation law the galaxies in our sample with $t_{dep} \sim 0.1$ Gyr have $\Sigma \geq 200\,M_\odot/pc^2$. High gas densities of the order of and greater than $200\,M_\odot/pc^2$ indicate that these galaxies are in the ULIRG, LIRG,

starburst regime. Four of the galaxies with the lowest t_{dep} are known to be starbursts or to possess have active nuclei. J0441-02 is classified as an AGN and J2025-25 is classified as a LIRG (Liu 2001, Sanders et al. 2003). J1403-06:S2 and J1509-11:S1 are Syfert 2 galaxies (Veron-Cetty & Veron 2006) and these all have low t_{dep} values. J2025-24 and J0441-02 have the most active cores and have $t_{orb} \sim 0.1\,\mathrm{Gyr}$. These results are consistent with high redshift starburst galaxies with very low t_{dep} values similar to what studies such as Genzel et al. (2010) and Daddi et al. (2010) found in their analyses. Our galaxies have central t_{dep} values that lie between 0.1 and 100 Gyr, therefore the galaxy centers have behaviours that range from starburst-like low t_{dep} to galaxy centers with very little gas and high t_{dep} values. The expected range in Q_g is not as large as the range in t_{dep}, therefore even if Q_g is assumed to vary between galaxies a single t_{dep} value cannot explain the range in our data.

Constant Q Assumption

The correlation between Σ_{SFR} and α is dependent on the assumption that Q_g is constant. Q_g has been shown to be roughly constant over large regions of galaxies (e.g., Leroy et al. 2008, Meurer et al. 2013), however it does show some variation with r. These variations can be large ($\delta Q \geq 1$) at very small r and at large r. Q_g is dependent on σ_g, α and the Σ_g. In order to keep Q_g constant for a constant σ_g the gas surface density is correlated with α. Our analysis shows that the there is only a weak correlation between α_0 and $\Sigma_{\mathrm{SFR},0}$, this suggests that either Q_g is not constant or σ_g is not constant.

Tamburro et al. (2009) and Mogotsi et al. (2016) show that σ_g in disk galaxies is not constant and it often declines with increasing radius. Different values of σ_g are assumed in different studies where Q_g is calculated. σ_g values in the range $11 - 6\,\mathrm{km/s}$ are normally used. Meurer et al. (2013) find that even if σ_g varies with r, it does not change the overall shape of Q_g as a function of r. The changes in σ_g seem to only affect the absolute values of Q_g but not its variability. Like Leroy et al. (2012) they find that Q_g values are not constant in the inner regions of galaxies and are roughly flat at intermediate radii. They also find that at very large radii (different radii for each of the galaxies in their sample) Q_g values are not constant. The breakdown of constant Q_g in the inner regions (predominantly $r{<}0.5r_{25}$) contributes to the weakening of the measured correlation between α_0 and Σ_{SFR}. And this means that our model is too simple to fully describe the processes in the inner regions of galaxies that affect Σ_g and Σ_{SFR}. The single-gas Q_g formulation used in this analysis is a simple parameteriza-

tion and it does not take into account the effects of the stars. As shown previously, the stellar surface density has a large effect on the gravitational potential well of the inner parts of galaxies, therefore it is an important to consider it when determining the stability of the disk. A more complex stability parameterization that includes the effect of the stars was considered. And analysis of the star formation models using this parameterization is performed in the following section.

If Q_g is not constant and the star formation efficiency is constant it indicates that insufficient gas is being transported to the inner parts of galaxies to maintain the constant Q_g required for the model. This is because the rate of consumption of the gas (through star formation) is too high or that gas is prevented from efficiently being transported to the central regions due to resonances, star formation feedback, AGN feedback or other processes in the central regions of galaxies. If less gas than is required to compensate for the high α values is present then the Q_g should increase. Hints of this kind of behaviour is seen in Leroy et al. (2008). This scenario may be the natural outcome if there is no additional mechanism (apart from angular momentum loss) to efficiently transport gas to the inner parts of galaxies.

In these previous sections attempts were made to isolate different parameters and determine whether the model can reproduce values found in the literature. However, ideally, degeneracies between Q_g, ϵ_{orb} and σ_g should be studied in order to determine how these parameters affect the model and which parameter has the greatest effect on the disagreement between the data and model. This study should be done by using direct high-resolution measurements of Σ_g, σ_g and ϵ_{orb} in the central regions of galaxies. Degeneracies between these parameters have not been studied extensively, further studies are necessary in order to better understand them. Degeneracies between σ_g and α_0 would result in some departure from the model, however if there is such a degeneracy it would not cause minor variations compared to the uncertainties in measuring Σ_g. Direct σ_g and Σ_g data were not available for this analysis, therefore studying the degeneracies is beyond the scope of this analysis

Velocity Gradient Uncertainties

Uncertainties in α_0 are discussed in the previous chapter and the effects of non-circular motions and observational limitations can affect the α_0 measurements so as to change the power law index of the $\alpha_0 \propto \Sigma_{\mathrm{SFR},0}$ relation. Higher resolution kinematic analyses and observations with better sampling of the galaxy velocity fields would improve the measurements and reduce the uncertainties, therefore improving tests of the rela-

tion. More accurate distance measurements would also reduce the uncertainties in α_0. Agreement with studies such as Lelli et al. (2013, 2014) and Erroz-Ferrer et al. (2016) indicates that our measurements of α_0 are reasonable. The uncertainties in the measurements of α_0 contribute to the weakening of the correlation between α_0 and $\Sigma_{\rm SFR,0}$ and future studies of the correlation will require improved measurements of α_0.

6.1.5 Conclusion

Tests of the star formation model have shown that the correlation between α_0 and $\Sigma_{\rm SFR,0}$ is very weak, but it increases when $\Sigma_{\rm SFR,0}$ is calculated using Hα emission to when mid-IR tracers are used. A power-law index of ranging between 3.4 and 5.1 was found for the α_0 and $\Sigma_{\rm SFR,0}$ relation, and the logarithms of the parameters had a maximum correlation coefficient of 0.56 . This power-law index is higher than the expected value from our model (2) and the correlation between the parameters is weak. Uncertainties in α_0 and $\Sigma_{\rm SFR,0}$ measurements weaken the correlation between the parameters. Most of the galaxy centers were consistent with ϵ_{orb} values between 0.001 and 0.1. The Kennicutt (1998) t_{orb} SFR Law used was assumed to hold for this analysis, and a constant Q_g is also assumed for for this model. This analysis suggests that ϵ_{orb} and Q_g may not be constant over such a diverse sample of galaxies, different spatial scales and for galaxy centers. Velocity dispersions also vary between galaxies and within galaxies but the variation that is seen in them is not large enough to explain the variation we see in the analysis.

Therefore $\Sigma_{\rm SFR,0} \propto \alpha_0^{\sim 4}$, however the correlation coefficient between α_0 and $\Sigma_{\rm SFR,0}$ is low and the fit poor due to varying ϵ_{orb} and Q_g values for different galaxy centers. Either of these can vary by a few orders of magnitude therefore the assumptions that the model is based on do not hold, hence the model fails to describe the star formation in the center of galaxies.

6.2 Two Fluid Q Analysis

The result of the analysis in Section 6.1 is that the constant single fluid gas-only Q_g model does not hold in the center of galaxies due to the breakdown of either the constant Q_g assumption or constant ϵ_{orb} from the Kennicutt (1998) t_{orb} star formation law. In this section I test star formation models based on the two-fluid Wang & Silk (2002) Q formulation: Q_{WS}. This model assumes a constant Q_{WS} which takes into account the stellar and gas disks of galaxies. The gas-only Q_g formulation is the most

commonly used stability parameterization (e.g., Kennicutt 1989, Martin & Kennicutt 2001, Wong & Blitz 2002), however as the results in Chapter 4.3 indicate that the stellar component of galaxies affects the inner potential well of galaxies hence is an important component of the central part of galaxies. Therefore more realistic stability parameterizations should include the effect of the stellar component on the stability of galaxy disks. The use of the Q_{WS} results in models where $\Sigma_{\rm SFR,0}$ is related to the central velocity gradient α_0 and central stellar surface density $\Sigma_{s,0}$. The $\Sigma_{\rm SFR,0}$ is calculated using the hybrid star formation recipe described in Section 6.1.3 (based on the Calzetti et al. 2007 star formation recipe). The central stellar mass surface densities and scale lengths are derived from R-band observations. I test the constant Q_{WS} model for the Kennicutt (1998) t_{orb} star formation law in Section 6.2.1, and I test the model for the Bigiel et al. (2008) molecular star formation law in Section 6.2.2.

6.2.1 Orbital Timescale Star Formation Law Analysis

Assuming that the Kennicutt (1998) t_{orb} SFR law holds and disks have a constant Q_{WS}, the relation between $\Sigma_{\rm SFR}$, Σ_s and α was determined to be (in expanded form):

$$\Sigma_{SFR} = \frac{\sigma_g \epsilon_{orb}}{\pi^2 Q_{WS} G}\alpha^2 - \frac{\sigma_g \epsilon_{orb}}{2\pi\sqrt{G}}\left(\frac{\alpha\sqrt{\Sigma_s}}{\sqrt{l_s}}\right) \tag{6.8}$$

Figure 6.19 is a plot of the different components of Equation 6.8. In the figure $\log(\Sigma_{\rm SFR,0})$ is plotted against $\log\left(\alpha_0\sqrt{\frac{\Sigma_{\rm s,0}}{\rm l_s}}\right)$, and the symbols are colour-coded according to their $\log\left(\alpha_0^2\right)$ values. The y-axis of the plot is better correlated with $\Sigma_{\rm SFR,0}$ than α_0^2 is. $\rm Log\left(\alpha_0\sqrt{\frac{\Sigma_{s,0}}{l_s}}\right)$ increases with increasing $\Sigma_{\rm SFR,0}$ and increasing α_0^2. In order to compare the model with the single-fluid Q model, the model $\Sigma_{\rm SFR,0}$ was calculated using α_0 and $\Sigma_{s,0}$ values from this analysis. For the calculation of $\Sigma_{\rm SFR,0Model}$ I used Equation 6.8 and assumed $\sigma_g = 7\,{\rm km/s}$ and $Q_{WS} = 1.6$ (e.g., Leroy et al. 2008, Zheng et al. 2013). $\frac{\Sigma_{\rm SFR,0Model}}{\epsilon_{\rm orb}}$ was calculated and plotted in order to fit for ϵ_{orb}. Figure 6.20 shows a comparison between the model $\Sigma_{\rm SFR,0}$ and the $\Sigma_{\rm SFR,0}$ determined from Hα and $W4$ observations. The gradient of the logarithmic comparison between the model and the observed $\Sigma_{\rm SFR,0}$ equals one if the model fits the data and the y-intercept of the plot is ϵ_{orb} (because $\log\frac{\Sigma_{\rm SFR,0Model}}{\epsilon_{\rm orb}}$ is plotted in the Figure). Fitting for ϵ_{orb} allows us to test whether ϵ_{orb} between our galaxies is constant and matches the value found by Kennicutt (1998). The correlation coefficients between the model and observed $\Sigma_{\rm SFR,0}$ are $\zeta_S = 0.48$ and $\zeta_P = 0.49$. There is a large spread around the best linear fit ($\sigma_{\rm fit} = 0.67$, and the gradient of the best fit line is 0.51. The slope is much shallower than 1.0, which indicates that the data does not follow the same relation that

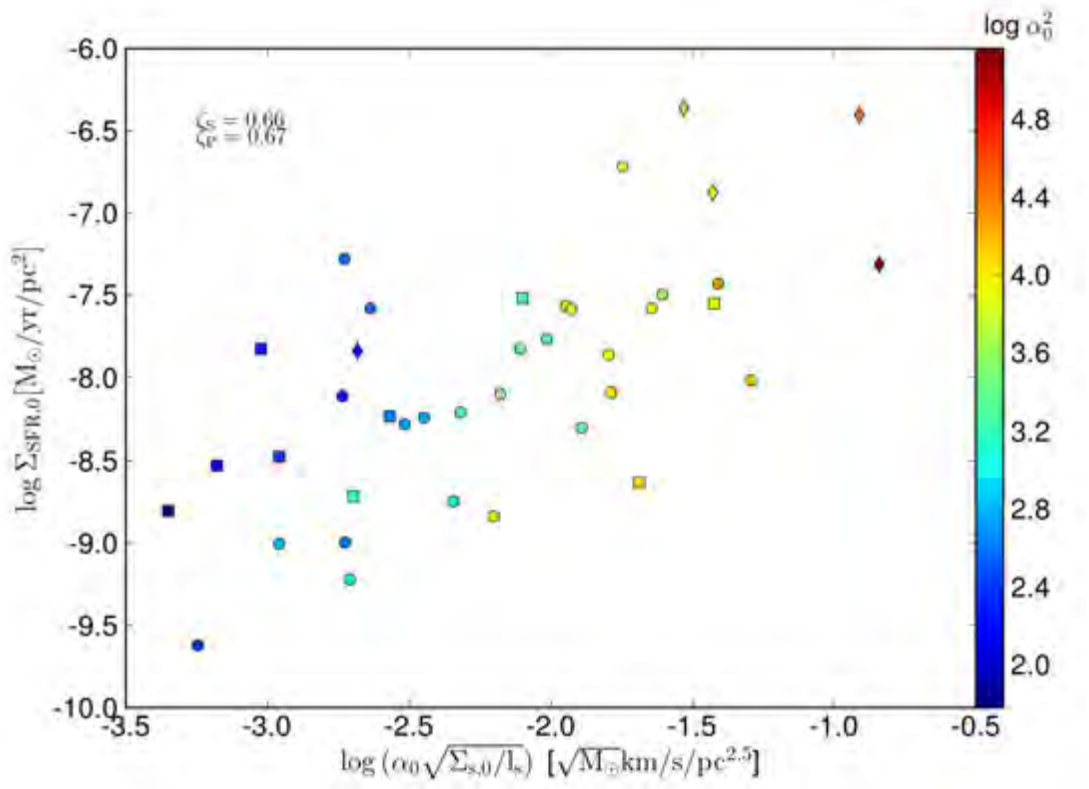

Figure 6.19: The $\Sigma_{\rm SFR,0}$ calculated from the Hα and W4 emission plotted against $\log\left(\alpha_0\sqrt{\frac{\Sigma_{\rm s,0}}{\rm l_s}}\right)$. Symbols are the same as Figure 6.1 and are colour-coded according to their $\log\alpha_0^2$ values.

the model does. This implies that the ϵ_{orb} is not constant, which confirms what was found in the Q_g analysis. If the gradient of the best fit line is fixed, the mean ϵ_{orb} is unphysically large (19.8).The assumed Q_{WS} values used in Figure 6.24 were varied from 1.0 to 10, but this did not result in reasonable mean ϵ_{orb} values. $\Sigma_{g,0}$ of each galaxy is calculated using the t_{orb} star formation law (with $\epsilon_{orb} = 0.03$) and the values that are calculated are in general much higher than would be expected.

Therefore even the two-fluid model that uses the t_{orb} model does not fit the data. Similar to the single-fluid model result this suggests that the Kennicutt (1998) t_{orb} star formation law does not hold for the central parts of galaxies and therefore cannot be used for the constant Q_{WS} model. This agrees with results such as Krumholz et al. (2012) and Krumholz & Kruijssen (2015) who showed that the t_{orb} star formation law is different for different spatial scales and that there can be a large scatter in that relation in the inner parts of galaxies. The modeled ϵ_{orb} parameter of the t_{orb} star formation

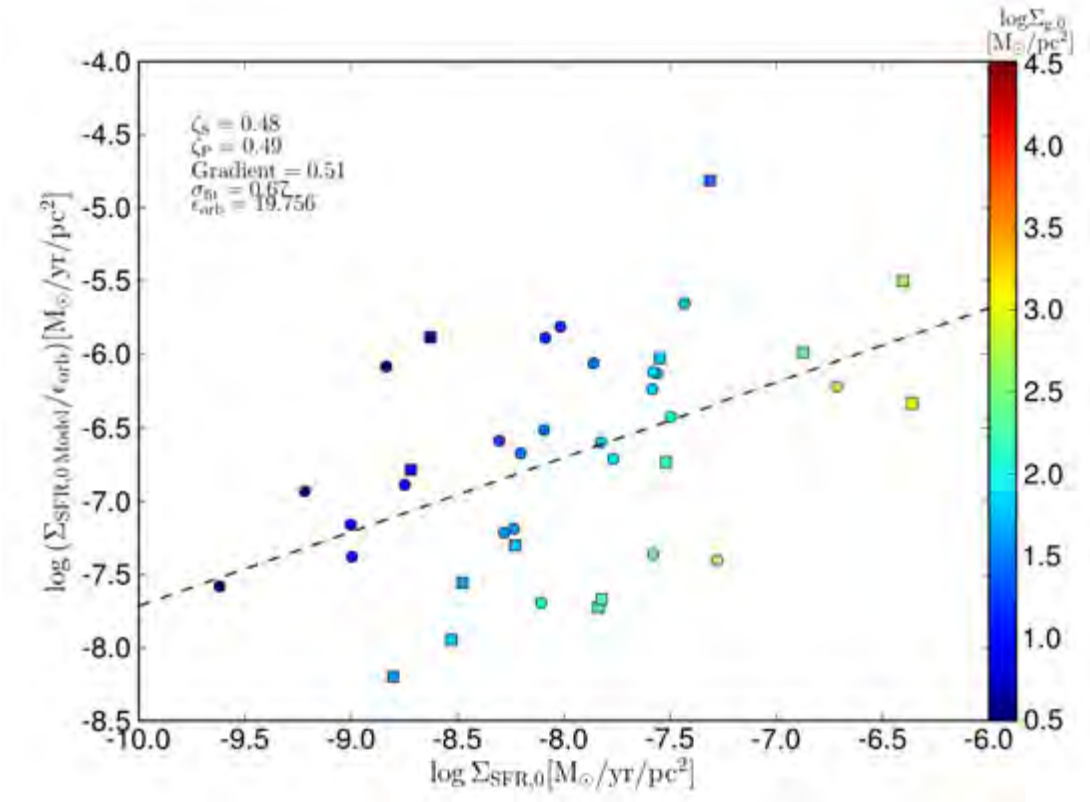

Figure 6.20: $\Sigma_{\rm SFR,0}$ calculated from the constant Q_{WS} and t_{orb} star formation law model plotted against the total $\Sigma_{\rm SFR,0}$ calculated from the Hα and W4 emission. Symbols are the same as Figure 6.1 and are colour-coded according to the $\Sigma_{g,0}$ of each galaxy, which were determined using the t_{orb} star formation law (with $\epsilon_{orb} = 0.03$).

law is not the same as that found by Kennicutt (1998) and is not constant between the different galaxy centers in our sample. The result is also consistent with a varying Q_{WS} such as seen in the inner regions of many galaxies (e.g., Leroy et al. 2008, Zheng et al. 2013).

6.2.2 Molecular Star Formation Law Analysis

If I assume that the Bigiel et al. (2008) molecular Star Formation Law (MSFL) holds, that disks have a constant Q_{WS} and a rotation curve with a constant inner gradient; the relation between $\Sigma_{\rm SFR}$, Σ_s and α was determined to be (in the expanded form) :

$$\Sigma_{\rm SFR} = A_1 \left(\frac{2\sigma_g \alpha \Sigma_s}{\pi G Q_{WS} \left(81\, M_\odot/pc^2 + \Sigma_s\right)} - \frac{\sigma_g \Sigma_s^{1.5}}{\sqrt{G l_s}\left(81\, M_\odot/pc^2 + \Sigma_s\right)} \right). \tag{6.9}$$

This relationship was derived using the Leroy et al. (2008) relationship between the molecular fraction R_{mol} and Σ_s. The constant A_1 is the MSFL constant of proportionality. For simplicity I will refer to $\left(\frac{2\sigma_g\alpha_0\Sigma_{s,0}}{\pi GQ_{WS}(81+\Sigma_{s,0})}\right)$ as Σ_a and $\left(\frac{\sigma_g\Sigma_{s,0}^{1.5}}{\sqrt{Gl_s}(81+\Sigma_{s,0})}\right)$ as Σ_b because they are both in surface density units. The central star formation surface density is plotted against Σ_b in Figure 6.21 and the data are colour-coded by $\log\Sigma_a$. Calculations of Σ_a and Σ_b were made assuming $\sigma_g = 7.2\,\mathrm{km/s}$ (Mogotsi et al. 2016) (as is used for the rest of this analysis) and $Q_{WS} = 1.7$ (e.g., Leroy et al. 2008, Zheng et al. 2013). There is a correlation between $\log\Sigma_b$ and $\log\Sigma_{\mathrm{SFR},0}$, the correlation coefficients are $\zeta_S = 0.78$ and $\zeta_P = 0.79$ respectively. The Σ_a values tend to increase with increasing $\Sigma_{\mathrm{SFR},0}$ and Σ_b. In order to study this $\Sigma_{\mathrm{SFR},0}$ is plotted against Σ_a, with a colourbar denoting Σ_b in Figure 6.22. The correlation coefficients between $\Sigma_{\mathrm{SFR},0}$ and Σ_a are $\zeta_S = 0.72$ and $\zeta_P = 0.71$ respectively. Therefore $\Sigma_{\mathrm{SFR},0}$ is correlated with both Σ_a and Σ_b.

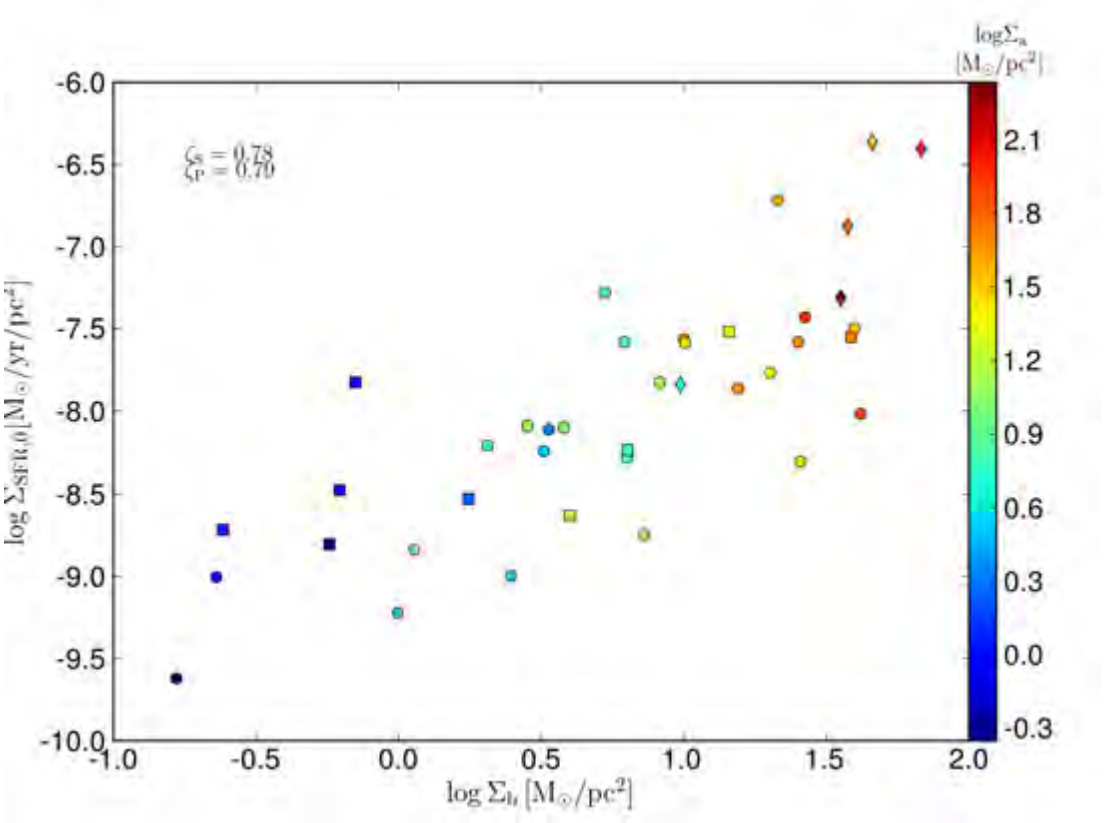

Figure 6.21: The $\Sigma_{\mathrm{SFR},0}$ is plotted against $\log(\Sigma_\mathrm{b})$. Symbols are the same as in Figure 6.1 and are colour-coded according to their $\log(\Sigma_\mathrm{a})$ values.

In this model if $\Sigma_b > \Sigma_a$ then there is no star formation. This is problematic because resolved extragalactic studies at hundreds of parsec scales and larger show that as long as there is a gas reservoir star formation occurs even in areas of high disk stability.

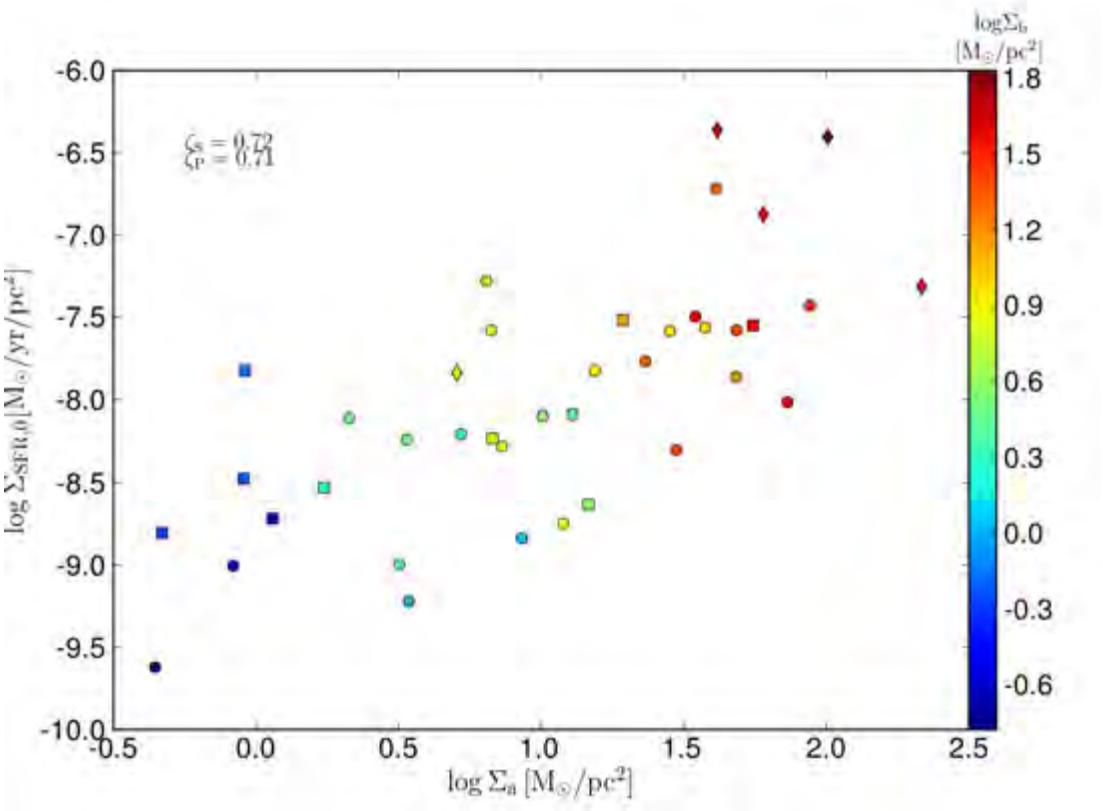

Figure 6.22: The $\Sigma_{\mathrm{SFR},0}$ is plotted against $\log(\Sigma_{\mathrm{a}})$. Symbols are the same as in Figure 6.1 and are colour-coded according to their $\log(\Sigma_{\mathrm{b}})$ values.

For constant Σ_s and α, as Q_{WS} increases the predicted $\Sigma_{\mathrm{SFR},0}$ decreases. The stability parameter only affects Σ_a, the two are inversely proportional to each other. Higher Σ_a results in higher $\Sigma_{\mathrm{SFR},0}$. The relationship between Σ_a, Σ_b, Q_{WS} and $\Sigma_{\mathrm{SFR},0}$ is explored in Figure 6.23. In the figure the product of Q_{WS} and Σ_a (which removes the dependence of Σ_a on Q_{WS}) is plotted against Σ_b. Lines of $\Sigma_a = \Sigma_b$ are plotted for different Q_{WS} values in the figure, this was done for ($Q_{WS} = 1$, 1.6 and 4). The plot shows that star formation is predicted to occur for all of our galaxy centers if they have $Q_{WS} = 1$, for higher Q_{WS} values fewer galaxy centers are predicted to form stars. When Q_{WS} is assumed to be equal to 1.6 as has been done in Figures 6.21 and 6.22 the occurrence of star formation does not seem correlated with the measured $\Sigma_{\mathrm{SFR},0}$. Galaxies for which the model does not predict star formation would occur at high Q_{WS} have a large range of $\Sigma_{\mathrm{SFR},0}$ values. The same is true when the plot is made for $\Sigma_{s,0}$ and $\Sigma_{g,0}$ (Calculated by using the Bigiel et al. 2008 total gas star formation law). According to the model the value of Q_{WS} is important in determining whether star formation will occur.

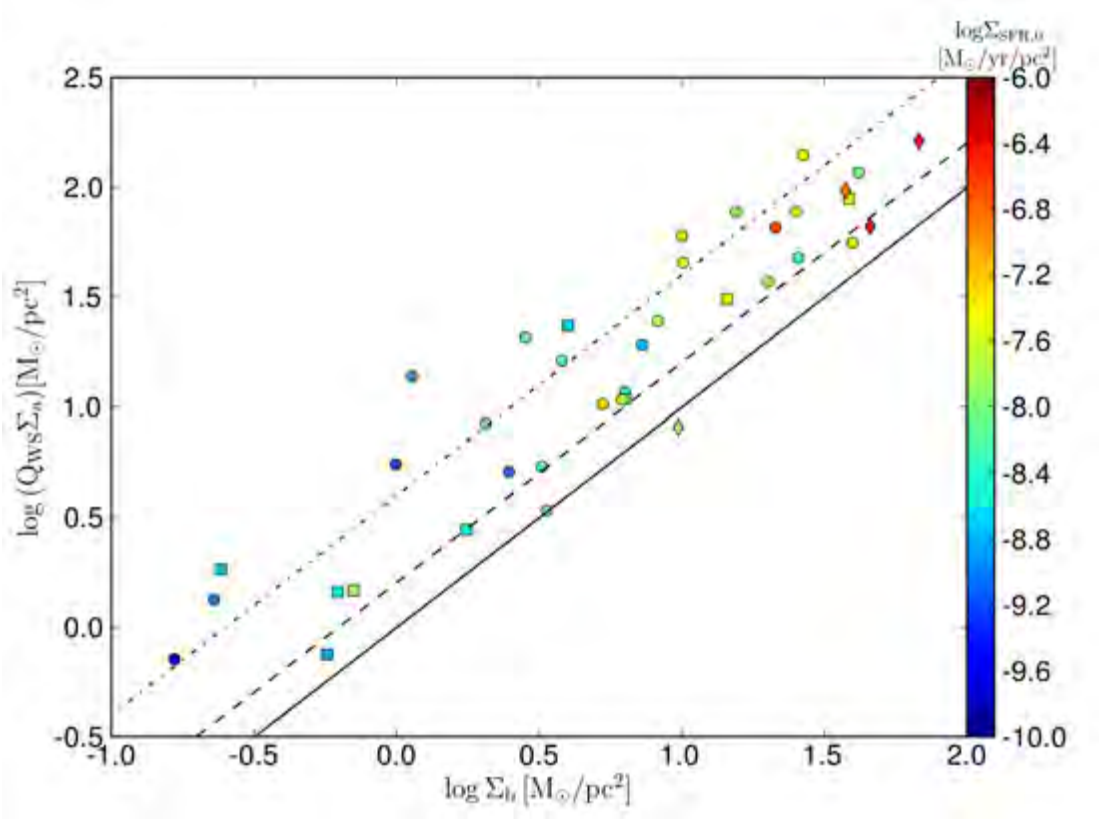

Figure 6.23: The $\Sigma_{\rm SFR,0}$ plotted against $\log(\Sigma_{\rm b})$. Symbols are the same as in Figure 6.1 and are colour-coded according to their $\log(\Sigma_{\rm a})$ values. The black diagonal lines are lines where $\Sigma_a = \Sigma_b$ for different Q_{WS} values: $Q_{WS} = 1.0$ is the solid line, $Q_{WS} = 1.6$ is the dashed line, and $Q_{WS} = 4.0$ is the dashed-dot line.

The value of the stability parameter is very important in this model, and next I perform studies to determine what value of Q_{WS} is required to match the observations and whether this value is constant across the sample. This will help to determine whether the model can describe the data. The gas depletion time is another important property to study in this analysis. Figure 6.24 and 6.25 show lines of constant Q_{WS} (Figure 6.24) and t_{dep} (Figure 6.25) plotted over the data. The lines of constant Q_{WS} were made assuming $t_{dep} = 2\,\mathrm{Gyr}$, which is expected for molecular gas dominated central regions of nearby disk galaxies. This was done for Q_{WS} values that ranged between 1 and 4 and for different values of Σ_b. The t_{dep} values are molecular gas depletion times. Figure 6.24 shows that the ranges of Q_{WS} at $t_{dep} = 2\,\mathrm{Gyr}$ are not enough to explain the $\Sigma_{\rm SFR,0}$ and Σ_b values of most of the galaxy centers. There are galaxies with high and low $\Sigma_{\rm SFR,0}$ values that would have to have much lower and higher Q_{WS} values than are typically found in the inner parts of galaxies (see Leroy et al. 2008, Zheng et al. 2008). Figure 6.25 shows that models with the typical range of t_{dep} values found for galaxies

can explain the $\Sigma_{\rm SFR,0}$ and Σ_b values of the galaxy centers. The high $\Sigma_{\rm SFR,0}$ galaxy centers are best described by a model with $t_{dep} \sim 0.1\,{\rm Gyr}$ and the very low $\Sigma_{\rm SFR,0}$ centers by models with t_{dep} reaching as high as 100 Gyr. It should be noted again that the t_{dep} values were not calculated from direct measurements of the gas surface density and $\Sigma_{\rm SFR}$. They are calculated by using our model and assumptions, therefore these values are theoretical and subject to the uncertainties of the models.

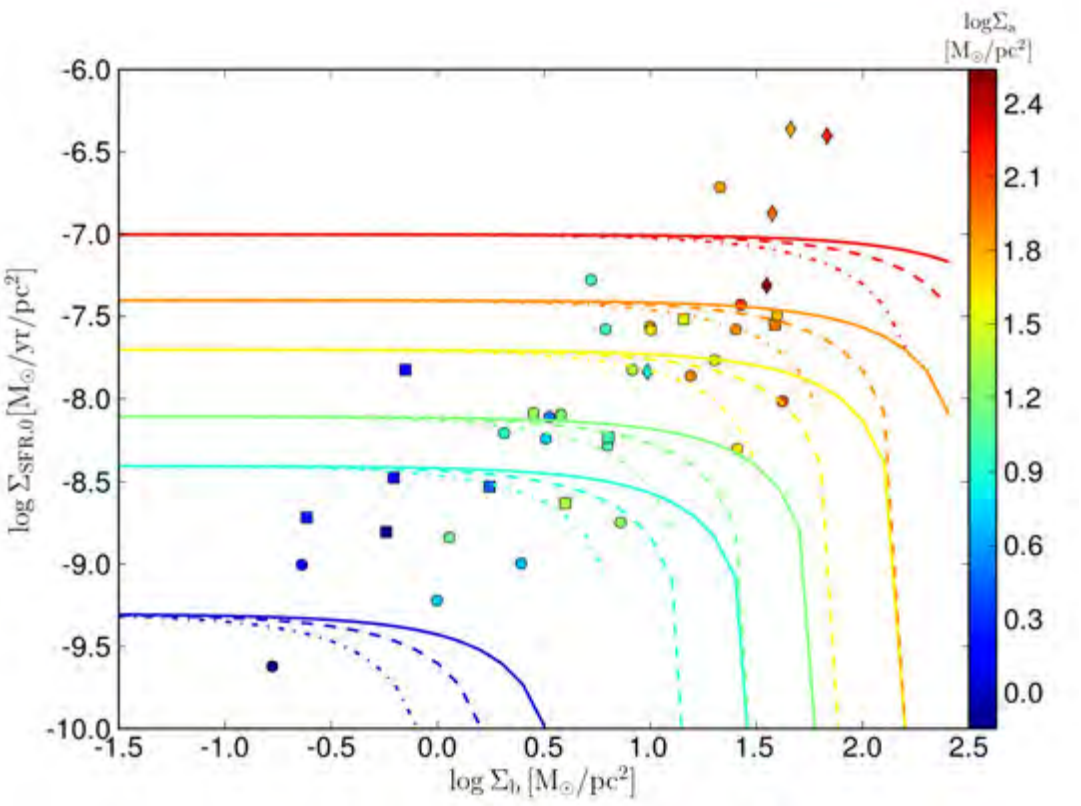

Figure 6.24: Same as Figure 6.21 but with lines of constant Q plotted over the data. Solid lines represent $Q = 4.0$, dashed lines $Q = 2.0$ and dashed-dot lines are for $Q = 1.0$ they are colour coded according to their $\log(\Sigma_{\rm b})$ values. The lines are of: $\log(\Sigma_{\rm b}) =$ 0.0, 0.9, 1.2, 1.6, 1.9, and 2.3.

The model $\Sigma_{\rm SFR,0}$ was calculated using Equation 6.9 in order to test the model. $Log\left(\frac{\Sigma_{\rm SFR,0Model}}{\rm A_1}\right)$ is plotted against $\log\Sigma_{\rm SFR,0}$in Figures 6.26. The gas surface density Σ_g was calculated using the MSFL and the Bigiel et al. (2008) A_1 value: $A_1 = 10^{-3.06}\,{\rm Myr}^{-1}$. This is based on the assumption that the molecular gas is the dominant gas component in galaxy centers. If the slope of the best fit line in the plots is one this would indicate that the model matches the observed $\Sigma_{\rm SFR,0}$. The model param-

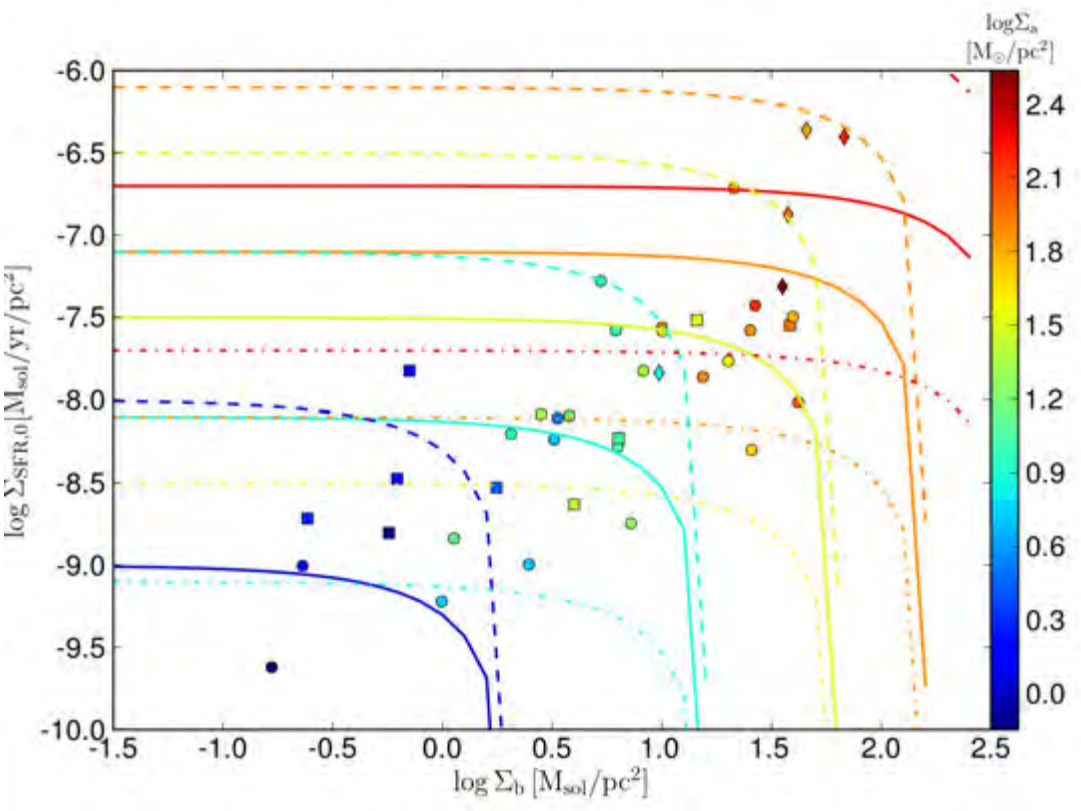

Figure 6.25: Same as Figure 6.21 but with lines of constant t_{dep} plotted over the data. Solid lines represent $t_{dep} = 1\,\mathrm{Gyr}$, dashed lines $t_{dep} = 0.1\,\mathrm{Gyr}$ and dashed-dot lines are for $t_{dep} = 10\,\mathrm{Gyr}$ they are colour coded according to their $\log(\Sigma_\mathrm{b})$ values. The lines are of: $\log(\Sigma_\mathrm{b}) = 0.0$, 0.9, 1.5, 1.9, and 2.3.

eter $\Sigma_{\mathrm{SFR},0}$ is plotted in order to determine A_1 from the y-intercept. Figure 6.26 has $\frac{\Sigma_{\mathrm{SFR,0Model}}}{\mathrm{A_1}}$ calculated for a disk with $Q_{WS} = 1.6$. The model that uses this value of Q_{WS} predicts that star formation should occur for most galaxies in the sample. The slope of the best fit line to the data in the plot is 0.61 , $\sigma_{\mathrm{fit}} = 0.67$ and the correlation coefficients are $\zeta_S = 0.58$ and $\zeta_P = 0.55$ respectively. The gradient of the fitted line is not unity, therefore the model does not fit the data. If the slope is fixed to unity the fitted molecular $t_{dep} = 0.44\,\mathrm{Gyr}$. If Q_{WS} is set to 1, the slope of the fit and correlation coefficients are roughly constant but if the slope is fixed to unity the fitted molecular $t_{dep} = 1.1\,Gyr$. The best fit t_{dep} in the $Q_{WS} = 1.6$ case is lower than typical measurements made within nearby galaxies (e.g., Leroy et al. 2008, Bigiel et al. 2008, Bigiel et al. 2011), even studies Saintonge et al. (2012) who studied the global t_{dep} for a large sample of galaxies found higher t_{dep} values than this. Such low t_{dep} have been shown to be possible when resolved studies high density gas studies of galactic molecular clouds are made (e.g., Heiderman et al. 2010, Lada et al. 2010, Lada et

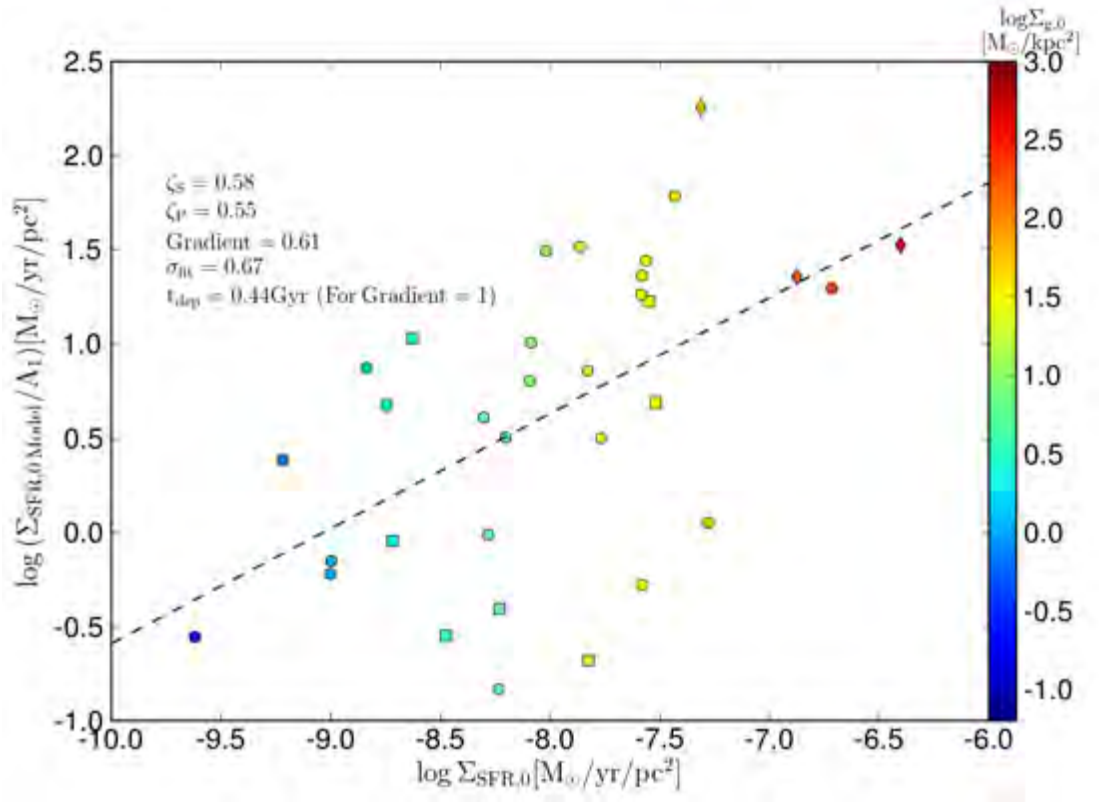

Figure 6.26: $\Sigma_{\rm SFR,0}$ calculated from the constant Q_{WS} and MSFL model plotted against the total $\Sigma_{\rm SFR,0}$ calculated from the Hα and W4 emission. The model $\Sigma_{\rm SFR,0}$ was calculated for $Q_{WS} = 1.6$. Symbols are the same as Figure 6.1 and are colour-coded according to the $\Sigma_{g,0}$ of each galaxy, which were determined using the MSFL (with $A_1 = 10^{-3.06}\,{\rm Myr}^{-1}$).

al. 2012, Krumholz et al. 2012, Kruijssen et al. 2014). These low Q_{WS} are plausible for some galaxy centers, however the following analysis shows that most of our galaxy centers have higher Q_{WS} values. The fitted slope is not unity for either of the Q_{WS} values that were used therefore A_1 (hence t_{dep}) is not constant for all of our galaxies.

The other assumption used in the model along with the MSFL is that Q_{WS} is constant. The Q_{WS} values based on the MSFL are examined in Figure 6.27 and Figure 6.28. The central gas surface density $\Sigma_{g,0}$ was calculated by using the MSFL, the Bigiel et al. (2008) total gas value for A_1 ($A_1 = 10^{-9.06}\,{\rm yr}^{-1}$) and the Leroy et al. (2008) R_{mol} to Σ_s relation. The $\Sigma_{g,0}$ was used to calculate Q_g, which was used along with $\Sigma_{s,0}$ to calculate Q_{WS}. The two-fluid stability parameter Q_{WS} is plotted against $\Sigma_{\rm SFR,0}$ in Figure 6.27. The plot shows that Q_{WS} decreases with increasing $\Sigma_{\rm SFR,0}$ and the best

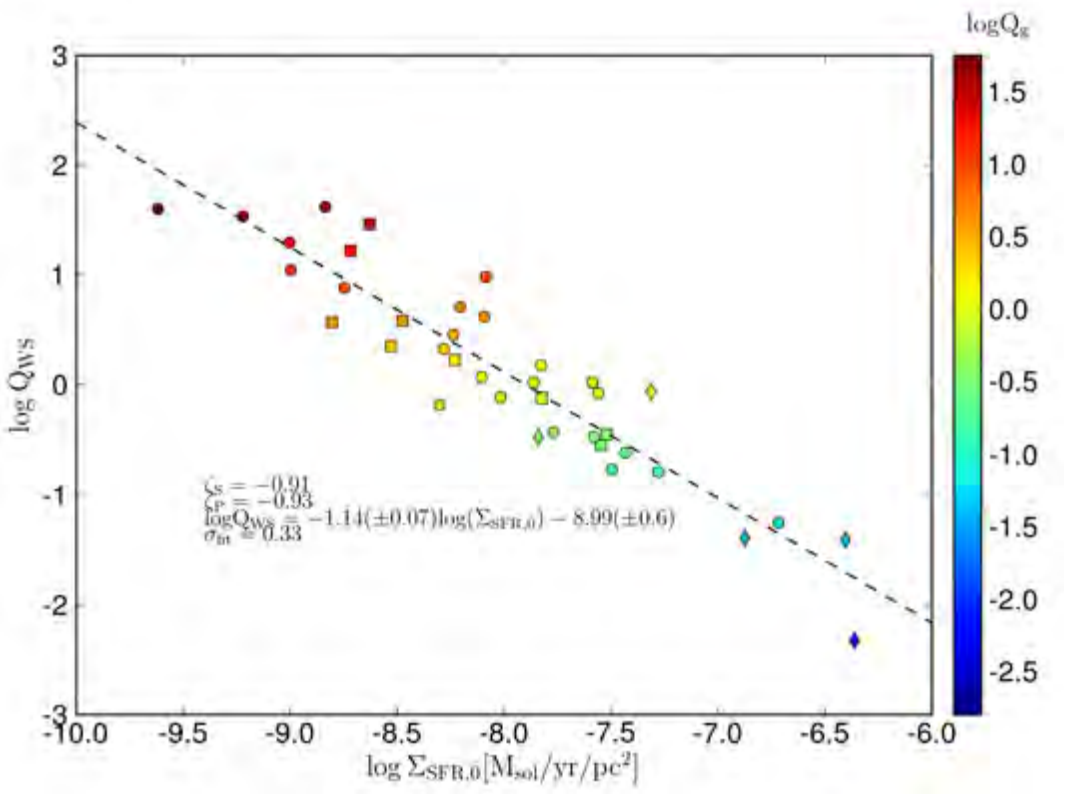

Figure 6.27: The two-fluid stability paramter Q_{WS} plotted against $\Sigma_{\rm SFR,0}$. Data points are colour-coded according to their $\log Q_g$ values. $\Sigma_{g,0}$ values were calculated using the MSFL.

linear fit to the data in the plot is: $\log Q_{WS} = -1.14(\pm0.07)\log(\Sigma_{SFR,0}) - 8.99(\pm0.60)$. The correlation coefficients between the parameters are $|\zeta_S| = 0.91$ and $|\zeta_P| = 0.93$ and the dispersion around the fitted line is $\mathrm{sigma_{fit}} = 0.33$. The stability parameter Q_{WS} is plotted against $\Sigma_{g,0}/\Sigma_{s,0}$ in Figure 6.28. The central gas surface density was calculated in the same manner as for Figure 6.27. Galaxies with the highest gas fractions have the lowest Q_{WS}. The best linear fit to the data in the plot is: $\log Q_{WS} = -1.3(\pm0.2)\log(\Sigma_{g,0}/\Sigma_{s,0}) - 0.42(\pm0.13)$. The correlation coefficients between the parameters are $|\zeta_S| = 0.62$ and $|\zeta_P| = 0.73$, and $\sigma_{\rm fit} = 0.62$. Low t_{dep} values are found in galaxies with high star formation rates and gas densities (e.g., Genzel et al 2010), and these result in a higher A_1 than the Bigiel et al. (2008) fit. If A_1 is increased for the high $\Sigma_{\rm SFR,0}$ galaxies the slopes of the relationships shown in Figures 6.27 and 6.28 increase. These plots show that the Q_g and Q_{WS} values of our galaxy centers are not constant. Stability parameters range from 10^{-2} to $10^{1.5}$. Most of the galaxy centers have Q_{WS} values greater than 1, and the high $\Sigma_{\rm SFR,0}$ galaxy centers are the least stable. These galaxies have the highest gas to stellar surface density ratios. The maximum Q_{WS} and minimum values are beyond what was found by Leroy et al.

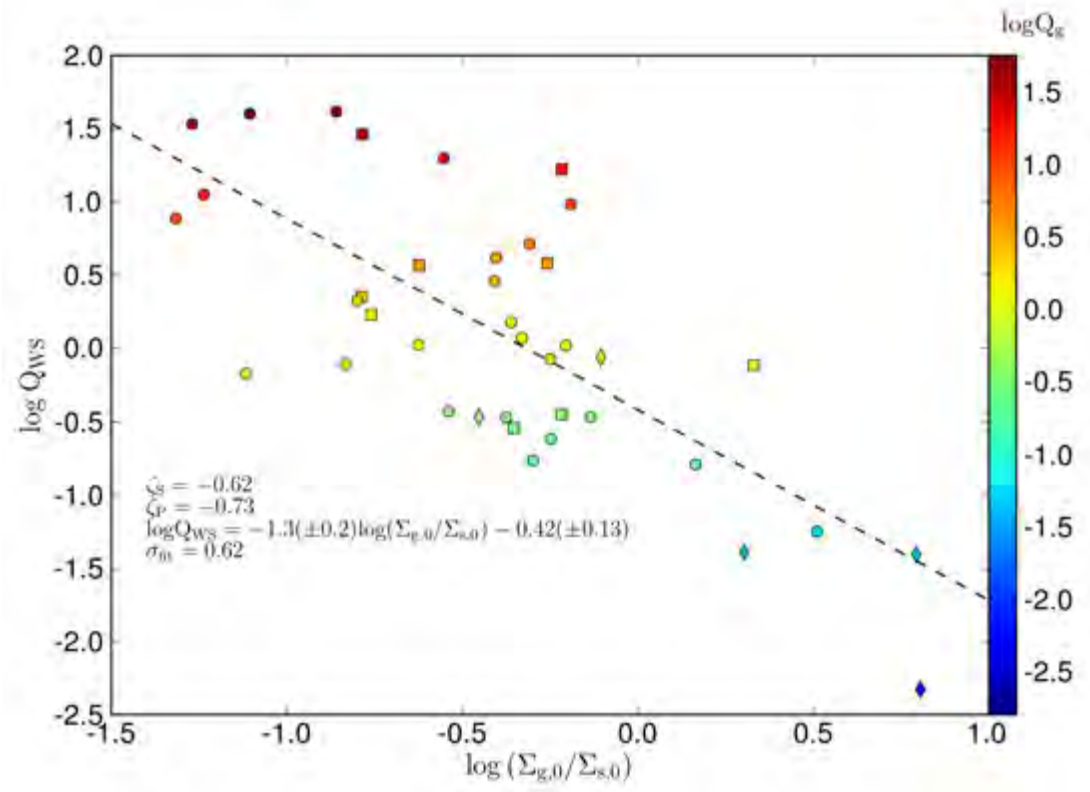

Figure 6.28: The two-fluid stability paramter Q_{WS} plotted against $\Sigma_{g,0}/\Sigma_{s,0}$. Data points are coloured according to their $\log Q_g$ values. $\Sigma_{g,0}$ values were calculated using the MSFL.

(2008) and Zheng et al. (2013). Galaxy centers with the highest gas-to-stellar surface densities are the least stable and they have the highest $\Sigma_{\mathrm{SFR},0}$.

The two-fluid stability parameter Q_{WS} provides a more complex model to describe the stability of the disk, and it incorporates the effect of the stellar disk, which is an important component of the inner disk. The results from using Q_{WS} did not result in significantly better fits and correlations to the data compared to what I found when I used Q_g. The analysis confirmed that there is a large variation in the Q_{WS}, efficiency parameters of the star formation laws (e.g., ϵ_{orb}, t_{dep}) between our galaxy centers. Therefore these models cannot fully fit our data, but I can still see correlations predicted by our models.

6.2.3 The Star Formation Surface Density and $\Sigma_{\rm SFR}$ Relation

The models in this section that are derived from the Q_{WS} stability parameterization incorporate the effect of the stars on the stability of the disk in order to model how the star formation distribution is related to dynamics of the galaxy. However, in Chapter 5 I also derived a relationship between the steepness of the inner gravitational potential well (traced by α_0) and $\Sigma_{s,0}$: $\alpha_0 \propto \Sigma_{s,0}^{0.5}$. Earlier in this section I derived a relationship between the steepness of the potential well and $\Sigma_{\rm SFR,0}$: $\Sigma_{\rm SFR,0} \propto \alpha_0^2$. Combining these two I find: $\Sigma_{s,0} \propto \alpha_0^2 \propto \Sigma_{\rm SFR,0}$, therefore $\Sigma_{s,0} \propto \Sigma_{\rm SFR,0}$. In order to test this relation I plotted $\Sigma_{s,0}$ against $\Sigma_{\rm SFR,0}$ in Figure 6.29, and the data points were colour-coded by their $\Sigma_{g,0}$ values. The $\Sigma_{g,0}$ values were calculated from the $\Sigma_{\rm SFR,0}$ using the MSFL and assuming $A_1 = 10^{-9.06}$ yr (Bigiel et al. 2008). As discussed earlier, J1103-23:S1 has very high $\Sigma_{\rm SFR,0}$ and is therefore not shown in the plot. The plot shows that there is a correlation between $\Sigma_{s,0}$ and $\Sigma_{SFR,0}$, and the correlation coefficients for the data in the plot are $\zeta_S = 0.77$ and $\zeta_P = 0.77$ and $\sigma_{\rm fit} = 0.47$. The best linear fit to the data is found to be:

$$\log \Sigma_{s,0} = 0.7(\pm 0.1) \log(\Sigma_{SFR,0}) - 9.35(\pm 0.2). \tag{6.10}$$

This is a tighter correlation and slope closer to the model than was found between α_0 and $\Sigma_{\rm SFR,0}$.

The correlation found between $\Sigma_{s,0}$ and $\Sigma_{\rm SFR,0}$ and a fitted power-law index that is close to the model value indicates that the stellar potential is closely linked to the density of star formation in galaxy centers. The higher correlation coefficient and a fit that is closer to the model compared to what was found for the α_0 – $\Sigma_{\rm SFR,0}$ correlations can be studied by examining the relationship between α_0 and $\Sigma_{s,0}$. In this analysis I found a correlation between α_0 and $\Sigma_{s,0}$. In the case of the R-band analysis the power-law index of the $\alpha_0 \propto \Sigma_{s,0}$ was less than the model value. The relationship is also dependent on disk thickness. The relation between the disk thickness and disk scale length are not constant between galaxies. Bizyaev & Mitronova (2002, 2009), Mosenkov et al. (2010) and Bizyaev et al. (2014) found that the ratio between the disk scale length and scale height ranges between 2.5 and 4.8. Therefore α_0 does not perfectly trace $\Sigma_{s,0}$. The central velocity gradient α_0 is a tracer of the potential well of a galaxy and in this analysis I showed that galaxy centers have a large range of f_b values. About 50% of galaxy centers were best described by models with $f_b = 1$, there are therefore galaxy centers best described by models where f_b (which is assumed to be dominated by the stars) is less than 0.5 . In the f_b analysis the calculated Δz from the exponential scale lengths are likely underestimating the true disk thicknesses.

Larger Δz values would result in lower f_b, therefore the number of galaxy centers where $f_b < 0.5$ is underestimated. With this in mind the correlation between $\Sigma_{s,0}$ and $\Sigma_{\rm SFR,0}$ suggests that $\Sigma_{\rm SFR,0}$ is better correlated with the Σ_s than with the total mass density. This correlation indicates that the conditions for high Σ_s and high $\Sigma_{\rm SFR}$ are similar. The low variation in Σ_{HI} seen by Walter et al. (2008) (factor ~ 2) in the optical disks of galaxies, the saturation of H I seen by Bigiel et al. (2008) and the tight correlation of the MSFL (e.g., Schruba et al. 2011) indicate that the change in Σ_{H2} is what what drives changes in $\Sigma_{\rm SFR,0}$ in these regions. Therefore for high Σ_g (above the H I saturation threshold) increasing R_{mol} tends to result in $\Sigma_{\rm SFR}$ increases. If the MSFL holds and the interstellar radiation field is correlated with the star formation rate then the molecular fraction is correlated with P_h (Elmegreen 1993). The molecular fraction R_{mol} and Σ_s are correlated with r and P_h. Leroy et al. (2008) showed that Σ_s is tightly correlated with R_{mol}, and therefore must be correlated with $\Sigma_{\rm SFR}$. Dopita & Ryder (1994) extended the Kennicutt-Schmidt law to include the effect of $\Sigma_{s,0}$ on $\Sigma_{\rm SFR}$ resulting in their $\Sigma_{\rm SFR} \propto \Sigma_s^{n_1}\Sigma_g^{n_2}$ relation. Their models indicated that if $n_2 = 0$ then a varying n_1 can be used to fit the data. Shi et al. (2011) also developed a star formation law where $\Sigma_{\rm SFR}$ is proportional to $\Sigma_s^{n_1}\Sigma_g^{n_2}$, based on the star formation efficiency being a function of the Σ_s. However, they found that $n_1 = 0.36 \pm 0.04$ which suggests that a Σ_g ($n_2 = 1.13 \pm 0.05$) has a much stronger influence on $\Sigma_{\rm SFR,0}$ than Σ_s.

Another way to view the relation is that the ratio between the star formation rate and stellar mass is the specific star formation ($sSFR$), therefore the relation in Figure 6.29 suggests that the specific star formation of these galaxy centers is constant. There is a tight correlation between the star formation rate and stellar mass (e.g., Elbaz et al. 2007, Noeske et al. 2007, Karim et al. 2011 and Wyuts et al. 2011, Speagle et al. 2014) out to a redshift of ~ 2, this is also known as the star forming sequence. The slope of the relation is the $sSFR$ and the dispersion around the mean slope is attributed to different star formation histories and short-term variations in the star formation rates (Dutton et al. 2010, Sparre et al. 2015). The dispersion of the $sSFR$ is ~ 0.3 dex for a wide range of galaxy masses (e.g., Rodighiero et al. 2011, Schreiber et al. 2015, Lilly et al. 2013) , but increases for nearby galaxies. This study focuses on the inner regions of galaxies where there is a large variation in the recent star formation history of galaxies. But the results of the fit indicate that the $sSFR$ relatively constant for these galaxy centers and the dispersion of the relation is comparable to what is found for other studies of nearby galaxies (e.g., Guo et al. 2015).

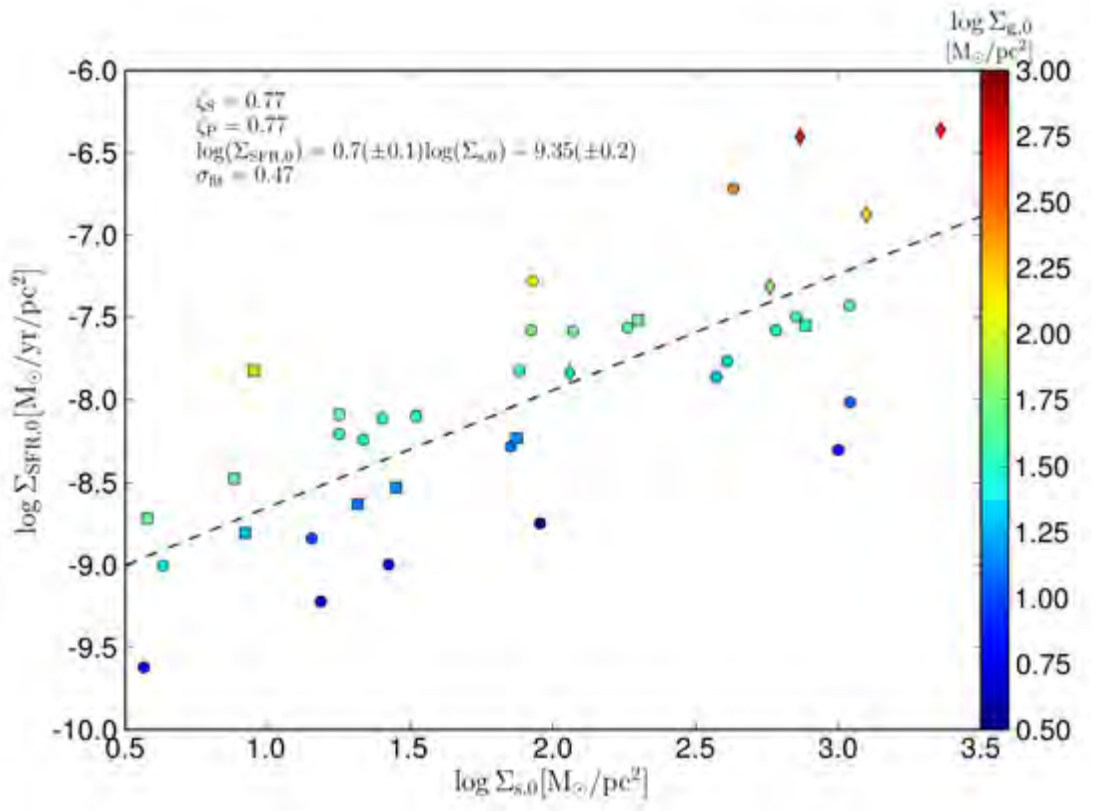

Figure 6.29: $\log \Sigma_{s,0}$ plotted against $\log \Sigma_{\rm SFR,0}$. The data points are colour-coded according to their $\log \Sigma_{g,0}$. The $\Sigma_{g,0}$ values were calculated from $\Sigma_{\rm SFR,0}$ using the MSFL. The best linear fit is shown as a dashed line.

6.2.4 Discussion

Whether I use the Q_g, or various Q_{WS} models the t_{dep}, ϵ_{orb} and Q varies widely between galaxy centers. *In this section I will discuss the ranges seen in implied t_{dep} and Q values.* Resolved nearby galaxy studies such as Leroy et al. (2008) and Bigiel et al. (2011) show that on average galaxies have constant molecular t_{dep}. The variation seen in our sample is about 4 dex (0.1 to 100 Gyr) is larger than that seen in the central regions of the Leroy et al. (2008) study. Studies such as Bigiel et al. (2008), Genzel et al. (2010) and Krumholz et al. (2012) showed that highly star forming galaxies such as starburst galaxies have lower t_{dep} values than more passive galaxies. Saintonge et al. (2012) who studied the globally averaged star formation and galaxy properties of a much wider sample than Bigiel et al. (2008) and Leroy et al. (2008), showed that inner structures such as bars and bulges affect the t_{dep} of galaxies. However, the variation in their t_{dep} values was $\sim$ 1 dex. These studies focused on molecular gas, but they also analyzed the H I and total gas behaviour. The star formation efficiency (hence t_{dep}) of the total gas is expected to be similar to that of the molecular gas in regions where the

molecular gas dominates the gas surface density (above $\Sigma_g \sim 10\,M_\odot/yr$). Variations in H I and total t_{dep} of these studies was less than what was found in this study. Lelli et al. (2014) and Filho et al. (2016) found similar (and sometimes greater) ranges in their studies of dwarf galaxies. Leroy et al. (2013) found that t_{dep} is affected by the total stellar mass, dust-to-gas ratio, metallicity, t_{orb} and morphology of galaxies with $M_s < 10^8\,M_\odot$. The gas surface density can trace some of these effects because even in the Bigiel et al. (2008) MSFL plots there are three regimes evident (a low density, intermediate density and high density regime). The low density regime ($\Sigma_g < 10 M_{sol}$) is where the molecular gas is not dominant, N has a much steeper slope than $N \sim 1.4$ and $\Sigma_{\rm SFR}$ is not as well correlated to Σ_g as in other regimes (Bigiel et al. 2008, Kennicutt & Evans 2012), the resultant depletion times in this regime are higher than the intermediate density (Σ_g ranging between 10 and $\sim 200 M_\odot/pc^2$) and high density regim ($\Sigma_g > 200 M_\odot$) (Bigiel et al. 2008, Kennicutt & Evans 2012). The intermediate regime is where the molecular gas studies by Leroy et al. 2008 are focused on and the high density regime is the low t_{dep} high star formation rate regime (e.g., Genze et al. 2010). It is important to note that the Kennicutt-Schmidt law does not have a constant N between all these regimes. Which shows the star formation law is dependent on the local gas density. The spatial resolution of the study also has an effect on measured star formation properties (Krumholz et al. 2012, Leroy et al. 2013, Kruijssen et al. 2014). The galaxies in our sample cover a wide range of properties and their central regions represent a wide range of environments, therefore the aforementioned properties will affect the t_{dep} and $\Sigma_{\rm SFR}$ in the central regions and result in the large variations seen in our galaxy centers.

Our results agree with studies by Leroy et al. (2008), Zheng et al. (2013) and Meurer et al. (2013) which show that Q_g and Q_{WS} are not constant in the inner parts of galaxies. Using the Kennicutt (1998) t_{orb} and the Bigiel et al. (2008) MSFL I find that Q_{WS} and Q_g vary from 0.03 to 300 (in the most extreme cases). These values are markedly different from the typical Q values found in the intermediate regions of disks, where Q_g and Q_{WS} are roughly constant. Most galaxy centers in our analysis have stability parameters that are greater than 1, and the very stable disks (ones with $Q > 10$) indicate very low star formation efficiencies (i.e., high t_{orb} values) or that not enough gas is being transported to the centers of galaxies. **Galaxies with the highest implied Q_g and Q_{WS} tend to have low $\Sigma_{\rm SFR,0}$ and $\Sigma_{g,0}$ values, less gas means less fuel for star formation. These very stable disks with little gas to fuel star formation contradict the self-regulating near-critical disk assumptions which the models are based on**.

The star formation laws I used in this analysis have efficiency constants : ϵ_{orb} and

A_1. But this analysis indicates that these are not constant between different galaxy centers, this is similar to what Krumholz et al. (2012) found when comparing data from various studies. The Q parameterizations and star formation laws used in the models assume that star formation is independent of galactic structure and the local environment. Stars form within molecular clouds, these assumptions suggest that on average their properties and ability to form stars should be independent on their environment. Bolatto et al. (2008) showed that the properties of giant molecular clouds are independent of environment, however detailed studies within galaxies by authors like Hughes et al. (2013) and Colombo et al. (2014) showed that molecular cloud properties are dependent on the environment. Our study focuses on galaxy centers, molecular clouds in these regions are affected by strong external pressures (e.g., Rathborne et al. 2014), radiation, cosmic rays and galactic shear (e.g., Kruijssen et al. 2014, Krumholz & Kruijssen 2015). It has been suggested that bulges can make galaxy disks more stable against collapse to form stars (Saintonge et al. 2012).

The availability of gas and efficiency of gas transport has been mentioned as a possible reason for the variation in Q. There are many factors which influence the availability and transport of gas to the central regions of galaxies. Bars can drive gas inwards to enhance star formation (e.g., Sakamoto et al. 1999, Sheth et al. 2005, Saintonge et al. 2012). The observed effect of bars on the gas transport and star formation depend whether the region is observed at the beginning of the bar driven inflow or when most of the gas has already been transported to the central regions (Jogee et al. 2005). Bars can can lead to the buildup of gas in molecular rings such as that found in the Central Molecular Zone (Molinari et al 2011). The high Σ_g and high levels of turbulence in these regions are similar to those found in high redshift galaxies (Kruijssen & Longmore 2013). As these regions evolve they move in the $\Sigma_{\rm SFR}$ – Σ_g plane and will have different t_{dep} and ϵ_{orb} depending on which part of their cycle they are observed in (Krumholz & Kruijssen 2015). The dynamics, environments and properties of clouds in the central regions does not match those in the intermediate or outer parts of disks (e.g. Kruijssen & Longmore 2013, Leroy et al. 2014, Rathborne et al. 2014). Therefore there is evidence that the local environment has an effect on the properties of molecular clouds and on how gas transported, both of which affect the rate and distribution of star formation. The dependence on the local environment and small-scale dynamics means that the assumptions required for the stability parameter and star formation laws break down.

Our analysis uses and extends star formation laws such as Kennicutt (1998), Bigiel

et al. (2008) to the central parts of galaxies. I also apply Q_g and Q_{WS} formulations that were developed for intermediate to the outer regions of thin disks. These star formation law parameters were not fitted in the central regions regions and the stability parameters were not developed for such conditions. These star formation rate laws and formulations of Q begin to break down at the centers due to the extreme and different conditions found here to where they were originally tested. As the spatial resolution of the observations increases and regions closer to galaxy centers are considered the small scale dynamics of the molecular clouds and their environments become more important. These effects vary between different galaxies centers resulting in the breakdown of Q_g and Q_{WS} as accurate stability parameterizations; and they result in different Q, t_{dep} and ϵ_{orb} values. Evidence of this is found the in the large ranges of implied Q, ϵ_{orb} and t_{dep} from the models. It should be noted that this is based on published values of these parameters, which have large uncertainties. Ideally the degeneracies between these parameters should be studied by using direct high quality (sensitivity and resolution) measurements of the gas density and other properties, however due to the lack of direct gas density measurements this is beyond the scope of this analysis.

6.2.5 Conclusion

Despite the uncertainties in the α_0 and $\Sigma_{\rm SFR}$ measurements, the validity of the different Q parameters and the star formation laws I find that there is a weak correlation between α_0 and $\Sigma_{\rm SFR,0}$; and there is one between $\Sigma_{s,0}$ and $\Sigma_{\rm SFR,0}$ as well. Therefore galaxy dynamics do affect the star formation surface density. However the results did not match the expectations from the models. The assumptions of constant Q disks breaks down because Q is not constant in our galaxy centers and the star formation laws do not seem constant (indicated by the large range in implied depletion times and depletion timescales) across our sample of galaxy centers. This is due to local dynamics of the central regions of galaxies and because of the large variation of galaxies in our sample. The high implied Q values also do not match the assumption that disks are self-regulating and have near-critical stability, which the models are based on. These disks have low central gas densities which can be a result of local dynamics or lack of gas supply to the central regions of galaxies.

Chapter 7

Conclusion

The kinematics of a sample of galaxies with a wide range of properties and H I masses ranging from $10^{7.7}$ to $10^{10.7}\,M_{\odot}/pc^2$ were studied by determining rotation gradients and rotation curves using the DISKFIT and ROTCUR packages and the 3D Plane model (which is method developed for determining the gradients in cases where the lack of data and galaxy properties do not allow for the rotation curve derivation via traditional methods). The results of the different fitting methods were compared to each other and the photometrically determined geometric parameters. The velocity gradients and kinematic parameters determined using these methods were used in conjunction with optical (Hα and R-band) and near-infrared (3.4, 4.6, 12 and 22 μm; referred to as W1, W2, W3, W4 respectively) photometric observations to study how star formation is related to galaxy dynamics in the inner parts of galaxies.

The velocity gradient was used as a tracer of the steepness of the inner potential well and the W1 and R-band observations were used as tracers of the stellar surface density. Both the R-band and W1 central surface brightnesses are correlated to the central velocity gradient. When these surface brightness values were converted to stellar surface densities there was an even tighter correlation between the product of the disk scale height and central velocity gradients and the stellar surface density : $\alpha_0 \Delta z \propto \Sigma_{s,0}^{\sim 0.5}$. The fraction of baryons compared to dark matter in the inner parts of galaxies was determined. I found that a large fraction ($\sim$ 50% in the R-band) of galaxy centers were consistent with models that have $f_b = 1$, but there was a large variation in f_b values across our sample (f_b values ranging from 0.1 to 1) and they did not correlate with $\Sigma_{s,0}$ or the total stellar mass. When W1 data was used there were many galaxies whose $\alpha_0 \Delta z$ values were too low to be explained by the model, therefore indicating that the Δz values were being underestimated and/or the stellar mass ratios M_s/L_s were overestimated. The analysis could not constrain f_b very well and better estimates

of the M/L and disk scale height are needed in order for better constraints. The results show that the stellar disks typically dominate the potential well of the inner regions of the disks just as Lelli et al. (2013, 2014) and Erroz-Ferrer et al. (2016) found in their analysis.

Models for the distribution of star formation based on a self-regulating constant Q disk with a constant inner velocity gradient and using the t_{orb} star formation law or molecular star formation law were developed. The $H\alpha$, W3 and W4 photometric bands were used as tracers of the star formation surface density. The model where gas-only Q_g stability parameter was used predicts that central star formation surface density is correlated to the central velocity gradient, a weak correlation was found between the parameters and the fitted relationships ranged between $\Sigma_{\rm SFR,0} \propto \alpha_0^{5.1\pm1.6}$ (for the Hα observations) to $\Sigma_{\rm SFR,0} \propto \alpha_0^{3.4\pm0.7}$ (for W3 observations). However the model predicts a power law index of 2, which is lower than the observations. Models that take into account the large effects of the stellar disk disk and dynamics in the inner regions were derived using the Q_{WS} formulation of the two-fluid (gas and stars) disk stability parameter. These models predict a relationship between the star formation surface density, stellar surface density, velocity gradient and scale lengths in the inner regions of the galaxy. There were relationships between these parameters but the implied values of Q_{WS}, the orbital timescale ϵ_{orb} and the gas depletion time t_{dep} from the models were not constant therefore the assumptions that the models are based on do not hold in the central regions of galaxies. The implied Q_g and Q_{WS} are higher than the assumption made for the models that disks are self-regulating and have near-critical stability. Galaxies with the highest implied stability parameters have the lowest $\Sigma_{g,0}$ fractions which may be caused by local dynamics and that not enough gas is being transported to the central regions of these galaxies. Models that incorporate varying Q_g, Q_{WS}, ϵ_{orb} and t_{dep} are required in order to describe the relationship between the $\Sigma_{\rm SFR,0}$ and galaxy dynamics.

Appendix

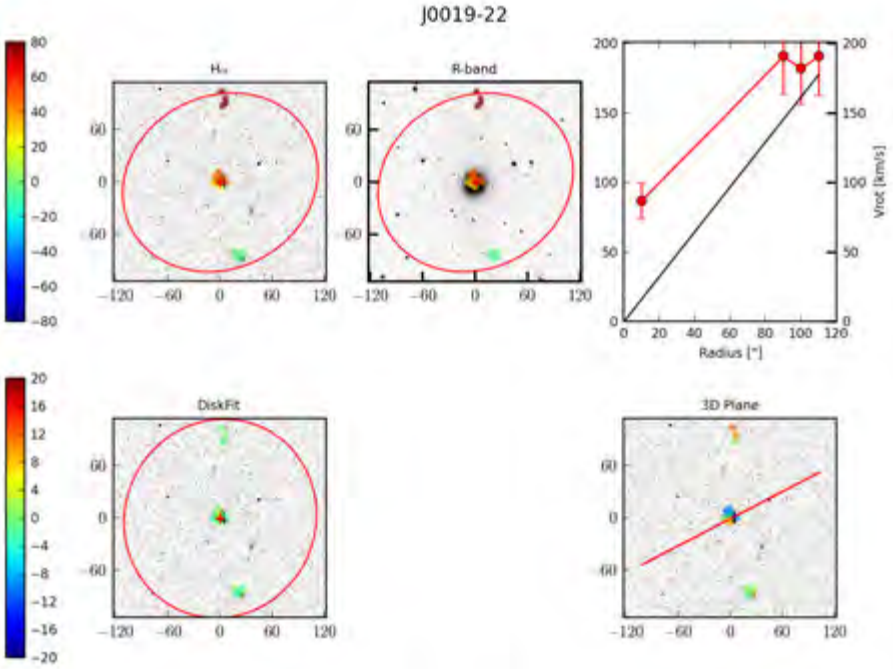

Figure A1: Same as Figure 4.1, but for J0019-22

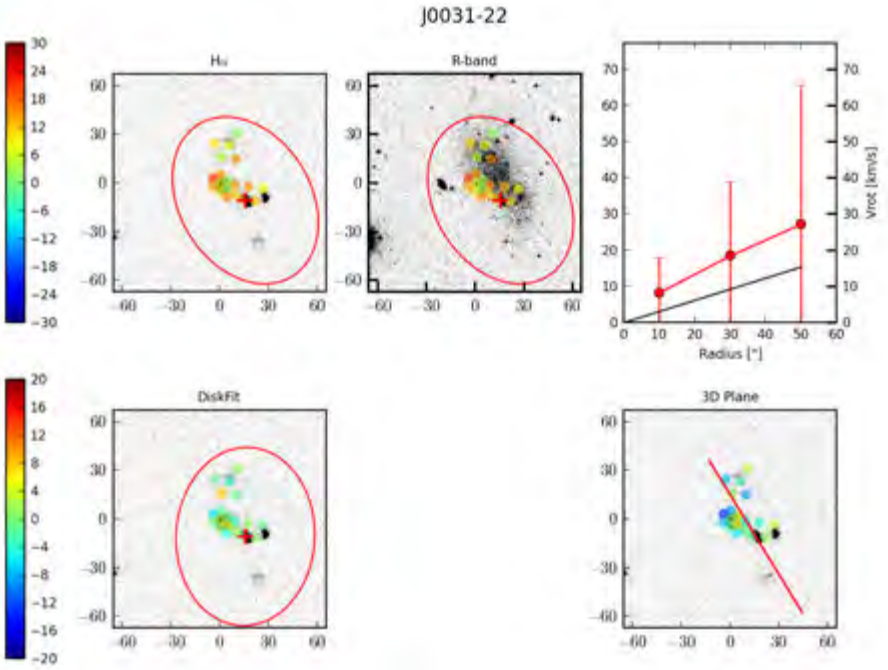

Figure A2: Same as Figure 4.1, but for J0031-22

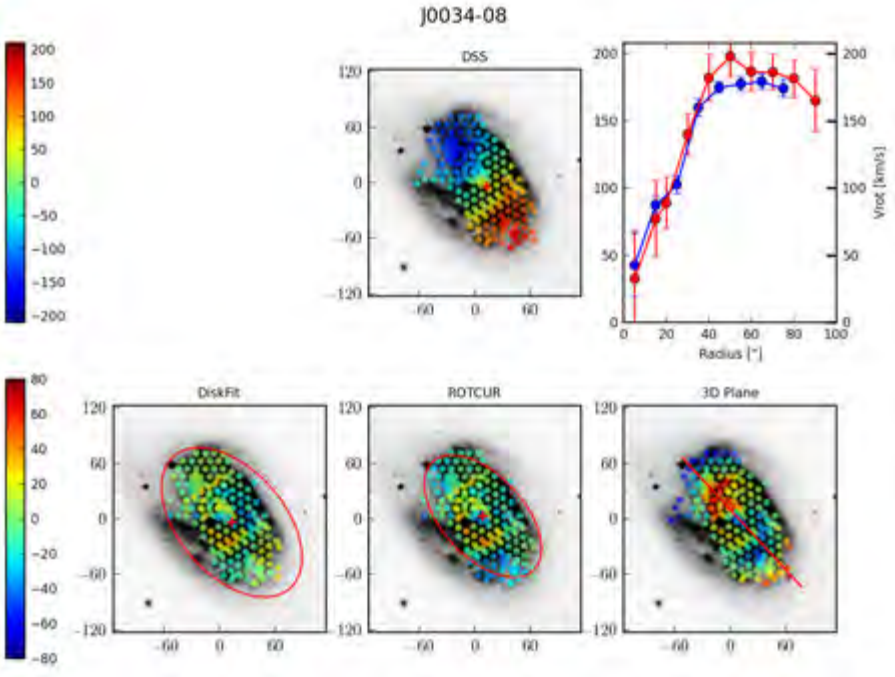

Figure A3: Same as Figure 4.1, but velocity and residual velocity fields are overlayed over DSS images of J0034-08

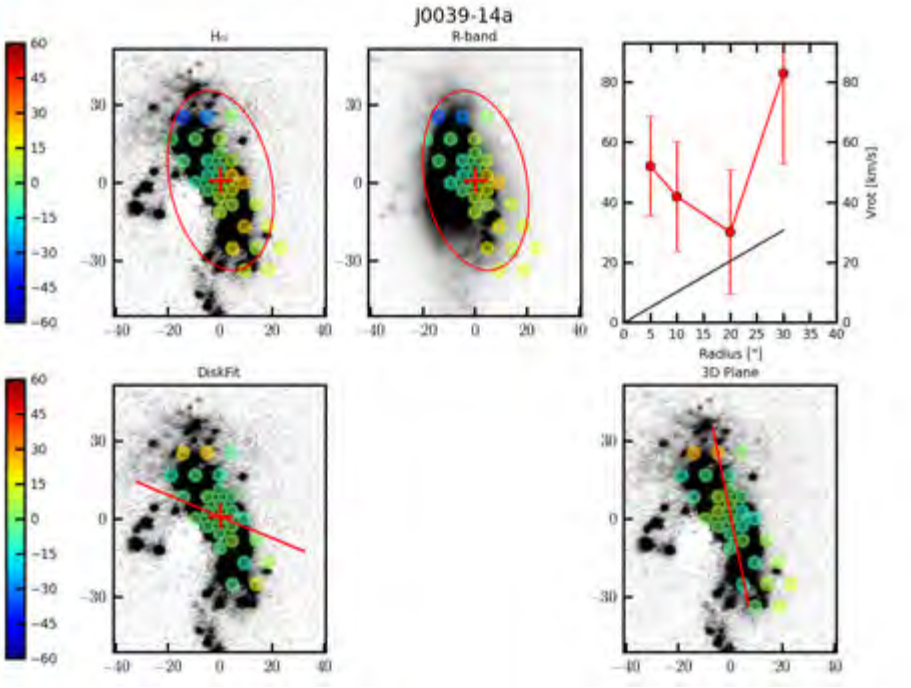

Figure A4: Same as Figure 4.1, but for J0039-14a

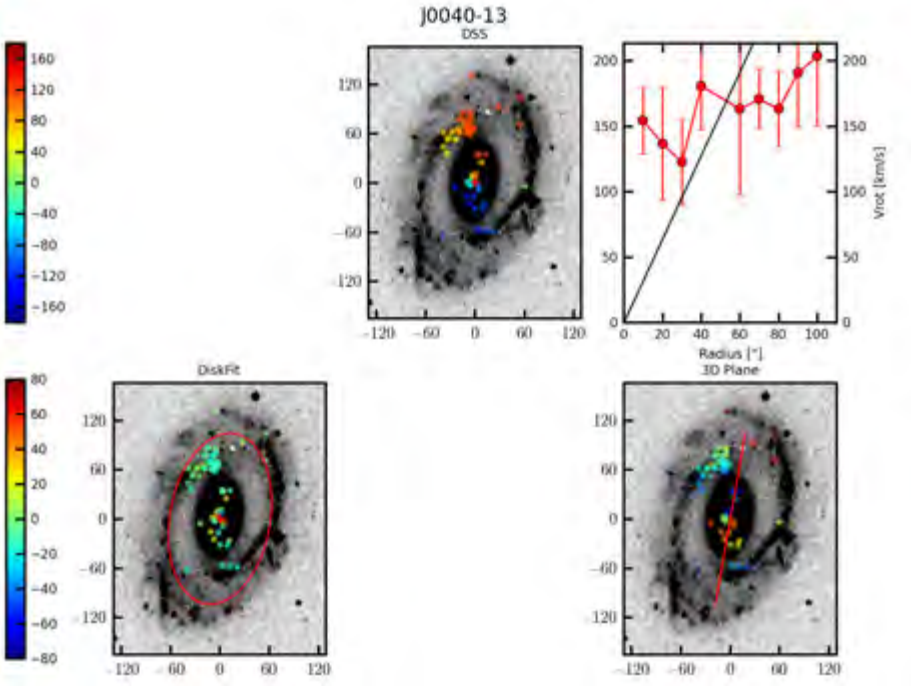

Figure A5: Same as Figure 4.1, but velocity and residual velocity fields are overlayed over DSS images of J0040-13

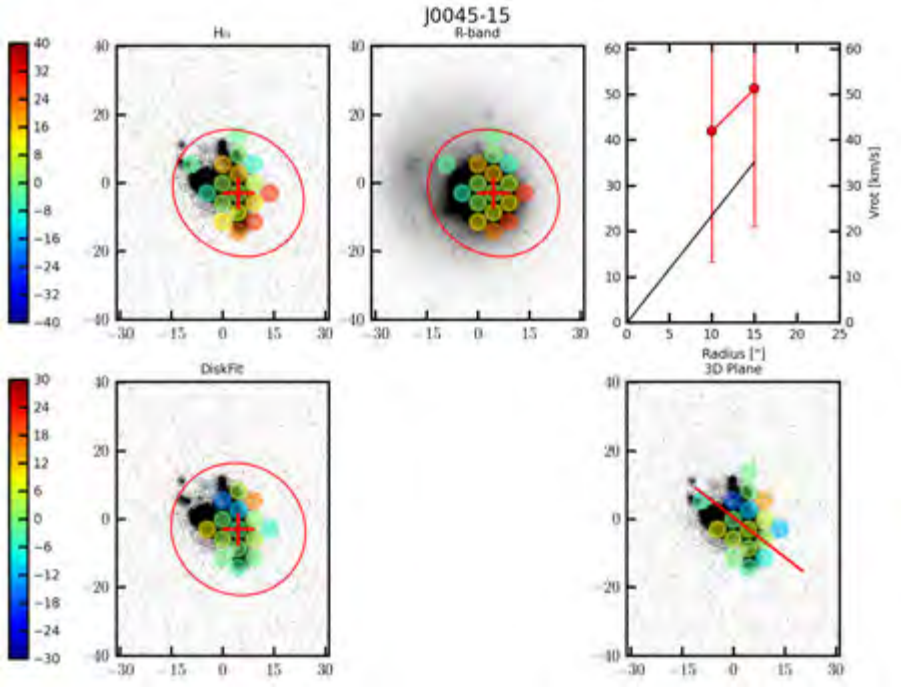

Figure A6: Same as Figure 4.1, but velocity and residual velocity fields are overlayed over DSS images of J0045-15

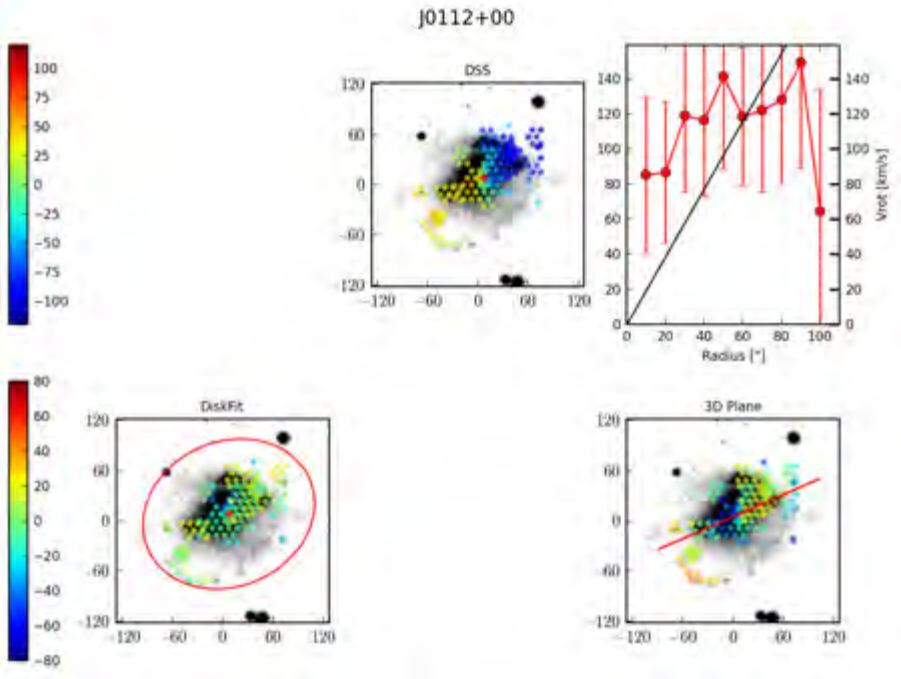

Figure A7: Same as Figure 4.1, but velocity and residual velocity fields are overlayed over DSS images of J0112+00

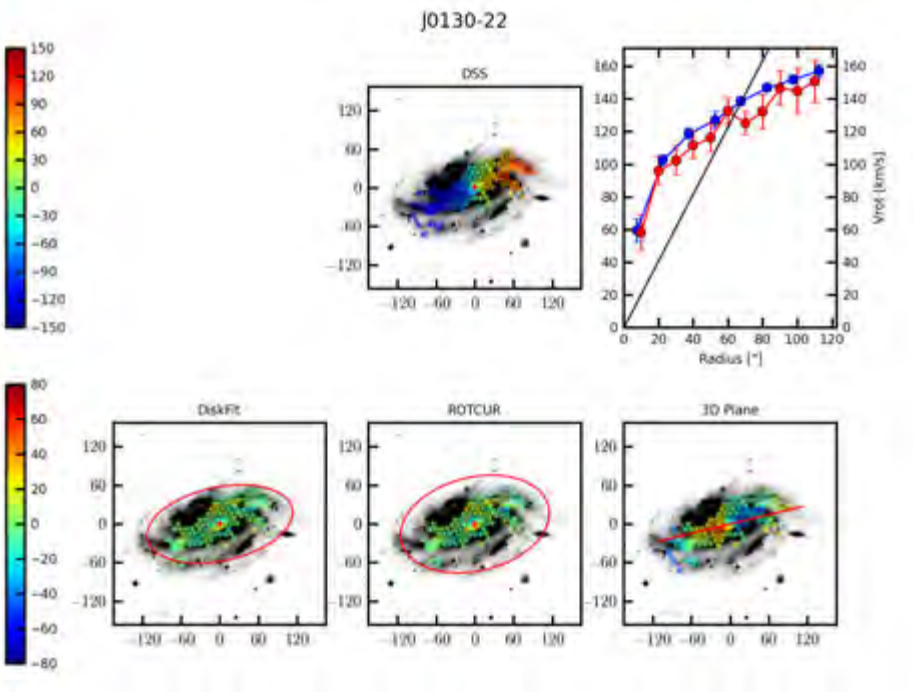

Figure A8: Same as Figure 4.1, but velocity and residual velocity fields are overlayed over DSS images of J0130-22

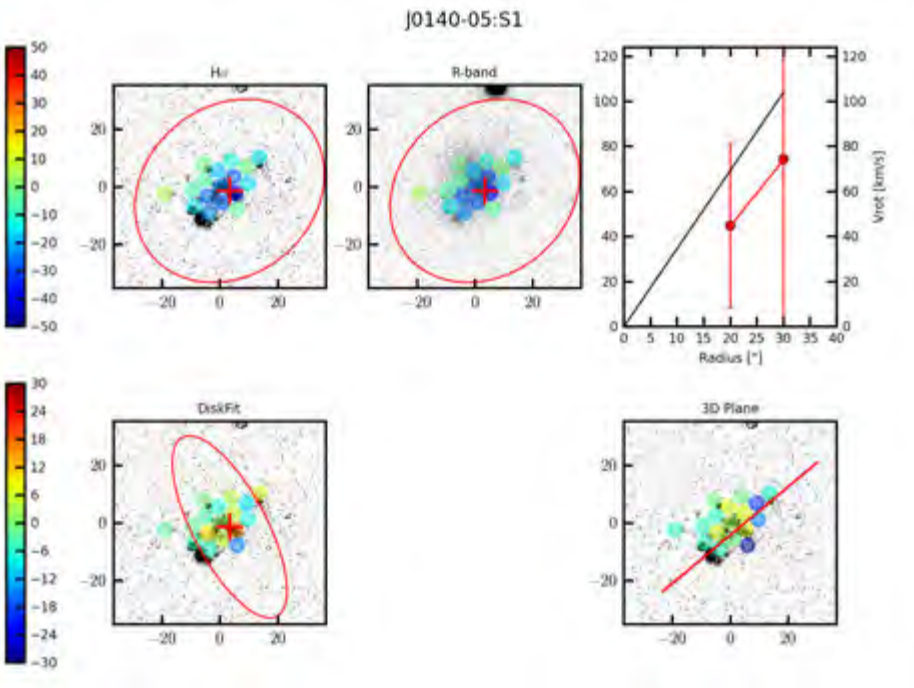

Figure A9: Same as Figure 4.1, but velocity and residual velocity fields are overlayed over DSS images of J0045-15

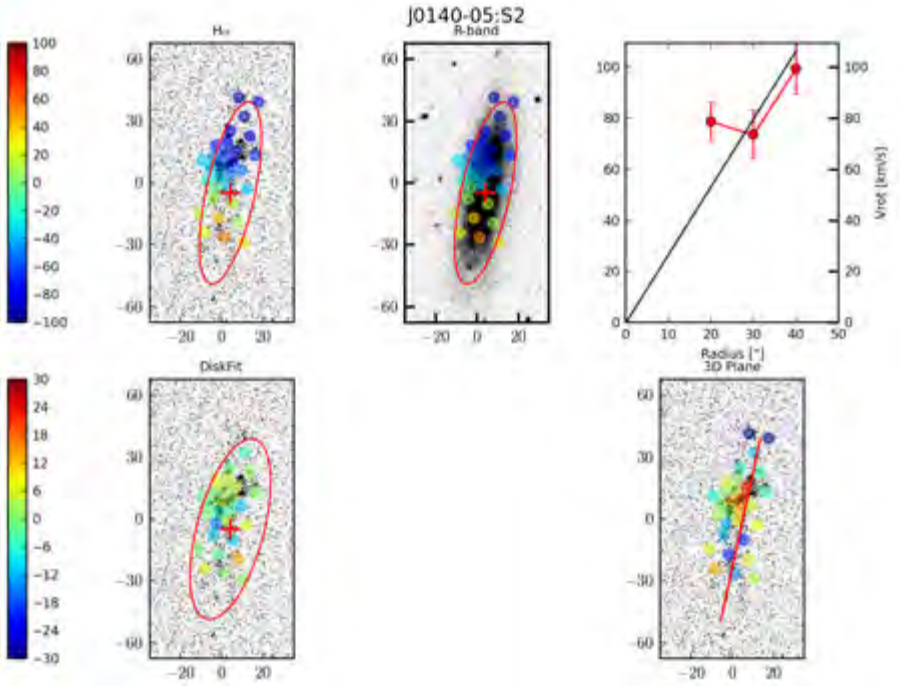

Figure A10: Same as Figure 4.1, but for J0140-05S2

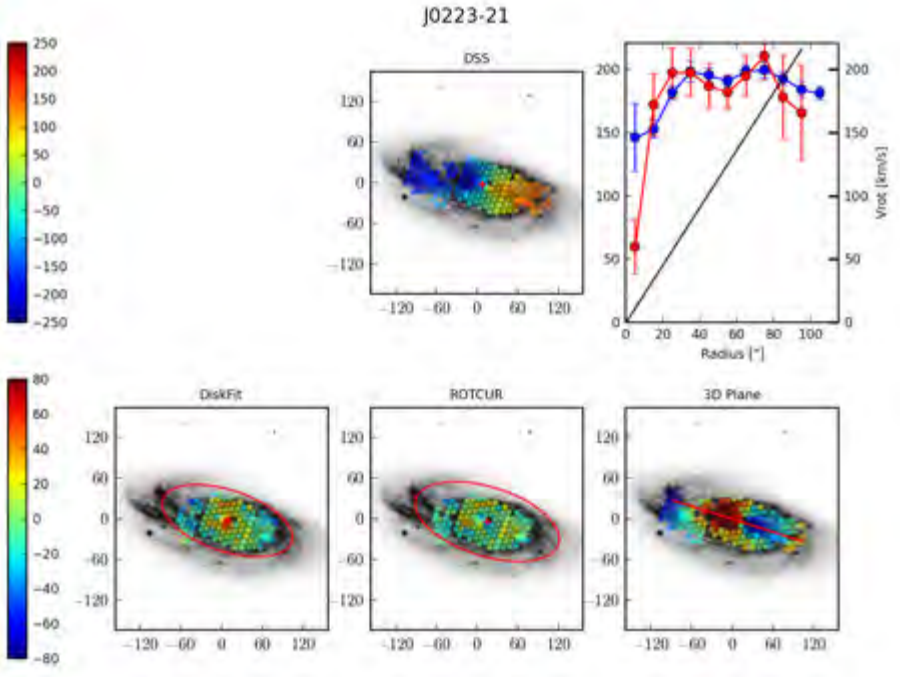

Figure A11: Same as Figure 4.1, but velocity and residual velocity fields are overlayed over DSS images of J0223-21

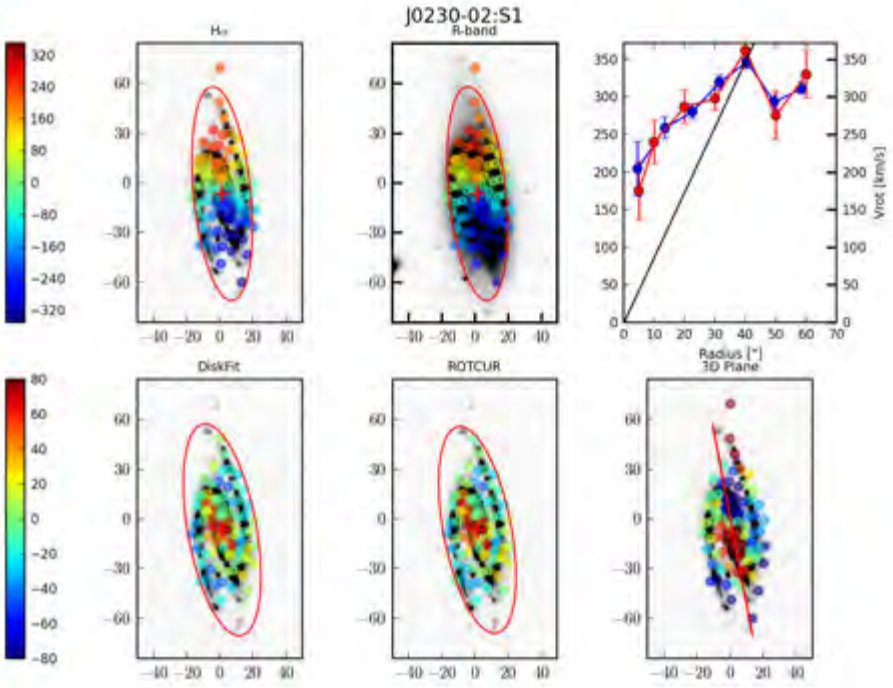

Figure A12: Same as Figure 4.1, but velocity and residual velocity fields are overlayed over DSS images of J0230-02:S1

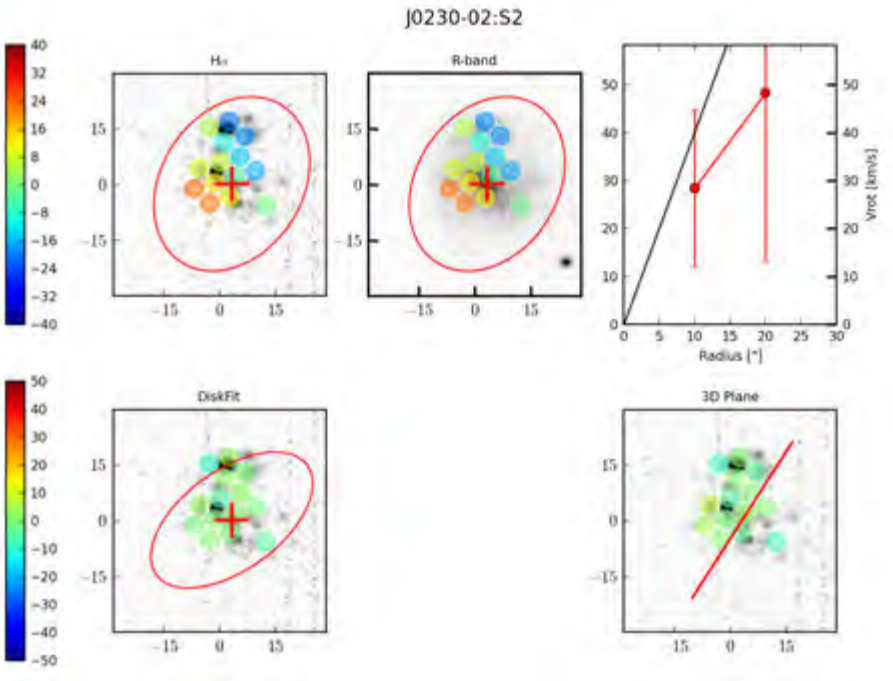

Figure A13: Same as Figure 4.1, but velocity and residual velocity fields are overlayed over DSS images of J0230-02:S2

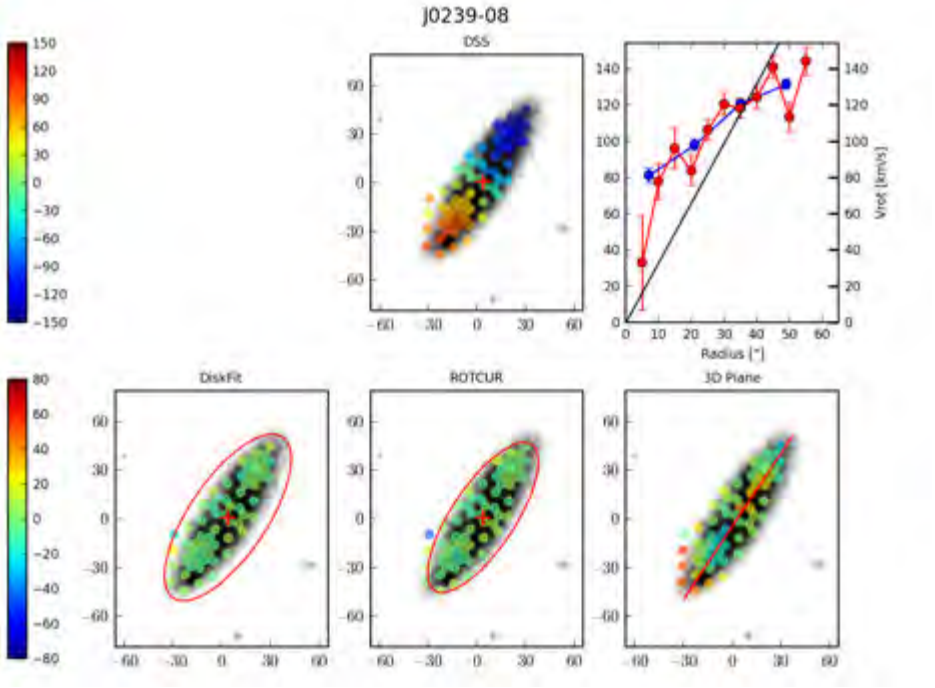

Figure A14: Same as Figure 4.1, but velocity and residual velocity fields are overlayed over DSS images of J0239-08

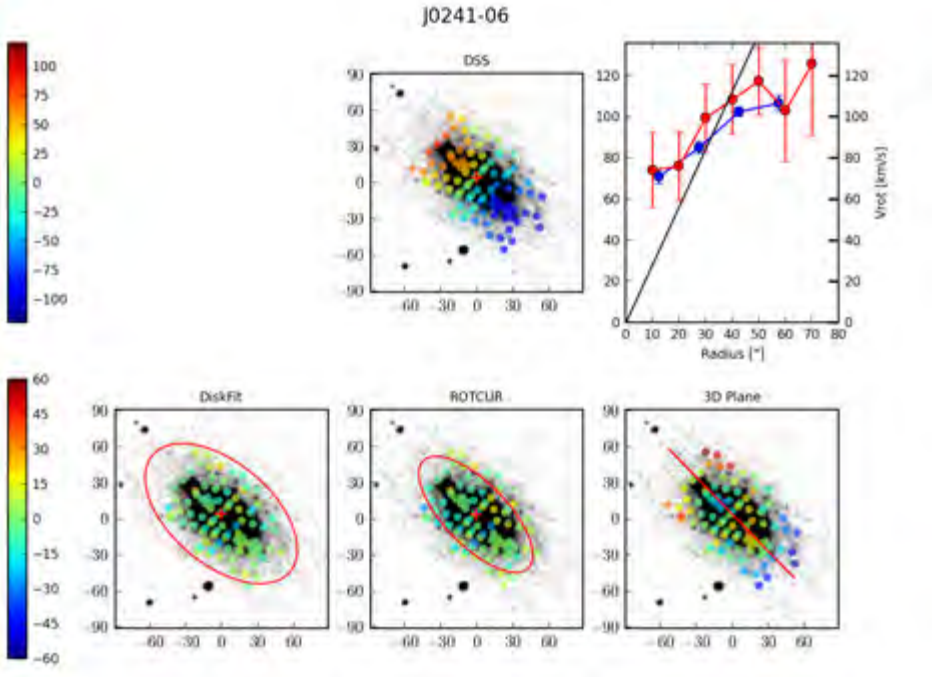

Figure A15: Same as Figure 4.1, but velocity and residual velocity fields are overlayed over DSS images of J0241-06

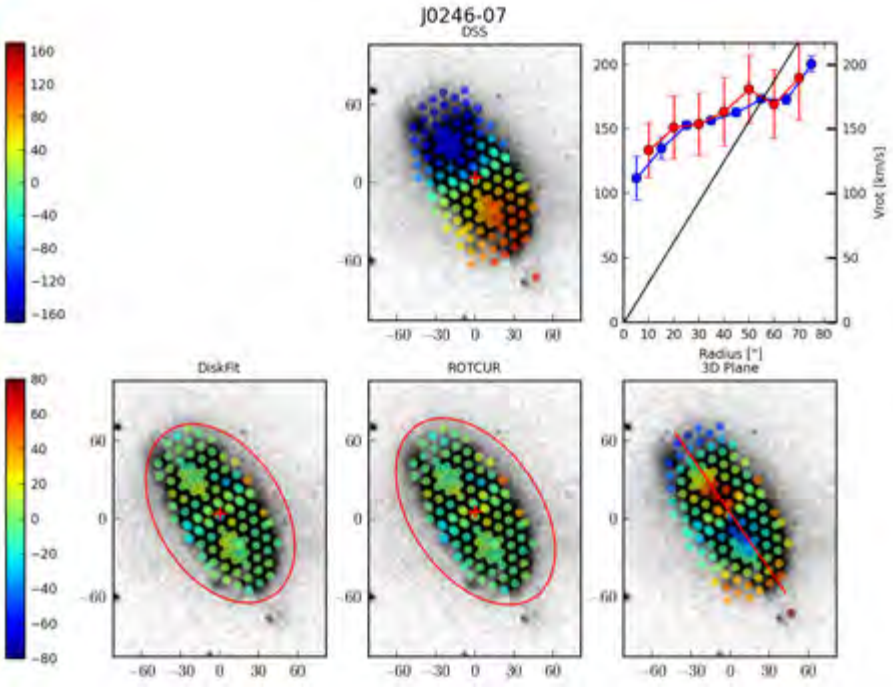

Figure A16: Same as Figure 4.1, but velocity and residual velocity fields are overlayed over DSS images of J0246-07

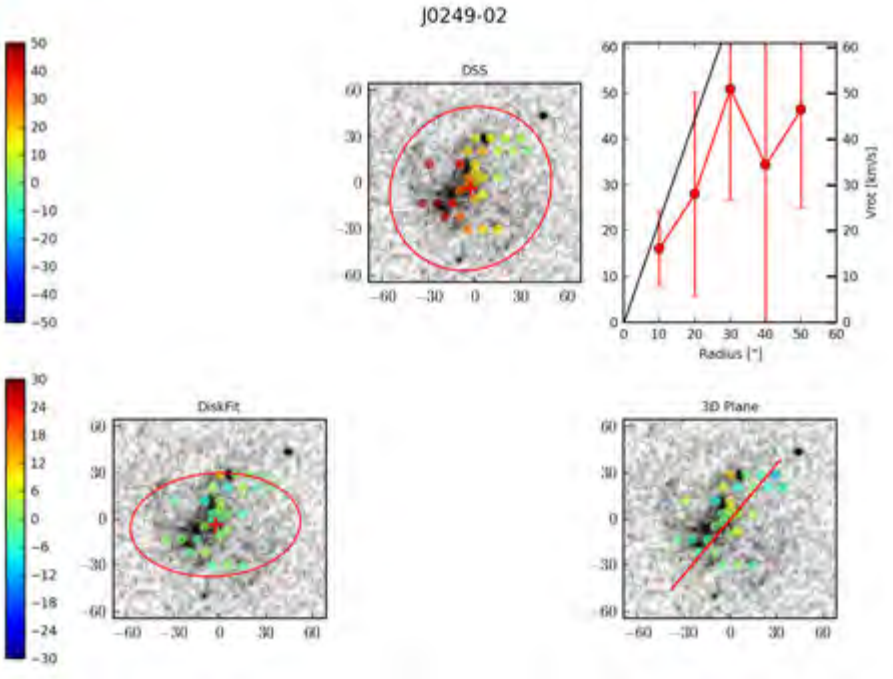

Figure A17: Same as Figure 4.1, but velocity and residual velocity fields are overlayed over DSS images of J0249-02

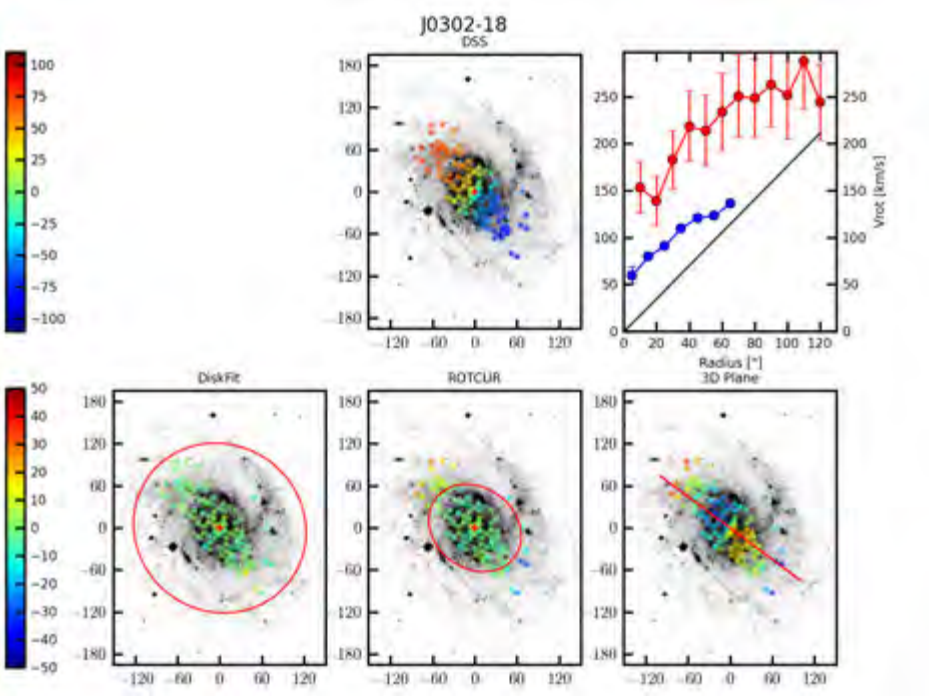

Figure A18: Same as Figure 4.1, but velocity and residual velocity fields are overlayed over DSS images of J0302-18

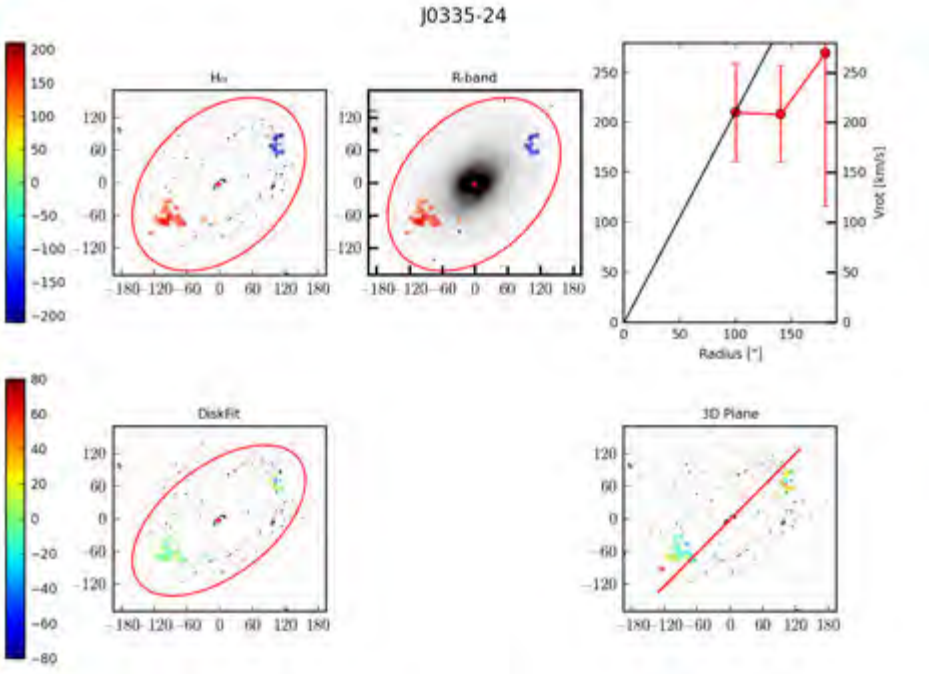

Figure A19: Same as Figure 4.1, but for J0335-24

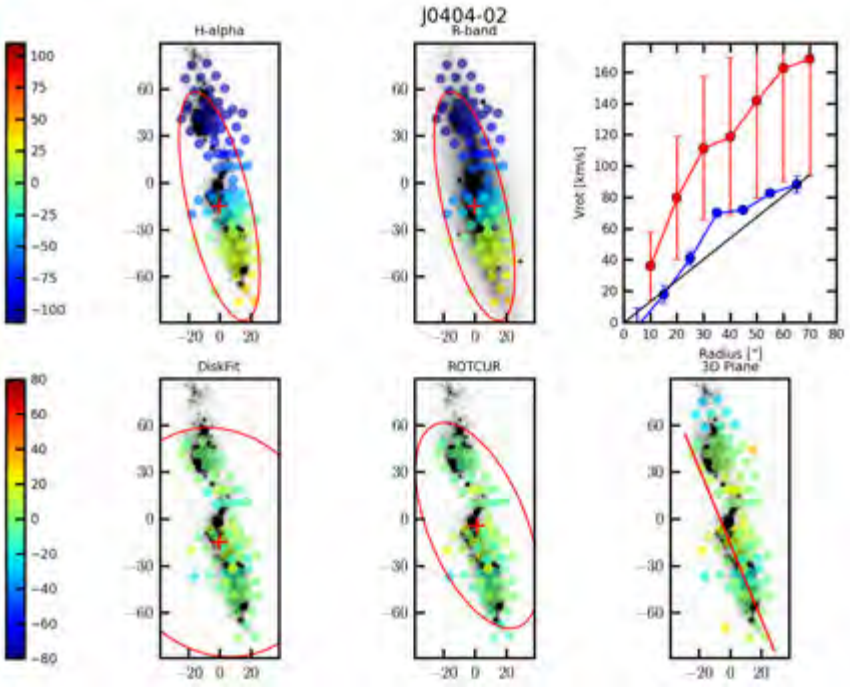

Figure A20: Same as Figure 4.1, but velocity and residual velocity fields are overlayed over DSS images of J0404-02

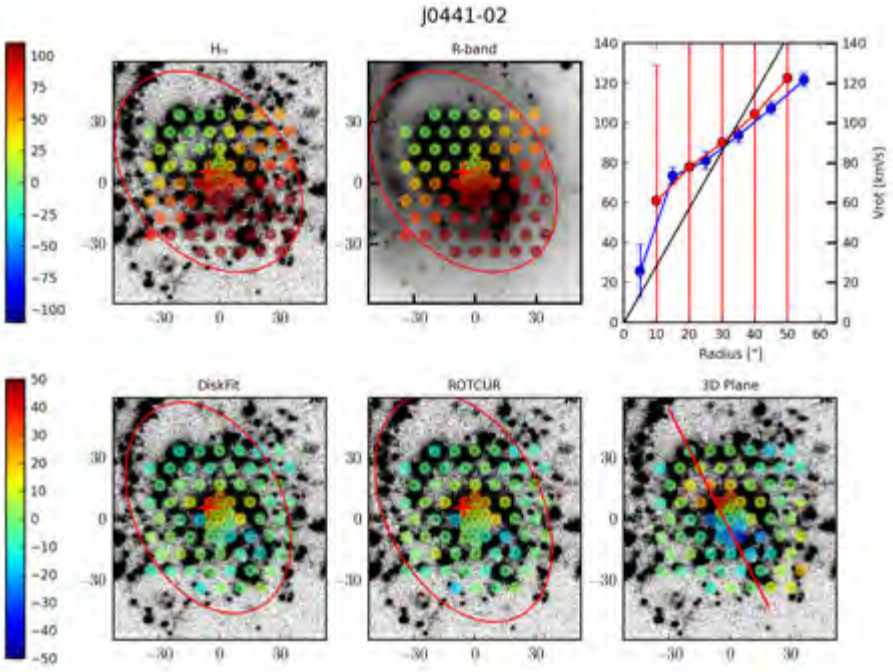

Figure A21: Same as Figure 4.1, but for J0441-02

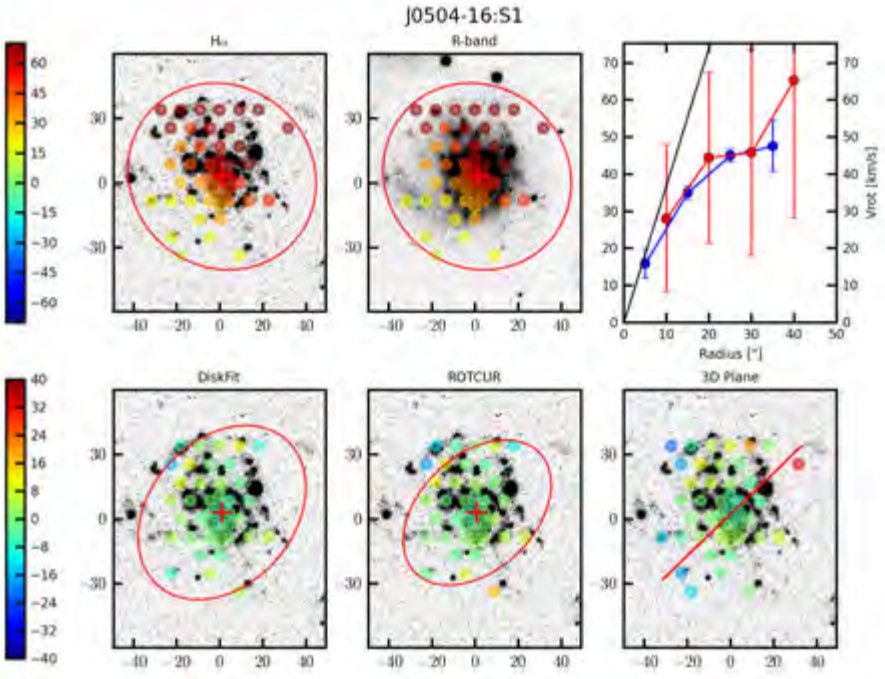

Figure A22: Same as Figure 4.1, but for J0504-16:S1

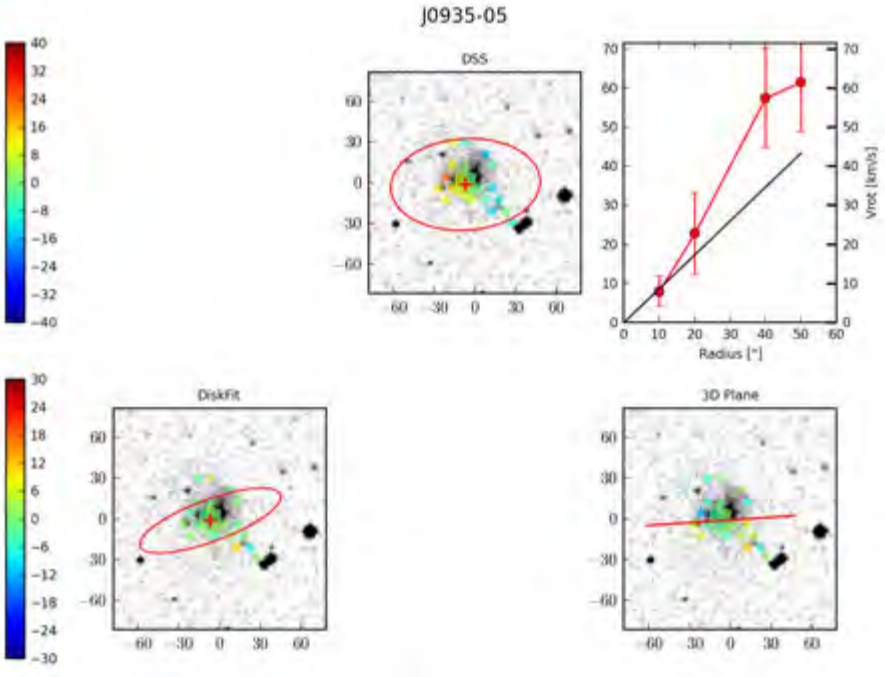

Figure A23: Same as Figure 4.1, but velocity and residual velocity fields are overlayed over DSS images of J0935-05

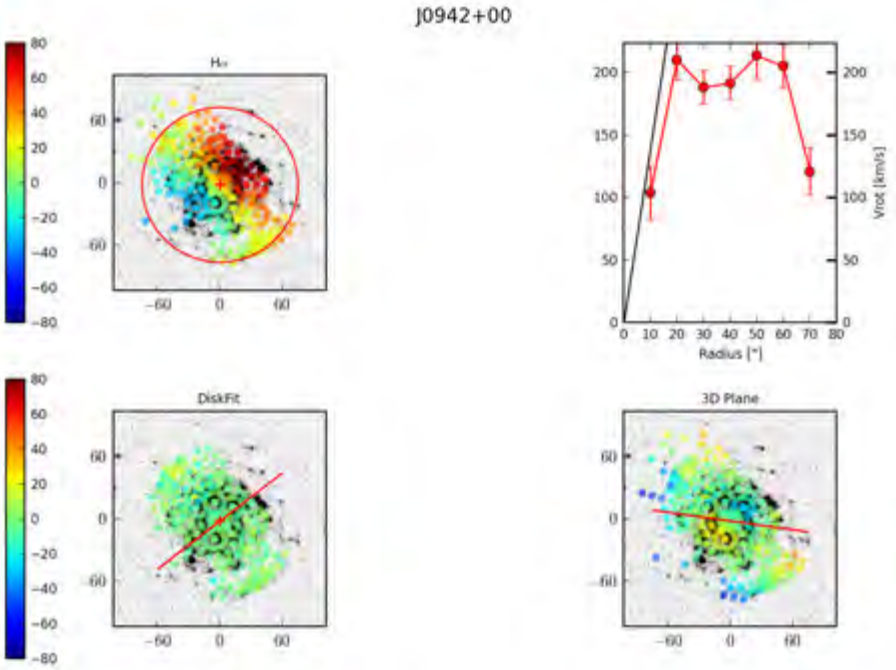

Figure A24: Same as Figure 4.1, but for J0942+00

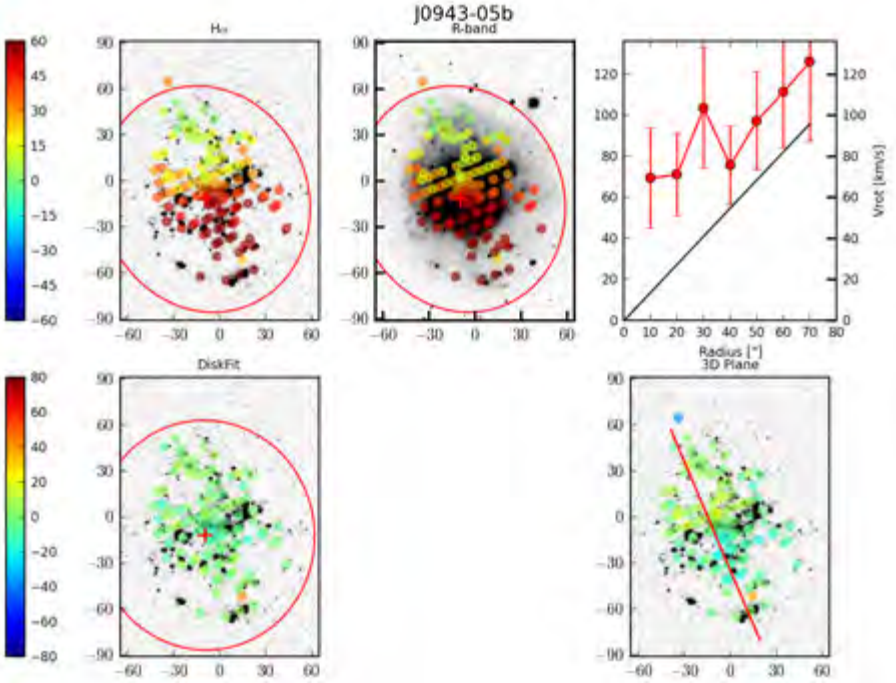

Figure A25: Same as Figure 4.1, but for J0943-05b

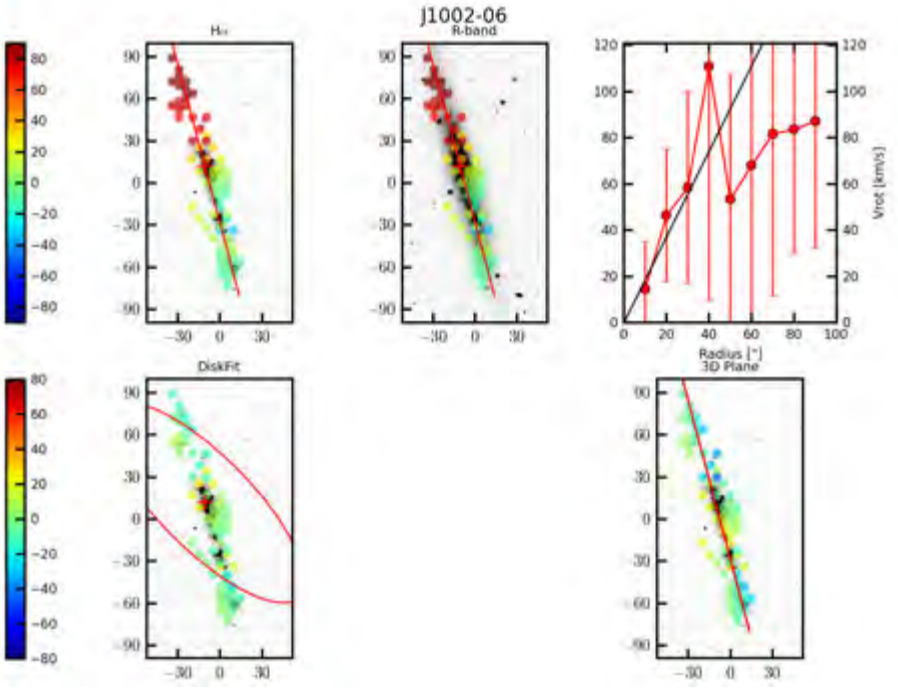

Figure A26: Same as Figure 4.1, but for J1002-06

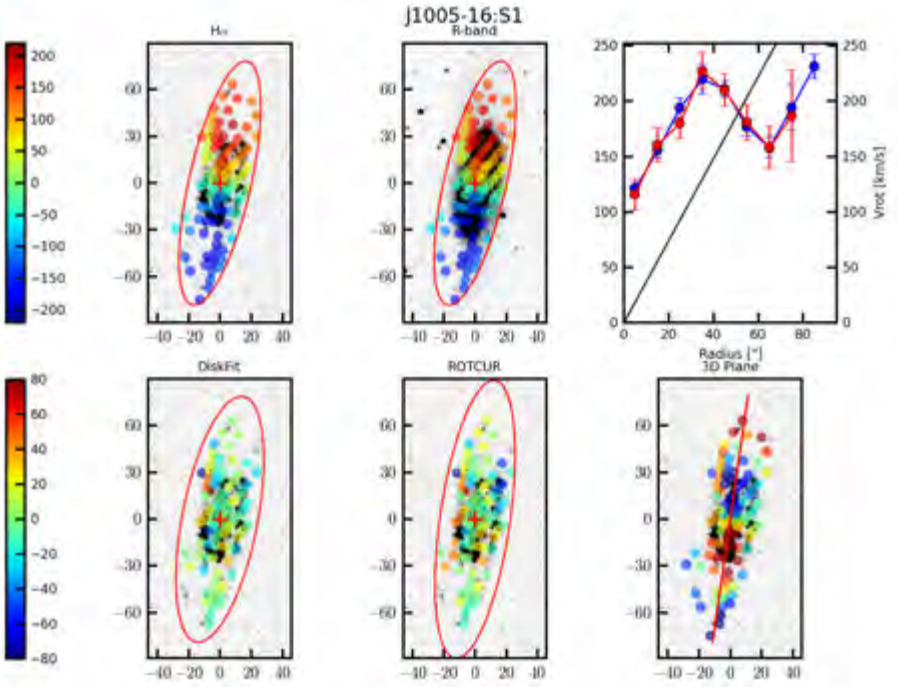

Figure A27: Same as Figure 4.1, but for J1005-16S1

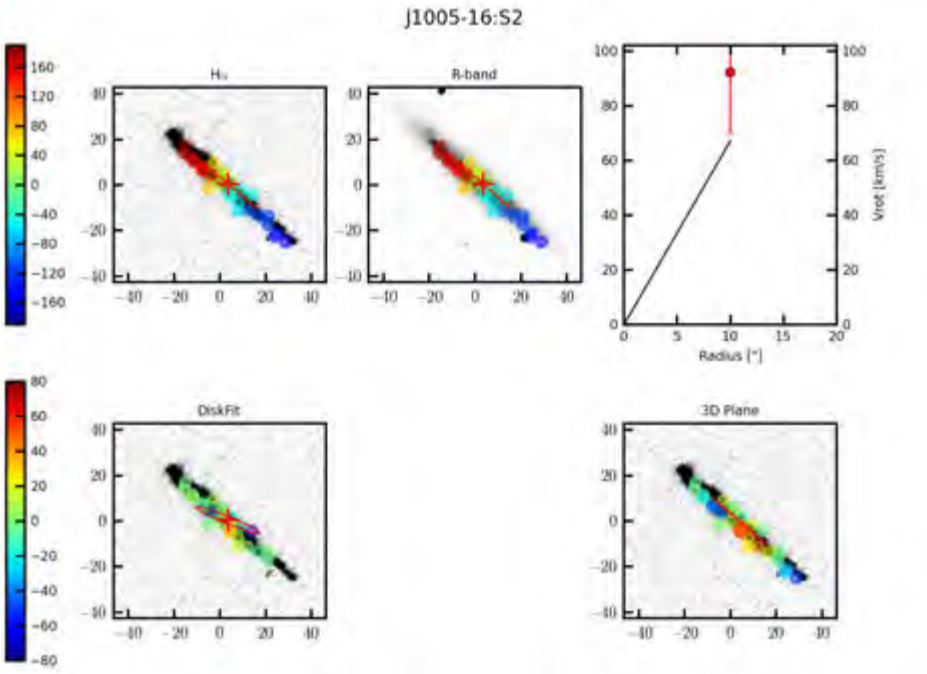

Figure A28: Same as Figure 4.1, but for J1005-16S2

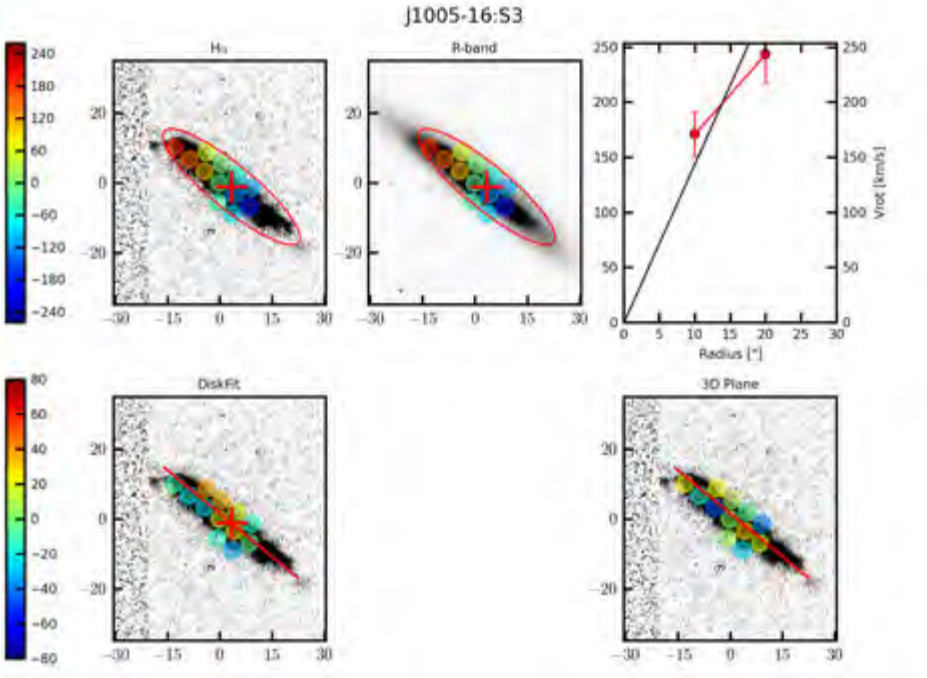

Figure A29: Same as Figure 4.1, but for J1005-16S3

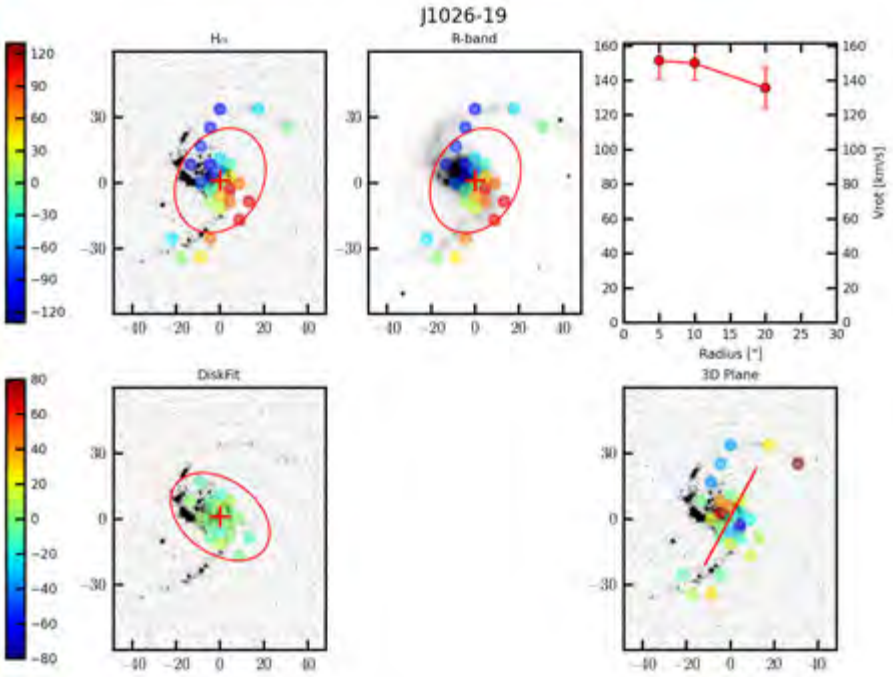

Figure A30: Same as Figure 4.1, but for J1026-19

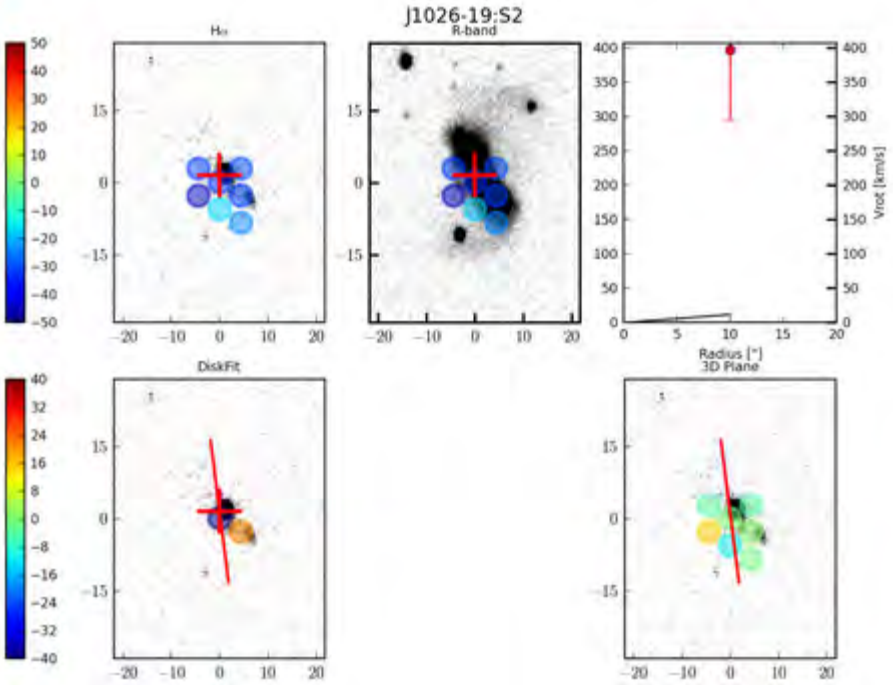

Figure A31: Same as Figure 4.1, but for J1026-19S2

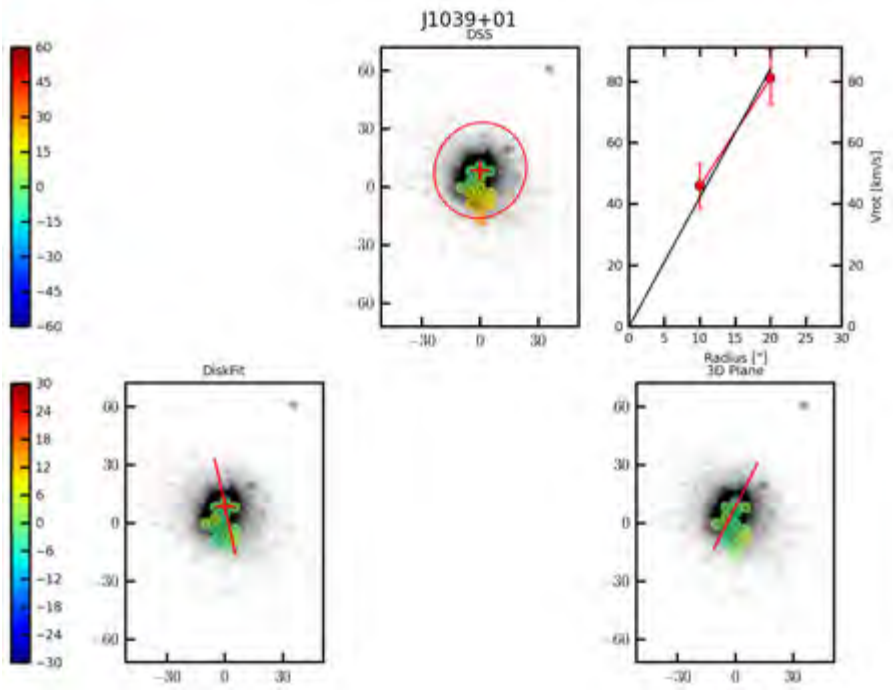

Figure A32: Same as Figure 4.1, but velocity and residual velocity fields are overlayed over DSS images of J1039+01

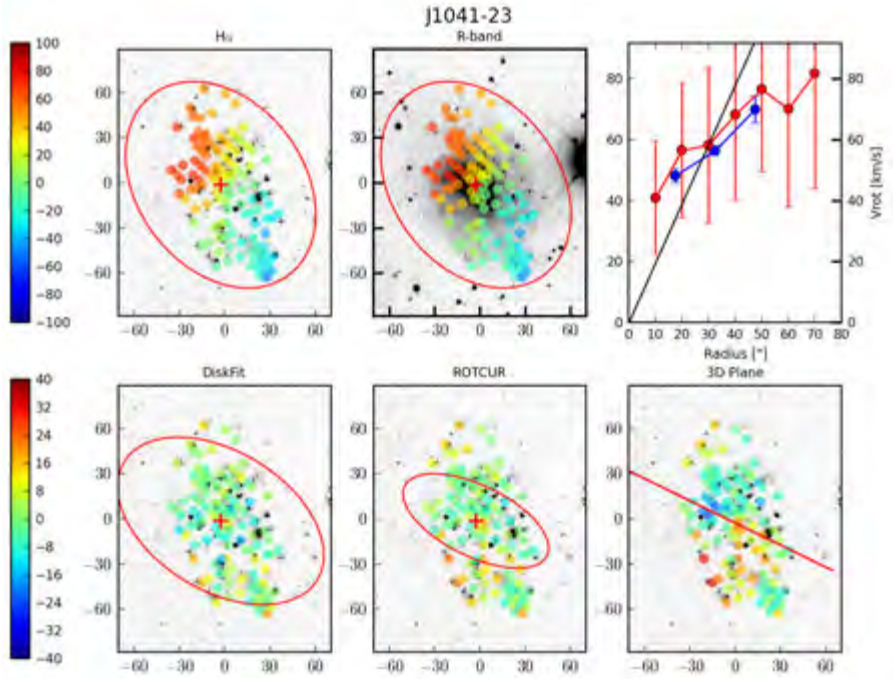

Figure A33: Same as Figure 4.1, but for J1041-23

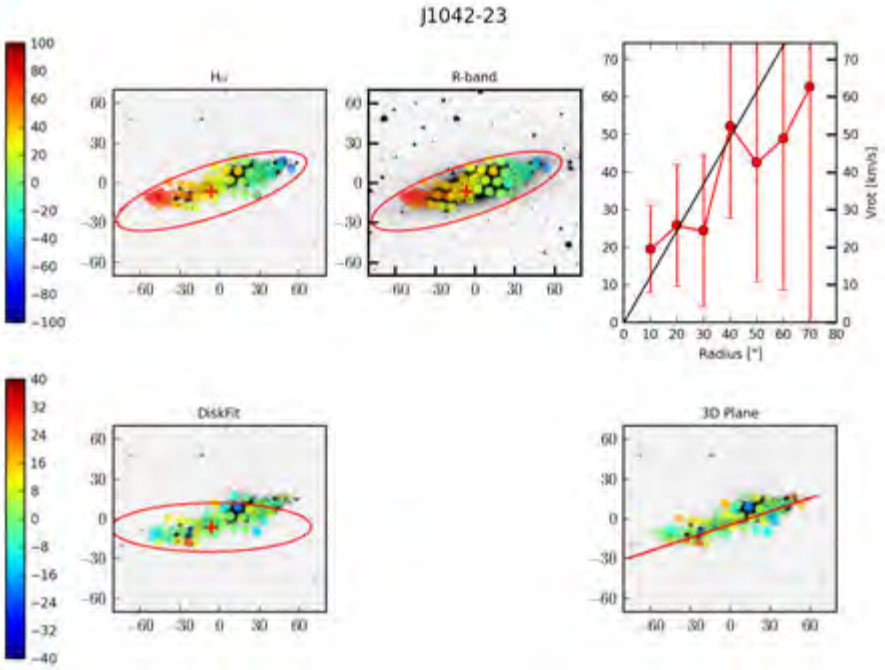

Figure A34: Same as Figure 4.1, but for J1042-23

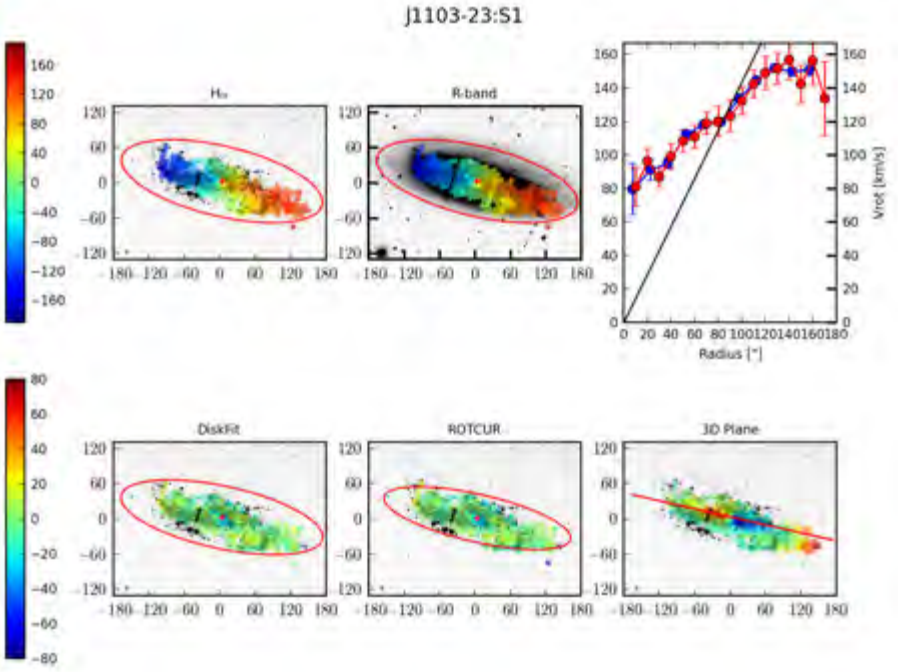

Figure A35: Same as Figure 4.1, but for J1103-23S1

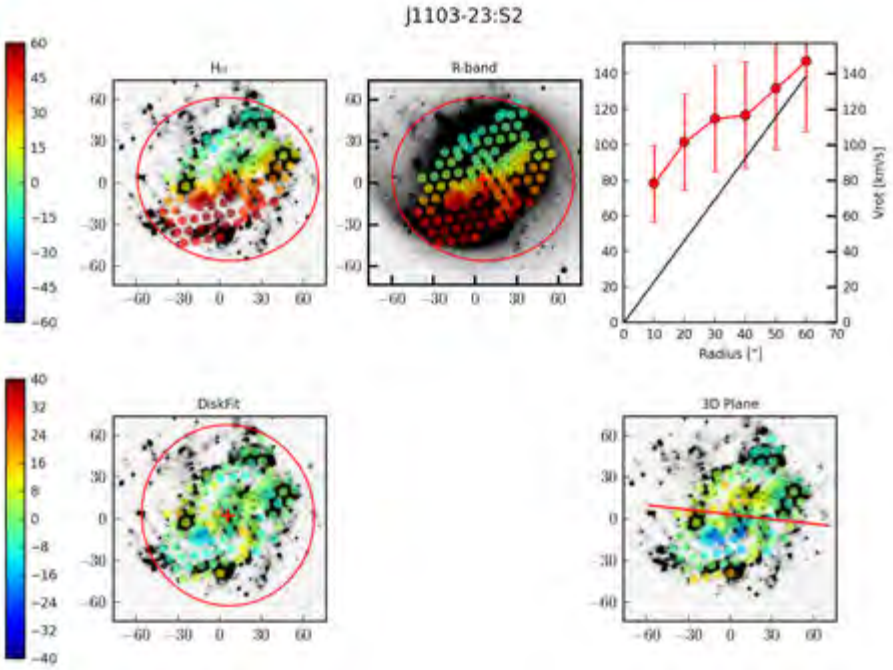

Figure A36: Same as Figure 4.1, but for J1103-23:S2

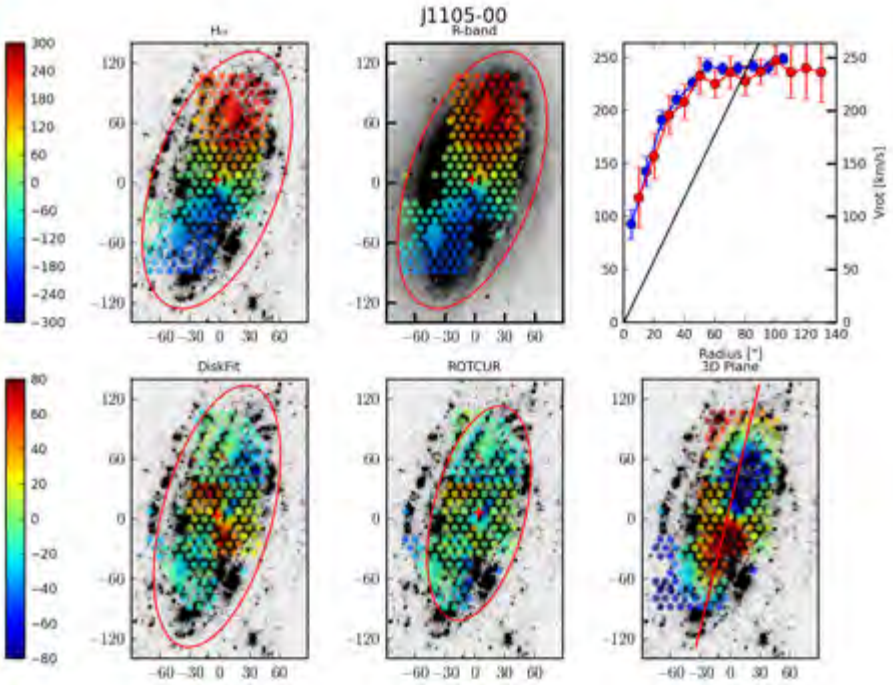

Figure A37: Same as Figure 4.1, but for J1105-00

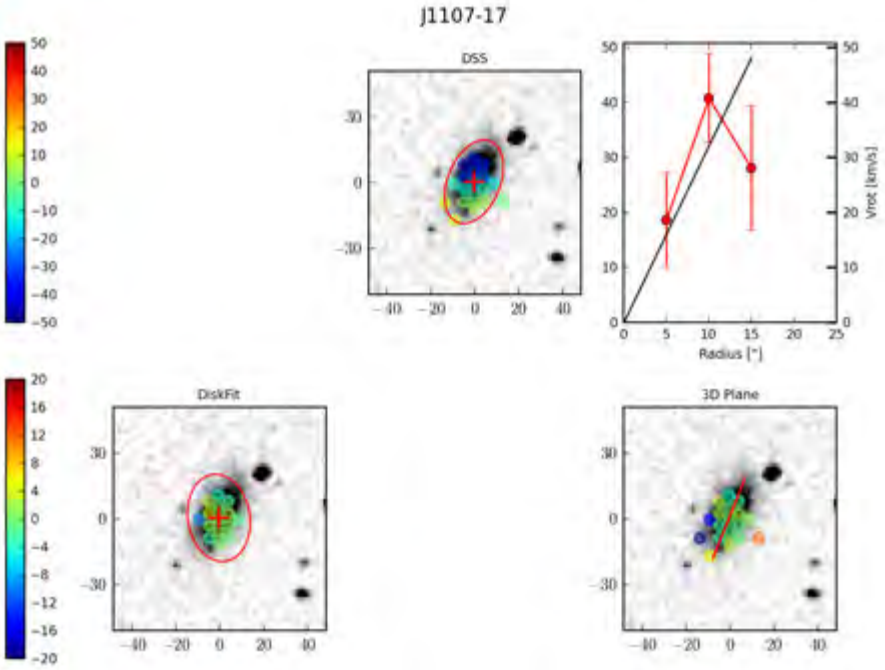

Figure A38: Same as Figure 4.1, but velocity and residual velocity fields are overlayed over DSS images of J1107-17

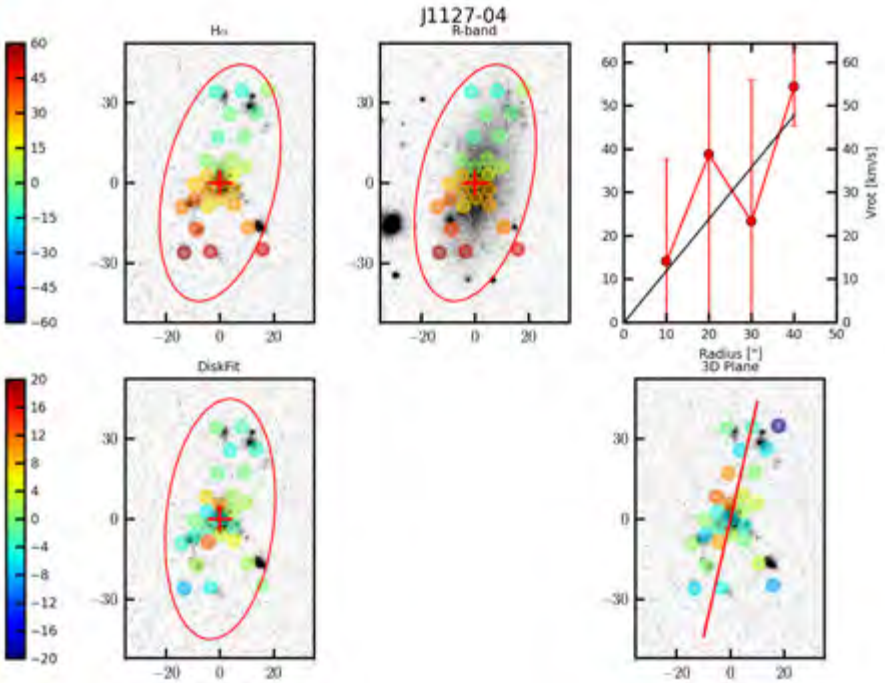

Figure A39: Same as Figure 4.1, but for J1127-04

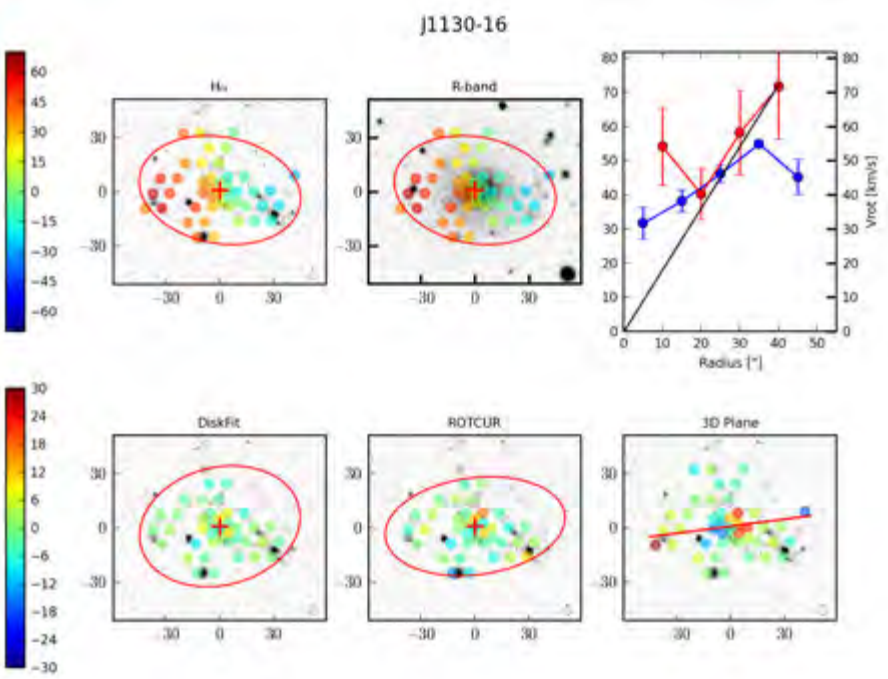

Figure A40: Same as Figure 4.1, but for J1130-16

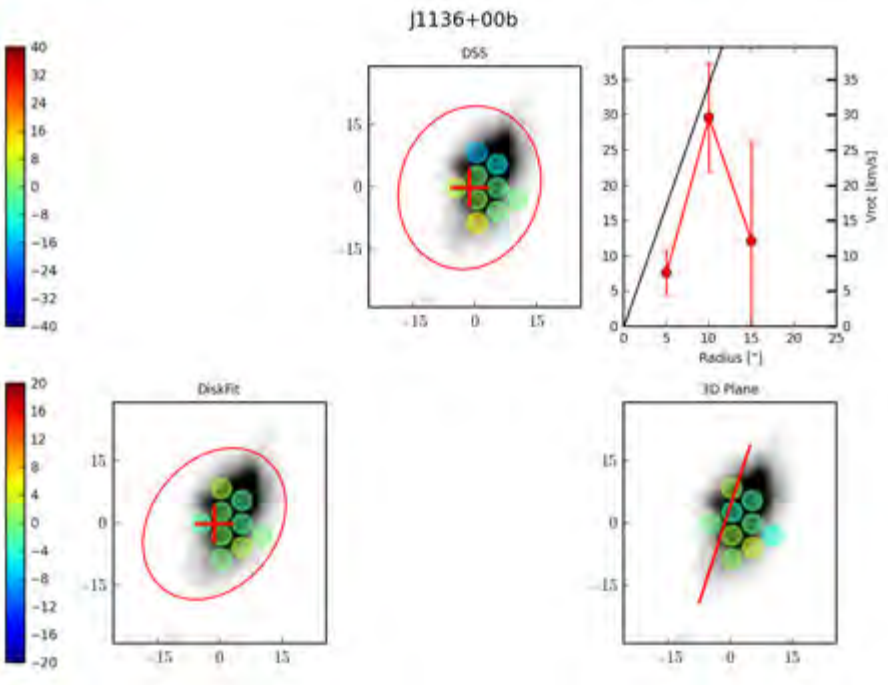

Figure A41: Same as Figure 4.1, but velocity and residual velocity fields are overlayed over DSS images of J1136+00b

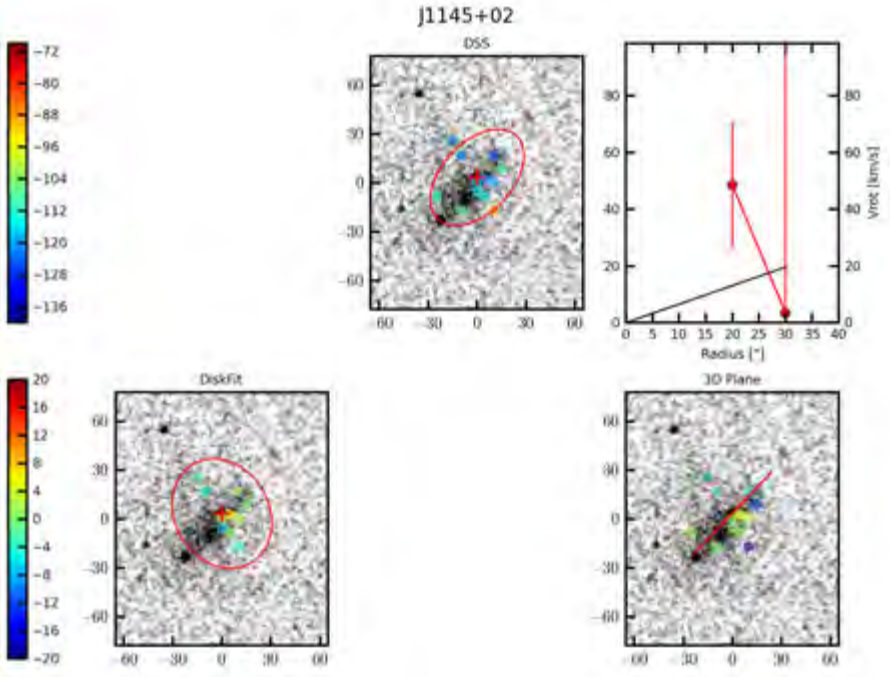

Figure A42: Same as Figure 4.1, but velocity and residual velocity fields are overlayed over DSS images of J1145+02

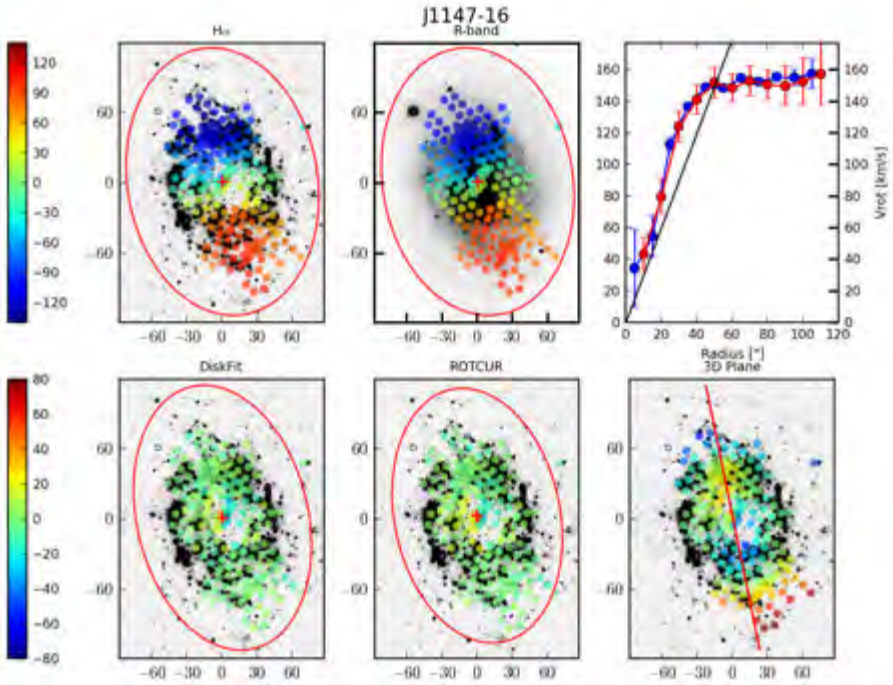

Figure A43: Same as Figure 4.1, but for J1147-16

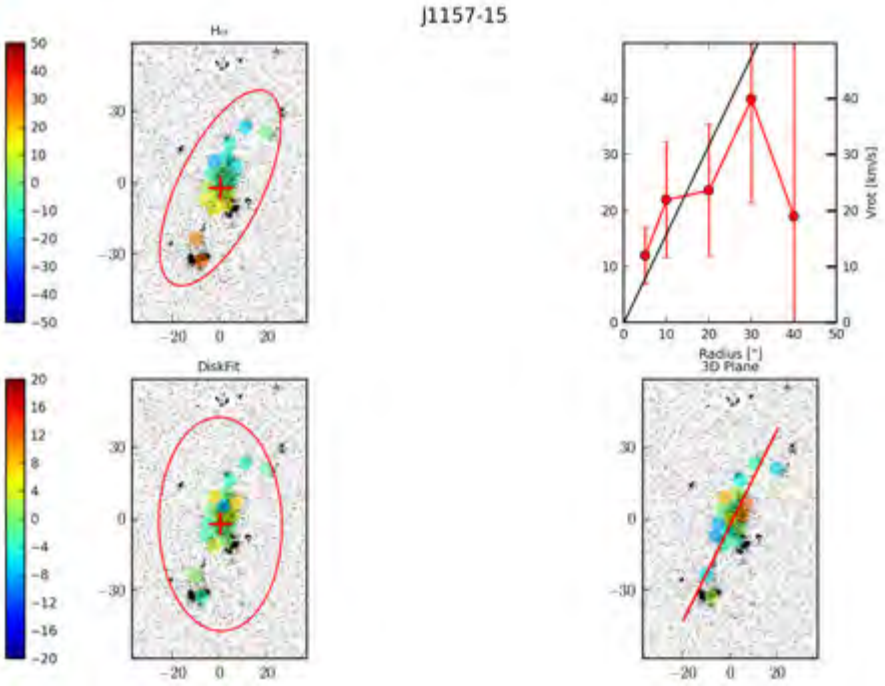

Figure A44: Same as Figure 4.1, but for J1157-15

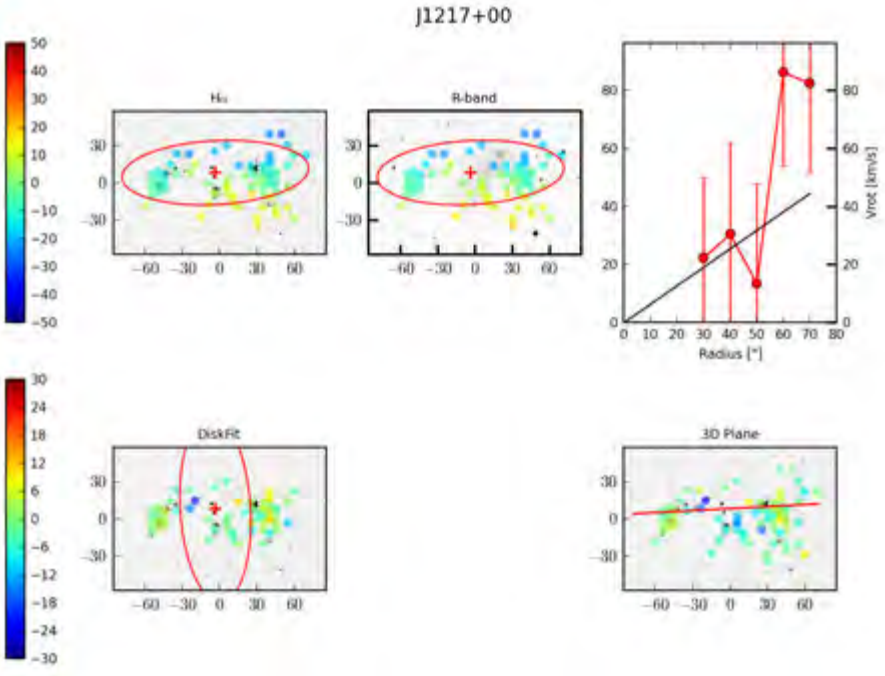

Figure A45: Same as Figure 4.1, but for J1217+00

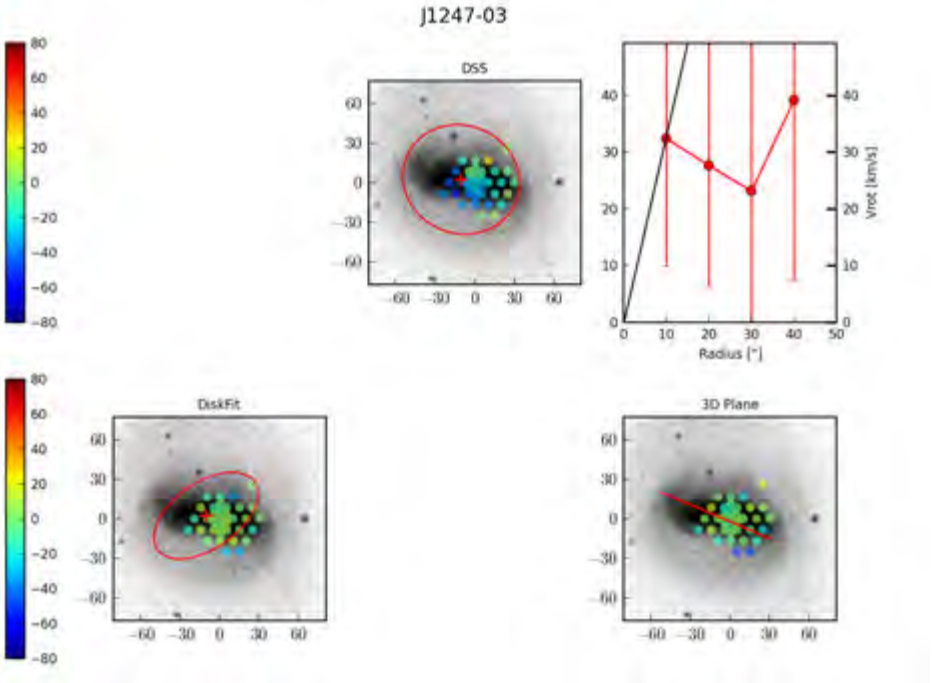

Figure A46: Same as Figure 4.1, but velocity and residual velocity fields are overlayed over DSS images of J1247-03

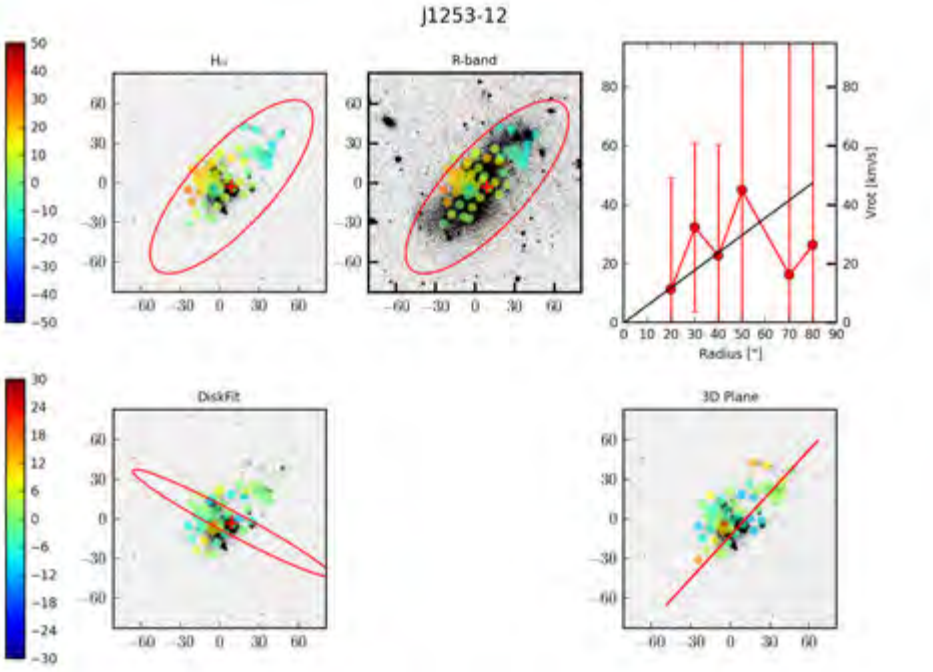

Figure A47: Same as Figure 4.1, but for J1253-12

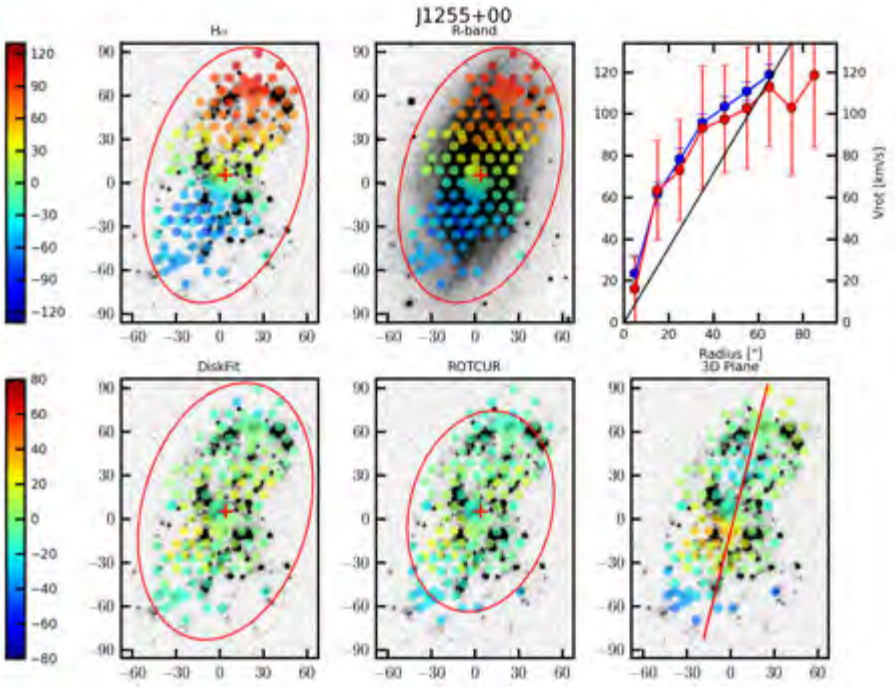

Figure A48: Same as Figure 4.1, but for J1255+00

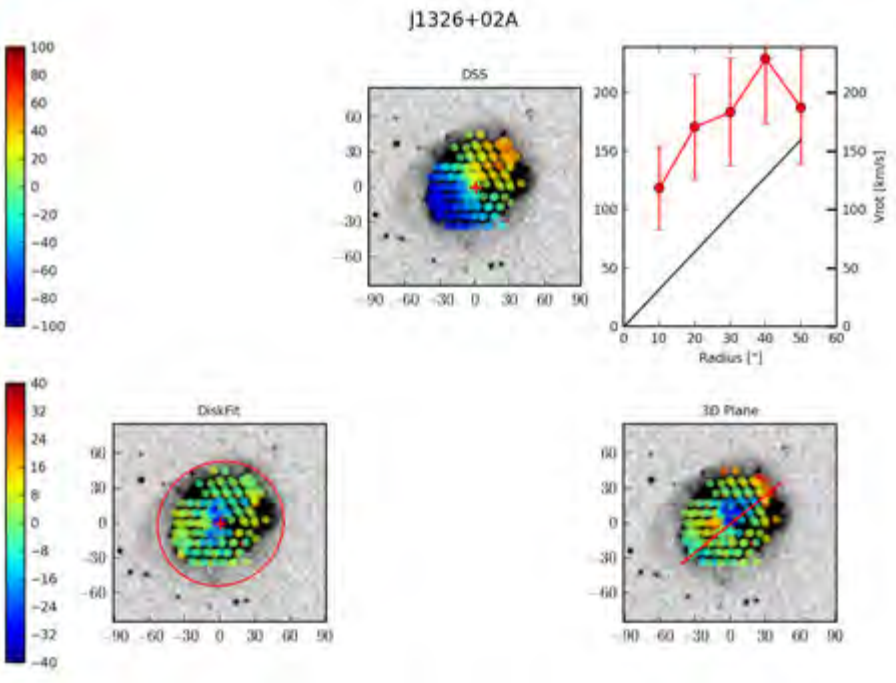

Figure A49: Same as Figure 4.1, but velocity and residual velocity fields are overlayed over DSS images of J1326+02A

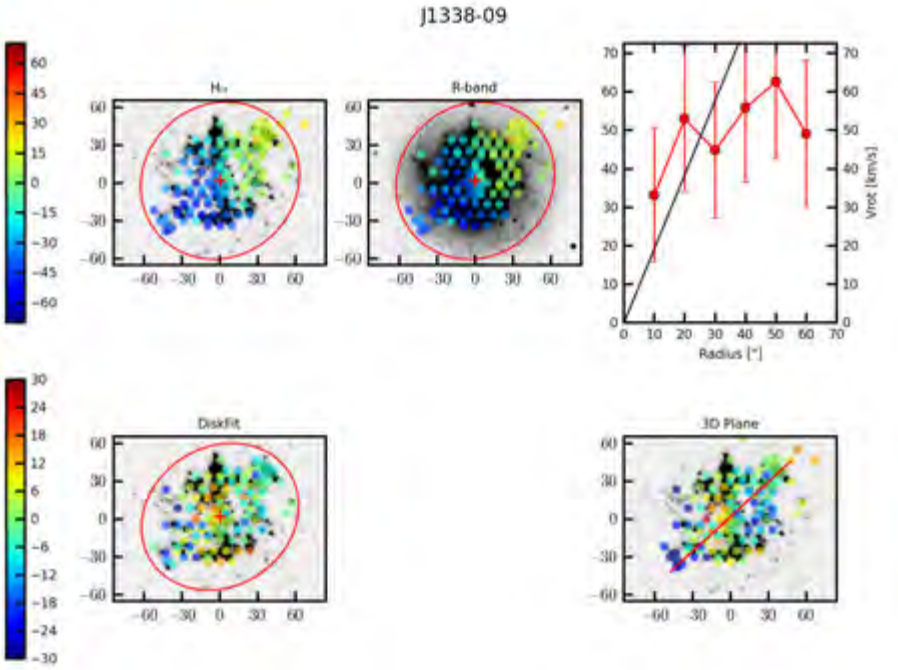

Figure A50: Same as Figure 4.1, but for J1338-09

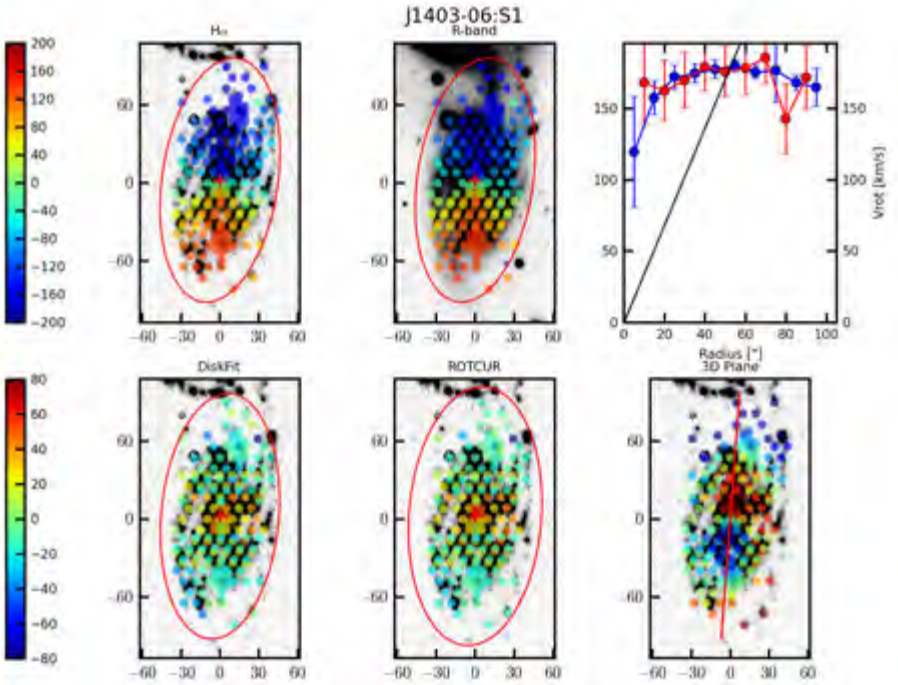

Figure A51: Same as Figure 4.1, but for J1403-06:S1

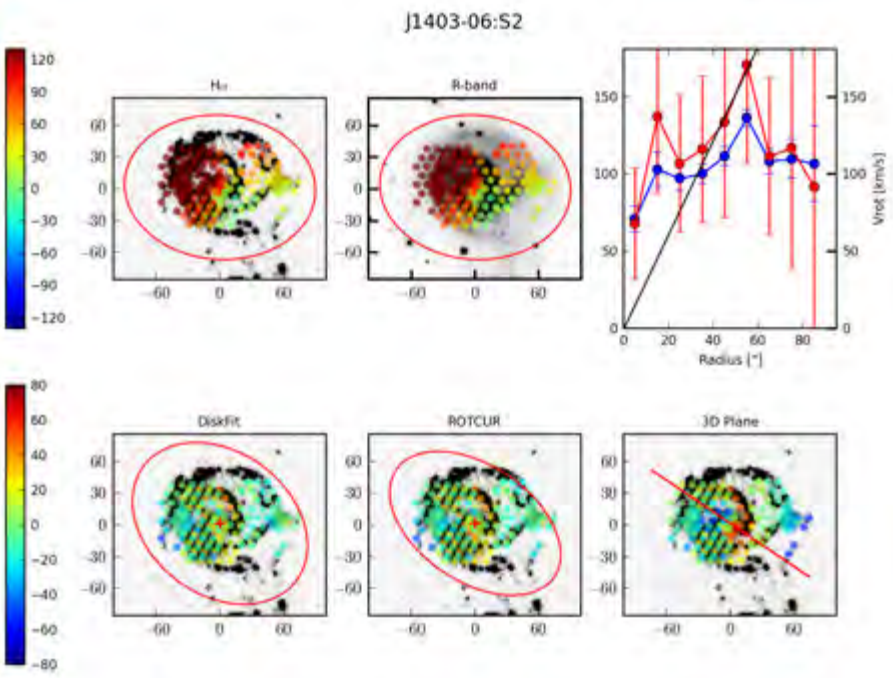

Figure A52: Same as Figure 4.1, but for J1403-06S2

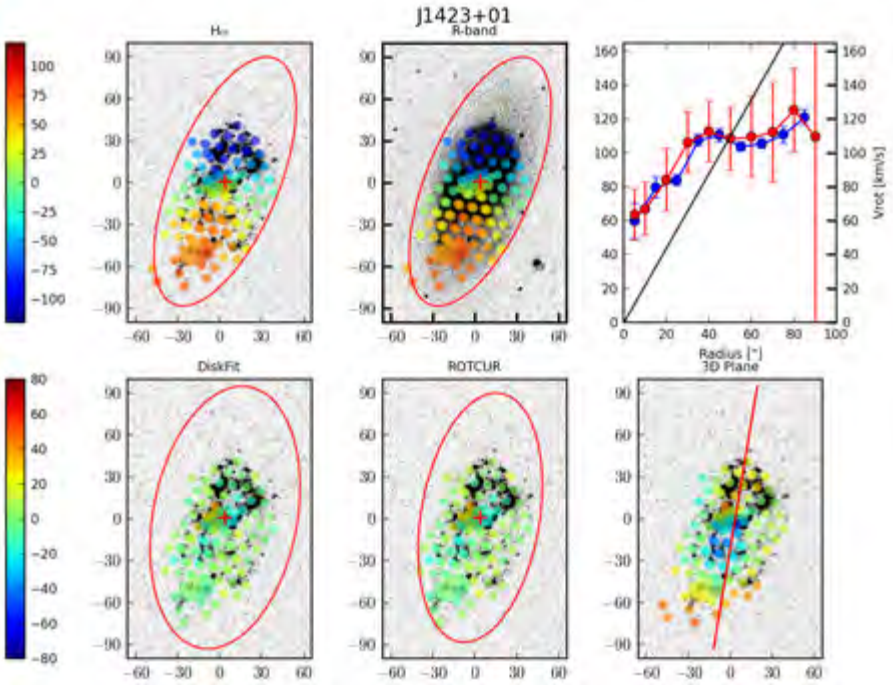

Figure A53: Same as Figure 4.1, but for J1423+01

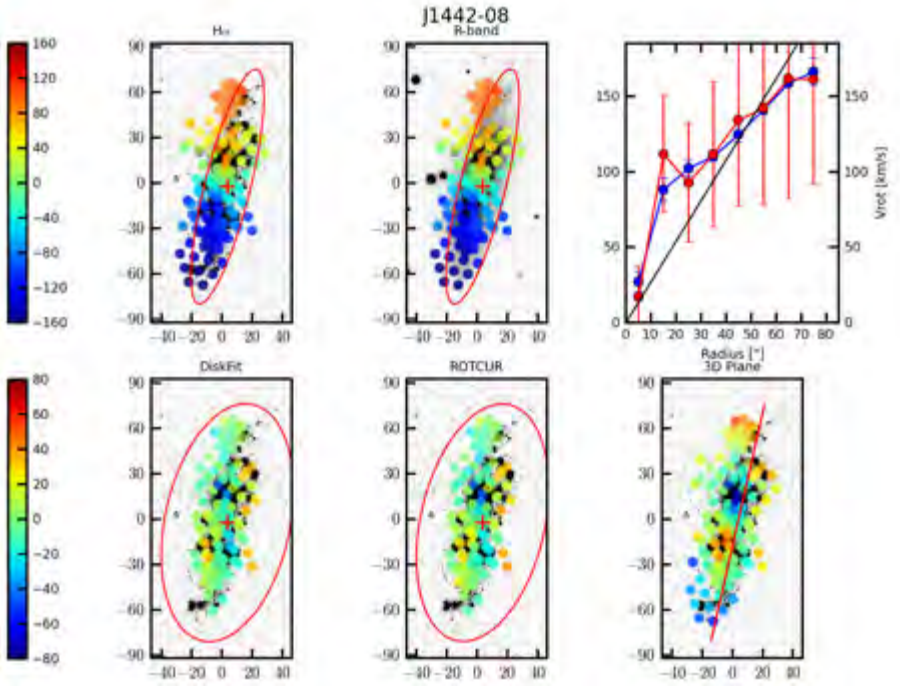

Figure A54: Same as Figure 4.1, but for J1442-08

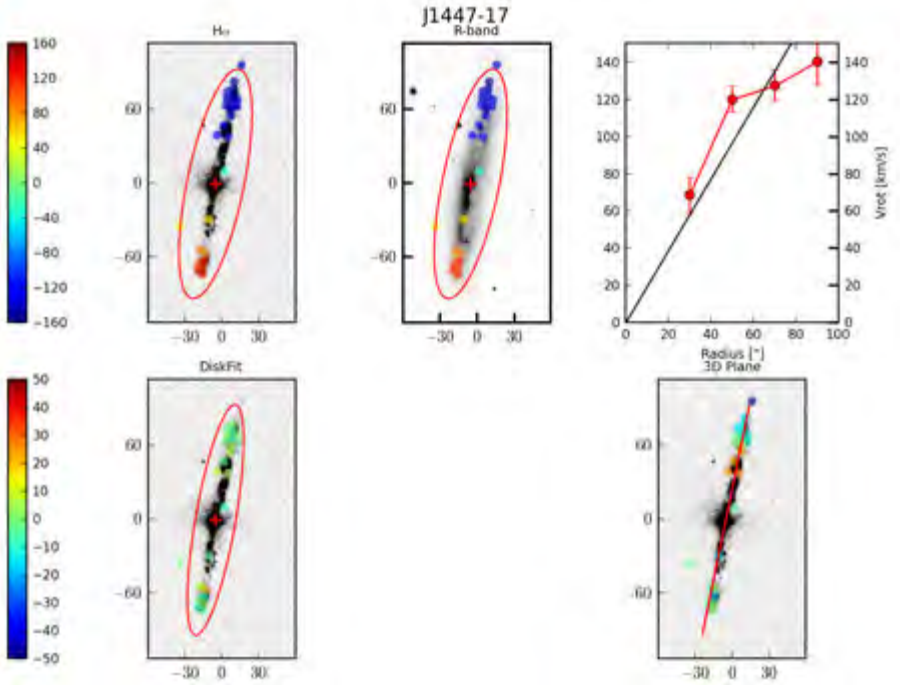

Figure A55: Same as Figure 4.1, but for J1447-17

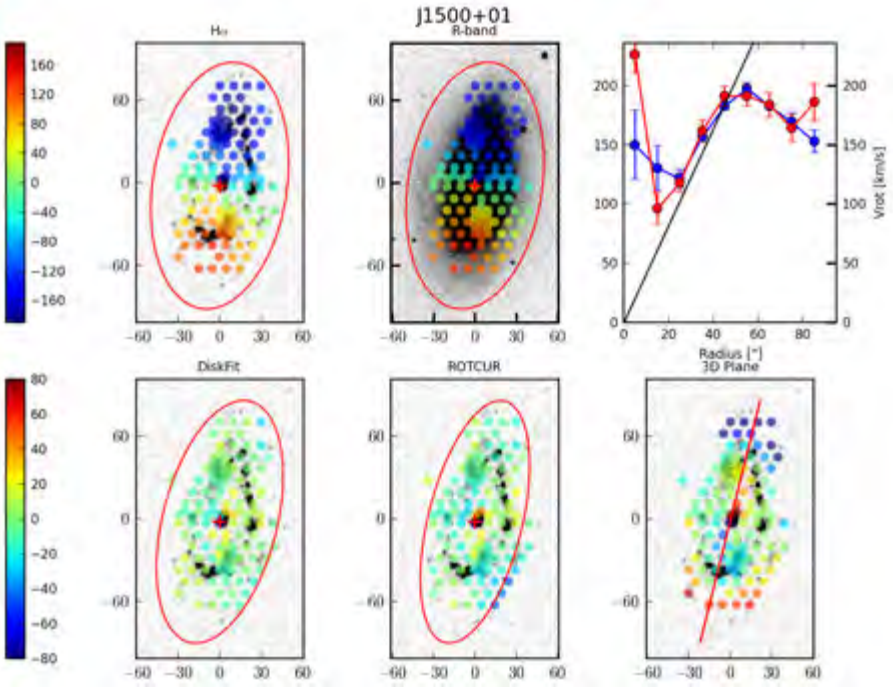

Figure A56: Same as Figure 4.1, but for J1500+01

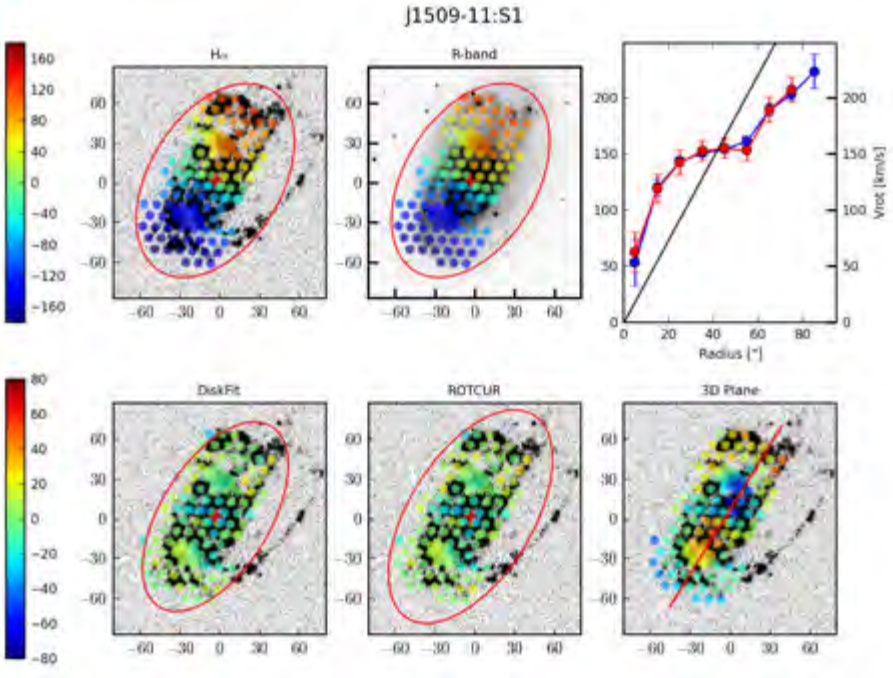

Figure A57: Same as Figure 4.1, but for J1509-11S1

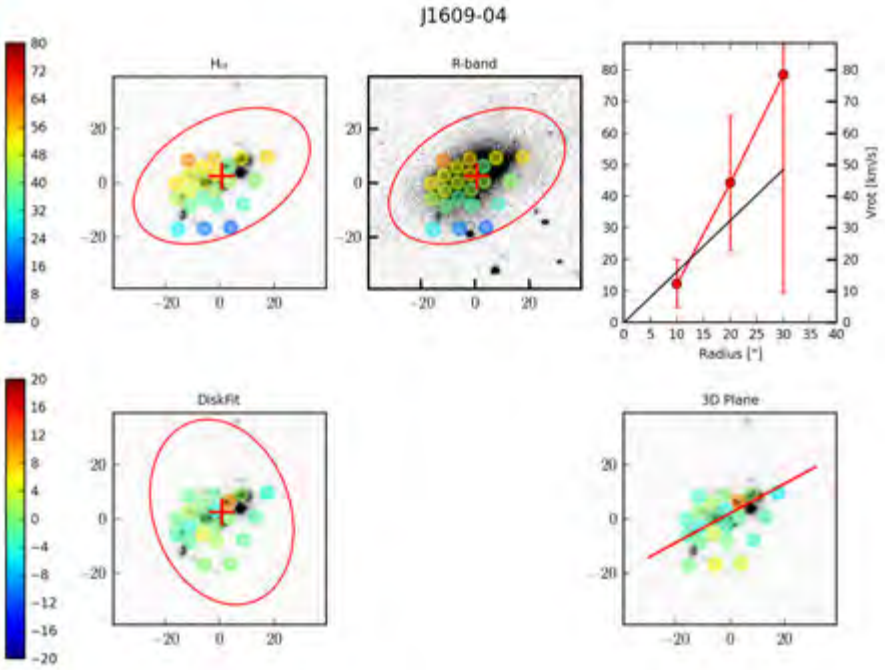

Figure A58: Same as Figure 4.1, but for J1609-04

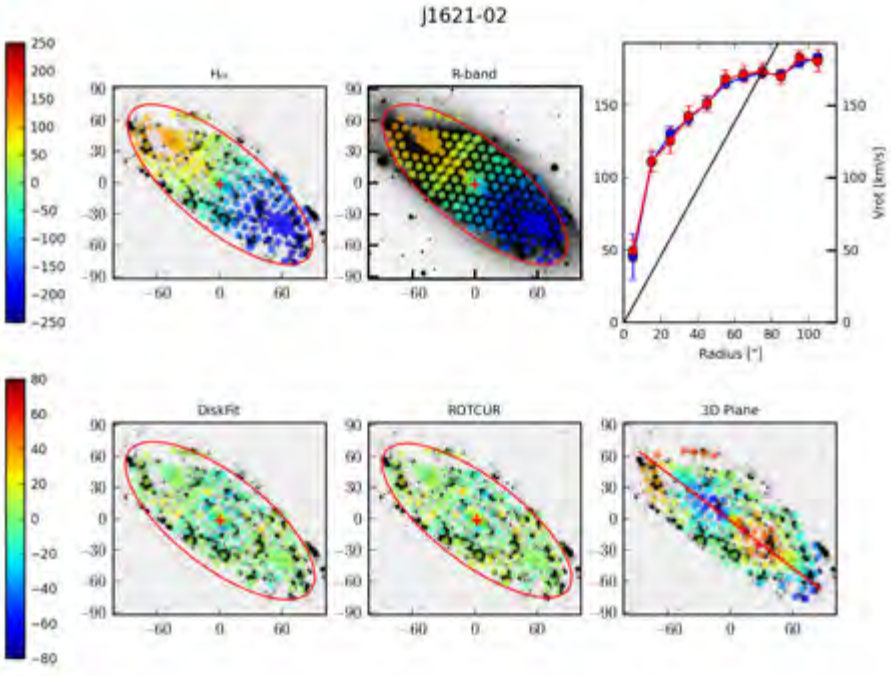

Figure A59: Same as Figure 4.1, but for J1621-02

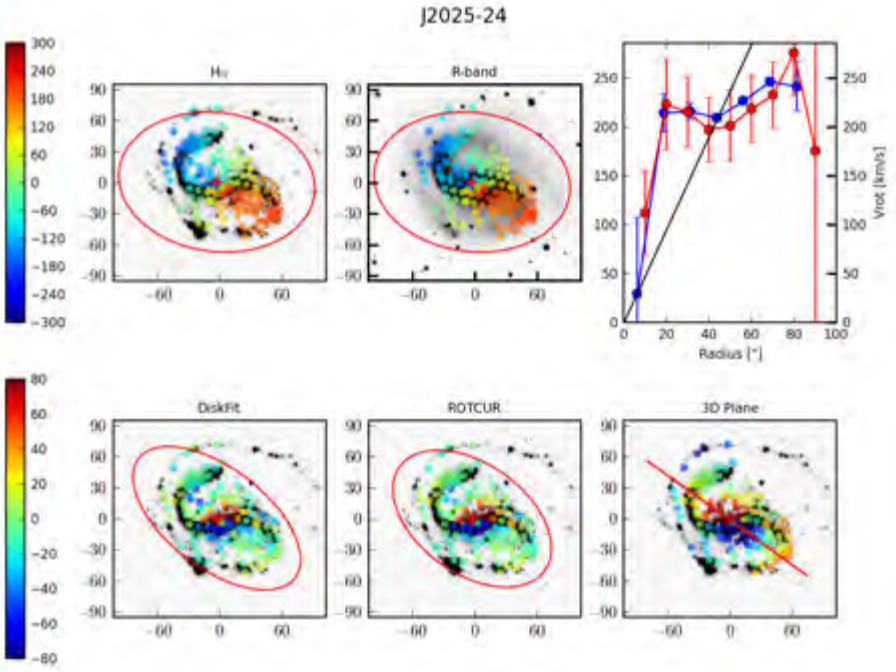

Figure A60: Same as Figure 4.1, but for J2025-24

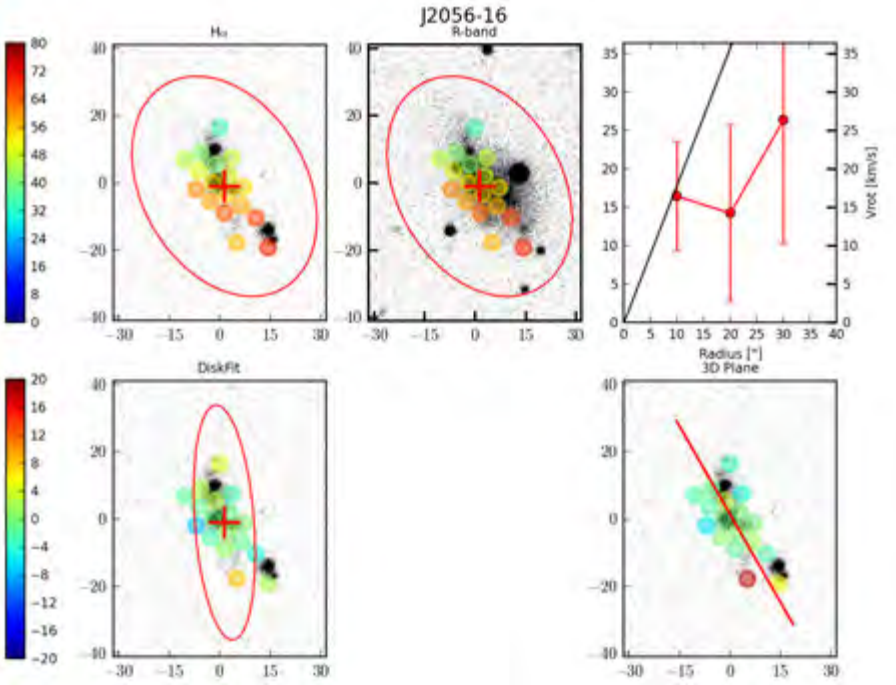

Figure A61: Same as Figure 4.1, but for J2056-16

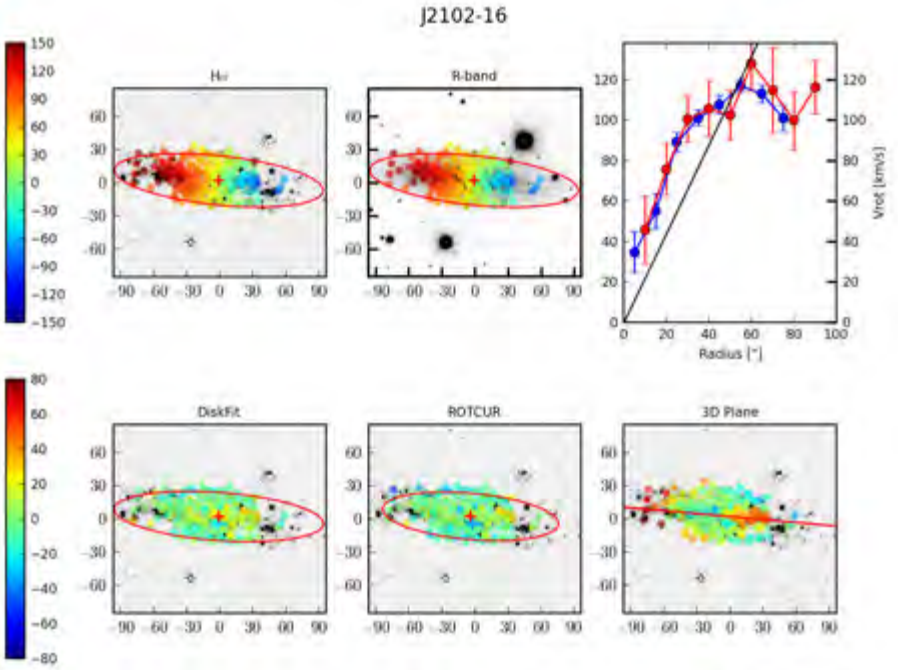

Figure A62: Same as Figure 4.1, but for J2102-16

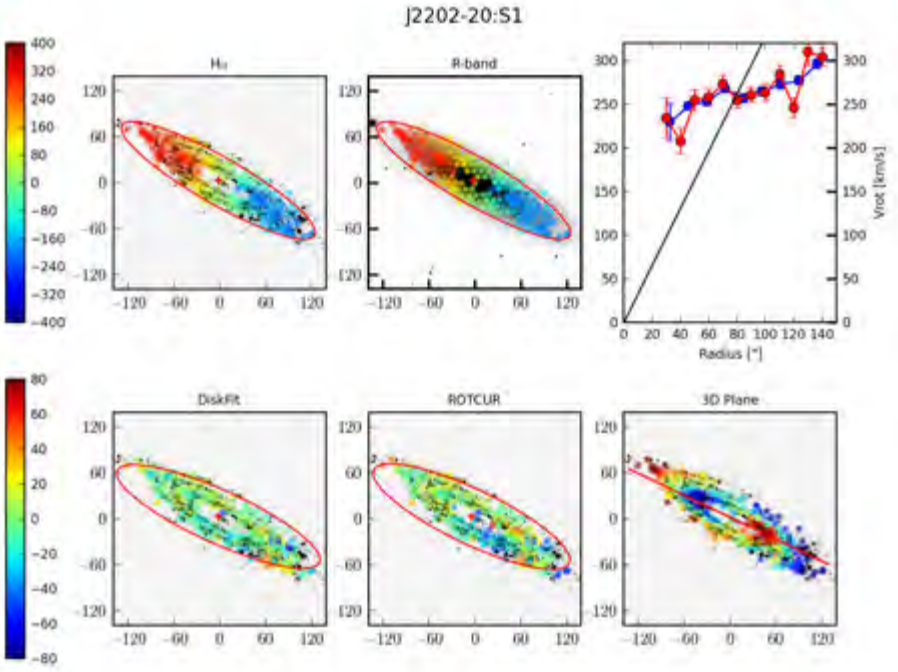

Figure A63: Same as Figure 4.1, but for J2202-20S1

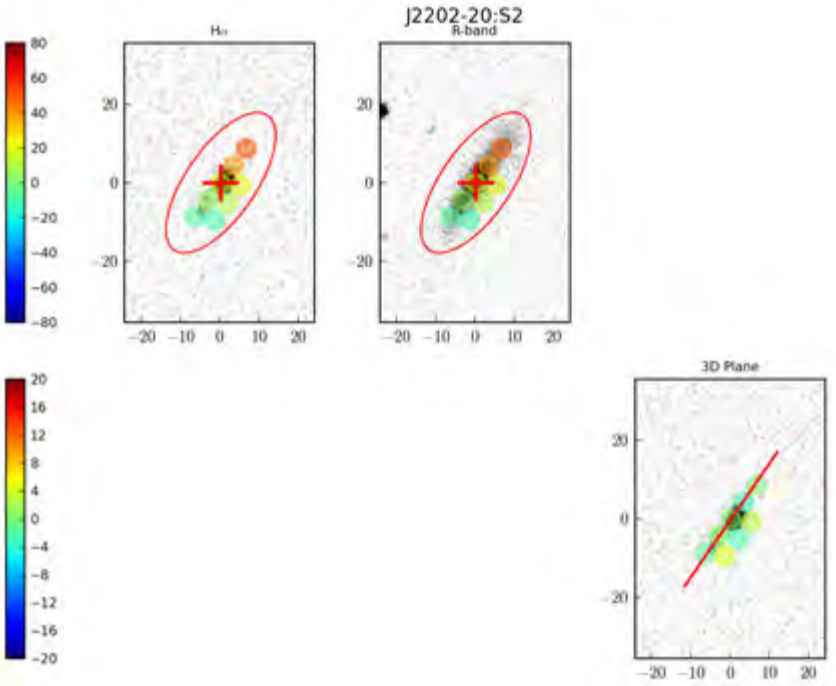

Figure A64: Same as Figure 4.1, but for J2202-20S2

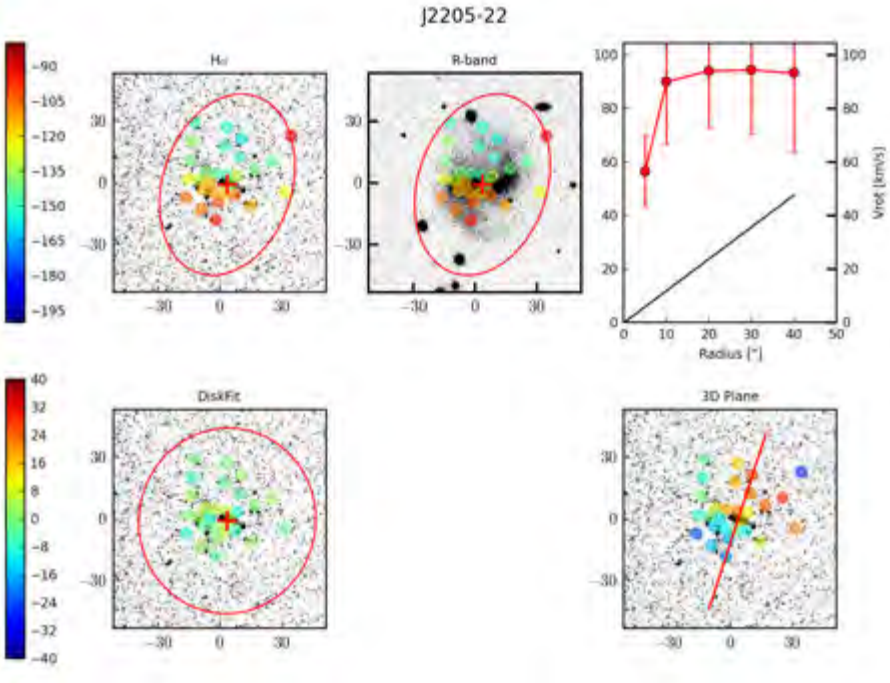

Figure A65: Same as Figure 4.1, but for J2205-22

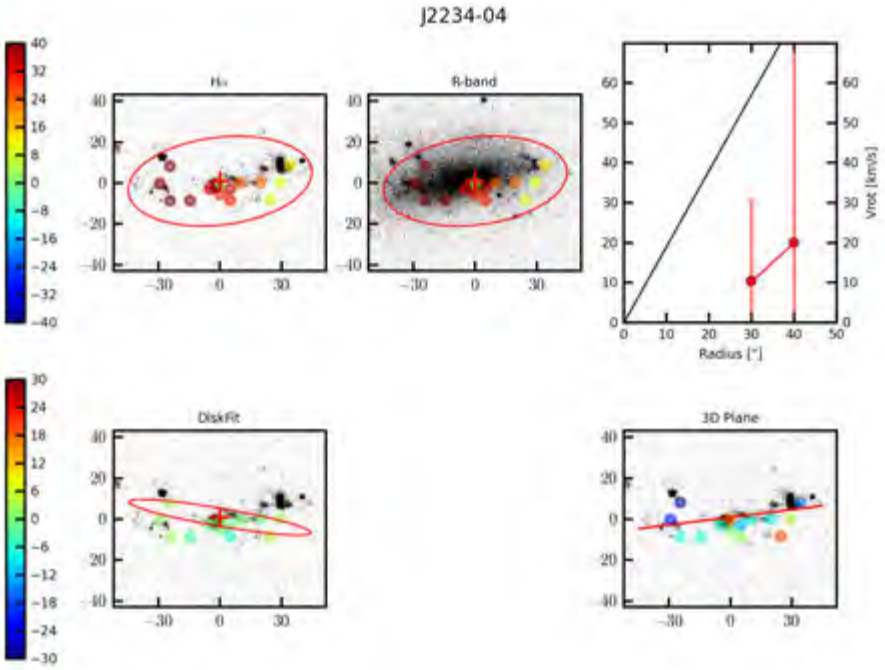

Figure A66: Same as Figure 4.1, but for J2234-04

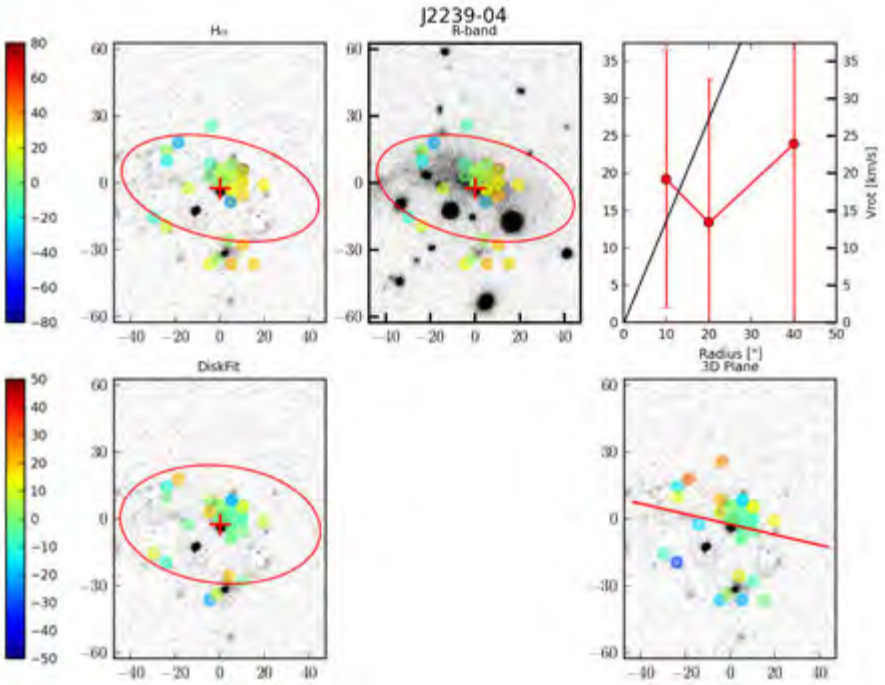

Figure A67: Same as Figure 4.1, but for J2239-04

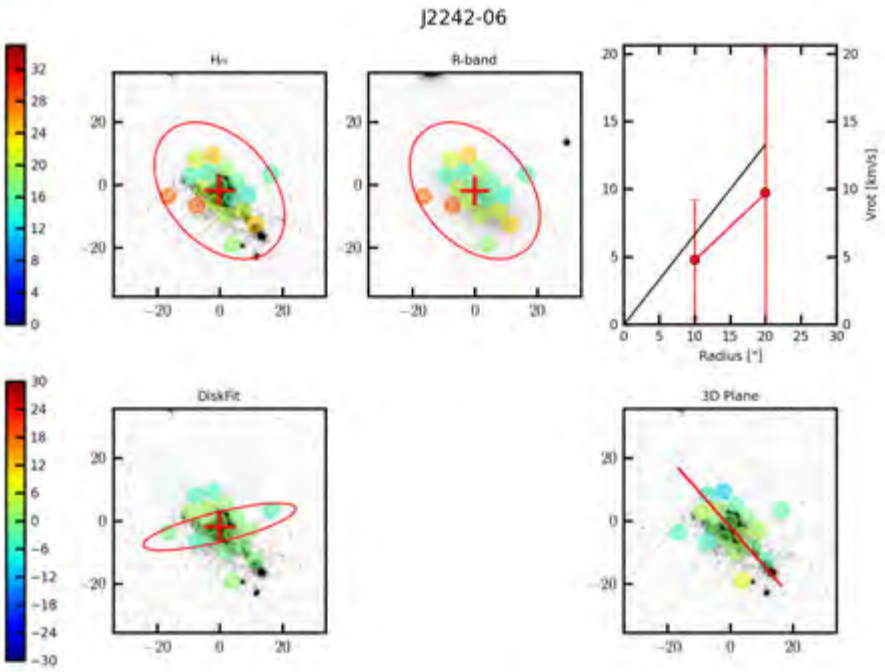

Figure A68: Same as Figure 4.1, but for J2242-06

Every reasonable effort has been made to acknowledge the owners of copyright material. I would be pleased to hear from any copyright owner who has been omitted or incorrectly acknowledged.

Bibliography

Allen, J.T., et al., 2015, MNRAS, 446, 1567

Argyle, E., 1965, ApJ, 141, 750

Babcock, H.W., 1939, Lick Observatory Bullentin, 19, 41

Bagnuolo, W.G., 1976, Ph.D. Thesis, California Institute of Technology, Pasadena.

Baldry, I.K., et al., 2004, ApJ, 600, 681

Barnes, E.I., & Sellwood, J.A., 2003, ApJ, 125, 1164

Barrera-Ballesteros, J.K., et al., 2014, A&A, 568, 70

Baum, W.A., 1959, PASP, 71, 106

Begeman, K., 1987, Ph.D. Thesis, Kapteyn Institute

Bell, E.F., et al., 2003, ApJS, 149, 289

Berkhijsen, E.M., 1977, A&A, 57, 9

Bershady, M. et al., 2004, PASP, 116, 565

Bershady, M.A., et al., 2005, AJS, 156, 311

Bershady, M.A., et al., 2008, SPIE, 7014, 0

Bershady, M.A., et al., 2011, ApJ, 2011, 739, 47

Bertin, G, & Romeo, A.B., 1988, A&A, 195, 105

Bertin, G., Lin C.C., Lowe, S.A., Thurstans, R.P., 1989, ApJ, 338, 78

Bertin, G., Lin C.C., Lowe, S.A., Thurstans, R.P., 1989, ApJ, 338, 104

Bierman,L., 1955, *Gas Dynamics of Cosmic Clouds*, 212, North Holland Pub. Co., Amsterdam, The Netherlands

Bigiel, F., et al. 2008, AJ, 136, 2846

Bigiel, F., et al. 2011, ApJ, 730, 13

Binggeli, B., & Popescu, C.C., 1995, A&A, 298, 63

Binney, J. 1978, MNRAS, 183, 779

Binney, J., & Tremaine, S., 1994, *Galactic Dynamics*, first ed., Princeton University Press: Princeton, USA

Bizyaev, D.V., & Mitronova, S., 2002, A&A, 389, 795

Bizyaev, D.V., & Mitronova, S., ApJ, 702, 1567

Bizyaev, D.V., et al., 2014, ApJ, 787, 24

Blais-Ouellette, S., et al., 1999, AJ, 118, 2123

Blitz, L. & Rosolowsky, E., 2006, ApJ, 650, 933

Bloemen, J.B.G., et al., 1986, A&A, 154, 25

Boissier, S., Prantzos, N., Boselli, A., Gavazzi, G., 2003, MNRAS, 346, 1215

Bolatto, A.D., et al., 2008, ApJ, 686, 948

Bolatto, A.D., Wolfire, M., Leroy A.K., 2013, ARA&A, 51, 207

Boselli, A., Lequeux, J., & Gavazzi, G., 2004, A&A, 428, 409

Boselli, A., et al., 2013, A&A, 550, 114

Bosma, A. 1978, Ph.D. Thesis, Groningen University

Bosma, A. 1981, AJ, 86, 1825

Bosma, A., 1981, AJ, 86, 1791

Bottema, R., 1993, A&A, 275, 16

Bottema, R., 1997, A&A, 328, 517

Bottema, R., & Verheijen, M.A.W., 2002, A&A, 388, 793

Bouché, N., et al. 2007, ApJ, 671, 303

Boulanger, F., et al., 1988, ApJ, 332, 328

Boulanger, F., et al., 1990, ApJ, 364, 136

Bournaud, F., Elmegreen, B.G., 2009, ApJ, 694, 158

Brinchmann J., et al., 2004, MNRAS, 351, 1151

Broeils, A., 1992, Ph.D. thesis, Univ. of Groningen

Bruzual, G., Charlot, S., 2003, MNRAS, 344, 1000

Buat, V., Deharveng, J.M., Donas, J., 1989, A&A, 223, 42

Buat, V., 1992, A&A, 264, 444

Buat, V., & Deharveng, J.M., 1988, A&A, 195, 60

Buat, V., & Xu, C., 1996, A&A, 306, 61

Buat, V., et al., 2011, A&A, 529, A22

Burbidge, E.M., & Burbidge G.R., 1960, ApJ, 132, 30

Burke, B.F., 1957, AJ, 62, 90

Burstein, D., Heiles, C., 1982, AJ, 87, 1165

Burstein, D., Rubin, V.C., 1985, ApJ, 297, 423

Bushouse, H.A., 1987, ApJ, 320, 49

Caldwell, J., et al., 1992, ApJ, 370, 526

Caldú-Primo, A., et al., 2013, AJ, 146, 150

Calzetti, D., Kinney, A.L., Storchi-Bergmann, T., 1994, ApJ, 429, 582

Calzetti, D., et al., 2007, ApJ, 666, 870

Calzetti, D., et al., 2010, ApJ, 714, 1256

Cappellari, M., et al., 2011, MNRAS, 413, 813

Cardelli, J.A., Clayton, G.C., Mathis, J.S., 1989, ApJ, 345, 245

Carignan, C., 1983, Ph.D. Thesis, Australian Natinal University

Carignan, C., & Freeman, K.C., 1985, ApJ, 294, 494

Carignan, C., & Freeman, K.C., 1988, ApJ, 332, 33

Carignan, C., Sancisi R., & van Albada, T.S., 1988, ApJ, 95, 37

Casertano, S., & van Gorkom, J.H., 1991, AJ, 101, 1231

Chabrier, G., 2003, ApJ, 586, 133

Ciotti, L., 1991, A&A, 249, 99

Ciotti, L., & Bertin G., 1999, A&A, 352, 447

Cluver, M.E., et al., 2013, ApJ, 765, 93

Cluver, M.E., et al., 2014, ApJ, 782, 90

Cohen, J.G. 1976, ApJ, 203, 587

Côté, S., Carignan, C., & Freeman, K.C. 2000, ApJ, 120, 3027

Colombo, D., et al., 2014, ApJ, 784, 3

Combes, F., Gottesman, S.T., Weliachew, L., 1977, A&A, 59, 181

Corbelli, E., 2003, MNRAS, 342, 199

Corradi, R.L.M., & Capaccioli, M., 1990, A&A, 237, 36

Cortese, L., et al., 2016, MNRAS, 459, 3574

Courtès, G., 1960, Ann. Astrophys., 23, 1151

Courtès, G., 1964, AJ, 69, 325

Courteau, S., 1997, AJ, 114, 2402

Courteau, S., et al., 2007, ApJ, 671, 203

Cowie, L.L., 1981, ApJ, 245, 66

Cox, D.P., 2005, ARA&A, 43, 337

Curtis, H.D. 1933, *Handbuch der Astrophysik*, 5, Part 2, 853, Springer, Berlin

Cutri, R., et al., 2011, *WISE* Explanatory Supplement

Dabrowski, I., 1984, CJP, 62, 1639

Daddi, E., et al., 2010, ApJL, 714, 118

Deharveng, J.M., et al., 1994, A&A, 289, 715

de Blok, W.J.G., McGaugh, S.S., Rubin, V.C., 2001, AJ, 122, 239

de Blok, W.J.G., & Walter, F., 2006, AJ, 131, 363

de Blok, W.J.G., et al., 2008, AJ, 136,2648

de Jong, T. et al., 1984, ApJ, 278, 67

de Vaucouleurs, G., 1954, Observatory, 74, 23

de Vaucouleurs, G., 1955, AJ, 60, 126

de Vaucouleurs, G., 1960, AJ, 65, 51

de Vaucouleurs, G., 1960, ApJ, 131, 574

Dib, S., 2011, ApJ, 737, 20

Dib, S., et al., 2013, MNRAS, 436, 3727

Dickman, R.L., Snell, R., & Schloerb, F.P., 1986, ApJ, 309, 326

Dieter, N.H., 1960, ApJ, 132, 49

Disney, M., & Phillipps, S., 1985, 216, 53

Donas, J. & Derhaveng, J.M., 1984, A&A, 140, 325

Donas, J., et al., 1987, A&A, 140, 12

Dopita, M.A., 1985, ApJ, 295, 5

Dopita, M.A., & Ryder, S., 1994, ApJ, 430, 163

Doyle, M.T., et al., 2005, MNRAS, 361, 34

Dunn, J.M., 2010, MNRAS, 408, 392

Dutton, A.A., van den Bosch, F.C., & Dekel, A., 2010, MNRAS, 405, 1690

Eeales, S.A., et al., 2010, A&A, 518, 62

Einasto, J., 1972, ApJL, 11, 195

Elbaz, D., et al., 2007, A&A, 468, 33

Elmegreen, B.G. 1979, ApJ, 231, 372

Elmegreen, B.G. 1989, ApJ, 338, 178

Elmegreen, B.G. 1992, in *Star Formation in Stellar Systems*, ed. G. Tenorio-Gagle, M. Prieto, & F. Sánchez, p. 381, Cambridge University Press, Cambridge

Elmegreen, B.G. 1993, ApJ, 411, 170

Elmegreen, D.M., & Parravano, A., 1994, ApJ, 435, 121

Elmegreen, B.G., 1997, RevMexAA, 6, 165

Elmegreen, B.G., 2000, ApJ, 530, 277

Elmegreen, B.G., 2011, ApJ, 737, 10

Emerson, J.P. 1977, *Recent Results in infrared Astrophysics*, Moffett Field Symposium, ed. P.Dyal, p.61

Epinat, B., et al., 2008, MNRAS, 388, 500

Epstein, E.E., 1962, Ph.D. Thesis, Harvard

Erroz-Ferrer, S., et al., 2016, MNRAS, 458, 1199

Ewen, H.I., & Purcell, E.M., 1951, Nature, 168, 356

Fanelli, M.N. O'Connell, R.W., & Thuan, T.X., 1988, ApJ, 334, 665

Farrah, D., et al., 2007, ApJ, 667, 149

Ferguson, A.M.N., et al., 1998, ApJ, 506, 19

Field, G.B., Goldsmith, D.W., & Harbing, H.J., 1969, ApJ, 155, 149

Filho, M.E., et al., 2016, ApJ, 820, 109

Freedman, W.R., 1984, Ph.D. Thesis, University of Toronto

Freeman, K.C., 1970, ApJ, 160, 811

Fukugita, M., Hogan, C.J., & Peebles, P.J.E., 1998, ApJ, 503, 518

Gallagher, J.S., & Hunter, D.A., 1984, ARA&A, 22, 37

Gao, Y., & Solomon, P.M., 2004, ApJ, 606, 271

García-Lorenzo, B., et al., 2015, A&A, 573, 59

Gatley,I., Becklin, E.E., 1981, IAUS96, ed. G.C. Wynn-Williams, D.P. Cruikshank, p.261. Dordrecht : Reidel

Genzel, R., et al., 2010, MNRAS, 407, 2091

Gil de Paz, A., et al., 2007, ApJS, 173, 185

Giovanelli, R., et al., 1994, AJ, 107, 2036

Goldreich, P. & Lynden-Bell, D., 1965, MNRAS, 130, 97

Guiderdoni, B., 1987, A&A, 172, 27

Guo, K., Zheng, X.Z., Wang, T., et al., 2015, ApJL,808, 49

Hamajima, K., & Tosa, M., 1975, PASJ, 27, 561

Hanish, D.J., et al., 2006, ApJ, 649,150

Hartwick, F.D.A., 1971, Ap, 163, 431

Hayes, M.P., et al., 1998, AJ, 115, 62

Haynes, M.P., & Giovanelli, R., 1984, 89, 758

Heiderman, A., et al., 2010, ApJ, 723, 1019

Helmboldt, J.F., et al., 2004, ApJ, 613, 914

Helou, G., Khan, I.R., Malek, L., & Boehmer, L., 1988, ApJS, 68, 151

Helou, G., 1986, ApJ, 311, 33

Heyer, M.H., Corbelli, E., Schneider, S.E. et al., 2004, ApJ, 602, 723

Hirashita, H., Buat, V., & Inoue, A.K., 2003, A&A, 410, 83

Hodge, P.W., & Hitchcock, J.L., 1966, PASP, 78, 79

Hodge, P., 1971, ARA&A, 9, 35

Hodge, P., 1973, PASP, 85, 286

Holmberg, E., 1946, Meddelanden fran Lunds Astronomiska Observatorium Series II, 117, 3

Holmberg, E., 1958, Meddelanden fran Lunds Astronomiska Observatorium Series II, 136, 1

Holmberg, E., 1975, *Galaxies and the Universe*, p.123, University of Chicago Press (Stars and Stellar Systems. Volume 9), Chicago, IL, USA

Houck,J.R., et al., 2004, ApJS, 154, 211

Houck, J.R., et al., 2007, ApJ, 671, 323

Hopkins, P.F., et al., 2013, MNRAS, 430, 1910

Hubble, E., 1922, ApJ, 56, 400

Hubble, E., 1922, CMWCI, 241,1

Hubble, E., 1926, ApJ, 64, 321

Huchra, J.P. 1977, ApJ, 217, 928

Hughes, A., Meidt, S.E., Colombo, D., et al., 2013, ApJ, 779, 46

Humason, M.L., Mayall, N.U., & Sandage, A.R., 1956, AJ, 61, 97

Humason, M.L., 1936, ApJ, 83, 10

Hunter, D.A., & Gallagher, J.S., 1986, PASP, 98, 5

Hunter, D.A., Elmegreen, B.G., & Baker, A.L., 1998, ApJ, 493, 595

Hutchmeier, W., 1975, A&A, 45, 259

Ianjamasimanana, R., et al., 2012, AJ, 144, 96

Israel, F.P., & van der Kruit, P.C., 1974, A&A, 32, 363

Israel, F.P., & Koornneef, J., 1979, ApJ, 230, 390

Jarrett, T.H., et al., 2000, AJ, 119, 2498

Jarrett, T.H., et al., 2011, ApJ, 735, 112

Jarrett, T.H., et al., 2012, AJ, 144, 68

Jarrett, T.H,. et al., 2013, AJ, 145, 6

Jog, C.J., & Solomon, P.M., 1984, ApJ, 276, 114

Jog, C.J. 1996, MNRAS, 278, 209

Jogee, S., Scoville, N., Kenney, J.D.P. 2005, ApJ, 630, 837

Jones, D.H., et al., 2004, MNRAS, 355, 747

Kalnajs, A.J., 1983, in Internal Kinematics of Galaxies, IAU Symposium 100, ed. E. Athanassoula (Dordrecht: Reidel), p. 87

Kamphuis, J., & Sancisi, R., 1993, A&A, 273, 31

Kaneda, H., et al., 2008, ApJ, 684, 270

Karim, A., et al., 2011, ApJ, 730, 61

Kauffmann, G., et al., 2003, MNRAS, 341, 54

Kennicutt, R.C., 1983, ApJ, 272, 54

Kennicutt, R.C., & Kent, S.M. 1983, AJ, 88, 109

Kennicutt, R.C., et al. 1987, AJ, 93, 1011

Kennicutt, R.C. 1989, ApJ, 344,685

Kennicutt, R.C., Tamblyn, P., Congdon, C.E., 1994, ApJ, 435, 22

Kennicutt, R.C. 1998, ApJ, 498,541

Kennicutt, R.C., et al., 2003, PASP, 115, 928

Kennicutt, R.C., et al., 2007, ApJ, 671, 333

Kennicutt, R.C., et al., 2009, ApJ, 703, 1672

Kennicutt, R.C. & Evans, N.J. 2012, ARA&A, 50, 531

Kerr, F.J., 1957, 62, 93

Kim, W-T., & Ostriker, E.C., 2001, ApJ, 559, 70

Kim, W-T., & Ostriker, E.C., 2007, ApJ, 660, 1232

Kleinmann, D.E., Low, F.J, 1970, ApJL, 159, L165

Komugi, S., et al., 2005, PASJ, 57, 733

Kormendy, J., Kennicutt, R.C., 2004, ARA&A, 42, 603

Kravtsov, A.V., et al., 1998, ApJ, 502, 48

Kregel, M., van der Kruit, P.C., de Grijs, R. 2002, MNRAS, 334, 646

Kroupa, P., 2002, Science, 295, 82

Kruijssen, J.M.D., & Longmore S.N. 2013, MNRAS, 435, 2598

Kruijssen, J.M.D., et al., 2014, MNRAS, 440, 3370

Krumholz, M.R., & McKee, C.F., 2005, ApJ, 630, 250

Krumholz, M., & Burkert, A. 2010, ApJ, 724, 895

Krumholz, M.R., Dekel, A., McKee, C.F. 2012, ApJ, 745, 69

Krumholz, M.R., et al., 2015, MNRAS, 453, 739

Kuzio de Naray,R., et al., 2012, MNRAS, 427, 2523

Lada, C.J., et al., 2010, ApJ, 724, 687

Lada, C.J., et al., 2012, ApJ, 745, 190

Larson, R.B., 1983, *Highlights Astronomy*, 6, 191

Larson, R.B., 1988, in *Galactic and Extragalactic Star Formation*, ed. R.E. Pudritz and M. Fich (Dordrecht:Reidel), p. 459

Leger, A., & Puget, J.L., 1984, A&A, 137, L5

Lehnert M.D. & Heckman T.M., 1996, ApJ, 472, 546

Lelli, F., Fraternali, F., Verheijen, M., 2013, MNRAS, 433, 30

Lelli, F., 2014, *Galaxies*, 2, 292

Lelli, F., Traternali, F., Verheijen, M. 2014, A&A, 563, 27L

Lequeux, J., 1980, *Star Formation, 10th Advanced Course of the Swiss Society of Astronomy and Astrophysics*, Saas-Fee, Geneva, Observatory

Lequeux, J., et al., 1981, A&A, 103, 305

Leroy, A.K., et al., 2008, AJ, 136, 2782

Leroy, A.K., et al., 2009, AJ, 137, 460

Leroy, A.K., et al., 2012, AJ, 144, 3

Leroy, A.K., et al., 2013, AJ, 146, 19

Li, A., & Draine, B.T., 2001, ApJ, 554, 778

Li, A., & Draine, B.T., 2002, ApJ, 572, 232

Lian, J.H., et al., 2016, MNRAS, 451, 1130

Lilly, S.J., et al., 2013, ApJ, 772, 119

Liu, G., et al., 2011, ApJ, 735, 63

Lonsdale, C.J., & Helou, G. 1987, ApJ, 314, 513

Lord, S.D.,1987, Ph.D. Thesis, Massachusetts University

Madore, B.F., et al., 1974, ApJ, 191, 317

Madore, B.F., 1977, MNRAS, 178, 1

Marcelin, M., Boulesteix, J., & Georgelin Y., 1983, A&A, 128, 140

Markwardt, C.B., 2009, ASPC, 411, 251

Marlowe, A.T., Meurer, G.R., & Heckman, T., 1999, ApJ, 522, 183

Martin, C.L., & Kennicutt, R.C., 2001, ApJ, 555, 301

Matthews, L.D., Gallagher, J.S., & van Driel W., 1999, AJ, 118, 2751

Mattoda, A.,I., Allamandola, I.J, & Hudgins, D.M., 2005, ApJ, 629, 1183

Mayall, N.U., 1939, Lick Observatory Bulletin, 497

Mayall, N.U., 1958, *The Large Scale structure of the Galactic System*, 23, ed. N Roman, Cambridge

Mayall, N.U., 1960, An.Ap, 23, 344

McKee, C.F., & Ostriker, J.P., 1977, ApJ, 218, 148

McCuskey, S.W., 1941, 94, 468

Meidt, S.E., et al., 2012, ApJ, 744, 17

Melioli, C., & de Gouveia Dal Pino, E.M., 2015, ApJ, 812, 90

Melioli, C., Brighenti, F., & D'Ercole, A., 2015, MNRAS, 446, 299

Meyer, M.J., et al., 2004, MNRAS, 350, 1195

Meyer, M.J., et al., 2008, MNRAS, 391, 1712

Meurer, G.R., et al., 1995, AJ, 110, 2665

Meurer, G.R., Staveley-Smith, L. & Killeen, N.E.B. 1998, MNRAS, 300, 705

Meurer, G.R., et al., 2006, ApJS, 165, 307

Meurer, G.R., et al., 2009, ApJ, 695,765

Meurer, G.R., Zheng, Z., de Blok, W.J.G., 2013, MNRAS, 429, 253

Mezger, P.G., & Smith L.F. 1976,*Stars and galaxies from observational points of view*, p.369

Mezger, P.G., 1978, A&A, 70, 565

Miller, G.E., & Scalo, J.M. 1979, ApJS, 41, 513

Mogotsi, K.M., et al., 2016, AJ, 151, 15

Molinari, S., et al., 2011, ApJ, 735, 33

Momose, R., 2012, Ph.D. Thesis, University of Tokyo

Momose, R., et al., 2013, ApJ, 772, 13

Monet, D.G., Richstone, D.O., & Schechter, P.L., 1981, apJ, 245, 454

Moré, J., 1978, *Numerical Analysis*, 630, 105

Morgan, W.W., 1958, *La Structure et l'Evolution de L'Univers*, 297, (Stoops, Brussels)

Morgan, W.W., & Mayall, N.U., 1957, PASP, 69, 291

Mosenkov, A.V., Sotnikova, N. Ya., Reshetnikov, V.P., 2010, MNRAS, 401, 559

Mould, J.R., et al. 2000, ApJ, 529, 786

Muhleman, D.O., & Walker, R.G., 1964, AJ, 69, 95

Muller, C.A., & Oort, J.H. 1951, Nature, 168, 357

Munch, G., 1960, An.Ap, 23, 357

Murakami, H., et al. 2007, PASJ, 59, 369

Narayanan, D., et al., 2012, MNRAS, 421, 3127

Neugebauer, G., 1984, ApJ, 278, 1

Noeske, K.G., et al., 2007, ApJL, 660, L43

Noordemeer, E., & Verheijen, M.A.W, 2007, MNRAS, 381, 1463

O'Donnell, J.E., 1994, ApJ, 437, 262

Oh, S-H., et al. 2011, AJ, 141, 193

Oh, S-H., et al. 2015, AJ, 149, 180

Oke, J.B., & Gunn, J.E., 1983, ApJ, 266, 713

Oort, J.H., 1940, ApJ, 91, 273

Oort, J.H., 1974, IAUS 58, 375

Ostriker, J.P., Peebles, P.J.E., Yahil, A., 1974, ApJ, 193, 1

Page, T., 1952, ApJ, 116, 63

Pease, F.G., 1916, PNAS USA, 2, 517

Pease, F.G., 1918, PNAS USA, 4, 21

Perez-Gonzalez, P.G., et al., 2006, ApJ, 648, 987

Pettit, E. 1954, ApJ, 120, 413

Pety, J., et al., 2005, A&A, 435, 885

Pilbratt, G.L. et al. 2010, A&A, 518, L1

Planck Collaboration et al., 2014, A&A, 566, A54

Prescott, M.K.M., et al., 2007, ApJ, 668, 182

Primack, J.R., 2003, NuPhS, 124, 3

Puche, D., & Carignan, C., 1991, ApJ, 378, 487

Quirk, W.J., 1972, ApJ, 176, 9

Rafikov, R.R., 2001, MNRAS, 323, 445

Rahman, N., et al. 2011, ApJ, 730, 72

Rahman, N., et al. 2012, ApJ, 745, 183

Randriamampandry, T.H., Combes, F., Carignan, C., & Deg, N., 2015, MNRAS, 454, 3743

Randriamampandry, T.H., Deg, N., Carignan, C., Combes, F. &, Spekkens, K.S., 2016, (in press)

Rathborne, J.M., et al., 2014, ApJ, 795, 25

Rickard, L.J., & Harvey, P.M., 1982, BAAS, 14, 611

Rieke, G.H., & Low, F.J., 1972, ApJ, 176, 95

Rieke, G.H., & Low, F.J., 1975, ApJ, 200, 67

Rieke, G.H., & Lebofsky, M.J., 1978, ApJ, 220, L37

Rieke, G.H., & Lebofsky, M.J., 1982, *The Galactic Center*, ed. G.R. Riegler, R.D. Blandford, p. 194. New York: Am. Inst. Phys.

Rieke, G.H., et al., 2009, ApJ, 692, 556

Rix, H-W., Guhatakhurta, P., Colless, M., & Ing, K, 1997, MNRAS, 285, 779

Roberts, M.S., 1962, AJ, 67, 437

Roberts, M.S., 1963, ARA&A, 1, 149

Roberts, M.S., Rots, A.H., 1973, A&A, 26, 483

Roberts, M.S., & Whitehurst, R.N, 1975, ApJ, 201, 327

Rodighiero, G., et al., 2011, ApJL, 739, LL40

Rogstad, D.H., & Shostak, S.S., 1971, A&A, 176, 315

Romeo, A.B., 1992, MNRAS, 256, 307

Romeo, A.B., & Wiegert, J., 2011, MNRAS, 416, 1191

Romeo, A.B., & Falstad, N., 2013, MNRAS, 433, 1389

Roychowdhury, S., et al., 2013, MNRAS, 436, 104

Rubin, V.C., Thonnard, N., & Ford, W.K., 1978, ApJ, 225, 107

Rubin, V.C., Ford, W.K., & Thonnard, N., 1980, ApJ, 238, 471

Saintonge, A., et al., 2012, ApJ, 758, 73

Sakamoto, K., et al., 1999, ApJ, 525, 691

Salim, S., et al. 2007, ApJS, 173, 267

Sandage, A., 1961, *Hubble Atlas of Galaxies*, Washington: Carnegie Institution of Washington, Pub 618

Sandage, A., 1975, in *Galaxies and the Universe*, ed. Sandage A, Sandage M., Kristian J., p. 839., The University of Chicago Press (Stars and Stellar Systems vol 9) , Chicago & London

Sanduleak, N. 1969, AJ, 74, 47

Sanchez, S.F., et al., 2012, A&A, 538, 8

Sánchez-Janssen, R, Méndez-Abreau, J., & Aguerri, J.A.L., 2010, MNRAS, 406, 65

Sancisi, R., 1976, A&A, 53, 159

Sancisi, R., 2004, IAUS, 220, 2338

Sanders, D.B., Solomon, P.M., & Scoville, N.Z., 1984, ApJ, 276, 182

Sauvage, M., & Thuan, T.X., 1992, ApJL, 396, L69

Schawinski, K., et al.,MNRAS, 440,889

Schaye, J., 2004, ApH, 609, 667

Schmidt, M., 1959, ApJ, 129, 243

Schmidt, M., 1963, ApJ, 137, 758

Schlegel, D.J., Ph.D. Thesis, University of California, Berkely

Schlegel, D.J., Finkbeiner D.P., Davis, M. 1998, ApJ, 500, 525

Schommer, R.A., & Bothun, G.D., 1983, AJ, 88, 577

Schreiber, C., et al., 2015, A&A, 575, A74

Schruba, A., et al., 2011, AJ, 142, 37

Schuster, K.F., et al., 2007, A&A, 461, 143

Scoville, N.Z., et al., 1983, ApJ, 271, 512

Searle, L., Sargent, W.L.W., & Bagnuolo, W.G., 1973, ApJ, 179, 427

Sellwood, J.A. & Sanchez, R.Z., 2010, MNRAS, 404, 1733

Sellgren, K., 1984, ApJ, 277, 623

Serra, G., Puget, J.L., & Ryter, C.E., 1980, A&A, 84, 220

Shapiro, K.L., Gerssen, J., van der Marel, R.P., 2003, AJ, 126, 2707

Shapley, H., *Bulletin of the Harvard College Observatory*, 908

Shapley, H., Nature, 142, 715

Sheth, K., et al., 2005, ApJ, 632, 217

Shi, Y., et al., 2011, ApJ, 733, 87

Shu, F.H., 1968, Ph.D. Thesis, Harvard University

Silk, J., 1987, in *Star Forming Regions*, ed. M. Peimbert and J. Jugaku (Dordrecht:Reidel), p.663

Silk, J., 1997, ApJ, 481, 703

Skibba, R.A., et al., 2011, ApJ, 738, 89

Skillman, E.D., 1987, in *Star Formation in Galaxies*, ed. C.J. Lionsdale, p.263

Slipher, V.M., 1914, Lowell Observatory Bulletin, 2, 66

Smith, LF., Bierman, P., & Mezger, P.G., 1978, A&A, 66, 65

Smith, B.J., et al., 2007, AJ, 133, 791

Sofue, Y., & Rubin, V., 2001, ARA&A, 39, 137

Soifer, B.T., et al., 1984, ApJ, 278, 71

Sparre, M., et al., 2015, 447, 3548

Speagle, J.S. et al., 2014, ApJS, 214, 15

Spekkens, K. & Sellwood, J.A., 2007, ApJ, 664,204

Spergel, D.N., et al., 2003, ApJS, 148, 175

Spinrad, H., 1962, AJ, 135, 715

Spitzer, L., 1941, ApJ, 93, 369

Spitzer, L., 1941, ApJ, 94, 232

Spitzer, L., & Baade, W., 1951, ApJ, 113, 413

Spitzer, L., 1968, *Nebulae and Interstellar Matter*, ed. B.M. Middlehurst, L.H. Aller., University of Chicago Press, Chicago, ILL USA

Staveley-Smith, L., Davies, R.D., & Kinman, T.D., 1992, MNRAS, 258, 334

Stebbins, J., & Whitford, A.E., 1952, ApJ, 115, 285

Stein, W.A., Soifer, B.T., 1983, 21, 177

Strateva, I., et al., 2001, AJ, 122, 1861

Sung, E.-C., et al., 1998, ApJ, 505, 199

Suzuki, T, et al., 2010, A&A, 521, 48

Swaters, R.A., et al., 2002, A&A, 390, 829

Swaters, R.A., et al., 2009, A&A, 493, 871

Swaters, R.A., 2009, Ph.D. Thesis, Unviersity of Groningen

Tacconi, L.J., & Young J.S., 1986, ApJ, 308, 600

Talbot, R.J. 1971, ApL, 8, 111

Talbot, R.J., & Arnett, W.D., 1975, ApJ, 197, 551

Talbot, R.J. 1980, ApJ, 235, 821

Tamburro, D., et al. 2008, AJ, 136, 2871

Tammann, G.A., 1980, Dwarf Galaxies, Tarenghi M., Kjar, M, eds, ESO, Geneva, 45

Tammann, G.A., 1984, Dwarf Galaxies, Meylan G, Prugniel, P., eds, ESO, Garching, 3

Tamburro, D., et al., 2009, AJ, 137, 4424

Tan, J.C. 2000, ApJ, 536, 173

Taylor, E.N., et al., 2011, MNRAS, 418, 1587

Telesco C.M. & Harper D.A., 1980, ApJ, 235, 392

Thackeray, A.D., 1948, Observatory, 68, 22

Tielens, A.G.G.M. 2008, ARA&A, 46, 289

Tinsley, B.M. 1968, ApJ, 151, 547

Tinsley, B.M. 1972, A&A, 20, 383

Tifft, W.G. 1958, PASP, 70, 463

Tokunaga, A.T., & Vacca, W.D., 2005, PASP, 117, 421

Toomre, A. 1964, ApJ, 139, 1217

Tubbs, A.D., & Sanders, S.R.H., 1979, ApJ, 230, 736

Tully, R.B., 1974, ApJS, 27, 415

Tully, R.B., & Fisher, J.R., 1977, A&A, 54, 661

Tully, R.B., et al., 1978, A&A, 63, 37

Turner, E.L, & Ostriker, J.P., 1977, ApJ, 217, 24

Twarog, B.A. 1980, ApJ, 242, 242

van Albada, T.S., & Sancisi, R., 1986, Phil. Trans. R. Soc. London, Ser. A, 320, 447

van Albada, T.S., et al., 1985, ApJ, 295, 305

van den Bergh, S., 1957, ZA, 43, 263

van de Hulst, H.C., 1945, An.Ap., 8, 1

van de Hulst, H.C., Raimond, E., & van Woerden, H., 1957, Bulletin of the Astronomical Institutes of the Netherlands, 14, 1

van der Hulst, J.M., et al., 1993, AJ, 106, 548

van der Kruit, P.C., & Allen, R.J., 1978, 16, 103

van der Kruit, P.C., 1976, A&A, 49, 161

an der Kruit, P.C., & Allen, R.J., 1978, ARA&A, 16, 103

van der Kruit, P.C., 1988, A&A, 192, 117

van Dokkum, P.G., 2001, PASP, 113,1420

van Driel, W., 1987, Ph.D. Thesis, University of Groningen

Vangioni-Flam, E., et al., 1980, A&A, 90, 73

Verheijen, M.A.W., 1997, Ph.D. thesis, University of Groningen

Verley, S., et al. 2010, A&A, 510, 64

Volders, L., 1959, Bulletin of the Astronomical Institutes of the Netherlands, 1, 323

Vorontsov-Velyaminov, B.A., 1959, *Atlas and Catalogue of Interacting Galaxies*, Moscow: Sternberg Institute, Moscow state University

Wang, B., Silk, J., 1994, ApJ, 427, 759

Walter, F., et al., 2007, ApJ, 661, 102

Walter, F., et al., 2008, AJ, 136, 2563

Warner, P.J., Writght, M.C., Baldwin, J.E., 1973, MNRAS, 163, 163

Walterbos, R.A.M., & Greenawalt, B., 1996, ApJ, 460, 696

Whipple, F.L., 1946, ApJ, 104,1

Wiegel, A.K., Schawinski, K., & Bruderer, C., 2016, MNRAS, 459, 2150

Wijesinghe, D.B., et al., 2011, MNRAS, 410, 2291

Willick, J.A., et al., 1997, ApJ, 486, 629

Willick, J.A., & Strauss, M.A. 1998, ApJ, 507, 64

Wolf, M., 1914, *Vierteljahresschrift Astron. Gesell.*, 49, 162

Wolfire, M.G., McKee, C.F., Hollenbach, D., et al. 2003, ApJ, 587, 278

Wong, T., & Blitz, L. 2002, ApJ, 569, 157

Wong, I.O., 2006, Ph.D. Thesis, University of Melbourne

Wong, I.O., Meurer, G.R., Zheng, Z., et al., 2016, MNRAS, 460, 1106

Wright, E.L., et al., 2010, AJ, 140, 1868

Wuyts, S., et al., 2011, ApJ, 742, 96

Wyder, et al., 2009, ApJ, 696, 1834

Wyse, R.F. 1986, ApJ, 311, 41

Wyse, R.F.G., & Silk, J., 1989, ApJ, 339, 700

York, D.G., et al., 2000, AJ, 120, 1579

Young, J.S., & Scoville, N.Z. 1982, ApJL, 260, 11

Zheng, Z., et al. 2013, MNRAS, 434, 3389

Zhu, Y.N., et al., 2008, ApJ, 686, 155

Zwicky, F., 1959, *Handbuch der Physik*, 53, 373, Berlin:Springer-Verlag